A COMPUTATIONAL STUDY OF THE MOLECULAR AND ELECTRONIC STRUCTURE OF SELF-ASSEMBLED NANOCRYSTAL SUPERLATTICES

A Dissertation

Presented to the Faculty of the Graduate School

of Cornell University

In Partial Fulfillment of the Requirements for the Degree of

Doctor of Philosophy

by

Ananth Prakash Kaushik

January 2013

A COMPUTATIONAL STUDY OF THE MOLECULAR AND ELECTRONIC STRUCTURE OF SELF-ASSEMBLED NANOCRYSTAL SUPERLATTICES

Ananth Prakash Kaushik, Ph.D.

Cornell University 2013

Nanocrystalline solids have become the subject of intense study due to their unique optical properties and their capacity to form self-assembled superlattices making them suitable for use in a variety of applications such as solar cells, light-emitting devices, etc. In this thesis, we have used atomically and molecularly explicit Molecular Dynamics simulations to create a fundamental understanding of these systems. We have shown that size of the nanocrystal and the grafting density of ligands can affect the morphology of the ligand corona. We have studied the links between processing conditions and the resultant symmetry of the superlattice, whether face-centered cubic (fcc) or body-centered cubic (bcc) structures. Our results for the free energies of the system provide definitive proof of a clear dependence of preferred superlattice symmetry on the ratio of ligand length to nanocrystal size. We also provide a fundamental understanding regarding the effect of microstructural details on the electronic structure and charge transfer properties in nanocrystal superlattices. Specifically, we have shown that the charge transfer rate between nanocrystals depends on the shape and ratio of the areas of the different facets on the nanocrystal core. The impact of this kind of study is the provision of key insights into molecular-scale information about the relative roles of surface-bound ligands and nanoparticle cores that are very difficult to determine experimentally. This insight, we hope, can be leveraged to ably guide future experimental studies.

BIOGRAPHICAL SKETCH

Ananth Kaushik was born in Bangalore, India in 1984. He completed his schooling till the 10th grade at Sri Aurobindo Memorial School in Bangalore and moved to The National College Jayanagar in Bangalore to complete his 11th and 12th grades. Following his high school education, he enrolled in undergraduate Chemical Engineering at the Indian Institute of Technology Madras in Chennai. He spent the summer of his third year interning at the Indian Institute of Science in Bangalore working under Professor Jayant Modak in the Chemical Engineering department. He graduated from IIT Madras after completing his final year research under Professor Arun Tangirala. The fall of 2007 saw his arrival at Cornell University where he pursued his PhD under the guidance and tutelage of Professor Paulette Clancy. He was awarded the Austin Hooey Graduate Excellence Recognition Award in 2012.

This thesis is dedicated to my family and friends.

ACKNOWLEDGMENTS

I would like to thank my advisor, Paulette Clancy, for her guidance and expertise during my PhD. She was very approachable, helpful, understanding and an invaluable source of support throughout my studies here, at Cornell.

I would like to thank Tobias Hanrath and his research group for their invaluable insight in the field of colloidal nanocrystals. His research group helped me join and conduct experiments at the Cornell High Energy Synchotron Source (CHESS) and in the lab. I would also like to thank Tobias Hanrath for the many stimulating discussions we have had which have been an invaluable source of knowledge. I would also like to thank David Bindel who served as my minor advisor for his help and guidance in understanding the algorithmic side of my computational work. I would also like to acknowledge King Abdullah University of Science and Technology (KAUST) who provided my funding and Intel Corporation for providing computers.

Many thanks also to undergraduate students Matthew Windt and Hassei Takahashi without whose dedicated work, this thesis would not have been possible. I would specially like to thank Luc Burnier, Alex Tait and Thibault Cremel who provided valuable data for chapters 2, 4 and 5 respectively. Dr. Joseph Goose deserves special mention for his academic mentorship and his friendship during my early years here.

My colleagues and friends made my research here both stimulating and enjoyable. Krishna Iyengar, Rebecca Cantrell, Brian Koo, Alex Raymunt, Jonathan Saathoff and all the Clancy group members played an integral part in both my academic and social life at Cornell. Finally, a thank you to my friends Samanvaya Srivastava, Vikram Singh, Tushar Desai, Amit Halder and Sasikrishnan Subramaniam with whom I have shared many an exciting adventure which I am certain I will reminisce fondly for many years to come.

TABLE OF CONTENTS

LIST OF FIGURES

LIST OF TABLES

CHAPTER 1

Introduction

A crystalline material which is size-restricted in three dimensions such that the electron wave functions are confined within its volume is called a quantum dot (QD). Nanocrystals (NCs) or Quantum Dots (QDs) are tiny crystals of metals, semiconductors, and magnetic material consisting of hundreds to a few thousand atoms each. Their size ranges from 2-3 nm to about 20 nm. The nanoscale dimensions of quantum dots allow quantum confinement of electrons and holes, leading to the remarkable observation that the properties of quantum dots of the same material are size-dependent. Generally, the smaller the size of the crystal, the greater the difference in energy between the highest valence band and the lowest conduction band becomes. Therefore more energy is needed to excite the dot, and consequently, more energy is released when the crystal returns to its resting state. Considerable research has been undertaken to try to create mono-disperse arrays of nanocrystals in controlled geometries, not only to exploit their unusual or unique electronic properties, but also to fabricate practical devices for applications such as solar cells, sensors, *etc.* Integrated circuits (ICs) might be further miniaturised by using NCs. QDs can be applied as stable fluorescent indicators in biological research; core-shell quantum structures of CdSe/ZnS have a very high luminescence quantum yield (up to 100%) [1]. Since they can easily be attached to DNA [2] or proteins by a sulphide bond they can act as a luminescing label to monitor biological reactions. Semiconductor colloids can also be employed in photocatalysis; TiO_2 colloids irradiated with UV-light can photo-oxidize organic contaminants [3]. Nanocrystal assemblies have been explored for a variety of applications, including solar cells [4-8, 9-14], field effect transistors [15-

17], light- emitting diodes [18-19], photo-detectors [20] and chemical sensors [21]. Nanocrystals formed from lead salts such as PbSe, PbTe, PbS, *etc.*, have received considerable attention in recent years [4-8], mainly due to their large Bohr exciton radius and narrow, yet size-tunable, band gaps [24]. Their ability to provide significant electronic coupling at close proximity [25] and to self-assemble into a variety of large two-dimensional (2D) and three-dimensional (3D) superlattices [22, 23, 26] make them ideally suited for use in photovoltaic devices and other optoelectronic applications [13, 14, 16, 17].

1.1 Energy Bands in Bulk Semiconductor Crystals

To discuss the origin of energy bands in bulk semiconductors and electron tunneling between two systems, a single electron in a crystal is considered [1]. The time-independent Schrödinger equation for an electron can be written as,

$$\frac{\hbar^2}{2m_e}\nabla^2\Psi(x,y,z) + U(x,y,z)\Psi(x,y,z) = E\Psi(x,y,z) \qquad (1)$$

where m_e is the mass of the free electron, E is the kinetic energy, and $\nabla^2 = \left\{\frac{\partial^2}{\partial x^2} + \frac{\partial^2}{\partial y^2} + \frac{\partial^2}{\partial z^2}\right\}$. In the free-electron approach, the potential energy of the electron due to the crystal lattice of core ions $U(x,y,z)$ is neglected, and is taken as a constant. In that case, the solution of equation (1) for Ψ(x, y, z) can be denoted as,

$$\Psi_{\vec{k}}(\vec{r}) = \frac{1}{\sqrt{V}} e^{i\vec{k}.\vec{r}} \qquad (2)$$

where $\vec{r}$ is the position vector (x, y, z), and $\vec{k}$ is the wave-vector (k_x, k_y, k_z). The plane periodic wave, $e^{i\vec{k}.\vec{r}}$, has a constant amplitude in any plane perpendicular to $\vec{k}$ and is periodic along lines parallel to $\vec{k}$ with a wavelength $\lambda = 2\pi/k$. The prefactor $\frac{1}{\sqrt{V}}$ is due to

the normalization condition, which requires that the particle must be present in the sample volume, V. The linear momentum of the electrons, is $\vec{p} = \hbar\vec{k}$ and the kinetic energy is given by

$$E\left(\vec{k}\right) = \frac{\hbar^2 k^2}{2m_e} \tag{3}$$

where m_e is the rest mass of the electron.

The occupation of the electron levels is in accordance with the Pauli exclusion principle. At 0 K, all energy levels below the Fermi-energy (E_F) are occupied by two electrons of opposite spin. The occupation of electron energy levels under thermal equilibrium at T > 0 K can be derived from statistical thermodynamics. The probability that an energy level, E, is occupied by an electron is given by the Fermi-Dirac function,

$$f(E) = \frac{1}{1 + e^{(E-\mu_e)/k_B T}} \tag{4}$$

where μ_e is the electrochemical potential (Fermi-level) and k_B the Boltzmann constant. The free electron model can be refined by taking into account the scattering of the electron waves by the periodic lattice potential energy, U(x,y,z). The distance between the centers of the core ions in the x direction is denoted as dx. Electrons with low energy have wavelengths much longer than d_x; however, at higher energy, there are free electrons with wavelengths λ_e obeying the condition for Bragg reflection

$$\frac{\lambda_e}{2} \cong \frac{d_x}{q} \qquad (q = \pm 1, \pm 2, \dots) \tag{5}$$

Due to Bragg scattering on the periodic lattice potential, propagation of these electrons will be prohibited in the x-direction and standing waves are formed. Two standing waves can be constructed by a linear combination of the waves travelling in the positive and

negative x–directions. The electron density corresponding to the first standing wave is centered at the core ions, that of the second wave between the core ions. The two standing waves correspond to considerably different energies. The energy difference can be estimated by a perturbation method; it is equal to the periodic lattice potential in the x-direction. The scattering of the free electrons by the periodic lattice leads to discontinuities in the E(k) relationship for k values at around $k = q\frac{\pi}{d}$ These discontinuities lead to the formation of energy bands, separated by energy gaps, as presented in Fig. 1.1. This derivation for the x-direction can be used in a similar way for the y and z-directions. The E(k) relationship for free electrons is a good approximation for most of the electrons in a band, except for those near the edge of the Brillouin zones.

1.2 Quantum Confinement in Nanocrystals

An exciton can be defined as the bound state of an electron-hole pair, which is due to a Coulomb interaction between the charge carriers. The distance between the electron and the hole is the Bohr radius of the exciton, a_B, and is given by,

$$a_B = \frac{4\pi\varepsilon_0\varepsilon_\infty\hbar^2}{m_0 e^2}\left(\frac{1}{m_e^*} + \frac{1}{m_h^*}\right) \quad (6)$$

where m_e^* and m_h^* are the effective electron and hole masses, respectively, and ε_∞ is the high frequency relative dielectric constant of the medium. The resulting Bohr radius is much larger than that of a hydrogen atom, since the effective masses are considerably smaller than the mass of the electron at rest, m_0, and ε_∞ is considerably larger than 1. Values for a_B for typical semiconductors are in the range 10-100 Å. Nanocrystals have crystalline order and dimensions corresponding to some tens of a

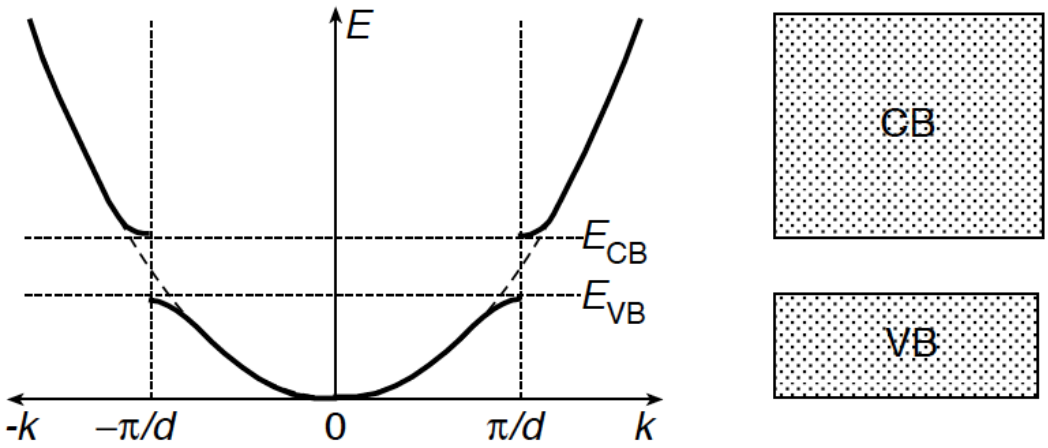

Figure 1.1: The formation of energy bands in a macroscopic semiconductor due to Bragg reflection of the electrons on the periodic lattice of the crystal. Illustration from [1].

lattice constant in each direction. Electron scattering within the lattice leads to band formation, as for macroscopic crystals. However, the free electron wavelength and the Bohr radius can be comparable to or even larger than the crystal dimensions. This means that the nanocrystal acts as a quantum box for quasiparticles. The symmetry of the box is important for the solution of the Schrödinger equation. In the literature, a spherical symmetry is often used. For simplicity, we consider a rectangular box of dimensions L_x, L_y, and L_z surrounded by infinitely high energy walls.

Stable solutions of the Schrödinger equation are standing waves. For instance in the x direction, the free-electron and free-hole standing waves must fulfill

$$L_x = n_e \times \frac{\lambda_e}{2} \qquad (n_e = \pm 1, \pm 2, \dots) \tag{7}$$

$$L_x = n_h \times \frac{\lambda_h}{2} \qquad (n_h = \pm 1, \pm 2, \dots) \tag{8}$$

where λ_e and λ_h are wavelengths of electrons and holes respectively. From equations (5), (7) and (8) it follows that size quantization in the x-direction gives discrete k_x values for the electrons and holes. The total number of discrete states depends on the well width and depth. In the case of walls with a finite height, the wave function does not vanish at the edge of the well, but decays exponentially in the classically forbidden region. Therefore, the probability of finding a particle inside the well is always less than unity and decreases with increasing E_n. As a result of the reduced number of states and the confinement of the electron wave functions, a part of the *E(k)* curve is replaced by discrete points as shown in Fig. 1.2.

Weakly quantized quantum dots (with R~a_B where R is the radius of the QD) contain a large number of atoms and unit cells; therefore Bragg reflection at the periodic lattice will

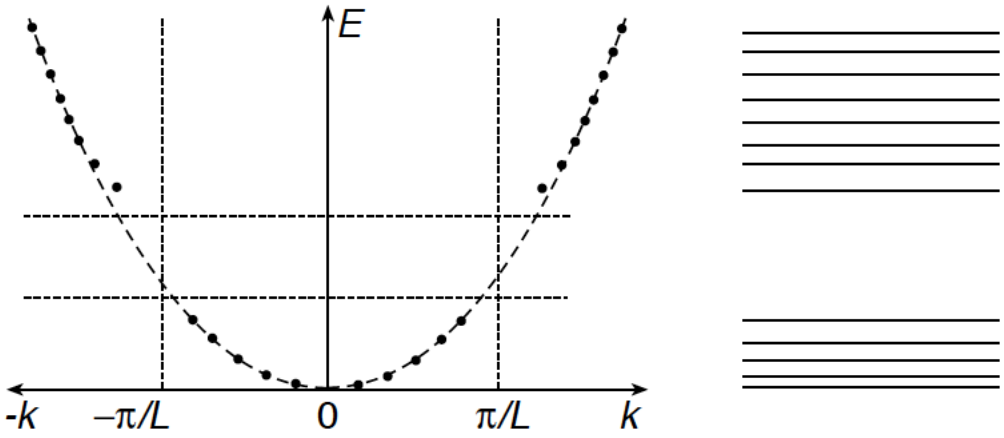

Figure 1.2: Illustration showing the formation of discrete energy states instead of energy bands. Illustration from [1].

lead to the formation of continuous energy bands. Only the levels at the top of the valence band and at the bottom of the conduction band, which correspond to the most delocalized electron wave function, will be discrete (see Fig. 1.3b). Highly quantized semiconductor quantum dots are sometimes called ‘artificial atoms’ because they exhibit a discrete optical spectrum determined by their size (see Fig. 1.3c). The electron and hole, confined in a space with dimensions smaller than the Bohr radius of the exciton, cannot however be considered as independent particles. The gap between the filled valence band levels and the empty conduction band levels increases when the radius of the particle decreases. Due to the electron-hole Coulomb interaction, the measured optical bandgap has a slightly lower energy than the 'actual' electronic band gap.

The increase of the band gap and the transition from continuous energy bands to discrete energy levels upon a decrease of particle size has been observed by optical absorption spectroscopy in many colloidal semiconductor systems. As the particle radius is decreased, the onset of the absorption and the emission maximum shift towards higher energies. A clear structure in the absorption spectra is observed for the smallest particles, corresponding to discrete optical transitions. A picture showing the different emission wavelengths of NCs of different sizes ranging from 2.3 nm to 5.5 nm diameter is shown in Fig. 1.4.

1.3 Colloidal Quantum Dots – Experimental Progress

Colloidal synthesis of inorganic nanostructures is developing into a new branch of synthetic chemistry. Starting with preparations of simple objects like monodisperse spherical nanoparticles [27-30], the field is now moving toward more and more

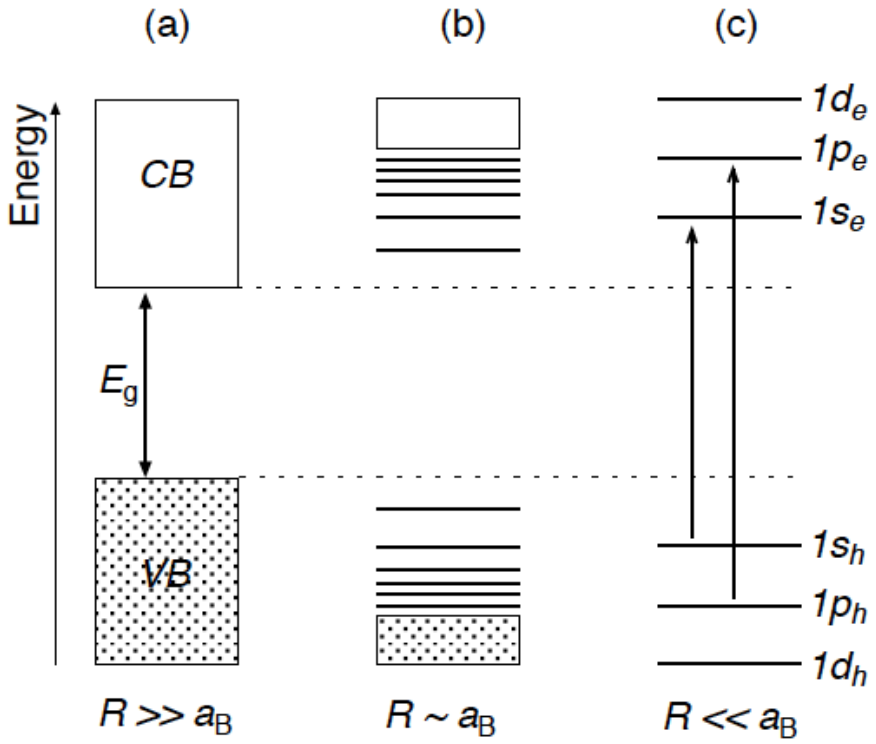

Figure 1.3: Illustration showing the effect of size on the electronic structure of a semiconductor crystal for three different size-ranges: a) A macrocrystalline semiconductor ($R>>a_B$) with continuous energy bands; the filled valence band (VB) and empty conduction band (CB) and the band gap energy (Eg) are shown, b) A semiconductor nanocrystal with a weak size-quantization ($R\sim a_B$) and c) A highly quantised dot ($R<<a_B$) with discrete atomic-like energy levels and optical transitions. Illustration from [1].

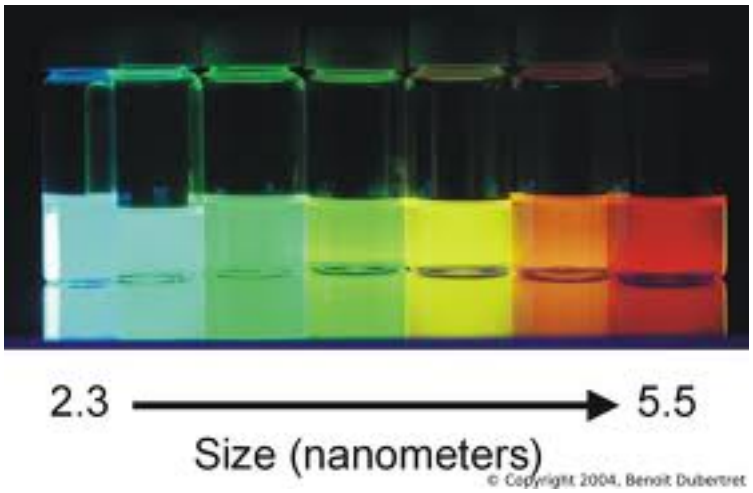

Figure 1.4: Picture showing the different colored wavelengths of light emitted from NCs of increasing sizes from 2.3 nm diameter to 5.5 nm diameter.

sophisticated structures where size, shape, and connectivity of multiple parts of a multicomponent structure can be tailored in an independent and predictable manner [31-37]. Hanrath [38] has described it as a means of controlling the electronic structure within individual NCs as a way to tune the properties of the "artificial atom." Recent progress in colloidal NC synthesis has enabled the creation of NCs with excellent control over tuning the energy gap of the NCs. Also, tuning the absolute energy levels of the valence and conduction band edges with respect to vacuum would enable control over the frequency of light that is absorbed by the NCs. Progress has been made by exercising control over the electronic coupling between the NCs as well as between the NCs and external contacts. There have been remarkable advances in resolving the insulating barrier caused by the capping ligands, which blocks the electronic coupling between the NCs, by tailoring the coupling across the NC boundary through chemical and physical treatments of the NC surface. Progress in directing the self-assembly of NCs into ordered assemblies has enabled the establishment of control over the structure of the artificial solid.

The successful operation of NC-based devices depends critically on understanding and controlling many interfacial processes. Fig 1.5 illustrates a typical NC-based photovoltaic device. In the illustrated example of a NC solar cell, an incident photon generates an electron-hole pair, or exciton, which must be split at the NC boundary and transported to their respective external electrodes. As seen in Fig 1.5a, the exciton that is generated in the NC assembly is split across the electron and hole transport layers. The electron transport layer blocks the holes and vice versa. The electrons and holes then pass through the electrodes into the external circuit thereby, generating current. This process is illustrated in Fig 1.5b.

a)

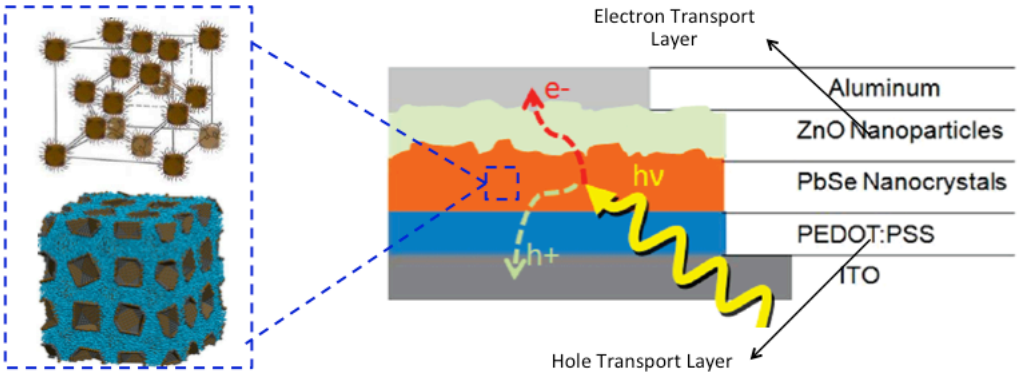

b)

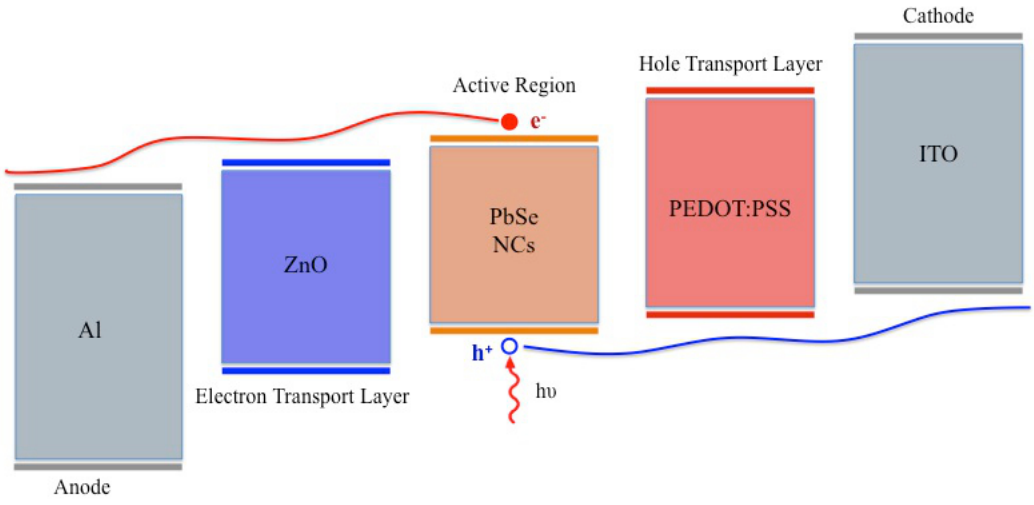

Figure 1.5: a) Schematic of a typical colloidal NC photovoltaic cell and b) Illustration of the generation of an exciton upon the incidence of a photon and subsequent splitting of the exciton.

Controlling energy levels inside the NC is important for tuning the wavelength of absorbed or emitted light [38]. Also, the energy levels of the interconnects and surfaces outside the NC matrix should be tuned so as to facilitate charge separation (in the case of a PV device) or charge injection (in the case of a LED). For NC PV cells, the charge transport through the film must be engineered to avoid charge trapping, as charge transport crucial for the type of interfaces that exist in typical NC-based PV cells [39]. The kinetics of the processes of separation and transport across the various interfaces must be faster than the competing recombination and trapping dynamics. Specifically, in a high-performance NC solar cell, photogenerated carriers must be extracted at a rate faster than the trapping and recombination rates. Among the various colloidal NC materials that are being investigated, group IV-VI compound semiconductors stand out as fundamentally intriguing and experimentally advantageous for the study of NC solids. These compound semiconductors exhibit strong quantum confinement effects enabling broad tunability of the NC energy levels. Lead salt NCs, in particular, are among the most strongly quantum-confined systems. They have a large Bohr exciton radius (46 nm in PbSe) [40-41], and commonly used NCs have a diameter between 2 and 10 nm which provides experimental control to prepare materials with a tunable energy gap ranging from 0.4 to nearly 2 eV [42-46]. Due to the low effective mass of electrons and holes in PbX NCs, the envelope wave functions extend significantly outside the boundary of the dot and enables efficient inter-NC coupling.

The ability to tune the electronic structure of the NCs offers a very versatile technique in the creation of artificial structures with properties by design. The hot-injection method pioneered by Murray [47-48] is arguably the most versatile and well-studied approach

where the versatility of the chemical interactions between solvent, ligand and precursor introduces synthetic degrees of freedom for the creation of NCs with varying size, shape, and composition. There has been intense research into various synthesis approaches to manufacture these NCs in organic and aqueous environments including heating-up [49], inverse micelle methods [50], as well as gas phase reactions [51] and supercritical fluid approaches [52]. NCs have also been prepared in solid matrices like glass [53] but the control over shape and size is not as refined as for the solution-based approaches.

The colloidal synthesis generally involves several consecutive stages: nucleation from initially homogeneous solution, growth of the preformed nuclei, isolation of particles reaching the desired size from the reaction mixture, postpreparative treatments, etc. Usually, the separation of nucleation and growth during synthesis is achieved by rapidly injecting the precursor solution into the colloidal growth environment. This injection leads to a rapid spike in precursor concentration and temporary drop of the overall reaction solution temperature. The initial burst of nucleation is thereby temporally separated from the subsequent growth phase. Nucleation and growth of NCs occurs in the solution phase in the presence of organic surfactant molecules, which dynamically adhere to the surface of growing crystals [54-55]. Once the concentration of available precursors is depleted, the particles may continue to grow either by addition of remaining precursors to the growing crystal or by Ostwald ripening—a process in which smaller particles (with higher surface energy) are dissolved in favor of forming larger particles.

Typical surfactants include long-chain carboxylic and phosphonic acids (e.g., oleic acid and n-octadecylphosphonic acid), alkanethiols (e.g., dodecanethiol), alkyl phosphines, alkylphosphine oxides (classical examples are trioctylphosphine, TOP, and

trioctylphosphine oxide, TOPO), and alkylamines such as hexadecylmine [56]. In the case of compound semiconductors including cadmium or lead chalcogenides (CdX or PbX), the NC synthesis is typically achieved by injecting a chalcogen precursor (e.g., Se-trioctylphosphine, TOP-Se) into a heated solution containing a preheated Cd or Pb precursor, typically in the form of an oleate. Following the initial nucleation, the particles are allowed to grow in the reaction environment for a specified growth period before the reaction is quenched by reducing the temperature. The average diameter of the NCs in the product can be tuned by adjusting basic synthesis parameters including growth time, growth temperature and precursor concentration. Typically, longer growth times naturally lead to larger particles.

Although simple nucleation and growth models [57] exist that describe colloidal NC formation, they fails to capture the relationship between NC growth and the molecular interactions between ligands and solvents, nor do they provide much information about the NC facets. This lack of understanding of the complex mechanisms at play provides a rich field for computational studies. Colloidal NC cores are usually approximated as spherical particles of a specific radius, r, which is an oversimplification since it does not capture the underlying relationship between crystal faceting and the true shape of the NC. Crystal faceting also has important implications on magnetic, optical, electronic, mechanical, and self-assembly properties of the NC [38]. Alivisatos *et al.* demonstrated a variety of NC shapes including rods, arrows, and tetrapods [58-59] in NCs made of CdSe. For PbSe NCs, the particle shape evolves from quasispherical to cubic with increasing NC diameter [60].

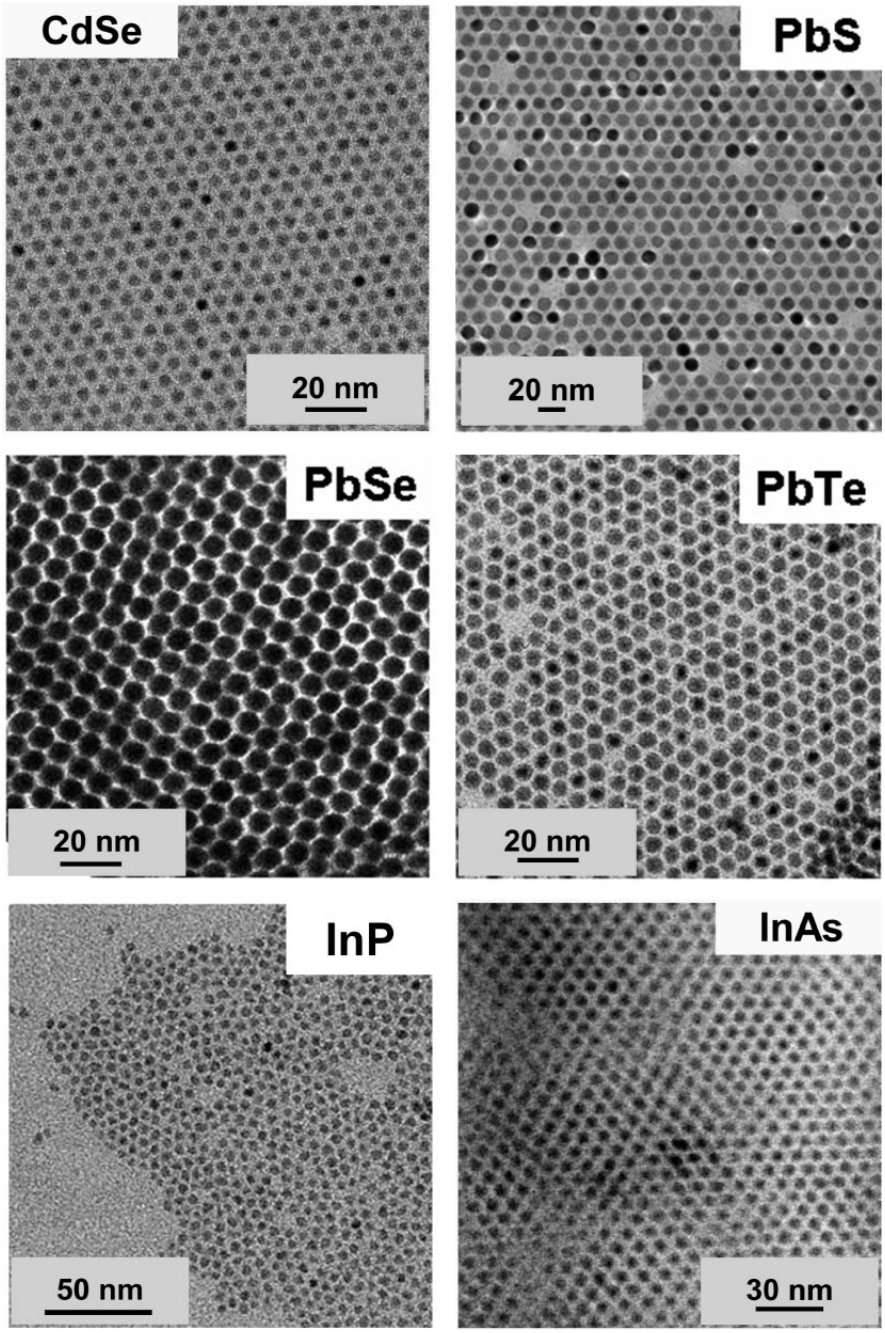

Figure 1.6: Self-assembled superlattices of colloidal semiconductor NCs. Picture from Talapin *et al.* Chem. Rev., 110, 389–458 (2010).

It is important to recognize that, even at room temperature, the ligands bound to the NC surface constitute a dynamic system in which ligands are constantly absorbing/desorbing and exchanging from the surface. Thus, the precise understanding of the nature of the surface of the NCs is very important not only for the design of better NC cores but also to understand the impact of surface reconstruction on the electronic structure and charge transport in the NCs. Again, this area once again provides a fertile ground for computational studies.

One approach to form arrays of close-packed NCs is to slowly evaporate colloidal solutions of NCs: upon evaporation, the NC volume fraction increases and interaction between the NCs develops and leads to the formation of a self-organized NC film. Fig 1.6 shows NC superlattices made of a variety of materials. Spin deposition and dip coating can also be used [61]. To form colloidal crystals with a high degree of order in the NC packing, the size distribution of the NC particles must have a mean deviation less than about 5% and uniform shape. The critical parameters that control inter-NC electronic coupling, and hence carrier transport, include interdot distance, NC surface chemistry, the work function and dielectric properties of the matrix containing the NCs, the nature of the NC capping species, NC orientation and packing order, uniformity of NC size distribution, and the crystallinity and perfection of the individual NCs in the array. The interstitial medium itself is comprised of a combination of molecules bound to the NC surface as ligands, remnant solvent molecules, or a functionalized interstitial organic or inorganic matrix. Long alkyl chains provide colloidal stabilization and passivated the NC surface, but present a large potential barrier for interdot coupling. In the condensed phase, the presence of long chain ligands on the NC surface generally results in a surface-to-

surface spacing of greater than 2 nm [38]. In the case of oleic acid-passivated PbS NCs, Shevchenko and co-workers showed that the interdot spacing depends on the structure of the NC solid; the spacing in faceted 3D NC solid crystals was ~25% smaller than in NC films formed by solvent evaporation [62]. Several studies of electronic coupling in colloidal NC arrays have been reported [63-69]. If the semiconductor NC cores are surrounded with such insulating organic ligands (to aid in solubility and surface passivation), the wide barrier created by the ligand shell effectively localizes the electron and hole wavefunctions within individual NCs resulting in negligible overlap between electronic wave functions across the dots. To overcome this problem, many chemical approaches have been suggested where the long chain ligands are replaced with shorter ones or linkers. Thus, there are many parameters involved in the reproducible synthesis of ordered NC arrays and in order to establish control over the tailoring of the superlattice structure and symmetry, molecular insight into the forces governing the self-assembly process is necessary. Experimentally, very little is known about the molecular mechanisms involved in these processes and computational studies are needed to gain an understanding of these phenomena.

There has been significant progress in controlling and understanding the interdot coupling in semiconductor NC films in recent years. The ligand exchange procedure typically involves an exposure of colloidal NCs to a large excess of competitive ligand, resulting in partial or complete exchange of surface molecules [47-48]. This procedure can be prolonged up to a few days or repeated multiple times to maximize the removal of original ligands, often accelerated by gentle heating. Guyot-Sionnest *et al.* have showed that exchanging trioctylphosphine oxide ligands on the surface of CdSe NQDs with 1,4-

phenylenediamine increases the conductivity by three orders of magnitude [71]. In the case of lead salt NC films, Talapin and Murray showed that hydrazine treatment of PbSe NC films removed the oleic acid ligand and decreased inter-NC spacing from 1.1 to 0.3 nm. This reduction of the nearest neighbor separation distance led to higher quantum exchange coupling and increased the conductance through the NC array by ten orders of magnitude [17]. These studies have demonstrated that treatments of the NC surface can profoundly influence their electronic structure. For example, in the case of hydrazine treated PbSe NQD films, vacuum treatment changed the transport characteristics from n-type to ambipolar and finally p-type; the n-type character can be restored by re-exposing the PbSe NQD film to hydrazine [17].

A typical limitation of the solution-phase exchange of larger ligands by smaller ones is the resulting decrease of colloidal stability often leading to nanoparticle aggregation. To address this issue, the ligands exchange can be applied not to solution of NCs, but to a film or a superlattice. This approach benefits from convenient fabrication of high-quality NC films using colloidal solutions stabilized by original ligands, followed by soaking the NC film in a solution containing new capping ligands. Typical examples include treatment of CdSe or PbSe NCs with various short-chain molecules such as methylamine, ethylamine, butylamine, ethanethiol, sodium hydroxide, pyridine, or hydrazine [72-75]. This approach is also very useful for NC cross-linking using molecules with two functional end groups such as diamines or dithiols. Such treatments significantly decrease the interparticle spacings and improve electronic transport in NC solids crucial for applications in electronic, photoconductive, and photovoltaic devices.

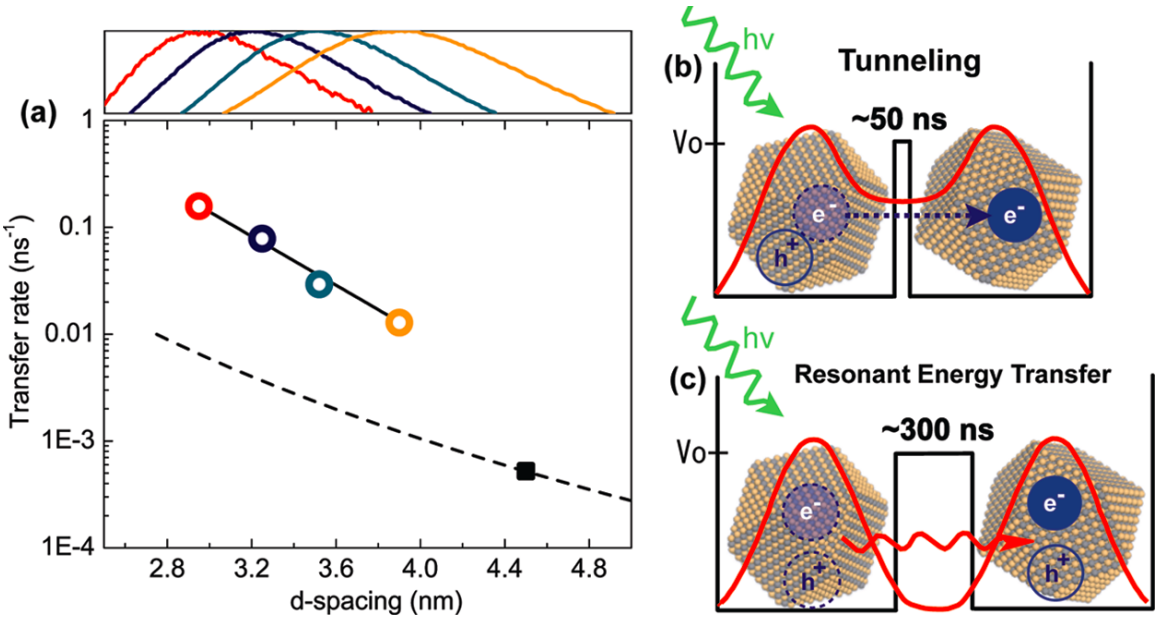

Figure 1.7: (a) Plot of charge transfer rates (same color legends as used in Figure 1), calculated from exciton lifetimes (Figure 2b), versus inter-NC spacing measured with GISAXS (Figure 1c). Single exponential decay fit (black solid line) indicates that the charge transfer occurs via tunneling of charge through a potential barrier. Resonant energy transfer is shown in the PbS_OA sample (black rectangle) and the calculated energy transfer rates (dotted line) for corresponding inter-NC spacing using a Förster radius of 5 nm shows an order of magnitude lower rate than the charge transfer rates. This indicates that exciton dissociation via tunneling is the dominant pathway in the regime of short inter-NC distance and high coupling energy, (b) whereas resonant energy transfer is dominant in low inter-NC coupling regime (c). All calculated transfer rates have error bars smaller than the symbols. Distributions in d spacing measured with GISAXS are shown on the top of (a). From Choi *et al.*, Nano Lett. 10, 1805 (2010)

Choi *et al.* demonstrated use of variable length bifunctional linkers allowing systematic tuning of the interdot spacing, with a series of n-phenyl dithiol linkers to illustrate the exponential relationship between exciton dynamics and interdot spacing [76]. As shown in Fig. 1.7, their study revealed the exponential relationship between interdot spacing and exciton dissociation rate. Wolcott *et al.* used variable length alkane-dithiol linkers to probe coupling between PbSe NCs as a function of interdot spacing [77]. In another study using alkane-dithiols as a variable length spacer, Law *et al.* demonstrated that carrier mobility decreases exponentially with increasing linker length as expected for hopping transport in granular conductors [78]. The inter-NC charge transport can be improved not only by introducing shorter or linking molecules, but also by using capping molecules that can support charge transport. Thus, ligand coatings based on conductive conjugated polymers and oligomers such as end-functional polythiophenes [79] or derivatives of poly (para-n-phenylene vinylene) [80] were applied to improve charge transport and film morphologies for solar cells and light-emitting devices.

Short-chain linkers such as 1,2-ethanedithiol (EDT) and 1,4-benzenedithiol (BDT) have emerged as commonly used molecules to couple PbX NCs. Although EDT is a slightly shorter linker than BDT and thus leads to stronger wavefuntion overlap, recent studies of both PbS [81] and PbSe [82] NC films suggested that BDT treatments result in a lower trap density and improved PV device performance and stability [83]. Asbury *et al.* compared the photovoltaic performance of PbS NC films treated with mercaptoproprionic acid (MPA) and EDT [84]. MPA treated films exhibited higher mobility than PbS NCs linked with EDT. They hypothesized that this difference was due to a lower density and energetic distribution of charge traps. Most recently, Kagan has shown that compact

ammonium thiocyanate ligands on lead chalcogenide NCs can promote impressive electron mobilities (on the order of 10 cm^2/Vs) while retaining quantum confinement. [85-86]. But the treatment of the NC films with shorter ligand molecules is not without drawbacks since it often results in the loss of long-range order and superlattice symmetry resulting in disordered, glassy films.

Even with the significant progress that has been made in this field, there still remain many unanswered questions such as the precise nature of the surface of the NC, the ligand density and the specific ligand binding chemistry, the effect of the ligand chemistry on the electronic structure, the effect of size and shape of NC and the role of NC facets on the electronic structure and electronic coupling, the role of solvent in determining the NC superlattice order and charge transport in the assembly etc. We attempt to provide some of the answers to these questions in the following chapters of this thesis.

1.4 Prior Computational Efforts

Despite decades of experimental research to study capped NCs, the relative extent of the roles played by ligands and nanocrystals in the assembly process remains unclear, especially as the processing parameters are altered (e.g., temperature, choice of solvent, aging, exposure to air, etc.). Indeed, even the nature of the binding between the ligands and the surface of the nanocrystal, and the density dependence of the ligands on different facets of the nanocrystal, is unknown. Further, there are few experimental probes that can truly answer these molecular-scale questions since they describe events at buried interfaces that are difficult to image or probe. This provides considerable motivation to employ molecular simulation approaches to shed some light on these complex questions,

even though the scale of these systems in terms of length and time scales also represents cutting-edge challenges to simulation.

It is clear from previous molecular simulation studies [87-91] that the ligands are not simply "spacers" between the nanoparticles in the superlattice to prevent sintering. They clearly play a defining role during the assembly process and in the resulting morphology of the superlattice. They also passivate surface states. Hence the representation of the ligands is a critically important task. Indeed, impressively large-scale (at the time) Molecular Dynamics simulations by Luedtke and Landman [87] in the 1990s, described the interactions of sub-3 nm gold nanocrystals capped with thiol-terminated alkyl chains. Their results suggested that the gold-gold interaction contributed just 1% to the overall energy per particle of the system. This work was also notable for their prescient suggestion of the importance of the ratio of ligand length to nanoparticle diameter, L/d, to determine the preferred morphology (fcc vs. bcc, etc.), although they were unable to confirm this in their simulations given resource constraints. On the other hand, they make a more disputable point of the tendency of ligands to "bundle" together at low temperatures as shown in Fig 1.8. Badia *et al.* [92] claimed to observe bundling for gold nanoparticles. Similar observations of bundling were made by Lane *et al.* [93] when modeling spherical nanoparticles capped by alkanethiol ligands in water, decane and in vacuum. More recent work by Schapotschnikow and Vlugt [88], also on sub-3 nm gold nanoparticles, was the first to include the effect of the role of the solvent to influence the adsorption of ligands during the assembly process, and the effect of the curvature of the gold surface on phase behavior. Lane *et al.* [93] and Yang *et al.* [94-95] have also studied

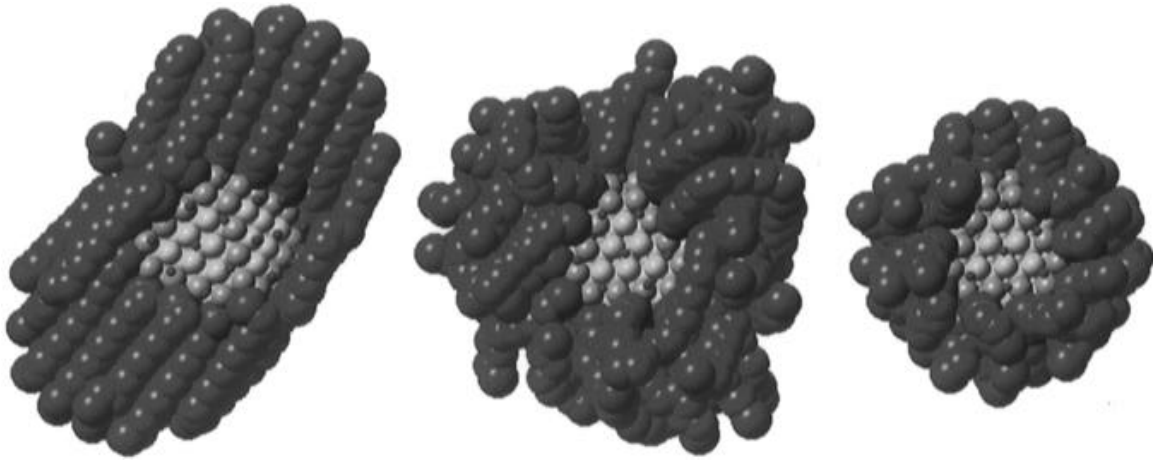

Figure 1.8: Equilibrium configurations of passivated Au_{140} isolated crystallites. The structures at the left and middle correspond to low- (200 K) and high-temperature (350 K) configurations for $Au_{140}(C_{12}H_{25}S)_{62}$ illustrating "bundling" at low temperature, and the structure on the right is for $Au_{140}(C_4H_9S)_{62}$ at 300 K. Picture reproduced from Landman *et al.* J. Phys. Chem., 100 (32), 13323-13329 (1996).

solvent effects on alkane ligands attached to nanoparticles in different solvents, such as water and decane.

Employing an explicit atomistic model for all the atoms of a large NC system can become very computationally demanding. The computational power of today's computers places severe restrictions on the system size and simulation time of atomically explicit systems. In order to circumvent these limitations, a simulation model called the United Atom (UA) model was developed to perform simulations of very large systems. In this technique, groups of atoms are represented as "united atoms" and treated using a mean field potential. The level of such coarse graining depends on how large the defined groups are and the level of detail used to model the interactions between these groups of atoms. One of the earliest, and still perhaps the most widely used UA models was proposed by Jorgensen *et al.* in 1984 [96] to simulate various systems and has shown good results for liquid or liquid-like systems. However, as early as 1990, Toxvaerd's studies on alkanes [97] showed the tendency of the Jorgensen model to produce overly attractive interactions among alkyl chain molecules. He posited that the Jorgensen UA model is unable to describe the van der Waals interactions between the carbon atoms on the backbone of the alkyl chain and the adjacent hydrogen atoms, which are necessary to accurately describe the flexibility of the alkyl chain. He suggested using an "anisotropic" UA model, but this model is rather complicated to implement. Siepmann *et al.* [98], in 1998, proposed a new "transferable potentials for phase equilibria" (TraPPE) force field [99], which proved to be superior to both OPLS [105] and SKS [100] in predicting phase equilibria; TraPPE is now widely used. The same year, Nath *et al.* introduced the NERD force field [100-101], which provided good agreement with experimental phase equilibria

data not only for pure alkanes and alkenes, but also their binary and ternary mixtures. Studies of a quite different system, polymers, in 2010 by Li *et al.* [102], compared the conformation of polyethylene chains using an explicit Dreiding model [104] with the Jorgensen *et al.* OPLS UA model. They observed that Jorgensen UA-modeled polyethylene chains adopted a lamellar conformation which was inflexible, while the same chain modeled with the all-atom explicit Dreiding model was much more flexible and adopted more random conformations. They suggested a possible correction that involved increasing the σ parameter of the van der Waals interaction for the carbon backbone to relieve some of the inflexibility of the alkyl chain. In contrast to Li *et al.*'s implication of *inter*molecular forces being at fault, Paul *et al.* [103] looked instead at the *intra*molecular forces and offered an alternative approach to a united atom representation. Due to the large number of models available in literature and the seemingly wide variability in the results produced by them, there appears to be very little consensus about the behavior of the ligands capping the NC surface. We shall address this issue in Chapter 3.

Although the property of self-assembly of nanocrystals to form stable arrays is an attractive way to make devices, precise control over the self-assembly process is still a challenging issue [106]. The nanocrystals are capped by organic ligands, which not only serve to passivate the surface of the nanocrystal cores, but also provide stability to the superlattice. Highly organized ligand-clad nanocrystal superlattices can be obtained from colloidal solutions using solvent evaporation [47, 63, 108], spin casting [63], or stabilization using a non-solvent [107]. Thus, understanding the precise nature of nanocrystal-nanocrystal interaction in the presence of a solvent will be critical in

controlling nanocrystal self- assembly. The efficiency of nanocrystal-based devices, *e.g.,* in photovoltaic cells, depends on a number of materials' parameters including the nanocrystal size, shape, the inter-nanocrystal distance, *etc*., as well as the significant effect of processing conditions [108]. The final symmetry of the superlattice may also have a profound effect on the stability and the charge transfer capacity of the superlattice. Experimentally, the self-organization of nanocrystals in solution invariably begins once they are drop-cast onto a substrate. As the solvent evaporates from dispersion on the substrate, the nanocrystal volume fraction increases, eventually reaching the point where the nanocrystalline array is formed [106, 47, 108-110]. The nanocrystals are able to sample a large number of spatial configurations during the solvent evaporation process before they achieve their lowest energy structures.

One of the first atomistically explicit simulation studies of nanocrystals was made by Landman *et al.* [31] who studied gold nanocrystals coated with densely packed alkane thiol ligands. They predicted that the formation of nanocrystal superlattices of various preferred symmetries depended on the temperature of the system, and the length and grafting density of the capping ligands, *etc.* However, the nanocrystals modeled were very small (less than 3 nm in diameter) and did not include consideration of a solvent, either explicitly or implicitly. More recent studies by Schapotschnikow *et al.* elucidated the importance of two-body and three-body interactions of alkanethiol ligand-capped gold nanocrystals [111-112]. They showed that ligand length plays an important role in the propensity of more than two nanocrystals to form highly stable 3D superlattices, monolayers or even nanowires.

Since then, there have been several papers analyzing the interactions of nanocrystals with both implicitly and explicitly modeled solvents. Rabani *et al.* [113] used coarse-grained Lennard-Jones spheres as nanocrystals in the presence of implicit solvents to study how the nature of interaction between the nanocrystals depends on the quality of the solvent. They showed that the interaction can be "tuned" from attractive to repulsive with increasing solvent density. Qin *et al.* [114] studied the solvation forces between two nanocrystals modeled in an implicit Lennard-Jones liquid. They showed that the nature of the interaction depends on the interplay between solvent-ordering and surface structure to change the interaction from net attractive to repulsive. They also showed that nanocrystal reorientation can occur due to local solvation forces leading to directed alignment of nanocrystals in solution, which plays an important role in nanocrystal self-assembly. Though the general *trend* of interaction strengths can be obtained from the use of implicit solvents, the precise interaction of solvent molecules with the ligand corona cannot be gained from this method. Lane *et al.* [115] measured the hydrodynamic drag on silica nanocrystals in the presence of explicitly modeled water or decane as the solvent. They observed that the long-range interaction forces were dominated by hydrodynamic drag and short-range interactions by close packing of ligand chains. The overall interaction was purely repulsive. This is very different from the simulations done in vacuum where both attractive and repulsive regimes are observed, once again highlighting the need to model the solvent explicitly. Yang *et al.* [116-117] observed the behavior of water molecules close to the surface of gold nanocrystals capped with both polar and non-polar alkane-thiol ligands. They saw that the residence time of the solvent as well as the strength of the hydrogen-bonding depended on the type of functional group present on

the ligand. The ligands, therefore, dictate the type of solvation shell formed by the solvent molecules around the ligand corona. This changes the interaction strength between the nanocrystals in solution. Although these simulation studies were performed to study the explicit interaction of solvent with nanocrystals [114-117], they dealt with only one, or at most a few, nanocrystals. The question of leveraging knowledge of these detailed microscopic interaction studies to examine the formation and stability of large macroscopic superlattices and our ability to control the self-assembly process remains to be answered.

The exploitation of these unique nanocrystal properties in effective electronic devices is currently constrained by our lack of understanding charge transport in NC systems. This transport is determined by a complex and interacting set of variables: the size distribution of the NCs, surface chemistry and stoichiometry, morphological order, and inter-NC distances. The effect of the (usually insulating, long-chain alkyl) ligands that are invariably employed to prevent NC sintering is also important in determining charge transport characteristics of NCs, both in terms of their physical intervention to deleteriously increase the inter-NC separation and in terms of providing a medium through which charge transport has to travel and hence creating a tunneling barrier.

Many studies have been performed to study charge transfer in NCs by approximating the structure of the NCs in some manner or other. These studies have assumed the NCs are some form of a truncated bulk crystal or whose surface "pseudo" atoms have been passivated. Luo *et al.* [118] for example studied the manner of decay of excited photons in truncated bulk semiconductor crystals which were used to approximate NCs. They introduced a figure of merit for carrier multiplication in a variety of NCs and found some

materials like CdSe, PbSe, etc., to have greater carrier multiplication than others. Franceschetti and Wang *et al.* [119] have studied the carrier localization due to confinement versus electron correlation in semiconductor nano dumbbells. They showed that the shape and size of the dumbbell wire could affect the localization. An *et al.* [120-121] have studied the excitonic splitting and radiative lifetime in *spherical* PbSe NCs using Configuration Interaction methods. Califano *et al.* [122] have studied the hole relaxation in CdSe NCs and show how the size and aspect ratio of nanostructures such as nanorods, etc., can affect hole relaxation. All these studies use screened atomic pseudopotentials to model the electronic structure which are not as accurate as *ab initio* methods like DFT. They also use ligand pseudopotentials at the surface to provide passivation. While this approach is efficient enough to overcome the computational cost of using larger ligand-passivated NCs, they completely ignore the specific ligand chemistry and the contribution of ligands to the total electronic structure of the NC. Studies performed by Talapin and Murray [17] have shown that the ligand chemistry is extremely important in determining the electronic structure and charge transfer in NC systems.

There have been many studies using *ab initio* methods such as DFT of NCs of Si, CdSe, CdTe, PbSe etc. Kiran *et al.* used DFT to find $(PbS)_{32}$ to be the smallest cubic cluster for which its inner $(PbS)_4$ core enjoys bulk-like coordination [123]. This helps provide a rubric for understanding the pattern of aggregation when $(PbS)_{32}$ clusters are deposited on a suitable surface. Gai *et al.* have studied the structural and electronic properties of non-stoichiometric PbSe NCs [124]. They hypothesized that dangling bonds may be responsible for introducing in-gap states. Contrary to this study, Voznyy has claimed that

it is not dangling bonds but ligands that are responsible for surface traps and in-gap states [125]. There have also been DFT and Time-Dependent DFT (TD-DFT) studies of the role of different ligand chemistries and the role of different solvents on the electronic structure of CdSe NCs [126]. More recently, there have also been studies of multi exciton generation and hot carrier relaxation in Si and PbSe NCs using *ab initio* methods [127-128].

The "cost" of using *ab initio* computational approaches to study charge transport in NCs is sufficiently high that, in practice, it essentially limits the study of such systems to those containing less than a few hundred atoms. This difficulty is exemplified in a recent study of charge transport between two spherical CdSe NCs linked by a compact $Sn_2S_6^{4-}$ connector [129]. While the charge transport has to be calculated using *ab initio* calculations, it is infeasible to study realistically sized NCs without making several assumptions. Chu *et al.* [129], studied charge transport in 2.5-5 nm diameter spherical NC dimer systems which involved a patchwork of electronic structure calculations for a representative motif of the spherical NC, linked to a set of other theoretical models to represent charge hopping. This study made predictions of the effect of NC size and temperature on mobility which await experimental confirmation. This study did not take into account the effect of shape of the NCs on the charge transport. Past *ab initio* studies of NCs thus roughly fall into two categories: either they involve assumptions about the ligand coverage and the electronic structure (pseudopotentials are used) [118-122] when charge hopping is considered, or else charge transport calculations are not performed if the actual ligand bonding is simulated and full *ab initio* methods are used (the studies

tended to be limited to calculations of Density of States (DOS) and a description of structure of the NCs) [123-129].

In this thesis, we try to address many of the drawbacks of previous studies introduced above. But before we describe the details of our work, we will review some of the theory behind commonly used techniques in computational studies of NC systems.

1.5 Methods

Atomistic modeling methods vary in their accuracy and computational cost as well as the length and time scales that they can be used to model. A diagram representing different atomistic modeling methods is given in Fig. 3. The main methods used in this thesis are Molecular Dynamics [130-131] and *Ab Initio* methods [132]. A brief description of the theory behind both these methods are given below.

1.5.1 Molecular Dynamics

Molecular Dynamics (MD) is a technique to simulate the motion of atoms and molecules in space and time. The atoms and molecules are allowed to interact for a period of time, giving a view of the motion of the atoms. In most common implementations of MD, the trajectories of molecules and atoms are determined by numerically solving the Newton's equations of motion for a system of interacting particles, where forces between the particles and potential energy are defined by molecular mechanics force fields. The method was originally conceived within theoretical physics in the late 1950s, but is applied today mostly in materials science and the modeling of biomolecules.

The results of molecular dynamics simulations may be used to determine macroscopic thermodynamic properties of the system based on the ergodic hypothesis:

the statistical ensemble averages are equal to time averages of the system collected in the simulation. MD can also be seen as a method of predicting the future by animating nature's forces and allowing insight into molecular motion on an atomic scale.

MD follows the laws of classical mechanics, most notably Newton's law:

$$\mathbf{F}_i = m_i \boldsymbol{a}_i \tag{9}$$

for each atom i in a system constituted by N atoms. Here, m_i is the atom mass, $\boldsymbol{a}_i = {}^{d^2\boldsymbol{r}_i}/_{dt^2}$ its acceleration, and $\mathbf{F}_i$ is the force acting upon it due to the interactions with other atoms. Therefore, in contrast with the Monte Carlo method, molecular dynamics is a deterministic technique: given an initial set of positions and velocities, the subsequent time evolution is in principle completely determined. In more pictorial terms, atoms will ``move" in the computer, bumping into each other, wandering around (if the system is fluid), oscillating in waves in concert with their neighbors, perhaps evaporating away from the system if there is a free surface, and so on, in a way similar to what atoms in a real substance would do.

The computer calculates a trajectory in a 6N-dimensional phase space (3N positions and 3N momenta). However, such a trajectory is usually not particularly relevant by itself. Molecular dynamics is a statistical mechanics method. Like Monte Carlo, it is a way to obtain a set of configurations distributed according to some statistical distribution function, or statistical ensemble. An example is the microcanonical ensemble, corresponding to a probability density in phase space where the total energy is a constant E:

$$\delta(H(\Gamma) - E) \tag{10}$$

Here, H(Γ) is the Hamiltonian, and Γ represents the set of positions and momenta, δ is the Dirac function, selecting out only those states which have a specific energy E. Another example is the canonical ensemble, where the temperature T is constant and the probability density is the Boltzmann function

$$\exp\left(-\frac{H(\Gamma)}{k_B T}\right) \tag{11}$$

According to statistical physics, physical quantities are represented by averages over configurations distributed according to a certain statistical ensemble. A trajectory obtained by molecular dynamics provides such a set of configurations. Therefore, a measurement of a physical quantity by simulation is simply obtained as an arithmetic average of the various instantaneous values assumed by that quantity during the MD run.

Statistical physics is the link between the microscopic behavior and thermodynamics. In the limit of very long simulation times, one could expect the phase space to be fully sampled, and in that limit this averaging process would yield the thermodynamic properties. In practice, the runs are always of finite length, and one should exert caution to estimate when the sampling may be good (``system at equilibrium'') or not. In this way, MD simulations can be used to measure thermodynamic properties and therefore evaluate, say, the phase diagram of a specific material.

The most important input needed for a molecular simulation is a suitable model for the physical system. For a molecular dynamics simulation this amounts to choosing the *potential*: a function $V(r_1,r_2,\ldots r_N)$ of the positions of the nuclei, representing the potential energy of the system whose atoms are arranged in a specific configuration. This function is translationally and rotationally invariant, and is usually constructed from

the *relative* positions of the atoms with respect to each other, rather than from the absolute positions.

Forces are then derived as the gradients of the potential with respect to atomic displacements:

$$\mathbf{F}_i = -\nabla_{r_i} V(\mathbf{r}_1, \ldots, \mathbf{r}_N) \tag{12}$$

This form implies the presence of a conservation law of the total energy $E=K+V$, where K is the instantaneous kinetic energy.

The simplest choice for V is to write it as a sum of pairwise interactions:

$$V(\mathbf{r}_1, \ldots, \mathbf{r}_N) = \sum_i \sum_{j>i} \phi\left(\left|\mathbf{r}_i - \mathbf{r}_j\right|\right) \tag{13}$$

The clause $j>i$ in the second summation has the purpose of considering each atom pair only once. In the past most potentials were constituted by pairwise interactions, but this is no longer the case. It has been recognized that the two-body approximation is very poor for many relevant systems, such as metals and semiconductors.

In molecular dynamics, the most commonly used time integration algorithm is probably the so-called Verlet algorithm. The basic idea is to write two third-order Taylor expansions for the positions r(t), one forward and one backward in time. Calling v the velocities, a the accelerations, and b the third derivatives of r with respect to t, one has:

$$\mathbf{r}(t+\Delta t) = \mathbf{r}(t) + \mathbf{v}(t)\Delta t + (1/2)\mathbf{a}(t)\Delta t^2 + (1/6)\mathbf{b}(t)\Delta t^3 + O(\Delta t^4) \tag{14}$$

$$\mathbf{r}(t-\Delta t) = \mathbf{r}(t) - \mathbf{v}(t)\Delta t + (1/2)\mathbf{a}(t)\Delta t^2 - (1/6)\mathbf{b}(t)\Delta t^3 + O(\Delta t^4) \tag{15}$$

Adding the two expressions gives

$$\mathbf{r}(t+\Delta t) = 2\mathbf{r}(t) - \mathbf{r}(t-\Delta t) + \mathbf{a}(t)\Delta t^2 + O(\Delta t^4) \tag{16}$$

This is the basic form of the Verlet algorithm. Since we are integrating Newton's equations, a(t) is just the force divided by the mass, and the force is in turn a function of the positions r(t)

$$\mathbf{a}(t) = -(1/m)\nabla V\big(\mathbf{r}(t)\big) \tag{17}$$

As one can immediately see, the truncation error of the algorithm when evolving the system by Δt is of the order of Δt^4, even if third derivatives do not appear explicitly. This algorithm is at the same time simple to implement, accurate and stable, explaining its large popularity among molecular dynamics simulators.

A problem with this version of the Verlet algorithm is that velocities are not directly generated. While they are not needed for the time evolution, their knowledge is sometimes necessary. Moreover, they are required to compute the kinetic energy *K*, whose evaluation is necessary to test the conservation of the total energy *E*=*K*+*V*. This is one of the most important tests to verify that a MD simulation is proceeding correctly. One could compute the velocities from the positions by using

$$\mathbf{v}(t) = \frac{\mathbf{r}(t + \Delta t) - \mathbf{r}(t - \Delta t)}{2\Delta t} \tag{18}$$

However, the error associated to this expression is of order Δt^2 rather than Δt^4. To overcome this difficulty, some variants of the Verlet algorithm have been developed. They give rise to exactly the same trajectory, and differ in what variables are stored in memory and at what times. The leap-frog algorithm, the velocity-verlet algorithm and the predictor-corrector algorithm are some variants where velocities are handled somewhat more accurately.

The interaction potential contains several types of interactions between the atoms of the system. These could be bonded interactions representing the bonding between atoms in a

molecule, angle-bending interactions, torsional (dihedral) interactions and out-of-plane interactions. One of the most important interactions that needs to be accounted for is the van der Waals' interactions between the atoms of the system. The van der Waals' interactions are usually pairwise additive interactions and there are many formulations to describe these interactions. One of the most widely used potentials is the Lennard-Jones potential.

The Lennard-Jones 12-6 potential is given by the expression

$$\phi_{\mathrm{LJ}}(r) = 4\varepsilon\left[\left(\frac{\sigma}{r}\right)^{12} - \left(\frac{\sigma}{r}\right)^{6}\right] \tag{19}$$

for the interaction potential between a pair of atoms where σ and ε are the zero-crossing point and the minimum of the potential respectively. The total potential of a system containing many atoms is then given by the pairwise sum of all the individual interactions. This potential has an attractive tail at large distance *r*, it reaches a minimum at 1.122 σ, and it is strongly repulsive at shorter distances, passing through 0 at r= σ and increasing steeply as *r* is decreased further.

The term $\sim 1/r^{12}$, dominating at short distance, models the repulsion between atoms when they are brought very close to each other. Its physical origin is related to the Pauli principle: when the electronic clouds surrounding the atoms starts to overlap, the energy of the system increases abruptly. The exponent 12 was chosen exclusively on a practical basis because it is easy to compute. In fact, on physical grounds, an exponential behavior would be more appropriate.

The term $\sim 1/r^{6}$, dominating at large distance, constitutes the attractive part. This is the term which gives cohesion to the system. A $1/r^{6}$ attraction is originated by van der Waals dispersion forces, originated by induced dipole - induced dipole interactions in turn due

to fluctuating dipoles. These are rather weak interactions, which however dominate the bonding character of closed-shell systems, that is, rare gases such as Ar or Kr. Therefore, these are the materials that a LJ potential represents most closely. The parameters ε and σ are chosen to fit the physical properties of the material.

The interaction potential in MD has an infinite range but this is impractical to compute within a simulation. In practical applications, it is customary to establish a cutoff radius R_c and disregard the interactions between atoms separated by more than R_c. This results in simpler programs and enormous savings of computer resources, because the number of atomic pairs separated by a distance r grows as r^2 and quickly becomes intractable.

A simple truncation of the potential creates a new problem though: whenever a particle pair ``crosses'' the cutoff distance, the energy makes a little jump and the force experiences an impulse. A large number of these events is likely to spoil energy conservation in a simulation. To avoid this problem, the potential is often shifted in order to vanish at the cutoff radius

$$V(r) = \begin{cases} \phi_{\mathrm{LJ}}(r) - \phi_{\mathrm{LJ}}(R_c) & \text{if } r \leq R_c \\ 0 & \text{if } r \leq R_c \end{cases} \tag{20}$$

Physical quantities are, of course, affected by the potential truncation. The effects of truncating a full-ranged potential can be approximately estimated by treating the system as a uniform (constant density) continuum beyond R_c. For a bulk system, this usually amounts to a constant additive correction. For example, the potential tail (attractive) brings a small additional contribution to the cohesive energy, and to the total pressure. Truncation effects are not so easy to estimate for geometries with free surfaces, due to the lower symmetry, and can be rather large for quantities like surface energy.

Commonly used truncation radii for the Lennard-Jones potential are 2.5σ and 3.2σ. It should be mentioned that these truncated Lennard-Jones models are so popular that they acquired a value of their own as reference models for generic two-body systems. In many cases, there is no interest in evaluating truncation corrections because the truncated model itself is the subject of the investigation.

Bulk crystals and very large periodic systems present an impossible situation to handle explicitly in simulations due to the constraints in system length-scales because of limited computational power of computer systems. A solution to this problem is to use *periodic boundary conditions* (PBC). Using PBC, particles are enclosed in a box, and we can imagine that this box is replicated to infinity by rigid translation in all the three cartesian directions, completely filling the space. In other words, if one of the particles is located at position $\mathbf{r}$ in the box, we assume that this particle really represents an infinite set of particles located at $\mathbf{r} + l\mathbf{a} + m\mathbf{b} + n\mathbf{c}$, $(l, m, n = -\infty, \infty)$, where l,m,n are integer numbers, and $\mathbf{a}$,$\mathbf{b}$,$\mathbf{c}$ the vectors corresponding to the edges of the box. All these ``image" particles move together, and in fact only one of them is represented in the computer program.

The key point is that now each particle i in the box should be thought as interacting not only with other particles j in the box, but also with their images in nearby boxes. That is, interactions can ``go through" box boundaries. In fact, one can easily see that (a) we have virtually eliminated surface effects from our system, and (b) the position of the box boundaries has no effect (that is, a translation of the box with respect to the particles leaves the forces unchanged).

1.5.2 Electronic Structure Calculations

Ab initio electronic structure calculations involve the simulation of the full (or partial) electronic structure of the material under consideration. This is usually accomplished using a Quantum Mechanical (rather than a classical) formulation of the physics of interactions of the atoms in the system. The equation describing the electronic structure of the N particle system is given by the time-independent Schrödinger equation:

$$\boldsymbol{H}\Psi_i\left(\overrightarrow{x_1}, \overrightarrow{x_2}, \ldots, \overrightarrow{x_N}, \overrightarrow{R_1}, \overrightarrow{R_2}, \ldots, \overrightarrow{R_M}\right) = E_i\Psi_i\left(\overrightarrow{x_1}, \overrightarrow{x_2}, \ldots, \overrightarrow{x_N}, \overrightarrow{R_1}, \overrightarrow{R_2}, \ldots, \overrightarrow{R_M}\right) \quad (21)$$

where H is the Hamiltonian for a system of N electrons and M nuclei. The Hamiltonian consists of the kinetic energy and the potential energy terms given by

$$\widehat{H} = -\frac{1}{2}\sum_{i=1}^{N}\nabla_i^2 - \frac{1}{2}\sum_{A=1}^{M}\frac{1}{M_A}\nabla_A^2 - \sum_{i=1}^{N}\sum_{A=1}^{M}\frac{Z_A}{r_{i,A}} + \sum_{i=1}^{N}\sum_{j>i}^{N}\frac{1}{r_{i,j}} + \sum_{A=1}^{M}\sum_{B>A}^{M}\frac{Z_A Z_B}{R_{AB}} \quad (22)$$

where A and B run over the M nuclei and i,j run over the N electrons. Dealing with so many electrons and nuclei is a very hard problem to solve computationally. Thus, to simplify the problem, we make use of the Born-Oppenheimer approximation. The electron motion occurs on a much smaller time scale as compared to the nuclear motion. The approximation assumes that the nuclei remain fixed and the electrons move in a field created by the nuclei. Thus, the above expression becomes

$$\widehat{H}_{elec} = -\frac{1}{2}\sum_{i=1}^{N}\nabla_i^2 - \sum_{i=1}^{N}\sum_{A=1}^{M}\frac{Z_A}{r_{i,A}} + \sum_{i=1}^{N}\sum_{j>i}^{N}\frac{1}{r_{i,j}} = \hat{T} + \hat{V}_{Ne} + \hat{V}_{ee} \quad (23)$$

where T, V_{Ne} and V_{ee} refer to the kinetic energy of the electrons, the potential energy of interaction between the nuclei and the electrons and the potential energy of self-

interaction of the electrons respectively. The electronic Hamiltonian can therefore, be written as

$$\hat{H}_{elec}\Psi_{elec} = E_{elec}\Psi_{elec} \tag{24}$$

$$E_{tot} = E_{elec} + E_{nuc} \qquad \text{where} \quad E_{nuc} = \sum_{A=1}^{N}\sum_{B>A}^{M}\frac{Z_A Z_B}{R_{AB}} \tag{25}$$

The energy states of the electronic system are obtained using the expectation value operator as given below

$$E[\Psi] = \frac{\langle\Psi|\hat{H}|\Psi\rangle}{\langle\Psi|\Psi\rangle} \quad \text{where} \quad \langle\Psi|\hat{H}|\Psi\rangle = \int \Psi^{*}\hat{H}\Psi d\mathbf{r} \tag{26}$$

To find the energy states of the electrons from the Hamiltonian, the Variational Principle is utilized. This principle states that the energy computed from a trial wavefunction is an upper bound to the true ground-state energy E_0. So,

$$E_0 = \min_{\Psi\to N} E[\Psi] = \min_{\Psi\to N}\langle\Psi|\hat{T} + \hat{V}_{Ne} + \hat{V}_{ee}|\Psi\rangle \tag{27}$$

Thus, by iteratively adjusting the trial wave function to minimize E_0, we can achieve an estimate of the true ground state energy to within a tolerance value. There are many techniques available to estimate this ground state energy which can be classified as wavefunction-based or density-based. Two of the most commonly used methods are described briefly below.

1.5.2.1 Hartree Fock Theory

In computational physics and chemistry, the Hartree–Fock (HF) method is a method of approximation for the determination of the ground-state wavefunction and ground-state energy of a quantum many-body system.

The Hartree–Fock method assumes that the exact, *N*-body wave function of the system can be approximated by a single Slater determinant (in the case where the particles are fermions) or by a single permanent (in the case of bosons) of *N* spin-orbitals. By invoking the variational method, one can derive a set of *N*-coupled equations for the *N* spin orbitals. Solution of these equations yields the Hartree–Fock wave function and energy of the system, which are approximations of the exact ones.

The Hartree–Fock method is also called the self-consistent field method (SCF). The solutions to the resulting non-linear equations behave as if each particle is subjected to the mean field created by all other particles. The equations are almost universally solved by means of an iterative, fixed-point type algorithm.

The wave function of a two electron system as defined by the Pauli exclusion principle is given by:

$$\Psi(x_1 x_2) = \phi_1(x_1)\phi_2(x_2) - \phi_1(x_2)\phi_2(x_1) \tag{28}$$

where φ_1 and φ_2 are the wavefunctions (including spin) of the two electrons at 3 dimensional coordinates x_1 and x_2. It can be seen the total wavefunction is antisymmetric for fermions. This can also be written in the form of a determinant as

$$\begin{vmatrix} \phi_1(x_1) & \phi_2(x_1) \\ \phi_1(x_2) & \phi_2(x_2) \end{vmatrix} \tag{29}$$

So, for an N electron system, the total wavefunction can be represented by a Slater determinant

$$\Psi_{HF}(x_1 x_2 \dots x_N) = \frac{1}{\sqrt{N!}} \begin{vmatrix} \phi_1(x_1) & \phi_2(x_1) & \cdots & \phi_N(x_2) \\ \phi_1(x_2) & \phi_2(x_2) & \cdots & \phi_N(x_2) \\ \vdots & \vdots & \ddots & \vdots \\ \phi_1(x_N) & \phi_2(x_N) & \cdots & \phi_N(x_N) \end{vmatrix} \tag{30}$$

The Hartree-Fock approximation is one where an orthonormal basis φ_i is found that minimizes the energy of the determinant wave function

$$E_{HF} = \min_{\Psi_{HF} \to N} E[\Psi_{HF}] \tag{31}$$

The expectation value can be written as

$$E_{HF} = \langle \Psi_{HF} | \widehat{H} | \Psi_{HF} \rangle = \sum_{i=1}^{N} H_i + \frac{1}{2} \sum_{i,j=1}^{N} (J_{ij} - K_{ij}) \tag{32}$$

$$H_i = \int \psi_i^*(\mathbf{r}) \left[-\frac{1}{2} \nabla^2 - V_{ext}(\mathbf{r}) \right] \psi_i(\mathbf{r}) d\mathbf{r} \tag{33}$$

where H_i is the hamiltonian for the kinetic energy of the electrons plus the interaction potential between the electrons and nuclei. Thus,

$$J_{ij} = \iint \psi_i(\mathbf{r_1}) \psi_i^*(\mathbf{r_1}) \frac{1}{r_{12}} \psi_j^*(\mathbf{r_2}) \psi_j(\mathbf{r_2}) \, d\mathbf{r_1} d\mathbf{r_2} \tag{34}$$

$$K_{ij} = \iint \psi_i^*(\mathbf{r_1}) \psi_j(\mathbf{r_1}) \frac{1}{r_{12}} \psi_i(\mathbf{r_2}) \psi_j^*(\mathbf{r_2}) \, d\mathbf{r_1} d\mathbf{r_2} \tag{35}$$

where J_{ij} and K_{ij} are the Coulomb integral and the Exchange integral respectively. The HF potential is non-local. Thus the equations for the orbitals must be solved self-consistently.

Typically, in modern Hartree–Fock calculations, the one-electron wave functions are approximated by a linear combination of atomic orbitals (LCAO). These atomic orbitals are called Slater-type orbitals. Furthermore, it is very common for the "atomic orbitals" in use to actually be composed of a linear combination of one or more Gaussian-type orbitals, rather than Slater-type orbitals, in the interests of saving large amounts of computation time.

Various basis sets are used in practice, most of which are composed of Gaussian functions. In some applications, an orthogonalization method such as the Gram–Schmidt process is performed in order to produce a set of orthogonal basis functions. Other orthogonalization methods such as Davidson algorithm, Lanczos algorithm etc. are also often used.

1.5.2.2 Density Functional Theory

Density functional theory (DFT) is a quantum mechanical modeling method used in physics and chemistry to investigate the electronic structure (principally the ground state) of many-body systems, in particular atoms, molecules, and the condensed phases. With this theory, the properties of a many-electron system can be determined by using functionals, i.e. functions of another function, which in this case is the spatially dependent electron density. Hence the name density functional theory comes from the use of functionals of the electron density. DFT is among the most popular and versatile

methods available in condensed-matter physics, computational physics, and computational chemistry.

DFT has been very popular for calculations in solid-state physics since the 1970s. However, DFT was not considered accurate enough for calculations in quantum chemistry until the 1990s, when the approximations used in the theory were greatly refined to better model the exchange and correlation interactions. In many cases the results of DFT calculations for solid-state systems agree quite satisfactorily with experimental data. Computational costs are relatively low when compared to traditional methods, such as Hartree–Fock theory and its descendants based on the complex many-electron wavefunction. Density functional theory is an extremely successful approach for the description of ground state properties of metals, semiconductors, and insulators. The success of density functional theory (DFT) not only encompasses standard bulk materials but also complex materials such as proteins and carbon nanotubes.

In DFT the key variable is the particle density ρ(r) which for a normalized Ψ is given by

$$\rho(\vec{r}) = N \int \ldots \int |\Psi(\overrightarrow{x_1}, \overrightarrow{x_2}, \ldots, \overrightarrow{x_N})|^2 dx_1 dx_2 \ldots dx_N \tag{36}$$

The basis of DFT can be given by the two Hohenberg-Kohn theorems given below.

Theorem I: The external potential $V_{ext}(r)$ is (to within a constant) a unique functional of ρ(r); since, in turn $V_{ext}(r)$ fixes H we see that the full many particle ground state is a unique functional of ρ(r).

$$E[\rho] = E_{Ne}[\rho] + T[\rho] + E_{ee}[\rho] = \int \rho(\mathbf{r}) V_{Ne}(\mathbf{r}) d\mathbf{r} + F_{HK}[\rho] \tag{37}$$

$$F_{HK}[\rho] = T[\rho] + E_{ee}[\rho] \tag{38}$$

The energy can also be expressed as a unique functional of the density.

Theorem II: The functional that delivers the ground state energy of the system, delivers the lowest energy if and only if the input density is the true ground state density.

$$E_0 \leq E[\tilde{\rho}] = E_{Ne}[\tilde{\rho}] + T[\tilde{\rho}] + E_{ee}[\tilde{\rho}] \tag{39}$$

The explicit form of $F_{HK}[\rho]$ is the major challenge of DFT. Now we know that,

$$E_0 = min_{\rho \to N}(F[\rho] + \int \rho(\mathbf{r}) V_{Ne} d\mathbf{r} \tag{40}$$

where

$$F[\rho] = T[\rho] + J[\rho] + E_{ncl}[\rho] \tag{41}$$

The forms of $T[\rho]$ and $E_{ncl}[\rho]$ are not known. Thus, the interacting system is replaced by a non-interacting system at the same density as the real system.

$$T_S = -\frac{1}{2}\sum_{i}^{N} \langle \psi_i | \nabla^2 | \psi_i \rangle \text{ and } \rho_S(\mathbf{r}) = \sum_{i}^{N} \sum_{s} |\psi_i \mathbf{r}, s)|^2 = \rho(\mathbf{r}) \tag{42}$$

Obviously $T_S[\rho]$ is not the same as $T[\rho]$, so we express the equation (41) as

$$F[\rho] = T_S[\rho] + J[\rho] + E_{XC}[\rho] \tag{43}$$

where E_{XC} is the Exchange-Correlation energy is given by

$$E_{XC}[\rho] = (T[\rho] - T_S[\rho]) + (E_{ee}[\rho] - J[\rho]) \tag{44}$$

In other words, E_{XC} contains all that is not known about the self-interacting system. Thus, the final expression for the ground state energy as a function of the ground state density becomes

$$E[\rho] = T_S[\rho] + \frac{1}{2}\iint \frac{\rho(\mathbf{r_1})\rho(\mathbf{r_2})}{r_{12}} d\mathbf{r_1} d\mathbf{r_2} + E_{XC}[\rho] + \int V_{Ne}\rho(\mathbf{r}) d\mathbf{r}$$

$$= -\frac{1}{2}\sum_{i}^{N} \langle \psi_i | \nabla^2 | \psi_i \rangle + \frac{1}{2}\sum_{i}^{N}\sum_{j}^{N} \iint |\psi_i(\mathbf{r}_1)|^2 \frac{1}{r_{12}} |\psi_i(\mathbf{r}_2)|^2 d\mathbf{r_1} \mathrm{d}\mathbf{r_2}$$

$$+ E_{XC}[\rho] - \sum_{i}^{N} \int \sum_{A}^{M} \frac{Z_A}{r_{1A}} |\psi_i(\mathbf{r}_1)|^2 d\mathbf{r_1} \tag{45}$$

where E_{XC} is the only term that is left to be determined. The E_{XC} term can be further split as

$$\epsilon_{XC}\big(\rho(\mathbf{r})\big) = \epsilon_X\big(\rho(\mathbf{r})\big) + \epsilon_C\big(\rho(\mathbf{r})\big) \tag{46}$$

where E_X is the exchange part and E_C is the correlation part. The exchange part of the energy which is the energy of an electron in a uniform electron gas at a particular density was derived by Bloch and Dirac:

$$\epsilon_X = -\frac{3}{4}\left(\frac{3\rho(\mathbf{r})}{\pi}\right)^{1/3} \tag{47}$$

The major problem with DFT is that the exact functionals for exchange and correlation are not known, except for the free electron gas. However, approximations exist which permit the calculation of certain physical quantities quite accurately. In physics, the most widely used approximation is the local-density approximation (LDA), where the functional depends only on the density at the coordinate where the functional is evaluated

$$E_{XC}^{LDA}[\rho] = \int \rho(\mathbf{r})\epsilon_{XC}\big(\rho(\mathbf{r})\big)d\mathbf{r} \tag{48}$$

The local spin-density approximation (LSDA) is a straightforward generalization of the LDA to include electron spin

$$E_{XC}^{LSDA}[n_{\uparrow}, n_{\downarrow}] = \int \epsilon_{XC}(n_{\uparrow}, n_{\downarrow})n(\mathbf{r})d^3\mathbf{r} \tag{49}$$

Highly accurate formulae for the exchange-correlation energy density have been constructed from quantum Monte Carlo simulations of jellium. Generalized gradient approximations (GGA) are still local but also take into account the gradient of the density at the same coordinate:

$$E_{XC}^{GGA}[n_{\uparrow}, n_{\downarrow}] = \int \epsilon_{XC}(n_{\uparrow}, n_{\downarrow}, \boldsymbol{\nabla} n_{\uparrow}, \boldsymbol{\nabla} n_{\downarrow})n(\mathbf{r})d^3\mathbf{r} \tag{50}$$

Using the latter (GGA), very good results for molecular geometries and ground-state energies have been achieved.

Potentially more accurate than the GGA functionals are the meta-GGA functionals, a natural development after the GGA (generalized gradient approximation). The meta-GGA DFT functional in its original form includes the second derivative of the electron density (the Laplacian). The meta-GGA functional includes only the density and its first derivative in the exchange-correlation potential. These functionals include a further term in the expansion, depending on the density, the gradient of the density and the Laplacian (second derivative) of the density. Difficulties in expressing the exchange part of the energy can be relieved by including a component of the exact exchange energy calculated from Hartree–Fock theory. Functionals of this type are known as hybrid functionals.

1.6 Organization of this Thesis

We have presented our work in the area of computational modeling of PbSe quantum dots in this thesis to address some of the open questions in the field of colloidal NC assemblies. The overview is presented in Fig 1.9. In this chapter, we have briefly introduced QDs and their properties. We have discussed the origin of the novel electronic properties exhibited by quantum dots and the theory behind the physics of the electronic structure of QDs. It also provides a background of the experimental progress in the field of colloidal nanocrystals and some of the previous computational modeling work on NCs and their assemblies. This is followed by a primer about the various computational techniques used in this thesis including Molecular Dynamics (MD) and Density Functional Theory (DFT).

The second chapter deals with the study of self-assembled monolayers. Self-assembled monolayers are akin to ligands on a NC with an "infinitely" large surface. The study of these films gives insight into the structure and dynamics of the ligands on the "finite" facets of the NCs. The study deals with the effect of various parameters such as length, the structure and the grafting density of the molecules on the overall structure and dynamics of the film. The study also examines the effects of deposition of organic molecules into the matrix. This helps us understand the behavior of solvent molecules inside the ligand corona on a NC. The insights gained from this study are utilized in the analysis of ligand-clad NCs in the successive chapters.

The third chapter deals with a study of isolated NCs and the structure and dynamics of the NC core as well as the ligand corona capping the NC surface. Here we examine the effect of shape and size of the NC core and the effect of ligand length and ligand grafting

density on the structure of the ligand shell as well as the energetic interactions between two adjacent NCs. We also review some of the coarse-graining techniques utilized in the literature for reducing the computational complexity in modeling these systems and discuss the pros and cons of picking a particular coarse grained model over another.

The fourth chapter deals with the study of solvent effects on NC superlattices. We determine the effect of two different types of solvents, hexane and toluene, on the superlattice symmetry of the NC film. We find that the final superlattice symmetry chosen depends on the amount of residual solvent in the system as well as the ratio of ligand length to NC diameter. We also examine the effect of anisotropic ligand coverage on the superlattice symmetry chosen and provide an explanation for a transformation in superlattice symmetry that occurs in the case of NCs with only partial ligand coverage.

The fifth chapter deals with the electronic structure of the individual NCs and the electronic coupling and rate of charge transfer between two adjacent NCs. We show that the shape of the NC and the ratio of areas of different facets of the NC determine the electronic structure as well as preferential electronic coupling along certain directions. We examine NCs of different shape and sizes and also study the effect of having bare NC surface versus ligand passivated surfaces on the electronic structure and the charge transfer rate and charge mobility in superlattices.

The final chapters discuss some of our more recent work dealing with the electronic structure of NCs and also provide a brief discussion about some of the future directions that can be taken to provide insight into the mechanism of charge transfer in NC systems as well as providing useful information that would help successfully guide future experiments.

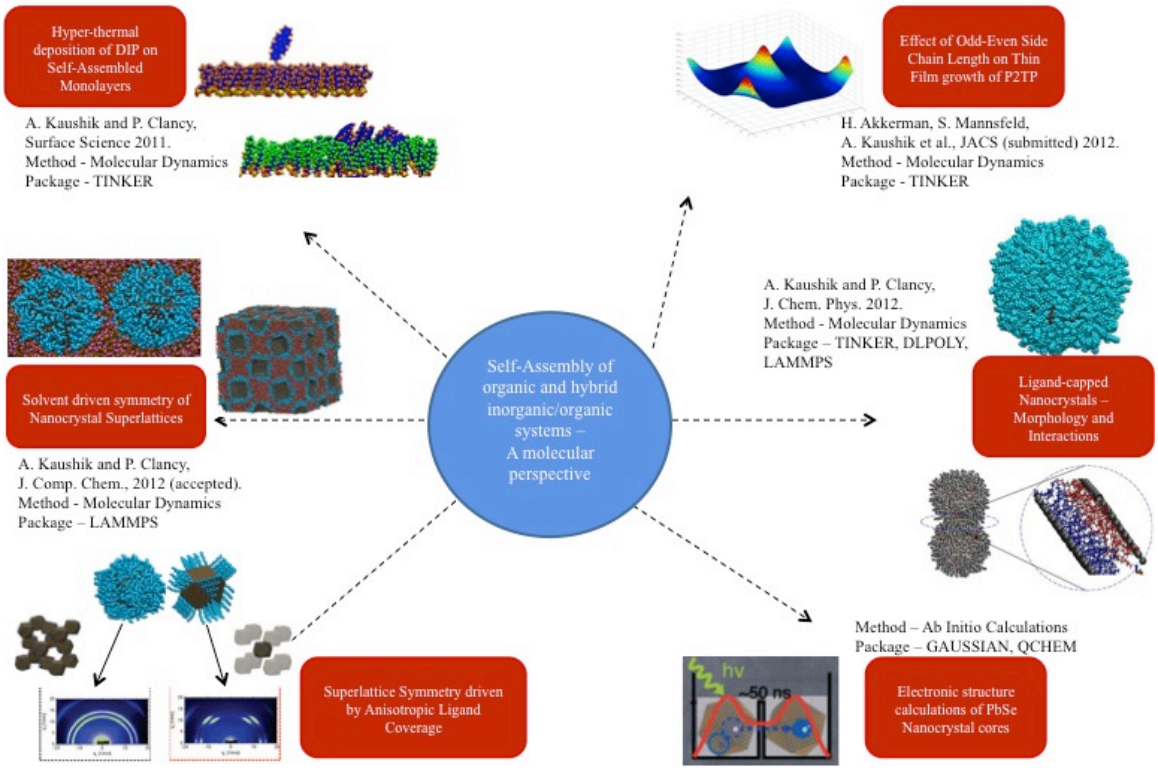

Figure 1.9: Overview of the Thesis.

REFERENCES

[1] E. P. A. M. Bakkers, Thesis, Universiteit Utrecht (2000).

[2] A. Franceschetti, and A. Zunger, Appl. Phys. Lett., 76, 1731-1733 (2000).

[3] P.W. Atkins, Physical Chemistry, Oxford University Press, Great Brittain (1990).

[4] P. Bhattacharya, S. Ghosh, A. D. Stiff-Roberts, Annu. Rev. Mat. Res., 34, 1 (2004)

[5] C. Murray, C. Kagan, M. Bawendi, Annu. Rev. Mat. Sci., 30, 545 (2000)

[6] M. Law, J. Goldberger, P. Yang, Annu. Rev. Mat. Res., 34, 83-122 (2004)

[7] M. S. Skolnick, D. J. Mowbray, Annu. Rev. Mat. Res., 34, 181-218 (2004)

[8] D. V. Talapin; J.-S. Lee; M. V. Kovalenko; E. V. Shevchenko, Chem. Rev., 110, 389 (2010)

[9] Y. Wu, C. Wadia, W. Ma, B. Sadtler, A. P. Alivisatos, Nano Lett., 8, 2551–2555 (2008)

[10] M. G. Panthani, V. Akhavan, B. Goodfellow, J. P. Schmidtke, L. Dunn, A. Dodabalapur, P. F. Barbara, B. A. Korgel, J. Am. Chem. Soc., 130, 16770–16777 (2008)

[11] J. J. Choi, Y-F. Lim, M. E. B. Santiago-Berrios, M. Oh, B-R. Hyun, L. Sun, A. C. Bartnik, A. Goedhart, G. G. Malliaras, H. D. Abruna, F. W. Wise, T. Hanrath, Nano Lett., 9, 3749–3755 (2009)

[12] W. Ma, J. M. Luther, H. Zheng, Y. Wu, A. P. Alivisatos, Nano Lett., 9, 1699–1703 (2009)

[13] J. M. Luther, M. Law, M. C. Beard, Q. Song, M. O. Reese, R. J. Ellingson, A. Nozik, Nano Lett., 8, 3488–3492 (2008)

[14] K. S. Leschkies, T. J. Beatty, M. S. Kang, D. J. Norris, E. S. Aydil, ACS Nano, 3, 3638–3648 (2009)

[15] J. J. Urban, D. V. Talapin, E. V. Shevchenko, C. R. Kagan, C. B. Murray, Nat. Mater., 6, 115–121 (2007)

[16] B. Sun, H. Sirringhaus, Nano Lett., 5, 2408–2413 (2005)

[17] D. V. Talapin, C. B. Murray, Science, 310, 86–89 (2005)

[18] S. Coe, W-K. Woo, M. Bawendi, V. Bulovic, Nature, 420, 800–803 (2002)

[19] A. H. Mueller, M. A. Petruska, M. Achermann, D. J. Werder, E. A. Akhadov, D. D. Koleske, M A. Hoffbauer, V. I. Klimov, Nano Lett., 5, 1039–1044 (2005)

[20] S. A. McDonald, G. Konstantatos, S. Zhang, P. W. Cyr, E. J. D. Klem, L. Levina, E. H. Sargent, Nat. Mater., 4, 138–142 (2005)

[21] A. N. Shipway, E. Katz, I. Willner, Chem. Phys. Chem., 1, 18–52 (2000)

[22] V. A. Akhavan, B. W. Goodfellow, M. G. Panthani, D. K. Reid, D. J. Hellebusch, T. Adachi, B. A. Korgel, Energy Environ. Sci., 3, 1600–1606 (2010)

[23] V. A. Akhavan, B. W. Goodfellow, M. G. Panthani, B. A. Korgel, Modern Energy Rev., 2, 25–27 (2010)

[24] C. B. Murray, S. Sun, W. Gaschler, H. Doyle, T. A. Betley, C. R. Kagan, IBM J. Res. Dev., 45, 47–56 (2001)

[25] P. Liljeroth, K. Overgaag, A. Urbieta, B. Grandidier, S. G. Hickey, D. Vanmaekelbergh, Phys. Rev. Lett., 97, 096803 (2006)

[26] B. Lee, P. Podsiadlo, S. Rupich, D. V. Talapin, T. Rajh, E. V. Shevchenko, J. Am. Chem. Soc., 131, 16386-16388 (2009)

[27] C. B. Murray, D. J. Norris, M. G. Bawendi, J. Am. Chem. Soc., 115, 8706 (1993).

[28] S. Sun, C. B. Murray, D. Weller, L. Folks, A. Moser, Science, 287, 1989 (2000).

[29] J. Park, J. Joo, C. G. Kwon, Y. Jang, T. Hyeon, Angew. Chem., Int. Ed., 46, 4630 (2007).

[30] J. Park, K. An, Y. Hwang, J-G. Park, H-J. Noh, H-J. Kim, J-H. Park, N-M. Hwang, T. Hyeon, Nat. Mater., 3, 891 (2004).

[31] Y. Yin, A. P. Alivisatos, Nature, 437, 664 (2005).

[32] K. S. Cho, D. V. Talapin, W. Gaschler, C. B. Murray, J. Am. Chem. Soc., 127, 7140 (2005).

[33] E. V. Shevchenko, M. I. Bodnarchuk, M. V. Kovalenko, D. V. Talapin, R. K. Smith, S. Aloni, W. Heiss, A. P. Alivisatos, Adv. Mater., 20, 4323 (2008).

[34] D. V. Talapin, J. H. Nelson, E. V. Shevchenko, S. Aloni, B. Sadtler, A. P. Alivisatos, Nano Lett., 7, 2951 (2007) .

[35] L. Carbone, C. Nobile, M. De Giorgi, F. D. Sala, G. Morello, P. Pompa, M. Hytch, E. Snoeck, A. Fiore, I. R. Franchini, M. Nadasan, A.F. Silvestre, L. Chiodo, S. Kudera, R. Cingolani, R. Krahne, L. Manna, Nano Lett., 7, 2942 (2007).

[36] D. J. Milliron, S. M. Hughes, Y. Cui, L. Manna, J. Li, L-W. Wang, A. P. Alivisatos, Nature, 430, 190 (2004).

[37] H. Zeng, S. Sun, Adv. Funct. Mater., 18, 391 (2008).

[38] T. Hanrath, J. Vac. Sci. Technol. A, 30, 030802 (2012).

[39] J. A. Tang, E. H. Sargent, Adv. Mater., 23, 12 (2011).

[40] A. L. Efros, A. L. Efros, Sov. Phys. Semicond., 16, 772 (1982).

[41] F. W. Wise, Acc. Chem. Res., 33, 773 (2000).

[42] X. M. Jiang, R. D. Schaller, S. B. Lee, J. M. Pietryga, V. I. Klimov, A. A. Zakhidov, J. Mater. Res., 22, 2204 (2007).

[43] H. Du, C. L. Chen, R. Krishnan, T. D. Krauss, J. M. Harbold, F. W. Wise, M. G. Thomas, J. Silcox, Nano Lett., 2, 1321 (2002).

[44] J. M. Pietryga, R. D. Schaller, D. Werder, M. H. Stewart, V. I. Klimov, J. A. Hollingsworth, J. Am. Chem. Soc., 126, 11752 (2004).

[45] D. Cui, J. Xu, T. Zhu, G. Paradee, S. Ashok, Appl. Phys. Lett. 88, 183111 (2006).

[46] C. Evans, L. Guo, J. Peterson, S. Maccagnano-Zacher, T. Krauss, Nano Lett., 8, 2896 (2008).

[47] C. B. Murray, C. R. Kagan, M. G. Bawendi, Ann. Rev. Mater. Sci., 30, 545 (2000).

[48] C. B. Murray, D. J. Norris, M. G. Bawendi, J. Am. Chem. Soc., 115, 8706 (1993).

[49] S. G. Kwon, T. Hyeon, Small, 7, 2685 (2011).

[50] A. Henglein, Ber. Bunsen-Ges. Phys. Chem. Chem. Phys., 86, 301 (1982).

[51] L. Mangolini, E. Thimsen, U. Kortshagen, Nano Lett., 5, 655 (2005).

[52] P. Shah, T. Hanrath, K. Johnston, B. Korgel, J. Phys. Chem. B, 108, 9574 (2004).

[53] N. F. Borrelli and D. W. Smith, J. Non-Cryst. Solids, 180, 25 (1994).

[54] Y. Yin, A. P. Alivisatos, Nature, 437, 664 (2005).

[55] S. G. Kwon, Y. Piao, J. Park, S. Angappane, Y. Jo, N. M. Hwang, J. G. Park, T. Hyeon, J. Am. Chem. Soc., 129, 12571 (2007).

[56] D. V. Talapin, J-S. Lee, M. V. Kovalenko, E. V. Shevchenko, Chem. Rev., 110, 389–458 (2010).

[57] V. K. Lamer, R. H. Dinegar, J. Am. Chem. Soc., 72, 4847 (1950).

[58] Y. Yin, A. P. Alivisatos, Nature, 437, 664 (2005).

[59] L. Manna, E. Scher, A. Alivisatos, J. Am. Chem. Soc., 122, 12700 (2000).

[60] J. M. Pietryga, R. D. Schaller, D. Werder, M. H. Stewart, V. I. Klimov, J. A. Hollingsworth, J. Am. Chem. Soc., 126, 11752 (2004).

[61] A. J. Nozik, M. C. Beard, J. M. Luther, M. Law, R. J. Ellingson, J. C. Johnson, Chem. Rev., 110, 6873–6890 (2010).

[62] B. Lee, P. Podsiadlo, S. Rupich, D. V. Talapin, T. Rajh, E. V. Shevchenko, J. Am. Chem. Soc., 131, 16386 (2009).

[63] C. B. Murray, C. R. Kagan, M. G. Bawendi, Science, 270,1335 (1995).

[64] C. P. Collier, T. Vossmeyer, J. R. Heath, Annu. Rev. Phys. Chem., 49, 371 (1998).

[65] C. A. Leatherdale, C. R. Kagan, N. Y. Morgan, S. A. Empedocles, M. A. Kastner, M. G. Bawendi, Phys. Rev. B, 62, 2669 (2000).

[66] V. J. Porter, S. Geyer, J. E. Halpert, M. A. Kastner, M. G. Bawendi, J. Phys. Chem. C, 112, 2308 (2008).

[67] T. S. Mentzel, V. J. Porter, S. Geyer, K. MacLean, M. G. Bawendi, M. A. Kastner, Phys. Rev. B, 77, 75316 (2008).

[68] J. M. Luther, M. C. Beard, Q. Song, M. Law, R. J. Ellingson, A. J. Nozik, Nano Lett., 7, 1779 (2007).

[69] B. L. Wehrenberg, D. Yu, J. S. Ma, P. J. Guyot-Sionnest, Phys. Chem. B, 109, 20192 (2005).

[70] C. B. Murray, D. J. Norris, M. G. Bawendi, J. Am. Chem. Soc., 115, 8706 (1993).

[71] D. Yu, C. Wang, P. Guyot-Sionnest, Science, 300, 1277 (2003).

[72] M. Law, J. M. Luther, Q. Song, B. K. Hughes, C. L. Perkins, A. J. Nozik, J. Am. Chem. Soc., 130, 5974 (2008).

[73] M. V. Jarosz, V. J. Porter, B. R. Fisher, M. A. Kastner, M. G. Bawendi, Phys. Rev. B, 70, 195327 (2004).

[74] D. C. Oertel, M. G. Bawendi, A. C. Arango, V. Bulovic, Appl. Phys. Lett., 87, 213505 (2005).

[75] D. Yu, B. L. Wehrenberg, P. Jha, J. Ma, P. J. Guyot-Sionnest, Appl. Phys., 99, 104315 (2006).

[76] J. J. Choi, J. Luria, B.-R. Hyun, A. C. Bartnik, L. Sun, Y.-F. Lim, J. A. Marohn, F. W. Wise, T. Hanrath, Nano Lett., 10, 1805 (2010).

[77] A. Wolcott *et al.*, J. Phys. Chem. Lett., 2, 795 (2011).

[78] Y. Liu, M. Gibbs, J. Puthussery, S. Gaik, R. Ihly, H. W. Hillhouse, M. Law, Nano Lett., 10, 1960 (2010).

[79] J. S. Liu, T. Tanaka, K. Sivula, A. P. Alivisatos, J. M. J. Frechet, J. Am. Chem. Soc., 126, 6550 (2004).

[80] H. Skaff, K. Sill, T. J. Emrick, Am. Chem. Soc., 126, 11322 (2004).

[81] F. Xu, X. Ma, C. R. Haughn, J. Benavides, M. F. Doty, S. G. Cloutier, ACS Nano, 5, 9950 (2011).

[82] G. Sarasqueta, K. R. Choudhury, F. So, Chem. Mater., 22, 3496 (2010).

[83] G. I. Koleilat, L. Levina, H. Shukla, S. H. Myrskog, S. Hinds, A. G. Pattantyus-Abraham, E. H. Sargent, ACS Nano, 2, 833 (2008).

[84] K. S. Jeong *et al.*, ACS Nano, 6, 89 (2011).

[85] C. Kagan, APS March Meeting 2012.

[86] J-H. Choi, A. T. Fafarman, S. J. Oh, D-K. Ko, D. K. Kim, B. T. Diroll, S. Muramoto, J. G. Gillen, C. B. Murray, C. Kagan, Nano Letters, 12, 2631−2638 (2012).

[87] W. D. Luedtke, U. Landman, J. Chem. Phys., 100, 13323-13329 (1996).

[88] P. Schapotschnikow, R. Pool, T. J. H. Vlugt, Nano Lett., 8, 2930-2934 (2008).

[89] P. Schapotschnikow, M.A. van Huis, H.W. Zandbergen, D. Vanmaekelbergh and T. J. H. Vlugt, Nano Lett., 10, 3966-3971 (2010).

[90] P. Schapotschnikow, T. J. H. Vlugt, J. Phys. Chem. C, 114, 2531-2537 (2010).

[91] S.O. Nielsen, C.F. Lopez, G. Srinivas, M. L. Klein, J. Phys.: Condens. Matter, 16, R481-512 (2004).

[92] A. Badia, L. Cuccia, L. Demers, F. Morin, R.B. Lennox, J. Am. Chem. Soc., 119, 2682-2692 (1997).

[93] J. M. D. Lane, G. S. Grest, Phys. Rev. Lett., 104, 235501 (2010).

[94] A. Yang, C. Weng, J. Phys. Chem. C, 114, 8697-8709 (2010).

[95] A. Yang, C. Weng, T. Chen, J. Chem. Phys., 135, 034101 (2011).

[96] W. L. Jorgensen, J. D. Madura, C. J. Swenson, J. Am. Chem. Soc., 106, 6638-6646 (1984)

[97] S. Toxvaerd, J. Chem. Phys., (1990) 93, 4290-4295.

[98] J. I. Siepmann, S. Karaborni, B. Smit, Nature, 365, 330-332 (1993)

[99] M. G. Martin, J. I. Siepmann, J. Phys. Chem. B, 102 (14), pp 2569-2577 (1998)

[100] S. K. Nath, F. A. Escobedo, J. J. de Pablo, J. Chem.Phys., 108, 9905 (1998)

[101] S. K. Nath, B. J. Banaszak, J. J. de Pablo, J. Chem. Phys., 114, 3612-3616 (2001)

[102] C. Li, P. Choi, P. R. Sundararajan, Polymer, 51, 2803-2808 (2010)

[103] W. Paul, Do Y. Yoon, G.D. Smith, J. Chem. Phys., 103, 1702-1709 (1995).

[104] S.L. Mayo, B.D. Olafson, W. A. Goddard, J. Phys. Chem. 94, 8897-8909 (1990).

[105] W.L. Jorgensen, D.S. Maxwell, J. Tirado-Rives, J. Am. Chem. Soc., 118 (45), 11225-11236 (1996).

[106] B. Lee, P. Podsiadlo, S. Rupich, D. V. Talapin, T. Rajh, E. V. Shevchenko, J. Am. Chem. Soc., 131, 16386-16388 (2009).

[107] E. V. Shevchenko, D. V. Talapin, A. Kornowski, F. Wiekhorst, J. Kotzler, M. Haase, A. Rogach, H. Weller, Adv. Mater., 14, 287-290 (2002)

[108] K. Bian, J. J. Choi, A. Kaushik, P. Clancy, D-M. Smilgies, T. Hanrath, ACS Nano, 5(4), 2815-2823 (2011).

[109] B. W. Goodfellow, R. N. Patel, M. G. Panthani, D-M. Smilgies, B. A. Korgel, J. Phys. Chem. C, 115, 6397-6404 (2011).

[110] B. A. Korgel, D. Fitzmaurice, Phys. Rev. B., 59, 14191-14201 (1999).

[111] P. Schapotschnikow, R. Pool, T. J. H. Vlugt, Nano Lett., 8, 2930-2934 (2008)

[112] P. Schapotschnikow, T. J. H. Vlugt, J. Phys. Chem. C, 114, 2531-2537 (2010).

[113] E. Rabani, S. A. Egorov, J. Phys. Chem. B, 106, 6771-6778 (2002)

[114] Y. Qin, K. A. Fichthorn, Phys. Rev. E., 73, 020401(R) (2006)

[115] J. M. D. Lane, G. S. Grest, Phys. Rev. Lett., 104, 235501 (2010)

[116] A. Yang, C. Weng, J. Phys. Chem. C, 114, 8697-8709 (2010)

[117] A. Yang, C. Weng, T. Chen, J. Chem. Phys., 135, 034101 (2011)

[118] J-W. Luo, A. Franceschetti, and A. Zunger, Nano Letters, 8, 10, 3174-3181 (2008).

[119] A. Franceschetti, L. W. Wang, G. Bester, A. Zunger, Nano Letters, 6, 5, 1069-1074 (2006).

[120] J. M. An, A. Franceschetti, A. Zunger, Nano Letters, 7, 7, 2129-2135 (2007).

[121] J. M. An, A. Franceschetti, S. V. Dudiy, A. Zunger, Nano Letters, 6, 12, 2728-2735 (2006).

[122] M. Califano, G. Bester, A. Zunger, Nano Letters, 3, 9, 1197-1202 (2003).

[123] B. Kiran, A. K. Kandalam, R. Rallabandi, P. Koirala, X. Li, X. Tang, Y. Wang, H. Fairbrother, G. Gantefoer, K. Bowen, J. Chem. Phys., 136, 024317 (2012).

[124] Y. Gai, H. Peng, J. Li, J. Phys. Chem. C, 113, 21506–21511 (2009).

[125] O. Voznyy, J. Phys. Chem. C, 115, 15927–15932 (2011).

[126] S. A. Fischer, A. M. Crotty, S. V. Kilina, S. A. Ivanovc, S. Tretiak, Nanoscale, 4, 904 (2012).

[127] H. Bao, B. F. Habenicht, O. V. Prezhdo, X. Ruan, Phys. Rev. B, 79, 235306 (2009).

[128] H. M. Jaeger, S. Fischer, O. V. Prezhdo, J. Chem. Phys., 136, 064701 (2012).

[129] I-H. Chu, M. Radulaski, N. Vukmirovic, H-P. Cheng, L-W. Wang, J. Phys. Chem. C, 115, 21409–21415 (2011).

[130] D. Frenkel, B. Smit, Understanding Molecular Simulation, Academic Press; 2 edition (2001).

[131] F. Ercolessi, http://www.fisica.uniud.it/~ercolessi/.

[132] D. A. McQuarrie, Quantum Chemistry, University Science Books (1983).

CHAPTER 2

Structure and Dynamics of Self-Assembled Monolayers – A study of trapping dynamics of Diindenoperylene and structure of Cn-P2TP-Cn lattice

2.1 Introduction

Self-assembled monolayers (SAMs) consist of a layer of functionalized long-chain molecules tethered to a solid substrate. Their presence as a “coating" on a surface is attractive in a number of applications due to the possibility they provide to tune the properties of the surface by selectively modifying functional groups on the SAM [1, 2]. SAMs of organosilane molecules are of particular technological interest in organic electronics because they can be assembled on hydroxylated surfaces such as SiO_2 for applications in areas such as organic electronics, electronic sensors and biosensors [3,4]. Not surprisingly then, they have been the subject of extensive theoretical and experimental research due, for instance, to their ability to improve the mobility of organic thin films for electronic devices, presumably by improving surface order.

There have been several molecular-level computational studies of SAMs, some relevant to the studies in this paper [1, 4-10]. Yamamoto *et al*. studied the influence of hydrogen bond conformations of alkanesilane SAMs using molecular mechanics and Molecular Dynamics simulations [1]. A study of the diffusion of tricresyl phosphate (TCP) molecules on an octadecyltrichlorosilane SAM [4] found that TCP molecules are highly mobile on the surface with a small isotropic diffusion activation barrier of about 0.1 eV (9 kJ/mol). TCP molecules prefer to diffuse over the surface rather than become inserted between the SAM molecules. The structural properties of alkanethiol SAMs have been

determined as a function of temperature, lattice spacing (density), and molecular chain length [5]. For instance, chains containing 13 carbons tilt from the surface normal by a collective angle of 25˚ along the next-nearest-neighbor direction at 300 K. The tilt angle can vary as much as 20˚ for a temperature increase of 200 K, and change by 30˚ for a lattice constant increase of 0.6 Å. There have also been studies of hyperthermal deposition of inert gas atoms on SAM surfaces. Simulations of Ar, Xe and Ne on SAMs showed inelastic scattering and trapping dynamics [4, 11-14]. Xe, in particular, showed a sort of directed ejection mechanism after insertion into the SAM matrix [15].

Experimentally, a variety of preparation methods are available for self-assembled monolayers and multilayers of alkyltrichlorosilanes, including studies that altered the molecule's functional groups in order to get specific desirable properties [16]. There have also been studies aimed at controlling surface properties by varying the alkyl chain lengths of the SAMs to enhance the electrical performance of field-effect transistors (FETs) of different organic molecules [17]. Effects of alkyl chain lengths of SAMs on the film growth of organic molecules like pentacene have been studied. In particular, Bao *et al*. have observed that the nature of film growth, and hence the performance of transistors, is significantly affected by the alkyl chain of the SAM molecule being odd or even in length and by the density of the SAM [18-20].

Despite these prior computational studies of the characteristics of SAMs in contact with a diffusing surface atom or molecule, there has been no previous study of the *deposition* of organic thin films on SAM surfaces, either at thermal or hyperthermal deposition conditions. Previously studied SAM surfaces have always been well packed; there have been no studies involving low packing densities of SAMs. However, experimental

studies, at least on amorphous SiO_2 surfaces, are often performed with a low density of SAM molecules and thus the ability to simulate deposition of molecular species on low-density SAM surfaces is of considerable importance. In this study, we considered three molecules that are capable of creating self-assembled monolayers (fluorooctatrichlorosilane (FOTS), octatrichlorosilane (OTS) and octadecyltrichlorosilane (ODTS)) on certain surfaces such as amorphous SiO_2. In addition, we looked at the behavior of hexamethyldisilazane (HMDS), a short-chain, surface-coating, ligand that provides an interesting contrast to the SAMs. These four molecules (OTS, FOTS, ODTS and HMDS) are used as a monolayer-thick "surface" upon which an organic semiconducting molecule, diindenoperylene (DIP), is to be grown as a thin film; see Fig. 1.1. The SAM molecules have long-chain carbon backbones terminated at one end by a methyl group (a fluorinated methyl group in the case of FOTS) and at the other end by trichlorosilane, $–SiCl_3$. These four molecules vary in chain length: HMDS has a very short (two-carbon) backbone, barely a chain. The FOTS and the OTS molecules have an 8-carbon backbone and the ODTS has an 18-carbon backbone; again, see Fig. 2.1.

In this paper, we will study the mechanistic processes which lead to the inadvertent trapping of deposited molecules between SAM molecules on the surface, (Fig. 2.2 (a-c)) which we will call "trapping dynamics," as opposed to surface-adsorption events which are the usual intent of a deposition process (Fig. 2.2 (d-f)). As shown in Fig. 2.2 (g-i), depositing molecules can also be "scattered," that is, they hit the surface, or are inserted into the SAM, but ultimately are expelled from the vicinity of the SAM without inclusion either on the surface or between SAM molecules. Whether "trapping" of molecules between SAM molecules is disadvantageous or not is not clear: At first glance, the

unintended trapping process seems likely to lead to problems with the creation of an ordered surface (depending, perhaps, on the length of the deposited molecules in relation to that of the SAM molecule). But it could also be speculated that the insertion process could lead to an effectively higher density SAM monolayer, perhaps one that enhances surface deposition, and hence be essentially a benign process in terms of the quality of film growth that can occur subsequently. We will investigate some of these issues here.

In this study, we have performed (MD) simulations to characterize the trapping dynamics of diindenoperylene (DIP) on some commonly studied SAM surfaces and to identify the major factors that affect the growth of DIP thin films on SAMs. The motivation for performing a molecular simulation study is that it allows an elucidation of the mechanisms of trapping in greater detail than is possible from experiments alone. In addition to studies that replicate the conditions of energetic deposition experiments by the Engstrom-led group at Cornell, molecular simulations also afford the chance to investigate trapping dynamics in regimes that are difficult or impossible to study experimentally: the effect of packing density, orientation of the incident DIP molecule and, to some extent, temperature on deposition outcomes fall into this category. In this paper, we will identify several key parameters which affect the trapping of DIP and which could be tuned to increase the efficiency with which SAMs are able to affect the ordered growth of DIP molecules (and, by extension, other small organic semiconductor molecules). One of the advantages of a computational study of this kind is the ability to observe deposition events at a molecular scale. This gives us an opportunity to calculate the outcome of a single deposition event without having to perform a post-mortem analysis once the bulk film has been deposited.

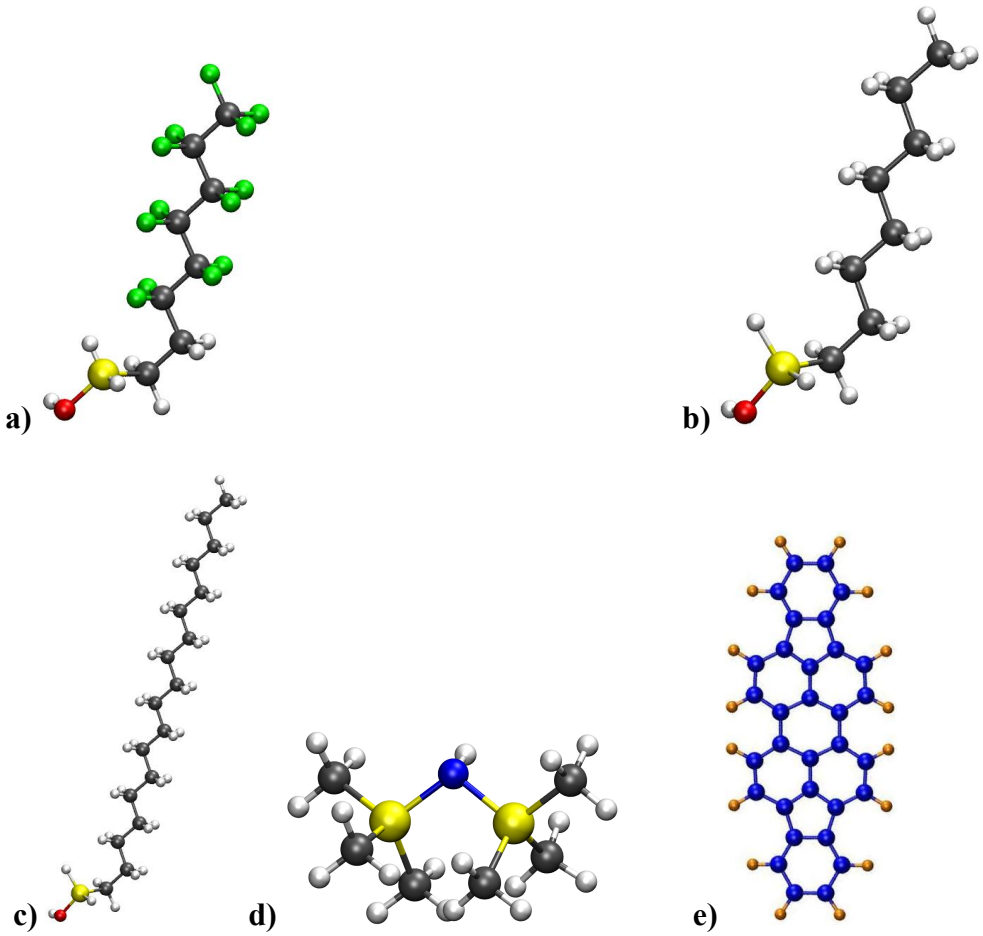

Figure 2.1: Molecular models of the molecules: (a) FOTS (b) OTS (c) ODTS (d) HMDS (e) DIP

In experiments, it is possible to calculate the fraction of DIP molecules that are not scattered from the SAM surface, but it is essentially impossible for experiments to differentiate between the fraction that becomes inserted into the surface and the fraction adsorbed on the surface. Such knowledge is potentially important since the fate of depositing molecules governs both the nature and quality of the bulk film grown. This study is intended to capture details of deposition events, some of which may not be accessible experimentally, in order to explain a few key aspects that affect the observed bulk properties of the deposited film.

2.2 Configuration of the system

In the experimental set up used by Engstrom *et al*. [21, 22], molecules that form surface coatings, like the SAMs and HMDS, are deposited on an amorphous silicon dioxide substrate. The head group, consisting of three Cl atoms, reacts with the -OH groups of the substrate, forming an -O-Si bond that tethers the molecule to the surface. In the simulation, we simply tethered each SAM molecule to an x-y location on an undefined substrate surface. Since the ligands are relatively long, an explicitly modeled surface beneath the SAM proved to be unnecessary. The FOTS, OTS and ODTS SAM molecules were tethered to hexagonal lattice points in free space at the oxygen atom, *i.e*., the position of the oxygen atom was fixed throughout the simulation. This choice followed experimental evidence which suggests that the oxygen atoms are attached to the substrate surface, thereby anchoring the SAM molecules at this point. It is possible that, on real surfaces, the SAM molecule could be tethered *via* more than one oxygen atom in the head group, which implies that the silicon atom of the head group is also essentially fixed in place [1].

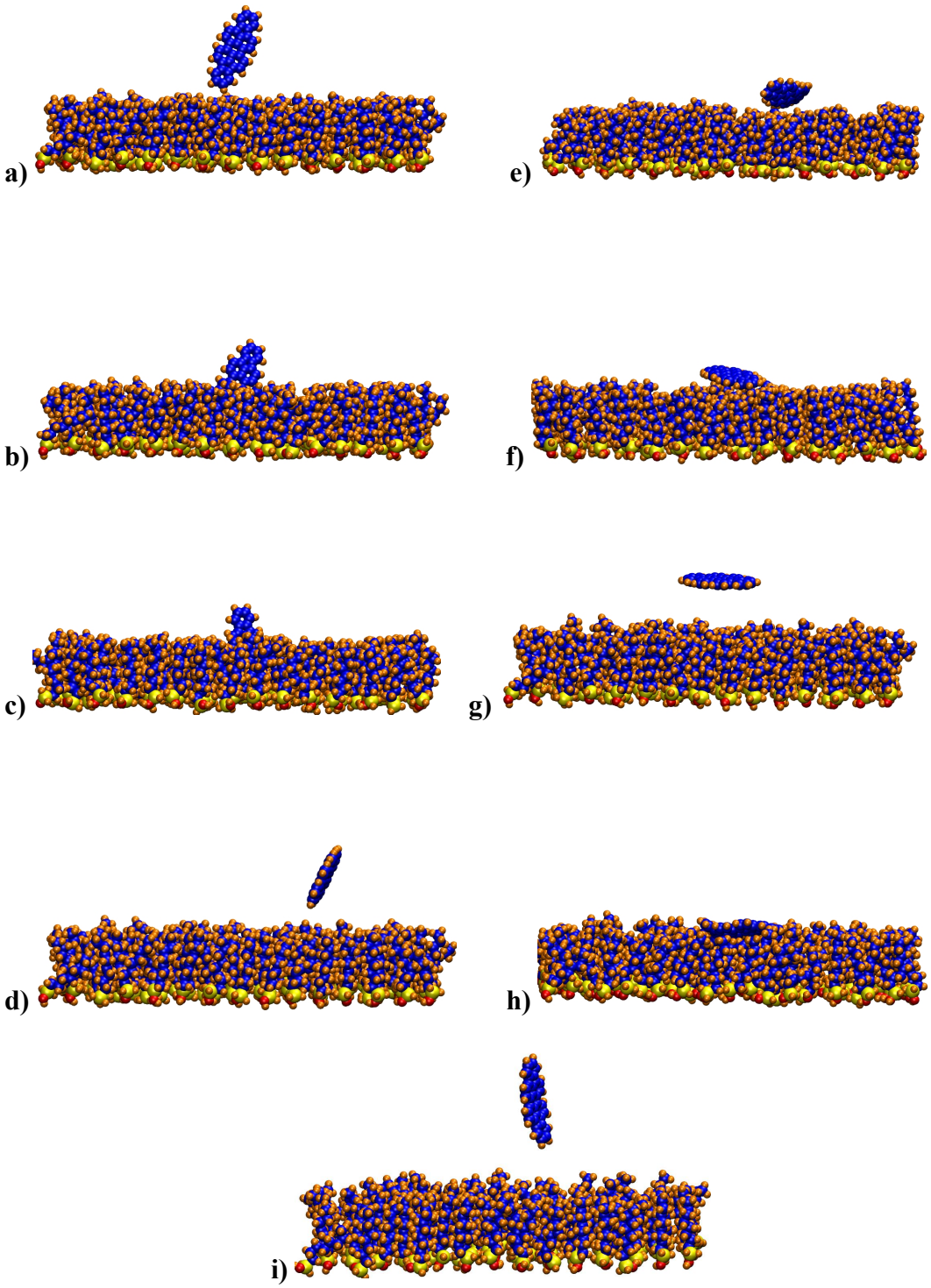

Figure 2.2: Possible events of DIP collision: (a-c) Insertion event, (d-f) Adsorption event and (g-i) Scattering event.

To study the impact of this eventuality and better define an appropriate initial system configuration, we conducted simulations in which *both* the silicon and oxygen atoms were fixed in place. The energetics of the system differed by less than 5% in energy and with no observable structural difference in the system whether just oxygen was fixed, or both oxygen and silicon were fixed. Thus all the remaining simulations described in this paper assumed that the SAM molecule is tethered to the substrate by one oxygen atom.

For the short HMDS ligand, we could not use the same approach since, at the lower densities considered here, incoming DIP molecules could readily move through gaps in the x-y plane where the substrate would be located in a physical system. To avoid this, we placed one fixed layer of a Si (111) crystalline face to represent the surface beneath the HDMS layer. HMDS molecules were arranged on a square lattice appropriate for the underlying Si lattice and the density of the HMDS was chosen to be 3.24 molecules/nm^2. The effect of changing the density of all three tested SAMs (OTS, ODTS, FOTS) on the trapping dynamics is explored below.

The simulation set-up involved a hexagonal lattice of 98 SAM molecules, consisting of 7x7 unit cells with two molecules per unit cell. For FOTS and OTS, this involves the consideration of 2,940 atoms (and 5,928 atoms for the longer ODTS molecule). The choice of a hexagonal lattice was arbitrary, but it is convenient as a close-packed lattice and is the most common choice in prior simulations of SAM monolayers [4, 18]. The characteristic lattice parameter of the hexagonal packing was chosen to match the packing density determined from X-ray reflectivity measurements [23]. The densities of the SAM surfaces were estimated from the experiments to be 2.0 molecules/nm^2 for FOTS, 2.75 molecules/nm^2 for OTS, and 2.83 molecules/nm^2 for ODTS.

The molecules were created using the Molden software package [24] and an energy minimization of the initial guessed structures was performed using a standard minimization algorithm - the limited memory L-BFGS minimization using a modified version of the algorithm of Nocedal which is a part of the TINKER software package [25]. The lengths of the SAMs, measured from the center of the oxygen atom to the center of the top carbon atom, were found to be 11.12 Å for FOTS and OTS; the length of the ODTS molecule was 22.96 Å. The optimized structures of the five molecules are shown in Fig. 2.1.

2.3. Intermolecular Potential Models

The choice of intermolecular potential model is a very important part of a molecular simulation. We chose to use the non-reactive semi-empirical MM3 potential to model all the SAM-SAM and DIP-SAM interactions. There are no DIP-DIP interactions to consider here, as we studied the fate of a single depositing DIP molecule. The MM3 potential has been shown, by us and others [6-9], to accurately describe hydrocarbons [6], fluorinated hydrocarbons [8] and multiply ringed molecules of the type we studied here. MM3 incorporates stretching, bending, and torsional energies, as well as the van der Waals interaction energies based on phenomenologically determined parameters. The total energy may be represented as follows:

$$E = E_b + E_a + E_{tor} + E_{aa} + E_{sb} + E_{stor} + E_{vdw} \quad (1)$$

with,

$$E_{vdw} = Aexp\{-r/\rho\} + C/r^6 \quad (2)$$

where E_b is the bond-stretch, E_a is the angle-bend, E_{tor} is the torsion, E_{aa} is the bend-bend, E_{sb} is the stretch-bend and E_{stor} is the stretch-torsion potential. The potential does not

involve electrostatic interactions. The intermolecular van der Waals' interactions take the form of a Buckingham potential modified with tapering polynomials so that the energy may smoothly decrease to zero at a cut-off distance of 9Å.

We have used this model extensively to study the energetics and structural characteristics of an array of small organic semiconducting molecules including the acenes, rubrene, DIP, sexiphenyl and C_{60} [9, 10] and have confidence in its ability to model conjugated systems. Our most recent study involved an extensive survey of twelve Density Functional Theory models, as well as the MM3 and MM3-π models for biphenyl and eight models (four DFT and four semi-empirical models) for the sexiphenyl molecule. We found virtually all the models to give consistent energetically preferred structures [26]. Both MM3 models (with and without an additional term to represent pi-bonding) represented the behavior of sexiphenyl and biphenyl molecules with quantitative accuracy compared to the DFT models. Based on our studies and those of the Allinger group, we are confident in the ability of MM3 to be sufficiently accurate to capture the fate of a single DIP molecule on a SAM surface without having to resort to using MM3-π, a variant of MM3 which is more accurate for molecules with an extensive π-electron system but which is about 20 to 100 times slower in execution time.

2.4. Simulation Details

The time evolution of the system was followed using a simulation approach using the Modified Beeman Algorithm as part of the TINKER software package. As mentioned above, optimized structures of the SAM molecules and the DIP molecule were obtained from an energy minimization of an initial guess structures using a standard minimization algorithm, here, the limited memory L-BFGS minimization using a modified version of

the algorithm of Nocedal [27]. The system was first thermalized at 300 K using a Nosé-Hoover thermostat in the canonical (NVT) ensemble for a period of 50~ps with a time step of 1.0 fs (*i.e.*, 50,000 time steps) in order to suppress significant fluctuations in temperature and equilibrate the system of SAM molecules (before the deposition of the DIP molecule). Anticipating a result described more fully below, the simulated value of the film thickness was found to be within one standard deviation of the experimentally calculated value; this helps to justify the choice of hexagonal packing of the SAM molecules, though it does not preclude another geometry from working equally well.

Since the consideration of each additional DIP molecule adds another 48 atoms to the system, following the deposition process of DIP molecules onto the SAM surfaces quickly becomes computationally expensive. That being the case, the simulations in this paper were generally restricted to the deposition of only one molecule of DIP on the SAM surface, though we report some preliminary results for the deposition of multiple DIP molecules in section 7. The DIP molecule was given a random orientation at a height of 30 Å above the SAM surface in 3D space and a random initial (x-y) coordinate above the surface of the SAM. Simulations were performed at six incident energies of the DIP molecule that match the energies used in Engstrom's experiments [23]. Simulations of collisions between the DIP molecule and the SAM surface were carried out in the microcanonical NVE ensemble to avoid any unwanted bias due to velocity corrections used to scale the temperature to a desired value in the canonical ensemble. The effect of using NVE versus NVT has been tested for a related system, pentacene, and no issue has been found [9].

Each simulation in our study constitutes an individual deposition event. The simulations were routinely performed for a period of 25 ps with a time step of 0.5 fs (50,000 time steps). This time frame was found to be sufficient for the molecular collision to occur between DIP and the SAM surface and for the system to rethermalize to its original state. Longer simulations (~ 2 ns) were also performed to confirm this point, but no significant changes in the behavior of the DIP molecule or the structure of the SAM were found. The system relaxes quickly, even following the highest incident energy collisions. Each simulation (at a given incident energy of the DIP molecule and SAM density) was carried out 100 times, each time with a different initial random orientation of the DIP molecule so that we could gather enough statistics to accurately determine the probability of the DIP molecule sticking to the SAM surface. An alternative view of this set of 100 simulation runs is that we studied the low-coverage limit of DIP sub-monolayer growth for 2.5 ns at a deposition rate of 4×10^{10} molecules/second (in which no DIP was close enough to encounter another DIP molecule). We report the "sticking fraction" as the ratio of the number of events that led to a particular outcome (adsorption on the surface, insertion, scattering) divided by the number of events studied (here, 100).

The outcome of each DIP collision with the surface was recorded and observed to fall into one of the following categories: The DIP molecule can (a) deposit on top of the SAM monolayer (the experimentally intended outcome), (b) insert itself between SAM molecules, or (c) collide with the SAM and bounce off (a scattering event). The same process was carried out at six different incident energies matching the experimental values [23], E = 1.5, 5.07, 7.69, 9.0, 10.0 and 12.31 eV. Additional studies were carried out for the SAMs to look at the effect of varying the packing density (from 2.0 to 4.0

molecules/nm^2), the temperature (200 K to 400 K) and with different initial orientations of the DIP molecule (with the long molecular axis perpendicular to the surface, parallel to the surface and at orientations in between) to investigate the nature of the sticking of DIP on the SAM surfaces. Thus the behavior of SAMs of OTS, ODTS and FOTS molecules was studied in about two thousand different simulations.

2.5. Results

After thermalization to 300 K, the initially vertically oriented SAM molecules were observed to lean over to attain a minimum energy conuration, adopting a preferred angle with the surface normal. This translates to an observed film thickness that is smaller than the total length of the molecule, measuring film thickness as the vertical distance from the silicon atom to the top carbon atom. Table 2.1 compares the average film thicknesses of the different SAM surfaces obtained from experiments (XRD data) [23] and simulation, showing agreement that is typically within a standard deviation of the experimental data. What is less easy to capture in a quantitative way is the dynamics of the system realized in simulation movies of the system. We observed the SAM molecules to move in a random waving motion, akin to tall grass blowing in the wind. Fig. 2.3 shows the OTS SAM surface after thermalization. The FOTS SAM adopts a much more ordered configuration compared to the OTS SAM. This may be explained by stronger interactions between the molecules in the FOTS SAM in comparison to the OTS SAM, making the FOTS SAM appear “stiffer" than OTS. Not surprisingly, the longer ODTS SAM was found to be much more flexible than the other two SAMs.

Data from these simulations will show that the probability that a DIP molecule will become adsorbed on the surface of the SAM depends on several factors, each of which

can affect deposition and, in turn, affect the quality of the film of DIP on the SAMs. Some of these factors are considered in greater detail in the following sections.

2.5.1. Sticking coefficient of DIP on SAMs

We began by calculating the sticking coefficient of DIP as the fraction of molecules that are not scattered from the surface of the SAM. This value includes the fraction of DIP molecules that get adsorbed on the surface of the SAM *and* the fraction that insert into the SAM surface; this is essentially the quantity measured in experiments. The sticking fraction was calculated as the fraction of non-scattered molecules in 100 trial depositions, as described in the previous section. The outcome of the deposition event was then recorded (as scattered, adsorbed, or inserted).

Variation of the sticking coefficient with different incident energies of the DIP molecule on the three SAMs and HMDS is shown in Fig. 2.4. This figure shows that the experimental and simulated results follow a similar trend and are in fairly good quantitative agreement given that sticking coefficients can vary by many orders of magnitude on different surfaces. There was no guarantee, *a priori*, that the simulation predictions would be within an order of magnitude of the experimental results. Both experiment and simulation predict that the overall sticking coefficient decreases with increasing energy of incidence of the DIP molecule.

In order to remain on the surface of the SAM, the incoming DIP molecule has to lose some or all of its kinetic energy upon collision. The energy of the incident molecule will be dissipated into the lattice (through lattice vibrations in the form of surface phonons) and the torsional motion of the SAM molecules. Since the area of the SAM surface is large compared to the DIP molecule, we have observed that the temperature of the SAM

surface is largely unaffected by the appearance of the DIP molecule (a maximum temperature variation of ± 5 K occurs at the moment of impact and the surface returns quickly, within picoseconds, to the equilibrium temperature). We calculated the amount of energy transferred to any single mode (bond bending, lengthening or torsional modes) in the system and found that, even the most energetic DIP molecule that collides with 2-6 SAM molecules is not sufficient to break chemical bonds in the system. The maximum energy per mode is only about 5 kcal/mol; well below the ~85 kcal/mol needed to break a C-C bond, say. As the incident energy of the DIP molecule increases, the harder it becomes for the SAM surface to absorb and dissipate the energy. This means that there is an increasing tendency for the DIP molecule to retain a significant part of its incident energy after collision with the SAM and, consequently, for the DIP molecules to be ejected from the SAM as a scattered molecule. The same decreasing trend to stick on the surface with increasing incident energy is seen on all SAM surfaces: The tendency to stick is highest for ODTS, next for OTS, and least for FOTS. The tendency to remain on the surface after the first collision is almost zero for HMDS at energies above about 6 eV; we shall return to an explanation of the HDMS results later in this section. We shall show below that factors such as the length of the SAM molecule, the interaction energy of SAM with DIP, and the packing density of the SAM molecules, all contribute to these observed trends of the sticking fraction of DIP with increasing incident energy.

Surface	Experiment (Å)[a]	Simulation (Å)[a]	Tilt Angle (˚)
FOTS	6.32 (0.5)	7.5 (1.1)	48
OTS	6.27 (0.65)	7.9 (1.4)	45
ODTS	17.31 (1.75)	17.5 (2.7)	40

[a] The values in parentheses indicate the standard deviation from the average values.

Table 2.1: Film thickness of the SAM observed in experiments and by simulation. The computed tilt angle is expressed as being measured from the surface normal.

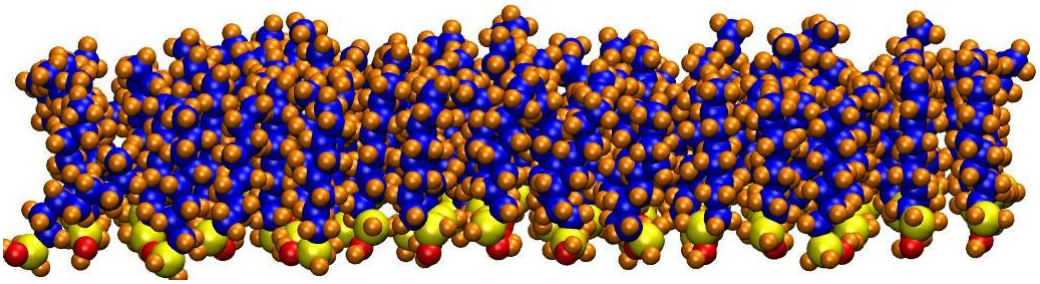

Figure 2.3: The OTS SAM surface after thermalization.

Our observations of hundreds of simulations of the way that DIP molecules interact with SAM surfaces has led to some overall conclusions about the tendency of DIP molecules to adsorb on the surface of the SAM rather than insert themselves into the SAM surface or scatter. Depending on the position of incidence and the local structure of the SAM surface, the DIP molecule has the opportunity to: (1) collide with one or more SAM molecules, or (2) land in the interstitial space between the SAM molecules. The more SAM molecules involved in the collision with DIP, the easier it becomes to dissipate the DIP's incident energy into the lattice. As mentioned above, the collective motion of the three SAMs we studied exhibited a wave-like motion, behaving like elastic springs tethered to an underlying substrate. Thus, if a DIP molecule collides with a single SAM molecule, this elasticity is capable of tossing it away from the surface. In practice, however, this effect is mediated by factors such as the orientation of the DIP molecule as it collides with the SAM molecule (*e.g.,* impact parameter), the proximity of the other SAM molecules around it (including affecting the effective local density), the energy of interaction between the SAM molecule and the DIP molecule, and -of course- the incident energy itself. At low incident energies, a single SAM molecule may be able to absorb and dissipate the energy. But, at higher incident energies, it is likely that the DIP molecule will be ejected. Collision with more than one SAM molecule is certainly more effective for energy dissipation, but the outcome of a given collision still depends on the factors described above. DIP molecules are adsorbed onto the surface of the SAM if they are able to successfully dissipate enough incident energy that the remaining energy is less than the binding energy between the DIP molecule and the SAM surface. We shall return to this binding energy below.

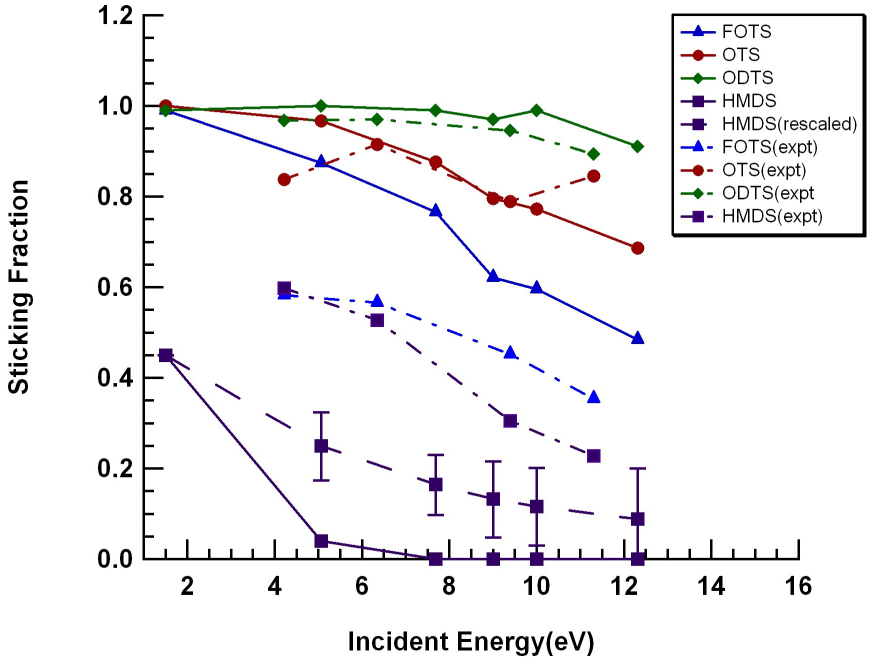

Figure 2.4: Overall sticking coefficients of DIP on four different SAMs as a function of incident energy at room temperature. Packing density: FOTS=2.5, OTS=2.75, ODTS=2.83 and HMDS=3.4 molecules/nm^2. Symbols joined by lines are simulation results. Dot-dashed lines correspond to experimental values [23]. The dashed line labeled as HMDS(rescaled) shows the sticking coefficient if the effect of a second collision of DIP with the HMDS surface is added.

If a DIP molecule lands in the space between the SAM molecules, it invariably leads to a direct insertion event in which the energy of interaction between the DIP molecule and neighboring SAM molecules is strong enough to hold the DIP molecule embedded in the lattice. Steric hindrance could also be a contributing factor, preventing the ejection of the DIP molecule after insertion. Even comparatively long simulation runs, of the order of a nanosecond (2 million time steps), showed no tendency of the DIP molecule to desorb from its interstitial position once inserted into the lattice. More insight into this tendency for DIP to remain inserted within the SAM will be evident when we consider binding energies in a later section.

The other possibility as a route to insertion events (found more commonly at lower incident energies) is that the DIP molecule could get initially adsorbed on the surface, diffuse across it and then undergo insertion. The waving motion of the SAM molecules can give rise to situations where the diffusing DIP molecule encounters an energy ``well'' caused by the instantaneous parting of two SAMs. In this situation, it is energetically favorable for the DIP molecule to insert since the interaction energy between the SAM molecules and the DIP molecule is higher than that for surface-adsorption, simply because there are more interaction sites.

Other factors were observed to govern the sticking coefficient, including the length of the SAM molecules and differences in interaction energies between DIP and different SAMs. Length affects the sticking probability: The data in Fig. 2.4 clearly show that the sticking fraction is highest for the longest molecule, ODTS, and least for the shortest one, HMDS, for all incident energies. However, the governing mechanism seems to be different in each case. In the case of ODTS, the length of the SAM is the strongest factor affecting

the sticking fraction. Since the backbone of the ODTS molecule is very long, it exhibits a greater degree of flexible motion compared to the other SAMs, thus creating a greater amount of interstitial space for insertion to take place. Most of the incident DIP molecules undergo insertion into the very flexible matrix of ODTS, leading to a low adsorbed fraction, as shown in Fig. 2.6c and an even lower scattered fraction (see Fig. 2.6a). Indeed, the fraction of DIP molecules that insert into ODTS is observed to go up with increasing energy, which accounts for the very high overall sticking coefficient. Thus, having a higher overall sticking coefficient may not be the best criterion to judge surface adsorption since this value will include insertion events. OTS and FOTS molecules show little variation in the fraction of molecules that adsorb on the surface, but the tendency to insert DIP in these two SAMs decreases steadily with increasing energy (see Fig. 2.6b), and an increasing tendency to scatter (see Fig. 2.6a), leading to an overall decrease in sticking with energy observed in Fig. 2.4. As we shall show in the next section, differences in sticking behavior between the identically long FOTS and OTS molecules arise due to the chemical nature of the molecules and the packing density of the SAMs. The reason for the precipitous fall in sticking coefficient of DIP on HDMS with increasing energy was harder to understand. Engstrom's experimental data show a decline in sticking on HMDS relative to the SAMS like the simulation results. But they do at least show some sticking at higher energies that the simulation is unable to match (simulation predicts no sticking at all above 6 eV after the first collision with the surface!). We eliminated possible procedural effects, and the effect of the underlying Si surface, and we have no reason to single out the potential energy function for the HMDS model as being at fault.

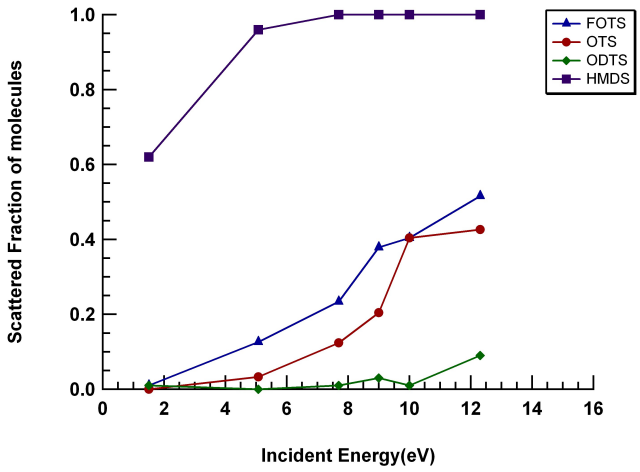

a)

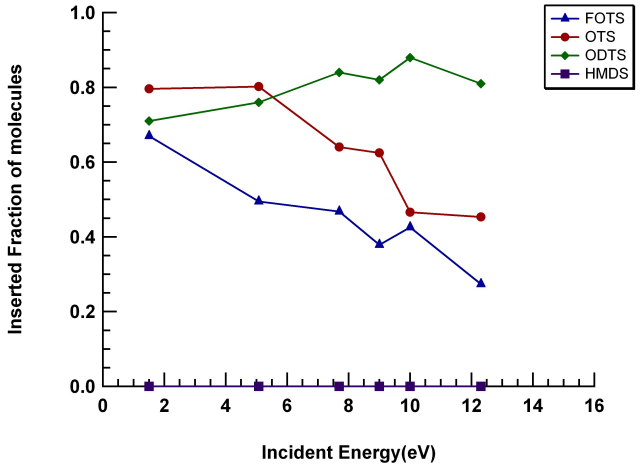

b)

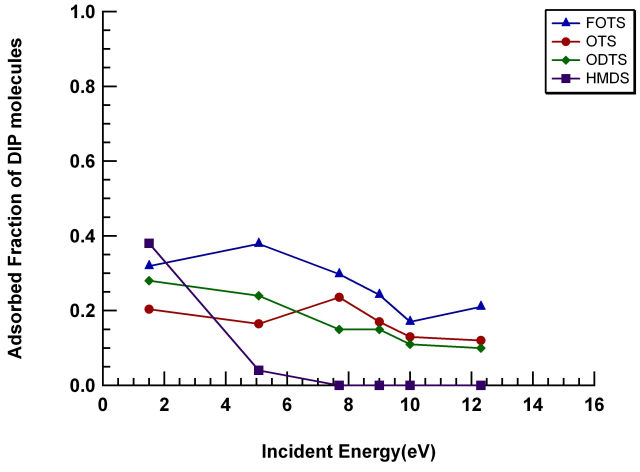

c)

Figure 2.5: Deposition of DIP on FOTS, OTS and ODTS at different incident energies showing (a) scattered (b) inserted and (c) adsorbed fractions. Packing density: FOTS=2.5, OTS=2.75 and ODTS=2.8 molecules/nm^2.

We suspect that the most likely reason is the inability of energetic DIP molecules to "scrub off" enough energy to either adsorb or insert *as a result of the first collision* on the short stubby HMDS surface, which is what we are measuring in the simulation. These results ignore the fact that DIP molecules could, and probably do, collide multiple times with the relatively "hard" HDMS surface before adsorbing or inserting. It seems reasonable that this effect will become more pronounced for higher incident energies. Considering only the first collision with the HMDS surface precludes access to a molecular mechanism open to the longer SAMS wherein the incoming energetic DIP molecules lose energy to the accommodating, more elastic, SAM molecules.

For the "unforgiving" HMDS surface, we suggest that it is important to follow the fate of individual molecules as they make multiple collisions with the surface. But the scope of such a study, following every scattered molecule as it traverses the surface, is inaccessible from a computational resource point of view. To compensate for this inability, we *estimated* the sticking coefficient after a second collision with the surface. To do this at a given incident energy, we measured the energy of the DIP molecule as it left the surface for all 100 attempts and then averaged them to find a mean exiting energy. For example, a scattered DIP molecule initially having a 5 eV incident energy is, on average, likely to leave the surface with 3 ± 0.6 eV. Similarly, DIP molecules with 12 eV incident energy that scattered from the surface did so with a mean energy of 4 ± 1 eV. If we assume that the DIP molecule has the opportunity to collide once more with the HMDS surface, we know from our measurement of its "exit" energy (which becomes its new incident energy for a second collision with the surface) its probability of sticking on the surface by interpolating data from the sticking fraction corresponding to that incident

energy based on our data for first surface collisions. We then simply add this additional, second collision, contribution to the sticking coefficient to the one that we found previously for the first collision. We show this “rescaled" sticking fraction of the DIP on HMDS in Fig. 2.4 as a dashed line. The results are clearly closer to Engstrom’s experiments. This approach does not allow us to predict what the energy of the molecule might be after a third collision.It is not unreasonable to imagine that experimental sticking coefficients *also* reflect a similar “ensemble average" of collision energies of DIP with HMDS.

Multiple surface collisions affect the sticking of all the systems we studied, but should be more critical for the stiff HMDS surface than the longer, more flexible, SAM molecules. This expectation is borne out by observing the exit kinetic energy of the DIP molecule (incident energy 7.7 eV) after colliding with the surface; the exit kinetic energy of the DIP molecule decreases with increasing SAM length (see Fig. 2.5). Despite the improvement caused by considering the effect of a second, energy-shedding collision with the surface, the disappointing comparison to experimental sticking coefficients for HMDS caused us not to consider this molecule further. Its inclusion here highlights that the sticking coefficient *is* sensitive to the molecular details of the surface and the strength of molecule-surface binding. Good agreement between experiment and simulation for sticking coefficients of the caliber given in Fig. 2.4 is not guaranteed.

2.5.2. Sticking coefficient of DIP: Effect of packing density of the SAM

Although experiments typically have little ability to control the density of the SAM (but see [18] as a contrary example), molecular simulations allow us to investigate changes in sticking outcomes as the density is altered. To do so, SAM molecules at room

temperature were packed at different densities ranging from 2.5 molecules/nm^2 to 5.0 molecules/nm^2 (essentially the close-packed limit), studying the DIP-trapping ability of the SAM (*i.e.*, the tendency of DIP to insert or adsorb). This range of densities was chosen to cover an experimentally accessible range. The larger fluorine atoms in the FOTS SAM generally require more "room" on the surface than the OTS SAM. The minimum distance that these molecules can pack together on the surface, r_{min}, was found to be 6.1 Å for FOTS but only 5.6 Å for its non-fluorinated analog, OTS. To allow a fairer comparison between different SAM molecules, the density of the FOTS SAM matrix was renormalized by the area, defined as the ratio of r_{min} of the FOTS and the OTS molecules.

The deposition of a single DIP molecule was simulated, as described earlier, at different densities for a representative incident energy of 7.69 eV onto FOTS, OTS and ODTS SAMs. In terms of *total* sticking fraction (Fig. 2.7a), density does not seem to have a pronounced effect in the case of all the SAMs until the density is above about 4.0 molecules/nm^2, at which point the sticking fraction decreases rather sharply with increasing density. Decomposing this result to look at the scattered, inserted and adsorbed fractions as a function of density (Fig. 2.7), we see two expected results, namely that the tendency to scatter DIP molecules off the SAMs goes up sharply above a density of about 3.5 molecules/nm^2 (as the surface becomes "harder") and that the tendency to insert decreases. The roughly *linear* decrease in tendency to insert as a function of density might have been more difficult to predict, but the trend is expected. More surprisingly, the fraction of trial depositions that result in molecules adsorbed on the surface at first increases with density up to 3.5-4.0 molecules/nm^2 and, above that energy, begins to fall.

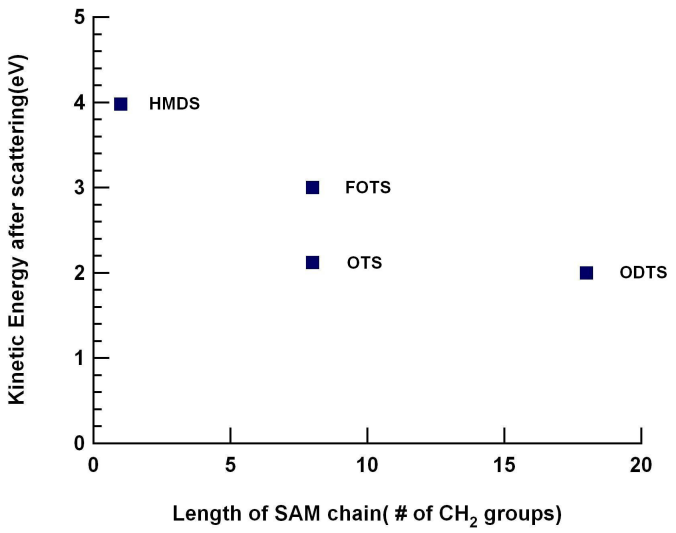

Figure 2.6: Exit kinetic energy of DIP on different surfaces for an incident energy of 7.7 eV.

Thus, unexpectedly, it appears that there is an optimal SAM packing density to maximize surface adsorption of DIP.

To explain this maximum in sticking fraction with density, consider the following. At low densities, the SAM molecules are quite far apart from one another and do not interact with one another very strongly. Thus, the SAM molecules tend to have greater rotational freedom and wave around their tethering point at the oxygen atom. In this situation, we have seen that it is probable for an incident DIP molecule to collide with only one SAM molecule and insert into the ample space between SAM molecules. The tendency for insertion decreases with increasing density as the SAM molecules become more rotationally constrained by their neighbors' proximity and the incident DIP molecule is most likely to collide with more than one SAM molecule, allowing it to dissipate its kinetic energy more easily and scatter less often. At high densities, the closely packed SAM molecules adopt a more upright stance and lose rotational freedom. The surface loses its capacity to provide a cushioning effect and becomes akin to a “hard" surface. This accounts for higher scattered fractions at higher densities. The two competing effects reach an equilibrium condition at a density of around 3.5 molecules/nm^2 for FOTS in which the adsorbed fraction is highest, and scattering and insertion events are less probable. This maximum is attained at remarkably similar densities, between 3.5 and 4.0 molecules/nm^2, for all three SAMs studied (FOTS, OTS and ODTS). At such densities, the conditions are optimal for DIP molecules to adsorb on the SAM surface.

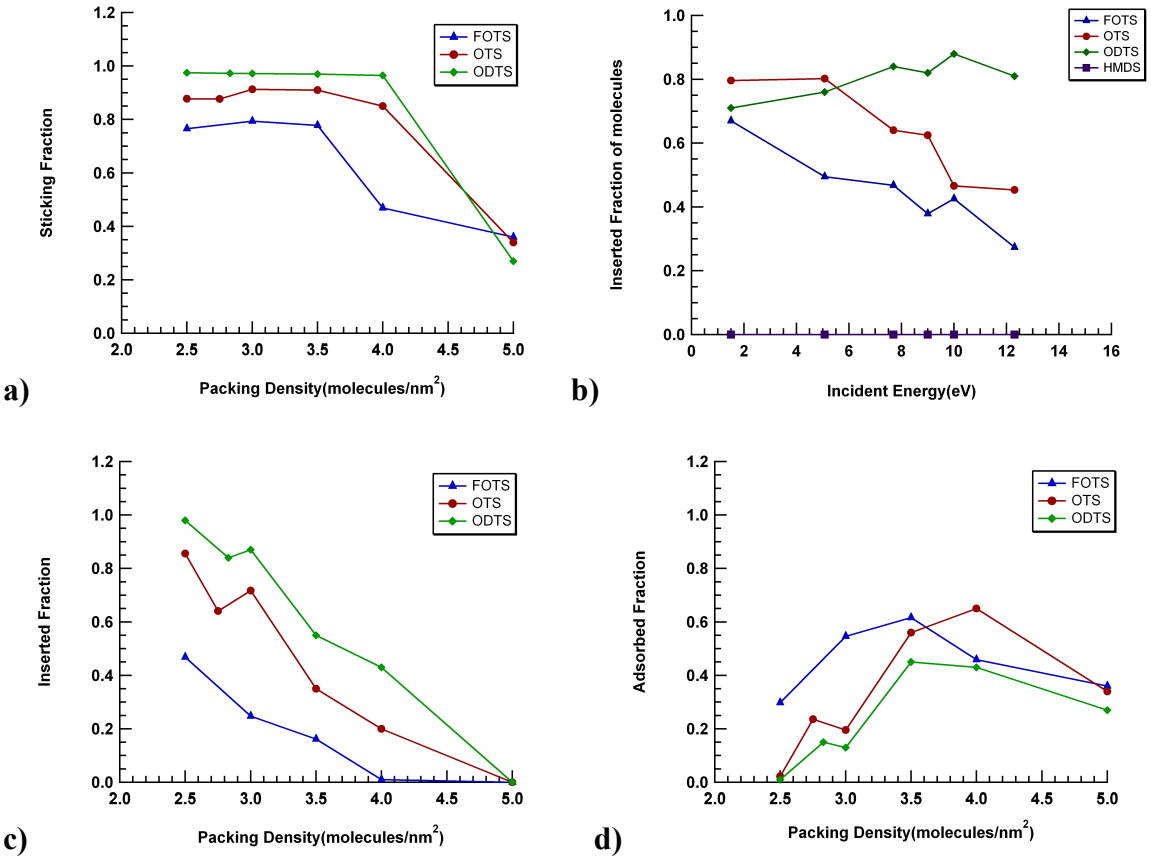

Figure 2.7: Effect of varying the SAM packing density on the tendency to (a) stick, (b) scatter, (c) insert and (d) absorb DIP molecules. Temperature= 300 K. Incident energy = 7.69 eV.

The density dependence, seen above, also explains an interesting puzzle: The intermolecular interaction energy between a DIP molecule lying on top of the terminal end group of multiple SAM molecules is about 0.1 eV stronger if the SAM is composed of FOTS (-0.54 eV) than with OTS (-0.43 eV); see section 6. One might be tempted to imagine that the sticking fraction should thus be greater on FOTS than on OTS, but this is not observed experimentally (or in the simulations shown here). The reason for this apparent anomaly involves the packing density of the SAM: The experimentally observed density of FOTS is less than OTS. Higher insertion in OTS leads to an increase in overall sticking fraction on OTS. However, as seen in Fig. 2.7d, the *adsorbed* fraction on FOTS is higher than on OTS and ODTS until the maximum adsorption for FOTS is reached. At densities higher than this maximum, the adsorbed fraction on FOTS drops below that of OTS. The fluorine atoms on FOTS interact strongly with one another, rendering the SAM surface “harder". The same maximum for the OTS and ODTS SAMs occurs at a slightly higher density since these SAMs are “softer." It is interesting to note that maximum adsorption may be achieved on the FOTS SAM at lower packing densities. To achieve the same extent of adsorption on OTS and ODTS would require a higher packing density, which is more difficult to obtain experimentally. Thus, by modifying the SAM molecules with suitable substituents, it could be possible to tune the adsorption characteristics of the DIP molecule.

2.5.3. Sticking coefficient of DIP: Effect of Temperature

To investigate the effect of temperature on the ability of DIP to stick/adsorb on SAM surfaces, we thermalized the SAMs at a packing density of 3.5 molecules/nm^2 (near-optimal for surface adsorption) at five different temperatures in an experimentally

accessible range (T = 200, 250, 300, 350 and 400 K). Fig. 2.8 shows the variation of sticking, scattered, inserted and adsorbed fractions of DIP with temperature. While there was essentially no change observed in the overall sticking fraction of DIP with increasing temperature, we observed that the fraction of DIP adsorbed onto the SAMs has a slight tendency to increase as the temperature is increased. The inserted fraction consequently decreased and no significant change was observed in the scattered fraction. At low temperatures, the SAM molecules have very little energy and some degrees of freedom are frozen out. This allows the DIP molecule to lose its initial energy into the SAM, but, since the SAM molecules themselves have very low energy at these temperatures, the prevalence of insertion events is very high. SAM molecules tend to part easily to accommodate the incoming DIP molecule. This accounts for the elevated inserted fraction at low temperatures and lower adsorbed fraction. At higher temperatures, there is an increase in the adsorbed fraction and a decrease in the inserted fraction. At these temperatures, the SAM molecules have greater degrees of freedom and the probability of an insertion event occurring is low because of the extensive vibrational and swaying motion of the SAM molecules as has been previously described. Due to this increased vibrational and disordered motion of the SAM molecules, the probability of surface adsorption of DIP is higher. It may, however, be difficult to conduct experiments at high temperatures since the SAM molecules have a tendency to desorb. Thus, room temperature may be optimal for experimental set ups, as is indeed typically the case.

2.5.4. Sticking coefficient of DIP: Effect of orientation of the DIP molecule

All the simulations described above were performed with the DIP molecule initially having a random orientation in space at some point above the surface. To confirm the

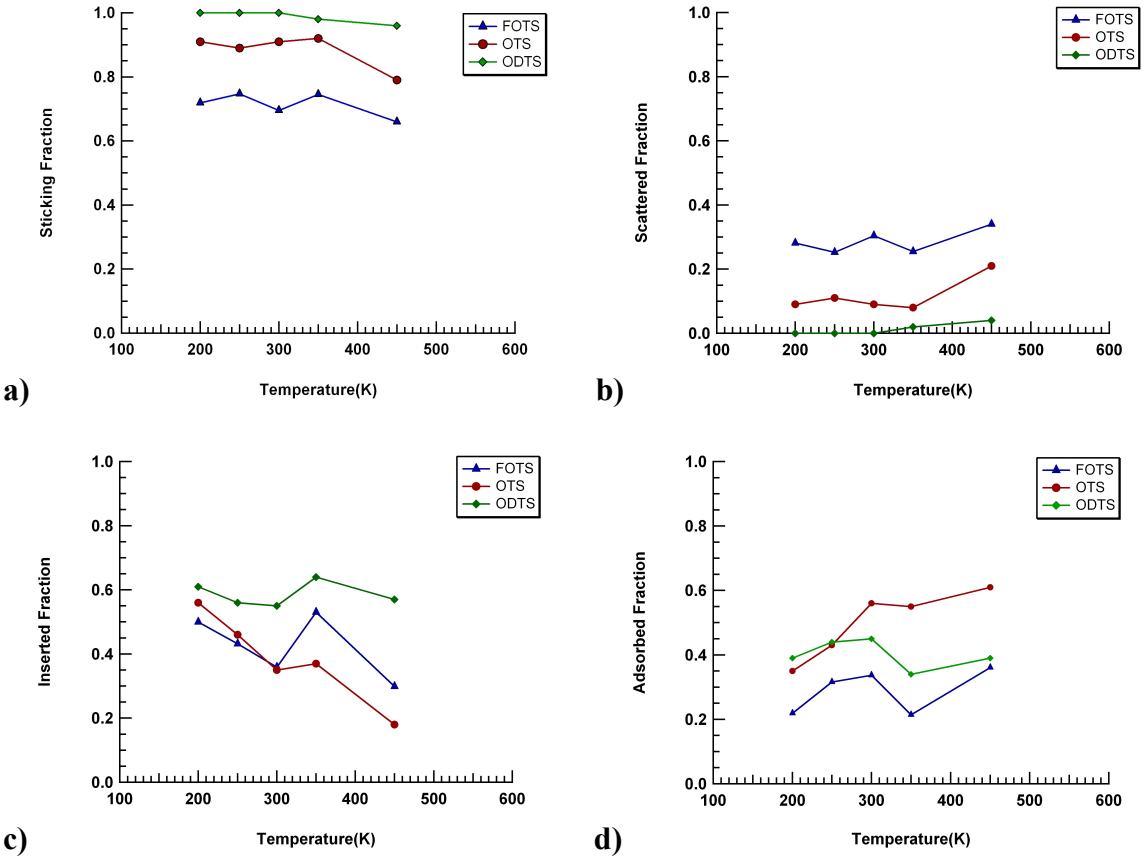

Figure 2.8: Effect of varying the temperature of the SAM surface on the tendency to (a) stick, (b) scatter, (c) insert and (d) adsorb DIP molecules at a density of 3.5 molecules/nm^2 and energy of 7.69 eV.

randomness of the DIP molecules as it strikes the SAM surface, the average angle off-normal of the DIP molecule was calculated to be around 47˚, which is roughly midway between a parallel and a perpendicular orientation. In this section, we study the effect of specific different orientations of DIP upon the collision dynamics, even though this is currently not possible to emulate in experiments. To do so, we undertook 100 runs with the DIP molecule initially having each of five different orientations with respect to the SAM surface (0, 30, 45, 60 and 90˚ from horizontal). The incident energy of the DIP molecule was set at 7.69 eV for all runs, with the SAMs set at a packing density of 3.5 molecules/nm^2 of the SAMs and a temperature of 300K. Figs. 2.9a,b,c and d show the variation of the overall sticking coefficient, and the scattered, inserted and adsorbed fractions of DIP on the SAM surfaces, respectively.

Fig. 2.9b shows little systematic variation of the scattered fraction as a function of incident angle of the DIP molecule across all three SAMs. In fact, the scattered fraction remains quite small in all three cases, and almost consistently zero in the case of ODTS. This is due to the very flexible nature of ODTS arising because of its length. In contrast, Fig. 2.9d shows a consistent and dramatic decrease in the adsorbed fraction as a function of incident angle of the DIP molecule; the more grazing the angle of incidence of DIP, the more likely it is to adsorb on the surface. A DIP molecule approaching the surface is able to dissipate incident energy more easily since it can collide with multiple SAM molecules and this orientation offers the strongest van der Waals interactions between the DIP and the SAM molecules (though comparatively still weak in an absolute sense). Thus, the adsorbed fraction in Fig. 2.9d is seen to steadily decrease from a parallel to a perpendicular orientation. Similarly, we might expect a DIP molecule approaching the

surface at an angle perpendicular to the surface to be more likely to “slice" through the SAM and increase the probability of insertion events (Fig. 2.9c), and this is indeed observed. These tendencies counteract one another with the result that the overall sticking fraction becomes only a weak function of angle of incidence, and will differ with the choice of SAM molecule depending on the relative ability to adsorb versus insert.

The fraction of DIP adsorbed on ODTS is greater than that on FOTS for parallel orientations, but is smaller for perpendicular orientations. This is because FOTS molecules appear “harder" to the incoming molecule and tend to scatter a parallel DIP molecule more than a “softer" ODTS molecule. For a perpendicularly inclined incident DIP molecule, the ODTS matrix is more flexible and allows easier insertion than a stiffer FOTS matrix. It may therefore be advisable (if experimentally possible) to have as much of a parallel orientation as possible during deposition to ensure a greater adsorbed fraction of DIP on the SAM, but at low enough incident flux that the surface ``shadowing" events that cause roughening and 3D growth in atomic systems are less of a concern. The role of shadowing in deposition of small-molecule organic semiconductors is largely unexplored.

2.6. Interaction Energy of DIP with different SAMs

It is clear that the interaction energy between DIP and the SAM surfaces (relative to the strength of SAM-SAM interactions) plays a role in the adsorption or scattering of the DIP molecule. To understand this better, we computed the intermolecular interaction energy between a DIP molecule and all the (typically 4-6) SAM molecules that interact with it at the respective densities of the SAMs mentioned in the previous sections. We performed such calculations for three interactions: DIP-SAM in a “T"-configuration redolent of the

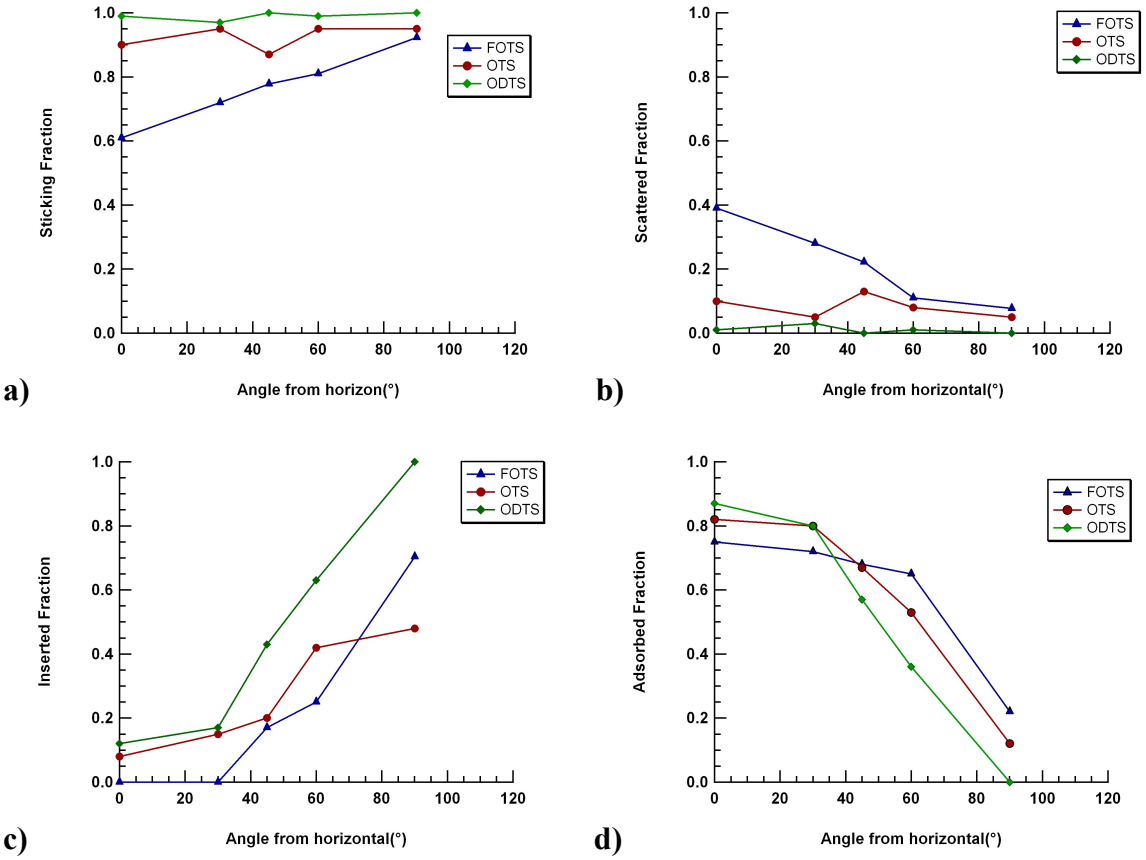

Figure 2.9: Effect of the orientation of the incident DIP molecule on the tendency to (a) stick, (b) scatter, (c) insert or (d) adsorb DIP. Temperature= 300 K. Incident energy = 7.69 eV. Packing density = 3.5 molecules/nm^2.

initial surface adsorption configuration, DIP-SAM in a co-facial configuration characteristic of insertion events, and SAM-SAM interactions to provide us with information about the competition for SAM molecules to prefer the proximity of other SAMs rather than interacting with DIP. The results are summarized in Table 2.2.

For the “T"-configuration, we computed the interaction energy as the DIP molecule was moved statically in incremental steps from a position close to the surface to one that was a large distance away from the SAM surface (large enough so that the DIP does not “feel" the SAM surface). The difference between the energy at maximum interaction and the energy at very large distance gives the binding energy of the DIP molecule to the SAM surface. In this idealized T-configuration, the computed binding energies correspond to high SAM density situations. The maximum interaction energy for each DIP-SAM interaction in this “T"-configuration, representative of surface adsorption, was found to be: FOTS: -0.5 eV, OTS and ODTS: -0.4 eV (see Table 2.2). [OTS and ODTS are identical except for their length and should produce the same binding energy]. At the experimental packing density of the SAM considered here, the DIP in the “T" configuration would be in contact with about 4-5 SAM molecules. Binding energies do not change if we calculate them dynamically at high packing densities of the SAM (like 4.0 molecules/nm^2), taking data directly from the MD simulations and averaging them. This largely density-independent interaction energy is because the number of SAM molecules with which the DIP comes in contact in the T-configuration does not change much in the range of packing densities considered. The stronger interaction found for DIP with the FOTS SAM is due to the presence of the fluorine atoms, which interact more

Configuration	FOTS	OTS	ODTS
T- DIP-SAM	-0.5(-0.35)[a]	-0.4(-0.3)[a]	-0.4(-0.3)[a]
Co-facial DIP-SAM	-1.8	-1.5	-1.7
SAM-SAM low density[b]	-1.0	-0.6	-1.7
SAM-SAM high density[c]	-1.9	-1.0	-2.0

Table 2.2: Interaction energies (in eV) of the DIP in "T" and co-facial configurations with different SAM surfaces. SAM-SAM interaction energies are given for comparison.

[a]Values in parentheses computed using DFT methods with M06 functional and a 6-31G(d,p) basis set.

[b]At the experimentally determined packing density.

[c]At a packing density of 4.0 molecules/nm^2.

strongly with the delocalized π electron clouds on the DIP. For the MM3 model, used here, this is only taken into account through the phenomenological parameterization fitting process. For comparison, the procedure was repeated using *ab initio* calculations with the software package Gaussian09 [28]. The energies were computed within the DFT formalism using the M06 functionals and using the 6-31G(d,p) basis set. The underlying SAM surface consisted of about 12 truncated SAM molecules (the length of the SAM molecules was reduced to 3 carbons in length to save computational time). The 12 molecules are sufficient to fit beneath the DIP molecule and to provide a ring of nearest neighbors around the DIP molecule. The energies computed using DFT are given in parentheses in Table 2.2. The values computed using MM3 are in good agreement with the DFT values (within 0.1 eV), validating use of the MM3 model. Again, the energy of interaction of DIP with FOTS is stronger than OTS. Thus, the presence of strong electron-accepting functional groups on the SAM molecules helps increase the adsorption probability of DIP.

The presence of fluorine atoms in FOTS also implies a stronger interaction energy between the SAM molecules (SAM-SAM interactions), as proved to be the case: At the density found in Engstrom's experiments, the average interaction energy of a group of 4-6 FOTS molecules (calculated dynamically from 25 ps simulations providing averages over 50,000 configurations) is about -1.0 eV, roughly twice that of a group of OTS molecules, -0.6 eV. The interaction energy (at the experimental density) of a group of ODTS molecules is larger, around -1.7 eV, due to the additional sites on the longer ODTS molecule. These values will increase as the packing density is increased: At a high density of 4.0 molecules/nm^2, for instance, the interaction energy for FOTS is about -1.9

eV, for OTS about -1.0 eV and for ODTS about -2.0 eV. Due to the waving motion of the SAMs, it is difficult to obtain a constant value for the interaction energy; hence all the energies in Table 2.2 are quoted to one decimal place only. Overall, the energy required to separate interacting FOTS molecules is greater than the energy required to separate chains of alkyl groups, such as OTS. This should reduce the probability of insertion of DIP molecules between the FOTS SAM molecules and facilitate the growth of smoother films, as is borne out in Fig. 2.5b.

In a co-facial configuration, the interaction energy between the DIP and FOTS SAM molecules, *i.e.*, the interaction that occurs once the DIP is inserted into the matrix, is about -1.8 eV, measured at the experimental density and averaged over 25 ps of MD simulation data. The interaction energy between DIP and OTS is about -1.5 eV, and that between DIP and ODTS is about -1.7 eV. Thus all three SAMs give roughly the same value, which (for OTS and ODTS at least) reflects the fact that DIP is interacting with the same chemical environment. The slightly higher value for FOTS is understandable given the more electronegative fluorine atoms. Just as for the T-configuration results described above, these values represent the interaction of one DIP molecule with 5-6 SAM molecules (the average number of SAM molecules with which the DIP comes in contact when inserted into the matrix).

If you compare these results to the SAM-SAM interactions reported above, the co-facial DIP-SAM interactions are greater than the interaction energy between SAM molecules at low density (but become comparable at very high density). From an energetic basis alone, then, it will be preferable for DIP molecules to insert into the SAM matrix (-1.5-1.8 eV for DIP-SAM vs. -0.6 to -1.0 eV for SAM-SAM), and far more likely than lying on the

surface (-0.4 to -0.5 eV). This does, indeed, happen in the MD simulations at experimental SAM densities.

Mediating these energetic considerations, entropic and stochastic considerations also play a role in determining the disposition of the DIP molecules to insert versus surface-adsorb. At high packing densities, adsorption is favored. An adsorbed DIP molecule would interact with only the terminal methyl- (or substituted methyl-) group of every SAM molecule. Since the strength of this interaction would be less than when inserted (as mentioned above), the DIP is able to diffuse over the surface of the SAM easily which may lead to formation of a more ordered film if this higher diffusivity contributes to a more 2D growth. Alternatively, a higher surface diffusion can bring sufficient DIP molecules together for them to spontaneously “flip" upright and form the nucleus for growth of a new ordered layer. Insertion may be prevented for sufficiently high packing densities of the SAM molecules. Thus, we have shown that there are a number of competing processes at play. But barring other factors, higher packing densities seem to be generally more favorable for surface adsorption of DIP and consequently for good film growth.

2.7. Deposition of multiple DIP molecules on OTS

We performed a few simulations to study the effect of depositing multiple DIP molecules on the surface of one of the SAMs, OTS. In these simulations, unlike the ones that have been previously described in this paper, once a DIP molecule is deposited on the surface, it was not removed from the simulation. The DIP molecule remains on the surface (adsorbed or inserted) as the next and further DIP molecules arrive. Since increasing the incident energy of the DIP molecules does not promote adsorption, we chose a

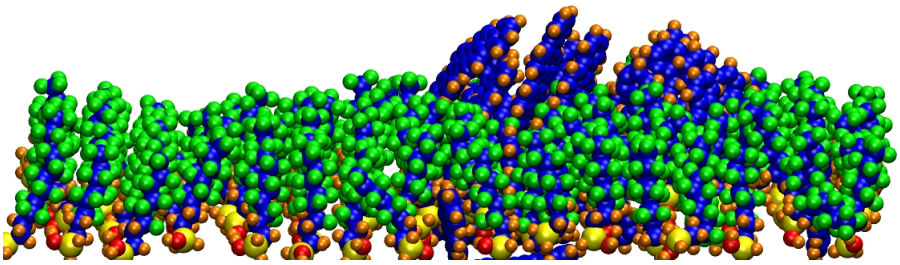

Figure 2.10: Multiple DIP molecules on the surface of OTS SAM. The H atoms on the OTS molecules are colored green to distinguish them from the H atoms of the DIP molecules.

reasonably low incident energy for the DIP particles (1.5 eV) and followed DIP deposition on an OTS SAM with a packing density of 3.0 molecules/nm^2 that is close to the optimum for adsorption. Each successive DIP molecule was deposited at 25 ps intervals from a random location above the SAM surface. This time interval was sufficient for the surface to re-equilibrate before another DIP molecule arrives. The simulations were carried out till the surface had accommodated the deposition of 25-30 DIP molecules (*i.e.,* following the deposition process for 625-750 ps). As the number of DIP molecules increases with each deposition event, the simulation becomes increasingly computationally expensive. We reached a practical limit of computational time at about 30 DIP molecules.

We found that, at this SAM density at least, many DIP molecules inserted into the SAM matrix. As the deposition process continued, we made two interesting observations. First, and unexpectedly, the inserted DIP molecules did not stay where they landed in the SAM surface, but tended to diffuse within the SAM matrix, rather like snakes weaving through grass. The DIP molecules diffused slowly towards the nearest cluster of inserted DIP molecules; see Fig. 2.10. This reflects a strong tendency of DIP molecules to cluster even when embedded inside a SAM, because of the stronger interaction energy between DIP molecules as compared to the interaction energy between DIP and SAM molecules, or indeed SAM molecules with themselves. As time went on, this diffusion and clustering of DIP molecules led to certain areas of the SAM surface having a substantial number of DIP molecules, while other parts of the surface were devoid of DIP molecules and essentially presented a "clean" surface to incoming DIP molecules. The second interesting observation was that the insertion of DIP molecules was self-limiting: As

more DIP molecules were inserted into the SAM matrix, the density of the SAM surface increased (at least in the area around the inserted DIP molecules). At a certain point, enough DIP had inserted into the SAM matrix to decrease the tendency to insert, and concomitantly increased the tendency to adsorb on top of the SAM. Thus the effective density of the SAM is a time-dependent quantity during deposition. This means that there exists a certain inserted fraction of DIP molecules that "saturates" the SAM matrix, preventing further insertion. We have not attempted to quantify any of these numbers in this preliminary study; this would require a detailed study of a large number of simulations. Such a study would greatly improve our understanding of deposition processes and the behavior of DIP molecules in a SAM film.

2.8. Conclusions

We have performed thousands of simulations on three different SAM surfaces (and a comparative HMDS surface) to study their propensity to trap DIP molecules incident on the SAM at hyperthermal velocities. The simulations yielded results for a sensitive property, the sticking coefficient, which were in good agreement with experimental data for the three SAMs studied. The results were much less impressive for HMDS, but highlighted the need for surface coatings to have degrees of freedom to dissipate the incident energy during collisions with the depositing material. This agreement illustrated the competency of the chosen intermolecular potential to model DIP and the SAMs studied. The sticking fraction of DIP decreased with increasing energy of incidence suggesting that hyperthermal deposition processes offer no obvious benefit in producing ordered thin films, in line with a complementary experimentally focused companion paper [23]. The molecular scale of the simulations enabled the distinction between

adsorbed and inserted fractions of DIP - an important feature that is invariably unobtainable experimentally. A new and unanticipated phenomenon deduced by the simulations was the prediction of an optimal SAM packing density to promote sticking on the surface. While experimental control of the density may be very difficult in practice, this result has implications for the design and choice of SAM molecules to maximize surface adsorption.

We have identified the key factors that govern the sticking fraction of DIP molecules on these SAM surfaces, which we believe can be reasonably expected to carry over to other choices of long alkyl chain SAMs. The more important factors seem to be the chemical functionality of the SAM, the incident energy of the DIP, and the packing density of the SAM -- all of which can be controlled experimentally. These results are driven by a balance of binding energies between the SAM molecules and the incoming molecule: T-configuration and co-facial energies compared to SAM-SAM interactions help differentiate surface-binding from insertion tendencies, respectively. Binding energies computed using the semi-empirical model MM3 are close to DFT-generated values. Factors such as the temperature of the surface seem less important in governing the deposition characteristics of the DIP molecule. The orientation of the incoming molecule is capable of strongly affecting the tendency to adsorb on the surface, but is essentially not experimentally controllable. Overall, grazing angles favor surface-adsorption and normal deposition facilitates insertion, but this is also dependent on the nature of the SAM. There is little or no experimental or simulation studies of the effect of grazing incidence on the nature of the grown film for small-molecule organic semiconductors. It would be interesting to compare the role of shadowing for simple monatomic systems

that causes oriented dendritic growth to that for small-molecule organics in which the highly anisotropic interactions may disrupt or enhance this tendency.

While we were able to explain a lot of the observed tendency to insert versus surface-adsorb in terms of the energetics of binding energies between DIP and SAM in comparison to SAM-SAM and DIP-DIP interactions, we noted that energetics alone do not control this complex process. Stochastic and entropically driven processes also play a role.

Since we are able to predict the behavior of the deposition of DIP based on the factors above, computation can be used to design a suitable SAM surface, which possesses the properties necessary to attain high adsorption of DIP on the surface. However, intelligently designing an optimized SAM surface computationally can present significant challenges of its own. For instance, the behavior of different organic semiconducting molecules such as the conformationally rich modes of rubrene molecules, or ones that differ considerably in shape, like C_{60}, needs to be examined to determine whether their deposition behavior is similar to that for the DIP molecules studied here. The behavior of similarly shaped, relatively rigid, acenes and perhaps the phenyls (biphenyl to sexiphenyl, say) might be expected to behave similarly to DIP.

The present study has not examined, in detail, the effect on sticking coefficient of the presence of other DIP molecules on the surface (from preceding deposition events), which is bound to affect the quality of subsequent film growth. But we have provided some simulations of the deposition of multiple DIP molecules on the surface of an OTS SAM at the optimum density for surface adsorption as a glimpse of what might occur. We found that DIP molecules tend to insert into the SAM matrix and cluster together

within the matrix. This clustering process eventually saturates the SAM with DIP molecules and artificially increases the density of the SAM surface. This was found to prevent the further insertion of the DIP molecules into the surface and to increase the adsorbed fraction of DIP. The resulting surface was found to become "patchy" with irregular clumps of DIP molecules interspersed between "clean" areas of the SAM surface that were devoid of DIP. The results of this preliminary study warrant further investigation due to their implications for film growth. Examining the effects of depositing a large number of DIP molecules on a SAM surface is computationally expensive, but it is the next logical step for computational studies intended to follow the growth of thin films of small-molecule organic semiconductors**.**

2.9. Crystalline structure of P2TP molecules on SAMs

This study involves using Molecular Dynamics (MD) computations to simulate the deposition of a monolayer of organic molecules on top of a self-assembled monolayer (SAM), in this case, octadecyltrichlorosilane (ODTS). The major aim is to study the effect of odd-even side chain length on the thin film growth of alkyl-substituted diphenyl-bithiophenes (5,5'bis(4-alkylphenyl)-2,2'-bithiophenes(Cn-P2TP-Cn))(Fig 2.11). Experimental studies have shown that the chain length (varied from 3 to 8 methyl groups) influences the self-assembly of P2TPs on top of the SAMs. More specifically, the odd and even number of chain lengths exhibit a different tilt angle and a different lattice constant. However, experimentally it is hard to find the reason for this, so MD studies could offer valuable insight.

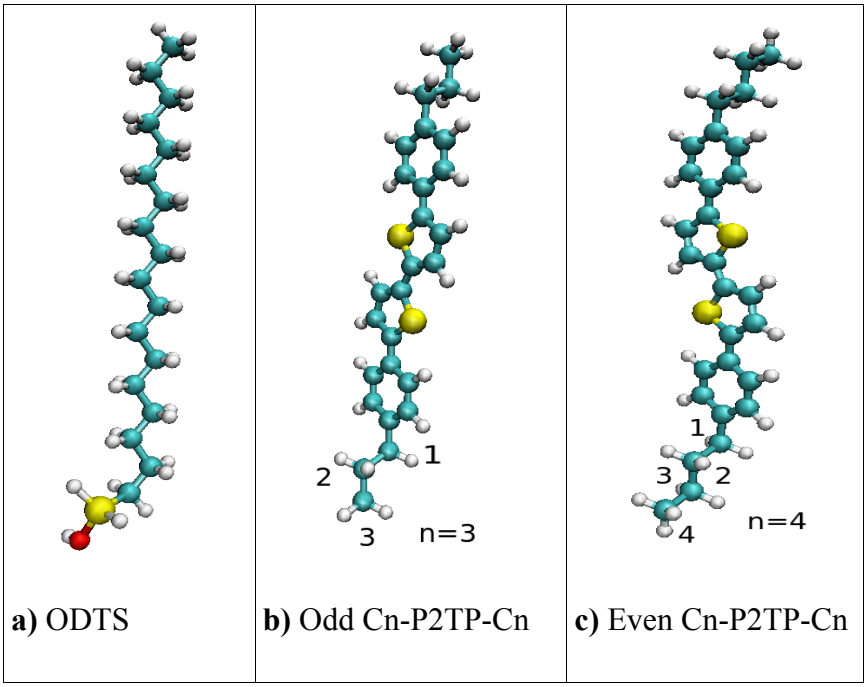

a) ODTS | **b)** Odd Cn-P2TP-Cn | **c)** Even Cn-P2TP-Cn

Figure 2.11: Optimized structures of molecules: a) ODTS, b) Cn-P2TP-Cn with n=3 and c) CnP2TP-Cn with n=4.

2.10. P2TP Molecules

In order to determine the lowest energy configuration of the molecule, different parameters must be optimized:

The angle between each molecule [31] has an influence on the energy of the system, as shown in Figure 2.12. The presence of two close minima at 240 and 300 degrees, necessitated two separate sets of simulations to determine the configuration giving rise to the lower energy. It was found that the total energy of the system presents an energy minimum at an angle of 300 degrees.

The intermolecular distance plays an important role in the global energy as it defines both the lattice parameters and the density of the monolayers. A first cursory fit allows the global energy to be minimized, and this was determined by scanning the molecule in the x and y directions. For C3-P2TPs the energy dependence of the distance is shown in Figure 2.13. After that, a minimization function of TINKER is used to optimize all the intermolecular distances. In order to accomplish this, the program moves the atoms and analyzes to see if it is energetically favorable. After this operation, the optimum configuration and appropriate parameters are determined.

The square lattice of the P2TPs consists of two molecules, rotated by 300 degrees in relation to each other and the lattice parameters are entirely dependent on the chain length of the molecule. Figure 2.14 represents the optimum configuration of the molecule for n=3 and n=4.

2.11. ODTS Surface

The ODTS forms a hexagonal [32] lattice and the experimentally measured tilt of the molecule is about 7 degrees. In the simulation, the oxygen and the silicon atoms are

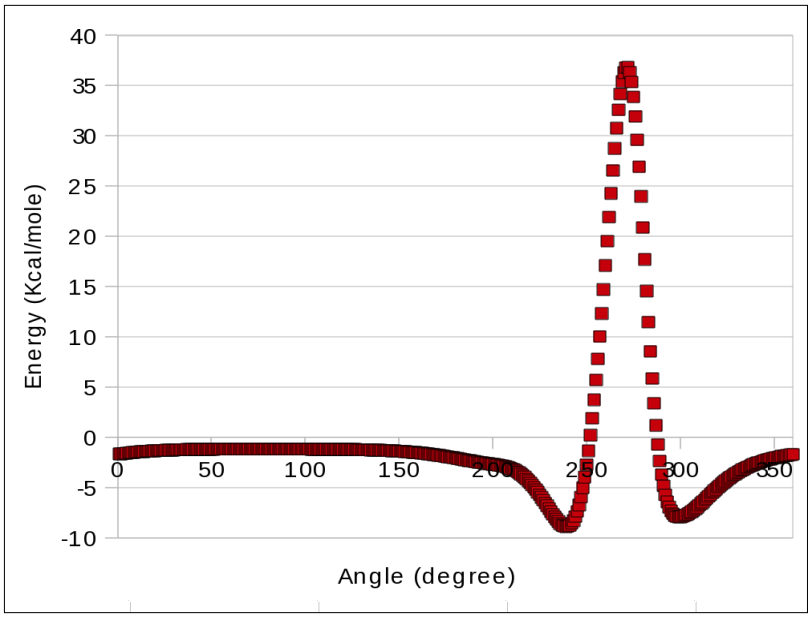

Figure 2.12: Energy as function of the angle between two molecules

fixed to simulate the liaison with the substrate (SiO2). After thermalization at 300 K, the simulation shows that the tilt angle of ODTS is directly linked to the SAM density, as shown in Table 2.3. Simulation and experimental values for the tilt angle agree well (6 and 7 degrees, respectively). Consequently, to represent the experimental conditions, the density of ODTS is fixed at 5 molecules/nm^2.

Furthermore, we determined that the ODTS molecules could be fixed in place during the simulation because their movement is quite limited and does not change the topography of the surface. The advantage of fixing the molecules is that it allows a very significant reduction in computational expenditure, without loss of accuracy.

2.12. P2TP monolayer on an ODTS SAM surface

The deposition of a molecule on a SAM involves different interactions, [33] such as the insertion of the molecule in the SAM, the absorption, or the scattering of the molecule. These different interactions could lead to different configurations of the deposited molecules. To simplify the simulation, only the absorption effect is considered, and hence the molecule cannot be inserted in the SAM. The deposition of a molecule on a SAM involves different possible outcomes, such as the insertion of the molecule in the SAM, adsorption on the surface, or the scattering of the molecule [33]. These different outcomes could lead to different configurations of the deposited molecules. However, for a high SAM density, only the surface adsorption effect was observed; no insertion or scattering events were seen. Experimental length scales are inaccessible using MD simulations. A feasible sized system in the simulation is composed of a herringbone lattice consisting of between 60 to 80 P2TP molecules. Periodic boundaries are employed in the lateral x- and y- directions, which simulate infinite 2D lattice

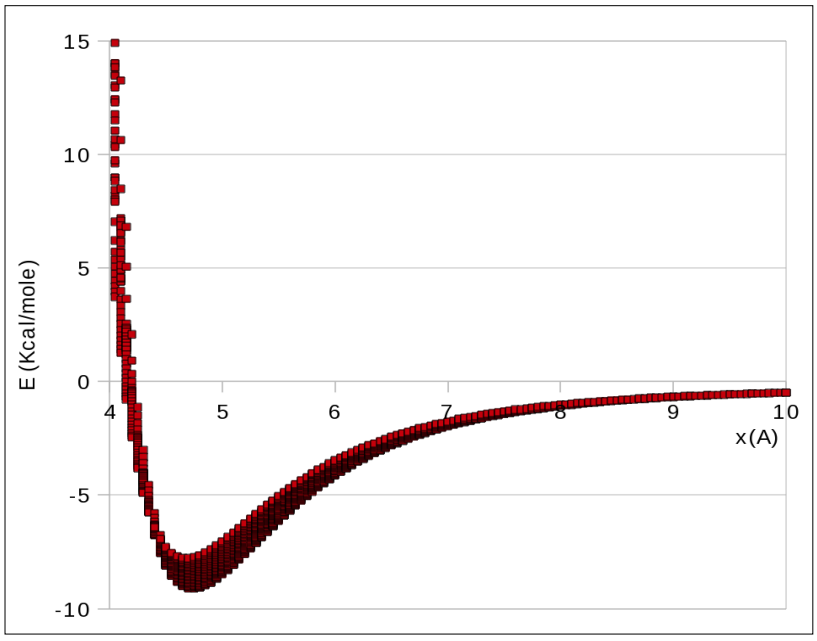

Figure 2.13: Energy as a function of the distance between two C3-P2TP-C3 molecules

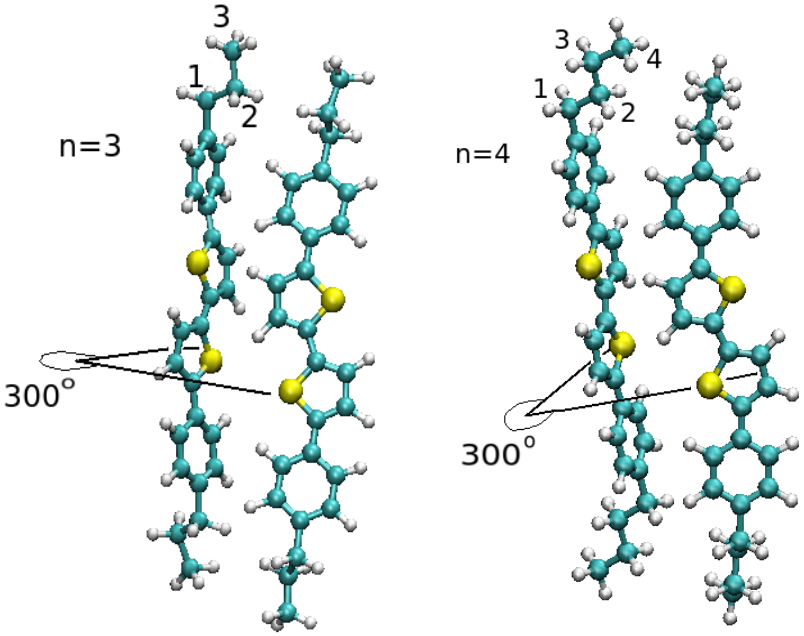

Figure 2.14: Left: molecule C3-2P2TP-C3 / Right: molecule C4-2P2TP-C4, after optimization

Density (molecules/nm^2)	3	4	5
Tilt (degrees)	30 ± 2	22 ± 2	6 ± 2

Table 2.3: Average tilt angle (degree) of ODTS for different densities (molecules/nm^2)

structures efficiently.

In this system, P2TPs molecules with an optimal lattice configuration are placed on top of a thermalized ODTS surface at a distance of approximately 3Å, corresponding to the minimum of the van der Waals interactions. Figure 2.15 shows the first step of the simulation for n=3 (C3-P2TP-C3).

To thermalize the system at 300K, a NVT ensemble is used to follow the time evolution for 70,000 time steps in order to stabilize the total energy. After that, the tilt angle and the lattice of the 2P2TPs molecules can be calculated and compared with experimental values.

2.13. Results

The experimental values were obtained in advance of publication from the Bao group at Stanford University. The lattice constants are obtained using X-ray diffraction in the synchrotron.

Table 2.4 shows the results obtained for the different chain length of the P2TP molecules (n=3,4,5). Table 2.5 shows the values obtained through simulations. The lattice parameters present some differences from experiment, principally for the b parameter. But the extent of the differences (typically ~0.5 A) is in line with the expected accuracy (even from DFT, which this is not). The simulations show a difference of tilt angle between odd- and even- chain lengths when the chain lengths are short (especially C3 and C4) that mirrors experimental findings.

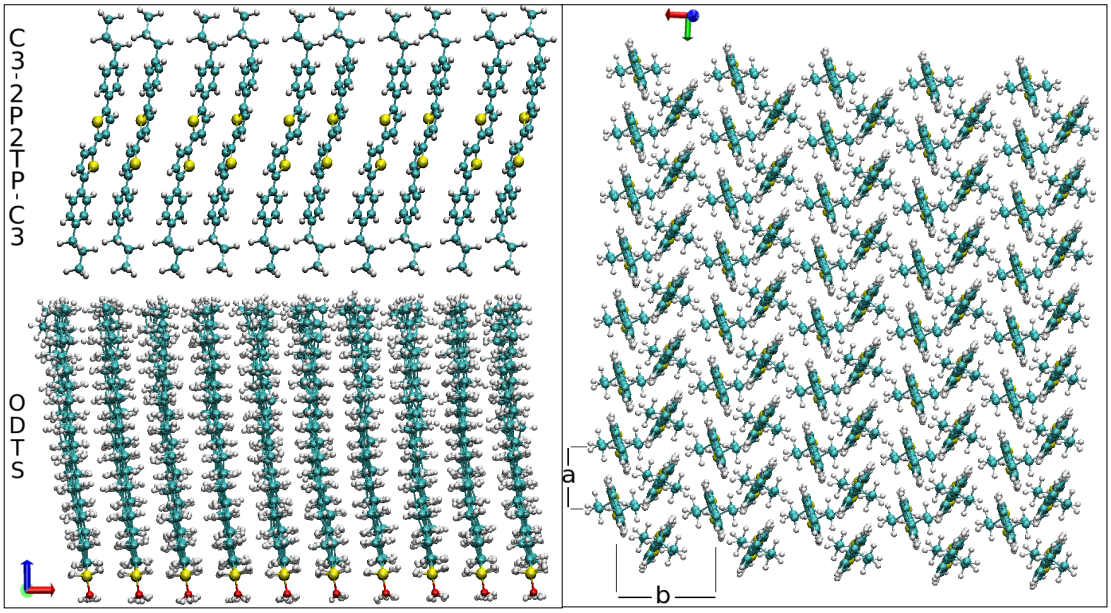

Figure 2.15: Left: side view of the system/ right: top view without ODTS (a,b lattice parameters)

Chain length (n)	Lattice parameters (Å)	Tilt (degrees)
3	a = 5.66 b = 7.85	1.01
4	a = 5.70 b = 8.46	22.79
5	a = 5.70 b = 7.86	5.95
6	a=5.71 b=8.42	20.41
7	a=5.74 b=7.81	1.20

Table 2.4: Experimental values of the lattice constant and the tilt angle of the P2TP molecule for different chain lengths

Chain length (n)	Lattice parameters (A)	Tilt (degrees)
3	a = 5.77 ± 0.3 b = 7.90 ± 0.3	3.5 ± 1.5
4	a = 6.12 ± 0.3 b = 8.07 ± 0.3	19± 1.5
5	a = 5.85 ± 0.3 b = 7.60 ± 0.3	4.2 ± 1.5
6	a = 5.61 ± 0.3 b = 9.37 ± 0.3	19 ± 1.5
7	a = 5.85 ± 0.3 b = 7.65 ± 0.3	4.5 ± 1.5
8	a = 5.63 ± 0.3 b = 9.64 ± 0.3	22 ± 2

Table 2.5: Simulation-derived values of the lattice parameters and tilt angles for different chain lengths.

This ‘odd-even’ effect arises, we believe, from the orientation of the last methyl group of the chain, which is different for odd- and even- length chains. We observed that the interaction energy between the last methyl group of P2TPs and the ODTS surface differs with the orientation of the molecule. For C4: The lowest energy occurs when the molecule is tilted by 19 degrees - a 2 kcal/mol advantage relative to no tilt and a difference in the central energy maximum of 11 kcal/mol. Figure 2.16 shows the van der Waals energy interaction of P2TPs molecules with the uppermost ODTS methyl groups. In this graphic, the last methyl groups of ODTS are situated at the coordinate: (0,0);(0,4.8);(4.1,2.4);(8.2;0);(8.2,4.8) which corresponds to a density of ODTS of 5 molecules/nm^2. The graphs are shown with the same energy scale on the y-axis so that you can readily see the relative differences between tilted and un-tilted potential energy surfaces. The position of lowest energy for both odd- and even- chain molecules lies in-between the terminal methyl groups of ODTS (not on top of ODTS). But even-chain molecules tilt away from the normal to the surface of ODTS in order to maximize the interaction of the last methyl group of the P2TP with the terminal methyl group of the ODTS. Figure 2.17 shows the lowest energy configuration of the P2TPs molecules for n=3 and 4 (left and right hand side, respectively). Moreover, the difference of tilt angle is maintained with increasing chain length. Figure 2.18 shows the results for n = 3, 4 and 5.

2.14. Conclusions

This study has revealed some key insights. Firstly, results for C17 and C18 SAM surfaces behave similarly, due to the high density considered here. Secondly, the preferred crystal structure of P2TPs for odd- and even- chain molecules is the same – a

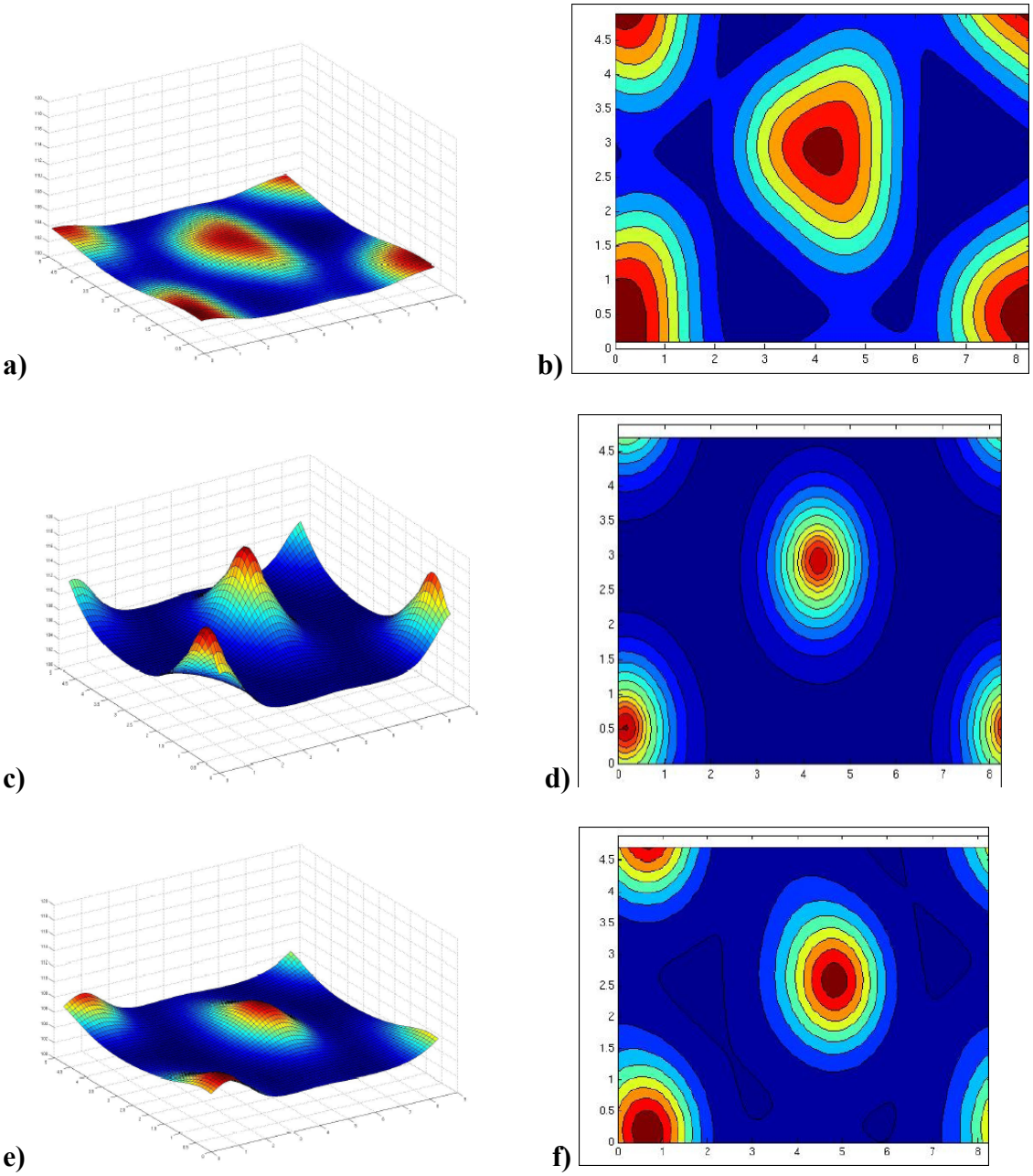

Figure 2.16: Energy interaction between P2TPs and ODTS as a function of x and y position of P2TPs on the surface. Left: 3D views. Right: Top views. a),b) n=3, tilt 3.5°, c),d) n=4, no tilt, e),f) n=4, tilt 19°.

herringbone lattice, as predicted by experiments. Again, this was a pre-requisite before any comparisons to experiment could be made. Thirdly, the tilt angles adopted by the odd- and even- chain P2TPs molecules observed in simulations and via experiments agree quite well. The origin of the odd-/even- effect is, we suggest, caused by maximizing the binding energy of the last methyl group of the chain length with the ODTS surface. To do so, the even-chain molecules have to tilt more than odd-chain molecules due to the orientation of the last methyl group with respect to the ODTS surface (Figure 2.16). For a better understanding of this phenomenon, a study following the deposition process itself is warranted, especially the transition of the orientation of deposited molecules from an orientation parallel to the surface (typical for a single isolated molecule) to one in which a cluster of molecules spontaneously "flip" upright to a vertical alignment once the critical cluster size has been exceeded.

This transition is driven by energy minimization: When molecules diffuse (in isolation) on the surface, they stay parallel to it in order to minimize the system energy [9,35]; however, when many molecules are present they self-assemble and start to align perpendicular to the surface. However, such a simulation is extremely computationally expensive. The organization of these first few molecules could determine the lattice parameters and their relative orientation and hence tilt angle and confirm this supposition.

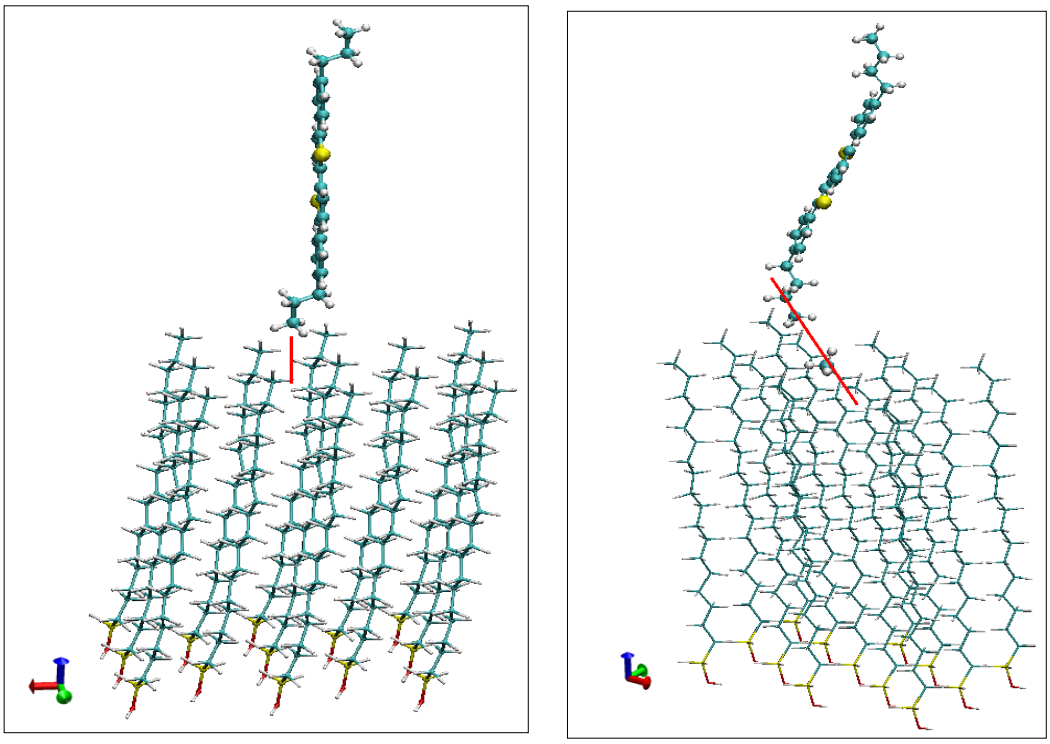

Figure 2.17: lowest energy position of the molecule on top of ODTS left: n=3, tilt = 3.5° / right: n=4, tilt =19°

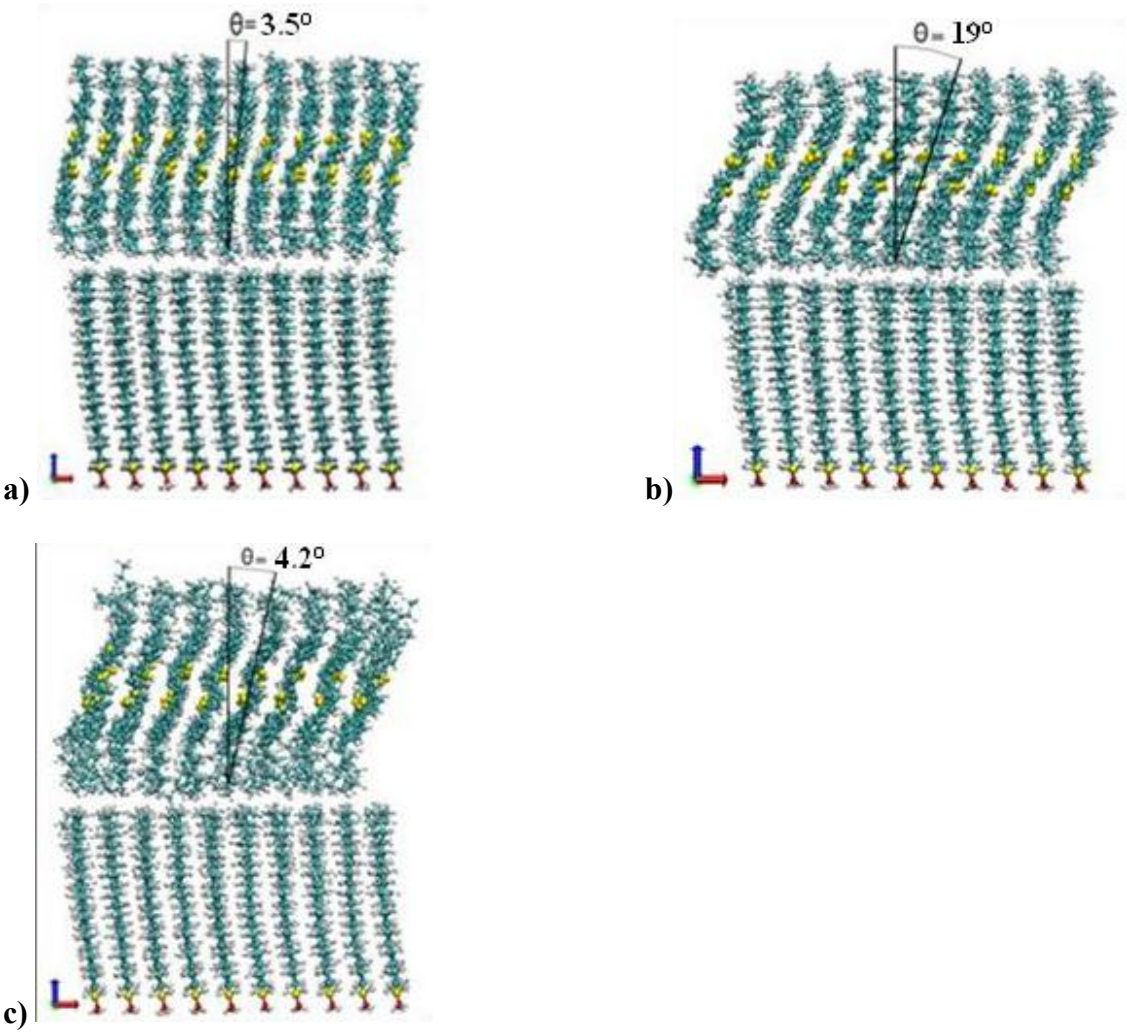

Figure 2.18: a: n=3, θ=3.5° / b: n=4, θ=19° / c: n=5, θ=4.2°, following constant-temperature Molecular Dynamics.

REFERENCES

[1] H. Yamamoto, K. Nishiyama, and I. Ohdomari, J. Phys. IV 132, 189 (2006).

[2] L. Zuppiroli, K. Kamaras, M. Bussac, and E. Moons, Eur. Phys. J. B 11, 505 (1999).

[3] M. Halik, H. Klauk, , and U. e. a. Zschieschang, Nature 431, 963 (2004).

[4] D. L. Irving and D. W. Brenner, J. Phys. Chem. B 110, 31 (2006).

[5] S. Vemparala, B. B. Karki, R. K. Kalia, and P. Vashishta, J. Chem. Phys. 121(9), 4323 (2004).

[6] N. Allinger, Y. Yuh, and J.-H. Lii, J. Am. Chem. Soc. 111, 8551 (1989).

[7] K.-H. Chen, J.-H. Lii, G. A. Walker, Y. Xie, H. F. S. III, and N. L. Allinger, J. Phys. Chem. A. 110, 7202 (2006).

[8] K.-H. Chen, G. A. Walker, and N. L. Allinger, Journal of Molecular Structure(Theochem) 490, 87 (1999).

[9] J. E. Goose and P. Clancy, J. Phys. Chem. C, 111, 43 (2007).

[10] R. Cantrell and P. Clancy, Surf. Sci., 602, 22, 3499 (2008).

[11] S. B. M. Bosio and W. L. Hase, J. Chem. Phys., 107, 9677 (1997).

[12] N. Isa, K. D. Gibson, T. Yan, W. L. Hase, and S. J. Sibener, J. Chem. Phys. 120, 2417 (2004).

[13] B. S. Day, J. M. Morris, W. A. Alexander, and D. Troya, J. Phys. Chem. B 110, 6832 (2006).

[14] B. S. Day, J. M. Morris, and D. Troya, J. Chem. Phys. 122, 214712 (2005).

[15] K. D. Gibson, N. Isa, and N. Sibener, J. Phys. Chem. A 110, 1469 (2006).

[16] A. Ulman, Adv. Mater. 2 12 (1990).

[17] D. H. L. Kim, H. S. Yang, H. Yang, and K. L. Cho, Advanced Functional Materials 18, 1363 (2008).

[18] Y. Ito, A. A. Virkar, S. Mannsfeld, J. H. Oh, M. Toney, J. Locklin, and Z. Bao, J. Am. Chem. Soc. 131, 9396 (2009).

[19] F. Tao and S. L. Bernasek, Chem. Rev. 107, 1408 (2007).

[20] P. T. Mikulski, L. A. Herman, and J. A. Harrison, Langmuir 21, 12197 (2005).

[21] S. Hong, A. Amassian, A. Woll, S. Bhargava, J. Ferguson, G. Malliaras, J. Brock, and J. Engstrom, Appl. Phys. Lett. 92, 253304 (2008).

[22] A. Amassian, T. Desai, S. Kowarik, S. Hong, A. R. Woll, G. Malliaras, F. Schreiber, and J. Engstrom, J. Chem. Phys. 130, 124701 (2009).

[23] T. V. Desai, S. Hong, A. R. Woll, K. J. Hughes, A. Prakash, P. Clancy, and J. R. Engstrom, submitted (2010).

[24] G.Schaftenaar and J. Noordik, J. Comput.Aided Mol. Design 14, 123 (2000).

[25] J. W. Ponder, Tinker - software tools for molecular design, http://dasher.wustl.edu/tinker/ (2010).

[26] J. E. Goose, E. L. First, and P. Clancy, Phys. Rev. B 81, 205310 (2010).

[27] J. Nocedal, Mathematics of Computation 35, 773 (1980).

[28] Gaussian 09, Revision A.1, M. J. Frisch, G. W. Trucks, H. B. Schlegel, G. E. Scuseria, M. A. Robb, J. R. Cheeseman, G. Scalmani, V. Barone, B. Mennucci, G. A. Petersson, H. Nakatsuji, M. Caricato, X. Li, H. P. Hratchian, A. F. Izmaylov, J. Bloino, G. Zheng, J. L. Sonnenberg, M. Hada, M. Ehara, K. Toyota, R. Fukuda, J. Hasegawa, M. Ishida, T. Nakajima, Y. Honda, O. Kitao, H. Nakai, T. Vreven, J. A. Montgomery, Jr., J. E. Peralta, F. Ogliaro, M. Bearpark, J. J. Heyd, E. Brothers, K. N. Kudin, V. N.

Staroverov, R. Kobayashi, J. Normand, K. Raghavachari, A. Rendell, J. C. Burant, S. S. Iyengar, J. Tomasi, M. Cossi, N. Rega, J. M. Millam, M. Klene, J. E. Knox, J. B. Cross, V. Bakken, C. Adamo, J. Jaramillo, R. Gomperts, R. E. Stratmann, O. Yazyev, A. J. Austin, R. Cammi, C. Pomelli, J. W. Ochterski, R. L. Martin, K. Morokuma, V. G. Zakrzewski, G. A. Voth, P. Salvador, J. J. Dannenberg, S. Dapprich, A. D. Daniels, Ö. Farkas, J. B. Foresman, J. V. Ortiz, J. Cioslowski, and D. J. Fox, Gaussian, Inc., Wallingford CT, 2009.

[29] T. A . Halgren, J . Am. Chem. Soc., 114, 7827-78433 (1992).

[30] Computational science series vol.1: Understanding Molecular Simulation, D. Frenkel, B. Smit, November 7, 2001, ISBN-10: 0122673514.

[31] R. Lustig, Mol. Sim., 37, 457–465, (2011).

[32] Q. Yuan, S. C. B. Mannsfeld, M. L. Tang, M. F. Toney, J. Luning, Z. Bao, J. Am. Chem. Soc., 130, 11 (2008).

[33] X. Liu, K. K. Goli, J. Genzer, O. J. Rojas, 27, 4541–4550 (2011).

[34] A. P. Kaushik, P. Clancy, Surf. Sci., 605, 13–14, 1185-1196, (2011).

[35] T. V. Desai, A. R. Woll, F. Schreiber, J. R. Engstrom, 114, 47, 20120 (2010).

CHAPTER 3

Explicit all-atom modeling of realistically sized ligand-capped nanocrystals

3.1 Introduction

The nanoscale dimensions of "quantum dots," also known as nanocrystals (NCs), allow quantum confinement of electrons and holes, leading to the remarkable observation that the properties of quantum dots of the same material are size-dependent. Considerable research has been undertaken to try to create monodisperse arrays of nanocrystals in controlled geometries, not only to exploit their unusual or unique electronic properties, but also to fabricate practical devices for applications such as solar cells, sensors, *etc.* [1-5] The main "bottom up" synthesis method used to achieve such monodispersed NCs involves, first, "capping" the nanocrystals with surfactant ligands, often functionalized alkyl chains. These ligand coatings allow the nanocrystals to approach one another closely (self-assemble), without allowing neighboring nanocrystals to aggregate together, or sinter, since that destroys the confinement. We are ultimately interested in simulating "capped" chalcogenide nanocrystals, like CdSe or PbS, that are under intense current scrutiny as potential photovoltaic solar cell materials [6-9]. For these systems, there are still some fundamental questions to ask of the self-assembly process, some of which this paper will attempt to answer.

In experiments, "capped" NCs assemble into superlattices of crystals in the 3-10 nm diameter range with facetted morphologies and near-perfect crystalline orientation. Difficulties in experimental control lead to the observation that the smaller the diameter of the nanocrystal, the larger the size dispersity of the array. Thus, in practice,

experimentalists typically work in the 6-10 nm range. In contrast, as we shall show below, molecular simulation studies of such systems have almost exclusively been conducted for NCs whose diameters, 1-3 nm [10-13], are far smaller than typical experiments, presumably due to computer resource limitations. In addition, most of these studies have approximated the representation of the ligand chains, not as explicit all-atom models, but as "united atom" (UA)-like representations [10-14]. For example, UA models represent a $-CH_2$ group as a single entity, like a bead on a chain. As we shall show, any UA approximation has to be made judiciously for this critically important task. Explicit all-atom simulations of capped nanocrystalline arrays of realistically sized particles remain essentially intractable, except to those with access to petascale or highly parallelized computational resources.

Despite decades of experimental research to study capped NCs, the relative extent of the roles played by ligands and nanocrystals in the assembly process remains unclear, especially as the processing parameters are altered (*e.g.*, temperature, choice of solvent, aging, exposure to air, *etc*.). Indeed, even the nature of the binding between the ligands and the surface of the nanocrystal, and the density dependence of the ligands on different facets of the nanocrystal, is unknown. Further, there are few experimental probes that can truly answer these molecular-scale questions since they describe events at buried interfaces that are difficult to image or probe. This provides considerable motivation to employ molecular simulation approaches to shed some light on these complex questions, even though the scale of these systems in terms of length and time scales also represents cutting-edge challenges to simulation.

It is clear from previous molecular simulation studies [10-14] that the ligands are not simply "spacers" between the nanoparticles in the superlattice to prevent sintering. They clearly play a defining role during the assembly process and in the resulting morphology of the superlattice. They also passivate surface states. Hence the representation of the ligands is a critically important task. Indeed, impressively large-scale (at the time) Molecular Dynamics simulations by Luedtke and Landman [10] in the 1990s, described the interactions of *sub*-3 nm gold nanocrystals capped with thiol-terminated alkyl chains. Their results suggested that the gold-gold interaction contributed just 1% to the overall energy per particle of the system. This work was also notable for their prescient suggestion of the importance of the ratio of ligand length to nanoparticle diameter, l/σ, to determine the preferred morphology (fcc *vs*. bcc, *etc*.), although they were unable to confirm this in their simulations given resource constraints. This is an issue we will take up here. On the other hand, they make a more disputable point of the tendency of ligands to "bundle" together at low temperatures. Badia *et a*l. [15] claim to observe bundling for gold nanoparticles. Similar observations of bundling were made by Lane *et al.* [16] when modeling *spherical* nanoparticles capped by alkanethiol ligands in water, decane and in vacuum. More recent work by Schapotschnikow and Vlugt [11], also on sub-3 nm gold nanoparticles, was the first to include the effect of the role of the solvent to influence the adsorption of ligands during the assembly process, and the effect of the curvature of the gold surface on phase behavior. Lane *et al.* [16] and Yang *et al.* [17, 18] have also studied solvent effects on alkane ligands attached to nanoparticles in different solvents, such as water and decane. We shall address solvent effects in a

subsequent paper. Here we consider only assembly *in vacuo*, which is the usual starting point for such simulations.

We will show in this paper that reports of bundling, *i.e.,* ligands grouping together in distinct orientations on the surface of *facetted* nanocrystals, can be an artifactual result of the choice of the potential model used. We will compare three different potential models – one explicit and two united atom models to simulate our nanocrystal systems. One of the UA models used is the Jorgensen united atom model [19] that has been used by Landman *et al*. [10]. We will show that this model produces bundled conformations of ligands not produced by the explicit all-atom MM3 model. Several papers have reported that the Jorgensen model over-emphasizes attractive ligand-ligand interactions [20, 25, 26, 28]. We will hypothesize that the phenomenon may the result of a combination of over attractive van der Waals' interactions and stiff dihedral interactions within the ligand molecules.

Computational efficiency has made commonplace the coarse-graining of (say) -CH_2 groups into "united atoms" or "beads," thereby reducing the overall number of interacting entities in the system [10-14]. One of the most important considerations when using the UA model is the quality of the interaction parameters chosen. The model should be able to reproduce, at least qualitatively, the trajectories of the system that were produced using the explicit all-atom method used before. Klein *et al*. reinforce this need and point to potential problems in their review article [14]: "Outside of the polymer community, however, Scott points out in a recent review that existing CG [coarse-grained] models 'suffer from a lack of connection to atomistic interactions, which must ultimately be responsible for phase separation and domain formation' [27]."

One of the earliest, and still perhaps the most widely used, UA models was proposed by Jorgensen *et al.* in 1984 [19] which has been widely used to simulate various systems and has shown good results for liquid or liquid-like systems. However, as early as 1990, Toxvaerd's studies on alkanes [20] showed the tendency of the Jorgensen model to produce overly attractive interactions among alkyl chain molecules. He posited that the Jorgensen UA model is unable to describe the van der Waals interactions between the carbon atoms on the backbone of the alkyl chain and the adjacent hydrogen atoms, which are necessary to accurately describe the flexibility of the alkyl chain. He suggested using an "anisotropic" UA model, but this model is rather complicated to implement. Siepmann *et al.* [21] used configurational-bias Monte Carlo in the Gibbs ensemble to calculate vapor-liquid coexistence curves of n-alkanes containing from 5 to 48 carbons. They found that the OPLS force field overestimated the critical temperatures of the n-alkanes and proposed a new force field (SKS). This force field gave improved results for medium- to long- chain n-alkanes, but overestimated the critical temperatures of shorter alkanes. In 1998, they proposed a new "transferable potentials for phase equilibria" (TraPPE) force field [22], which proved to be superior to both OPLS [29] and SKS [23] in predicting phase equilibria; TraPPE is now widely used. The same year, Nath *et al.* introduced the NERD force field [23, 24], which provided good agreement with experimental phase equilibria data not only for pure alkanes and alkenes, but also their binary and ternary mixtures. Studies of a quite different system, polymers, in 2010 by Li *et al*. [25], compared the conformation of polyethylene chains using an explicit Dreiding model [28] with the Jorgensen *et al.* OPLS UA model. They observed that Jorgensen UA-modeled polyethylene chains adopted a lamellar conformation which was inflexible,

while the same chain modeled with the all-atom explicit Dreiding model was much more flexible and adopted more random conformations. They suggested a possible correction that involved increasing the σ parameter of the van der Waals interaction for the carbon backbone to relieve some of the inflexibility of the alkyl chain. In contrast to Li *et al*.'s implication of *inter*molecular forces being at fault, Paul *et al.* [26] looked instead at the *intra*molecular forces and offered an alternative approach to a united atom representation. In the results section below, we will use the Jorgensen *et al*., Li *et al.,* and Paul *et al.* UA models and provide a comparison between the coarse-grained models that may be used to represent a system of alkyl ligand-capped nanocrystals.

In 2004, Kumar and co-workers produced an ambitious multiscale modeling study of the assembly of "capped" Co nanoparticles, starting from a simulation volume filled with Co atoms and ligand atoms [30]. The study began with *ab initio* calculations to provide an accurate starting point for the interactions between Co atoms and ligands and solvent. The next step involved a lattice-based MC simulation of NC assembly from Co atoms and surfactant ligands; this showed a preference to form 5 nm clusters and allowed the computation of an effective potential energy function between ligands. Finally, this second system of nanoparticles is coarse-grained such that each nanoparticle is reduced to a single point "particle" that interacts with other point "particles" through the effective potential obtained in step 2. Such coarse-graining facilitated the simulation of hundreds of nanoparticles (rather than hundreds of Co atoms in step 2). This elegant study, like all kinetic Monte Carlo methods, also has some limitations. For instance the drawback of using an'on-lattice' approach and effective potential constraints means that subtler interactions could be lost. There are also issues regarding the modeling of the solvent-

surfactant interactions and hence estimation of entropy effects. The most direct way to know how good a lattice-based approach will be in this situation is to explicitly model every atom in the capping ligands, the core nanoparticles, and the surrounding solvent. Unfortunately, for nanoparticles sizes that experimentalists can produce with a tight size distribution (5-10 nm diameter), such an explicit treatment is prohibitively expensive. An off-lattice KMC approach could loosen these constraints, but currently available codes are also too expensive for such an undertaking. This remains a viable option for the future with a suitably constructed code.

3.2 Configuration of the system

Our long-term interest lies in representing the properties of lead chalcogenide nanocrystalline arrays of varying diameters, passivated by long-chain organic ligands. The equilibrium structure for PbSe NCs is an FCC lattice, which consists of two interpenetrating FCC lattices made of Pb and Se in the rock salt (NaCl) structure. The lattice constant of the PbSe NC is 6.12 nm. Following Luedtke and Landman's result that the ligands dominate NC-NC interactions, and as a means to decouple ligand-ligand interactions from NC-NC interactions, we focus in this study mainly on the ligand-ligand interactions, and the conformations adopted by the ligands on the NC surface. We will confirm the Landman result that core-core (NC-NC) interactions will be weak for the length of chains typically used in experimental self-assembly of chalcogenide systems (typically 12 carbon backbone atoms in length).

We shall identify a number of key parameters that govern the conformations of the ligands as well the interaction between ligands on the same NC and interaction between ligands on different NCs. In the experimental setup, NCs are grown in solution

containing organic ligands as precursors. The ligands passivate the NC surface as the NC grows in solution. The size and shape of the NC is governed by the temperature of the solution and by the concentration of the precursors. Nanocrystals with very small diameters (< 3 nm) are more or less octahedral in shape. In this study, we have approximated the shape of such small NCs as being perfect octahedra (Figure 3.1b**)** and hence exhibiting only {111} facets, which are known to be purely Pb-terminated. Larger NCs with diameters in the 4-7 nm range have both {100} and {111} facets. There is some evidence that there may also be {110} surfaces around the corners and edges [31]. Very large NCs (10 nm or higher) are almost cubic [32]**.** In this study, we have assumed that the NCs of diameters of around 4 nm are truncated octahedra and larger NCs (diameters 6 nm) have a cube-octahedral shape with both {100} as well as {111} facets; see Figure 3.1b. The {100} facets are made of alternating Pb and Se atoms, whereas the {111} facets are Pb-terminated. This was chosen because there is experimental evidence that the oleic acid ligands typically used to passivate the NC surface have a greater preference for Pb atoms, thereby promoting the formation of Pb-terminated {111} facets [33].

The organic ligands chosen for this study were aliphatic chains made of 12 carbon atoms and associated hydrogen atoms ("C12" ligands), since these are close in length to the oleic acid ligands often used by experimental studies of chalcogenide nanocrystals. But, we have also studied the effect of varying ligand length, in which case, ligands were used with chain lengths from 4 C backbone atoms (a "C4" ligand) to ones with 18 C backbone atoms (a "C18" ligand). The parameters for all the interactions between the ligands are described in the next section. The ligand molecules were created using the Molden software package [34] and an energy minimization of the initial guessed structure

was performed using a standard minimization algorithm - the limited memory L-BFGS minimization using a modified version of the algorithm of Nocedal which is a part of the TINKER software package [35]. The structures of other shorter and longer chain ligands were obtained in a similar manner. The ligands used in experiments are generally acids like oleic acid (C12) or thiols. The head group of the ligands attach themselves onto the Pb atoms of the NCs. In our system, we have represented the attachment of the head group by a single C-Pb bond. The ligands were grafted onto the surface of the NC at a given density, typically the close packed density for that facet. We have performed simulations where ligands were grafted with the entire carboxylic acid head group and we did not find any significant differences in the final morphology of the ligands compared to the case if we used a simpler C-Pb bond for the grafting of the ligands onto the NC surface. Hence, all simulations reported in this study used the C-Pb bond (which is a part of the TINKER package) to link the ligand with the Pb atoms on the NC surface. In essence then, we have a corona of ligands attached to lattice sites appropriate to the shape of a PbSe NC, but one in which the core is hollow, devoid of particles.

3.3. Intermolecular Potential Models

The choice of intermolecular potential model is a critical part of any molecular simulation. The inter- and intra- molecular potential models and associated parameters determine the trajectory of the system and hence the morphology and conformations of the molecules in the simulation. As we shall describe in later sections, the manner in which the coarse-graining is performed can have a profound effect on the different conformations adopted by the system. Hence it is important that the system behaves in a reasonably consistent manner irrespective of the degree of coarse-graining or the choice

of the potential model used. As mentioned in the section above, all the molecular simulations performed on capped nanocrystal lattices to date have been performed on coarse-grained systems. There exist no results from an explicit all-atom simulation to act as a "gold standard" reference point, presumably due to the computational expense involved. In this paper, we redress this situation and show that this was necessary to highlight some misleading structural properties that can be determined if the coarse-graining is not performed carefully.

We chose to use the non-reactive semi-empirical all-atom explicit Molecular Modeling 3 (MM3) potential, developed by Allinger *et al*. [36], to model all the ligand-ligand interactions. Core-core interactions were not considered in these simulations (as discussed above in reference to Landman). The MM3 potential is an explicit all-atom potential similar to other explicit potentials such as OPLS-AA, Dreiding, CHARMM, *etc.* [28, 27, 37]. The MM3 potential has been shown, by us and others [38-43], to describe hydrocarbons quite accurately [36]; in many cases, in good agreement with *ab initio* calculations. MM3 incorporates stretching, bending, and torsional energies, as well as the van der Waals interaction energies based on phenomenologically determined parameters. The total energy may be represented as follows:

$$E = E_b + E_a + E_{tor} + E_{aa} + E_{sb} + E_{stor} + E_{vdw} \quad (1)$$

with,

$$E_b = \frac{k}{2}(r - r_0)^2 + \frac{k'}{3}(r - r_0)^3 + \frac{k''}{4}(r - r_0)^4 \quad (2)$$

$$E_a = \frac{k}{2}(\theta - \theta_0)^2 + \frac{k'}{3}(\theta - \theta_0)^3 + \frac{k''}{4}(\theta - \theta_0)^4 + \frac{k'''}{5}(\theta - \theta_0)^5 + \frac{k''''}{6}(\theta - \theta_0)^6 \quad (3)$$

$$E_{tor} = \frac{k}{2}(1 + \cos(\varphi)) + \frac{k'}{2}(1 - \cos(2\varphi)) + \frac{k''}{2}(1 + \cos(3\varphi)) \quad (4)$$

$$E_{aa} = k(\theta - \theta_0)(\theta' - \theta'_0) \quad (5)$$

$$E_{sb} = k(\theta - \theta_0)(r_1 - r_{10} + r_2 - r_{20}) \quad (6)$$

$$E_{stor} = \frac{k}{2}(r - r_0)(1 + \cos(3\varphi)) \quad (7)$$

$$E_{vdw} = Aexp\left[-\frac{r}{\rho}\right] + \frac{C}{r^6} \quad (8)$$

where E_b is the bond-stretch, E_a is the angle-bend, E_{tor} is the torsion, E_{aa} is the bend-bend, E_{sb} is the stretch-bend and E_{stor} is the stretch-torsion potential. Here, r is the distance between the two atoms linked through a bond, θ is the angle between three atoms and φ is the dihedral angle defined by four atoms. θ' is the angle between three other atoms which are interacting with the first triad of atoms. r_1 and r_2 are the distances between the vertex atom and the two other atoms of a triad of atoms defined by an angle. The subscript 0 refers to equilibrium values. The potential does not involve electrostatic interactions. The intermolecular van der Waals interactions take the form of a Buckingham potential, modified with tapering polynomials so that the energy smoothly decreases to zero at a cut-off distance of 10 Å. k, k′, k′′, k′′′, k′′′′, A, ρ and C are all constants. The values of these constants are given in the original MM3 paper by Allinger *et al.* [36] and were used unchanged in this paper.

We have used the MM3 model extensively to study the energetics and structural characteristics of an array of small organic semiconducting molecules including the acenes, rubrene, DIP, sexiphenyl and C_{60} [41, 42] and have confidence in its ability to model small molecule organic systems. Our most recent study involved an extensive study of Self-Assembled Monolayers [43] that involved the simulation of long-chain organic molecules very similar to the ligands attached to the NCs considered here.

All-atom explicit models, such as MM3, are computationally very expensive. For example, a system of 50,000 atoms simulated for a 100 ps can take almost 24 hours to

complete when run on a single processor of a Dell 410 system with a 2.93 GHz Xeon core. Given this expense, the simulations were limited to consideration of only one or two fully capped NCs in a given simulation cell. Thus, in order to simulate larger arrays of NCs, *e.g*., superlattices, it is necessary, for all practical purposes, to appropriately coarse-grain the system by (say) treating groups of CH_2 units in the ligands as a 'united atom.' We shall describe in later sections how this coarse-graining was achieved, as well as the potential models employed for such simulations.

3.4. Simulation Methodology

The time evolution of the system was followed using a molecular simulation approach employing a modified Beeman algorithm, which is currently part of the freeware TINKER software package [35]. As mentioned in the preceding section, optimized structures of the ligands were obtained from an energy minimization of an initial guess structures using a standard minimization algorithm, here, the limited memory L-BFGS minimization using a modified version of the algorithm of Nocedal [44]. The core of the NC was approximated by a hollow shell where only the outermost layer of atoms was considered. The NC core is either fixed or treated as a rigid body, as required. As described before, three different NC core shapes were considered, depending on the size of the NC core; see Fig. 3.1. The 3 nm NCs are octahedral, the 4 nm NCs are truncated 136ctahedral, and the 6 nm NCs are cube-octahedra. The ligands were attached to the Pb atoms of the core using a Pb-C bond. The grafting density of the ligands plays an important role in the interaction of the NCs, as will be described in a later section. But, for most simulations, the grafting density was fixed. The ligands were grafted onto every other Pb atom on the surface, *i.e.,* there is a free Pb atom between every two Pb atoms

that are linked to a ligand. This leads to a greater density of ligands on the {111} surfaces than the {100} surfaces because of the presence of Se atoms in-between the Pb atoms on the {100} surfaces. This choice of ligand grafting density and location was made from *ab initio* studies of preferential ligand attachment sites. [45]

The first system we studied consisted of an isolated NC in vacuum; the main purpose for this rudimentary study was to determine whether ligand bundling occurs even for a single NC, as Luedtke and Landman had suggested. The system was thermalized at 300 K using a Nosé-Hoover thermostat [46-49] in the canonical (NVT) ensemble for a period of 200-300 ps using a time step of 1 fs. It was necessary to simulate (at least) 200,000-300,000 time steps in order to suppress significant fluctuations in temperature and energy and equilibrate the conformations adopted by the ligands. The simulation box used periodic boundaries in all three Cartesian directions, but the size of the box was made large enough to avoid the interaction of the NC with its images across the periodic boundaries. The core of the NC was held fixed during this time. Once the system was judged to be adequately thermalized, typically 1 ns, the conformations of the ligands on the surface of the NC were used to determine radial and angular distributions of the ligands around the nanocrystal core. These observations are reported in successive sections. This procedure was repeated for all three NC core shapes – the octahedron, truncated octahedron and the cube-octahedron.

Systems involving two or more NCs were then studied; they were equilibrated in the same manner described above. The cores of the nanocrystals in these studies were frozen to investigate the ligand interactions alone. We identified several key parameters that affect the interaction energy and equilibrium distance; they include the shape and size of

the NC, ligand length, and grafting density of the ligands. These observations are discussed in relevant sections below. In order to study the true interactions between two nanocrystals, it was necessary to allow the nanocrystal cores to rotate freely. Such a study was performed where the centers of the cores of the nanocrystals were held fixed but the cores were allowed to rotate about the center. This study allowed us to calculate the Potential of Mean Force (PMF), which is a very useful measure to quantify the interaction of the NCs. The mean force, F_{mean}, for two NCs separated by a distance r is defined as: [50, 51]

$$F_{mean}(r) = \frac{1}{2}\langle(\overrightarrow{F_2} - \overrightarrow{F_1}).\vec{r}\rangle \quad (9)$$

where < > denotes an ensemble average of configurations taken when the system is in equilibrium at a temperature T and $\overrightarrow{F_1}$ and $\overrightarrow{F_2}$ are the total forces acting on the NC_1 and NC_2, respectively, and *r* is the vector connecting the centers of mass of the two NCs. The PMF can be obtained from the mean force as:

$$\varphi_{MF}(r) = \int_r^\infty F_{mean}(s)ds \quad (10)$$

A convenient way of evaluating the PMF is to attach a fictitious spring with a known spring constant between the NCs under considerations and then move them relative to one another at a constant velocity. This technique is called Steered Molecular Dynamics (SMD), which exploits Jarzynski's equality that relates equilibrium free energy difference to irreversible work in a non-equilibrium system [52, 53]. The two NCs are initially separated to a distance at which there is no interaction between them. The NC cores are not frozen, but have the ability to translate as well as rotate about their center of mass as a rigid body. The motion of NC cores was integrated using a constant-energy, NVE, microcanonical ensemble with rigid body dynamics. The ligands were maintained

under “equilibrium” conditions at 300 K; their motion was integrated using a constant-temperature, NVT, canonical ensemble. In this way, the entire system (NC core plus ligands), were maintained at thermal equilibrium over the entire course of displacement. The force of interaction between the two NCs was recorded as a function of time and the PMF was evaluated as the sum of the forces over the entire displacement of the NCs. The PMF was computed by averaging multiple trajectories over the same pulling path/reaction coordinate. The results are presented below for each of the NC shapes studied.

3.5. Results and Discussion

3.5.1 Isolated nanocrystal study

We began by simulating a single, isolated nanocrystal in vacuum to establish “baseline” observations of the conformation of the ligands at equilibrium for different nanocrystal diameters (3 nm, 4 nm and 6 nm). For this study, the core of the NC was fixed and the ligands were equilibrated at a temperature of 300 K for a period of 1 ns. The energy and temperature of the system was observed to achieve a constant mean value with an acceptable standard deviation of less than 1% of the mean value. The system was deemed to be at equilibrium at this point. The ligand conformations adopted by differently sized, isolated, NCs are shown in Figure 3.1a. The ligand conformations were observed for a range of temperatures from 150 K to 450 K. No significant differences in ligand morphology were seen for different core shapes, sizes and temperatures, except for the smallest NCs (described more fully in the next paragraph). The ligands, as expected, waved around much more actively at higher temperatures due to thermal excitation whereas they were relatively sluggish at lower temperatures.

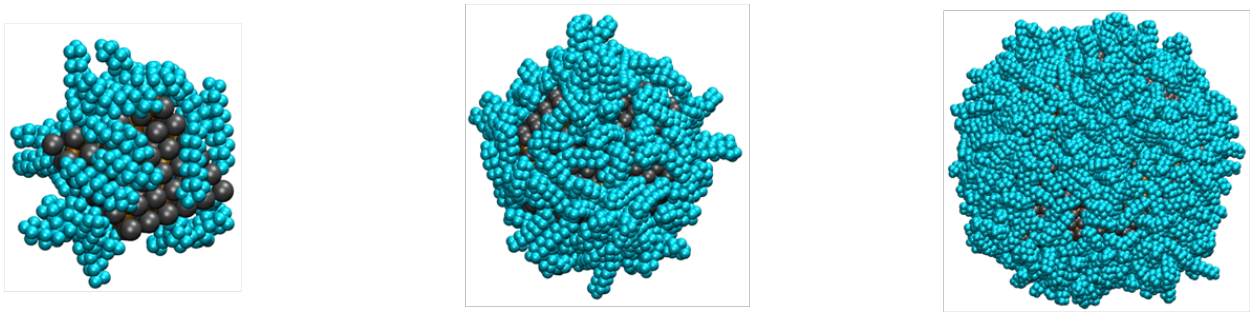

a

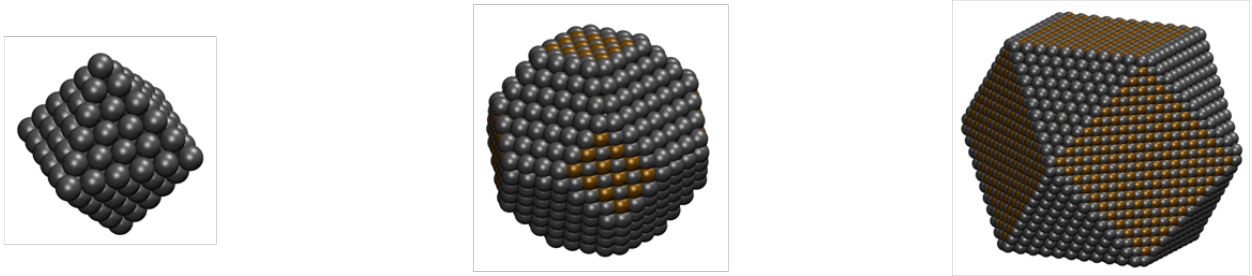

b

Figure 3.1: (a) MD snapshots of the conformations of thermalized ligand-capped nanocrystals at 300 K. From left to right: 3 nm, 4 nm and 6 nm diameter particles. The ligands are C12 ligands about 13 Å long; ligand coverage is 3.3 ligands/nm^2. (b) The underlying shapes of the cores corresponding to each of the ligand-capped nanocrystals in a.

Ligand conformations on the larger NCs are markedly different from the 3 nm NC (see Figure 3.1). Facets on the 3 nm NC are quite small and, consequently, can accommodate very few ligands. Indeed, the length of the ligand is comparable to the lateral dimensions of the facet itself. The ligands attempt to maximize their interaction with the NC facets and hence prefer to adopt a supine position with respect to the facet. This can be seen in Fig. 3.1a where some of the ligands are wrapping around the NC core. Larger NCs have concomitantly larger facets and hence a larger number of ligands on the surface. This provides the ligands the opportunity to interact with each other, lessening ligand interactions with the core. The presence of many ligands on the surface also makes it essentially impossible for ligands to lie flat against the facet of the core due to steric hindrance from the other ligands. Thus, the ligands on the larger NCs adopt a more upright position as measured from the surface of the core. Since these conformations can be difficult to see from the MD snapshots, we compared graphs of the angular distribution of the ligands on the 3 nm NC compared to the 6 nm NC, as shown in Fig. 3.2. The angles are measured as that made by the vector joining the ends of the ligands from the normal to the facet to which the ligands are attached. It can be clearly seen from the angular distribution profile that ligands wrap around the NC in the case of small NCs. The peaks in the 6 nm NC, correspond mainly to ligands standing upright on the corresponding {100} and {111} facets. No such peaks can be seen for the 3 nm NC; the distribution suggests that ligands adopt all possible angular conformations. This will lead to very different types of interactions between two or more NCs, as will be described in the next few sections.

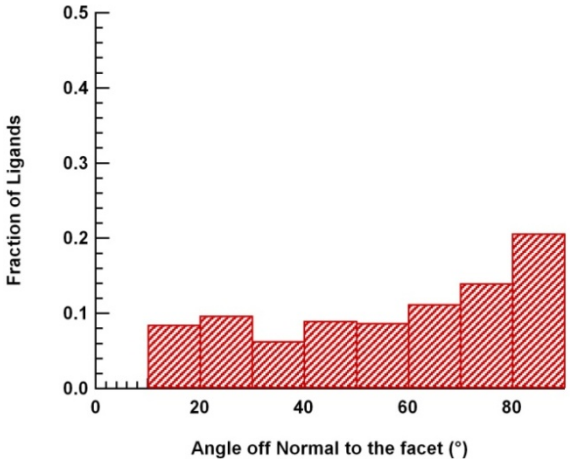

a)

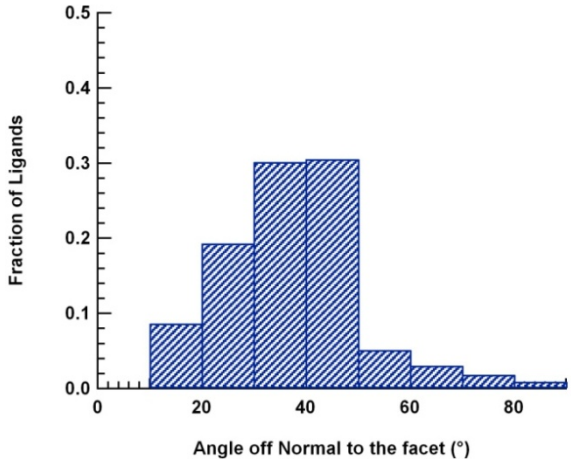

b)

Figure 3.2: Angular distribution of C12 ligands on the facets of (a) 3 nm and (b) 6 nm nanocrystals. The angle is measured as that made by the ligand with the normal to the facet of the NC to which it is attached. Ligands are about 13 Å long. Coverage is 3.3 ligands/nm^2.

3.5.2 Studies of pairs of NCs in a superlattice

The interaction between two NCs that are *not* in the neighborhood of other NCs is different from the interaction between NCs in a superlattice. The interacting NCs in a "two nanocrystal" system, unfettered by the interaction of other NCs, are free to sample many more conformations compared to NCs in a superlattice. In a superlattice, the NCs are rotationally and translationally constrained because of the presence of other nearby NCs. The ligands of the NCs drive the translational and rotational order of the NCs in the superlattice and, once the order has been established, the degrees of freedom of the NCs are severely constrained. Thus, in the following sections, we have examined the interaction between two NCs, *not* as an isolated system, but in a periodic superlattice by imposing periodic boundary conditions on the system. We have, however, examined an isolated "two-NC" system for comparison, which is described in section 5.3.

Both BCC and FCC superlattice symmetries were chosen in our studies since these are the two most commonly adopted symmetries in experimental studies. Only one unit cell was simulated, using periodic boundary conditions to simulate infinite extent, thus maximizing computational efficiency. There are two NCs in the BCC unit cell, and four NCs in the FCC unit cell, as shown in Fig. 3.3**.** The NCs in the unit cells were initially far enough apart that the ligands on one NC did not interact with the ligands of the other NC. Thus, the distance between nearest neighbors in the unit cell was initially well beyond the cut-off used for the van der Waals interactions. The cores of the NCs were held rigid while the ligands of the NCs were thermalized at a temperature of 300 K for 1 ns. Once the equilibration period was over, the unit cell was compressed slowly at a rate of 1 Å/ns while the system was constantly maintained in equilibrium at 300 K. The compression

process was thus as close to adiabatic (quasi-static) as possible. The compression of the system was interspersed by equilibration runs. The system was compressed for a period of 50 ps and then equilibrated for the next 50 ps. This was done to ensure that the system was maintained in equilibrium and fluctuations in energy and temperature were minimal. The ligands on the NCs were found to inter-digitate very slowly as the unit cell was compressed and the NCs were brought closer together as shown in Fig. 3.4. The interaction energy between the NCs displays a familiar Lennard-Jones-like curve with a long-range attractive portion, due to the favorable interaction between the ligands on the NCs, followed by a steeply repulsive portion due to the entropic repulsion between the interdigitated ligands. Compression of the unit cell was stopped once the repulsive portion of the curve was reached.

3.5.2.1 Effect of Ligand Length

In this section, we examined the effect of ligand length on the interaction between two NCs of size 3.1 nm in a periodic superlattice. The ligand grafting density was kept constant at 3.0 ligands/nm^2 which is in agreement with [45]. The length of the ligand was varied from 4 CH_2 backbone units to 18 CH_2 units. The parameters we examined were the separation distance between the centers of the NCs at the point of energy minimum (r_{min}) and the value of the interaction energy at the energy minimum (ε), as shown in Figs. 3.5, 3.6. It is clear that both these curves are relatively linear for longer ligand lengths, specifically beyond 8 CH_2 units on the ligand. Thus, the nature of the inter-NC interaction is predictably similar for ligand lengths beyond C8, the difference arising merely from the addition of further -CH_2 units. Similarly, the value of r_{min} increases with

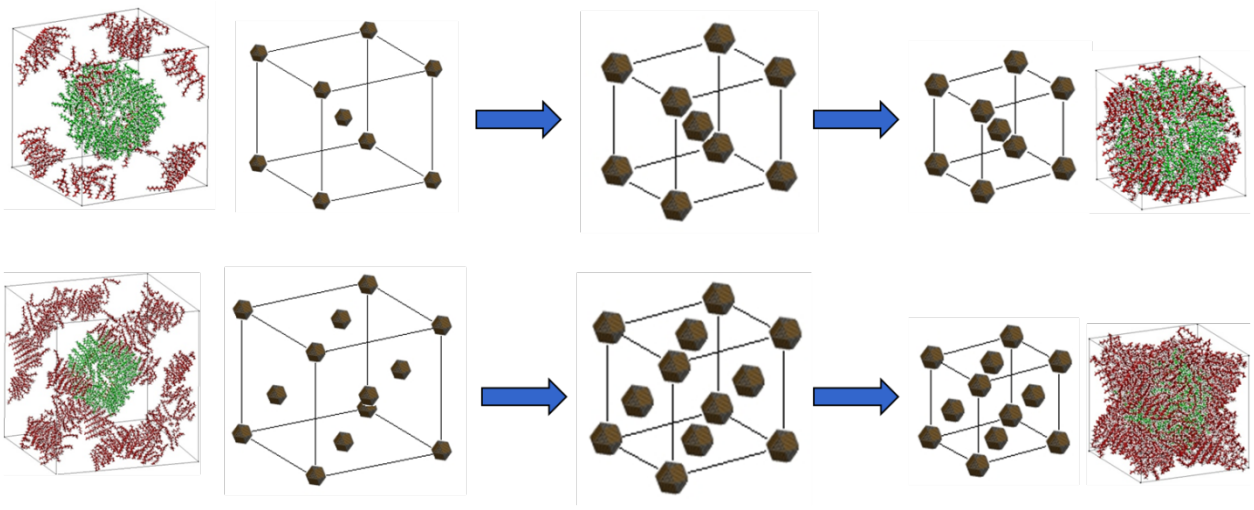

Figure 3.3: Quasi-static compression of unit cells of a BCC lattice (top) and an FCC lattice (bottom). Initially, the brown ligands on the image cores are not in contact with the green ligands of the centrally located NC (LHS images). As the compression proceeds, the ligands eventually interdigitate, as shown in the MD snapshot images on the RHS.

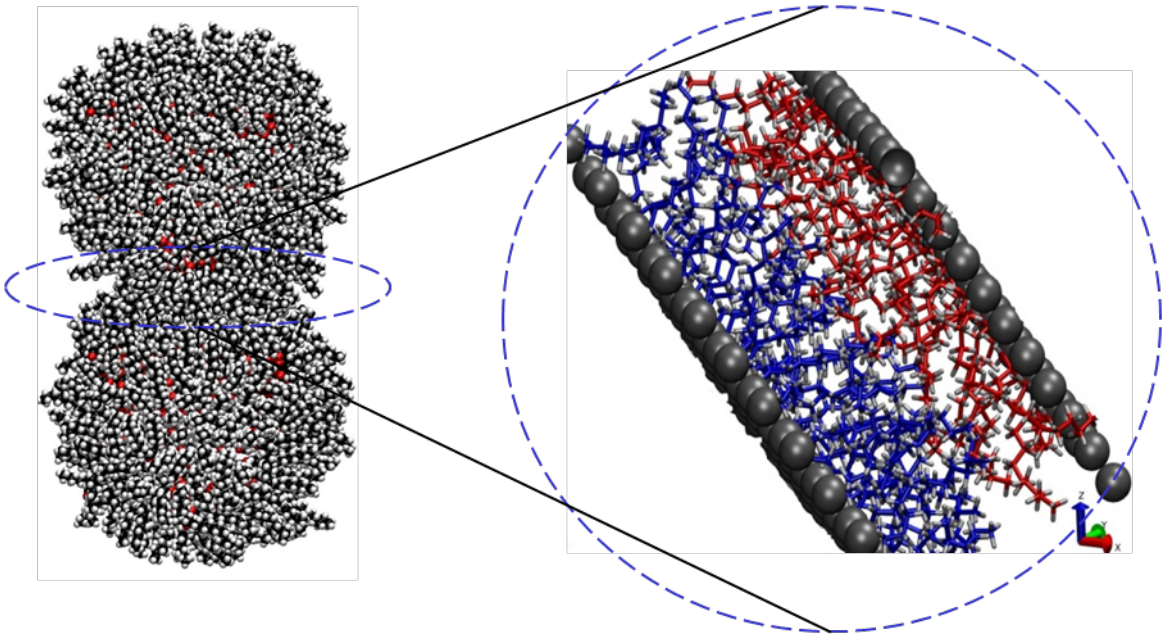

Figure 3.4: Interdigitation of ligands between a pair of adjacent nanocrystal facets is shown on the expanded view (RHS image) of a two-NC cluster (LHS image). The ligands on different (identical) nanocrystals are shown as red and blue to facilitate observation of the extent of interdigitation.

ligand length because longer ligands cannot be compressed by the same amount as shorter ones. The interaction energy increases because there are more interaction sites on the ligand chain as the ligand length increases. The extent of interdigitation is generally minimal: Only the outermost -CH_2 units of the ligands interdigitate due to the considerable steric hindrance, essentially regardless of ligand length (beyond about C8). The results for shorter ligand lengths (below 8 CH_2 units) deviate from this linearity. Short ligands interdigitate almost completely, so that the entire backbone of the ligand is involved in the inter-ligand interactions. Interdigitation increases as ligand length is reduced below C8. This largely linear increase in r_{min} with ligand length was not seen by Schapotschnikow *et al*. [11] in MD studies of sub-3nm capped nanocrystals. In their studies, the value of r_{min} showed variations about a mean value for different ligand lengths, leading them to suppose that the minimum of the potential of mean force is essentially independent of ligand length. This was not seen in our studies and we found that the longer the ligands, the farther out the potential minimum is in absolute distances. It is possible that, for very low grafting densities, or for small spherical NCs used by Schapotschnikow *et al*., the potential minimum is essentially independent of ligand length because of the inherent flexibility of the ligands and the possibility of adopting conformations that avoid excess interaction. The introduction of sharp facets on the NCs could also account for the difference in behavior between our observations and those of Schapotschnikow *et al*. since our NCs are not spherical.

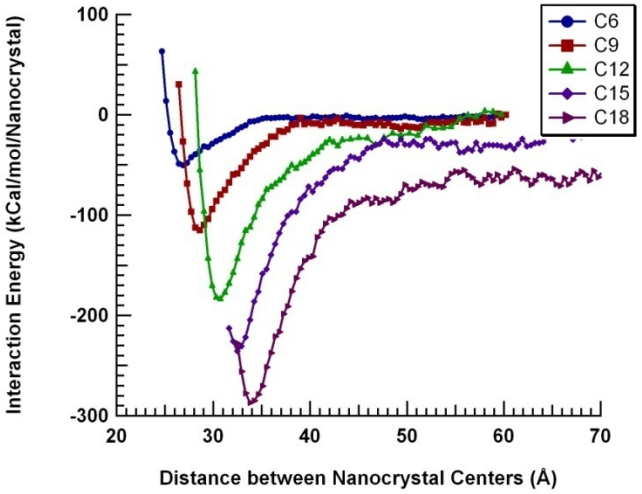

Figure 3.5: Graph of Interaction Energy Curve vs ligand length for a 3.1 nm Nanocrystal.

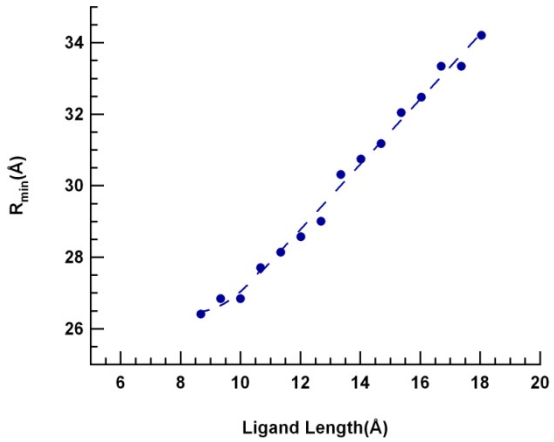

a)

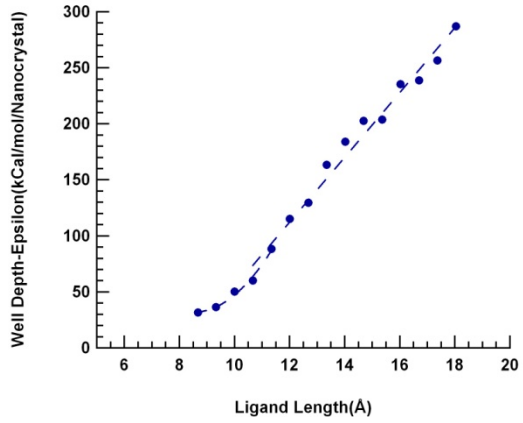

b)

Figure 3.6: Effect of ligand length on the values of the interaction energy, ε, and the separation distance, r_{min}, corresponding to the potential minimum (PMF). a) Separation distance and b) Interaction energy. Note the linearity of results for chains above about C8 in length.

3.5.2.2 Effect of Grafting Density of Ligands

We examined the effect of altering the grafting density of the ligands on the NC surface on the minimum interaction energy (ε) (i.e. when the interaction energy of the ligands reaches a minimum with reducing inter nanocrystal separation) and the corresponding inter-NC separation distance (r_{min}). The NC diameters were 3, 4 and 6 nm for this study. In this simulation, the ligands were grafted at random points on the NC surface. This lack of order of the ligand attachment on the nanocrystal core was adopted because experimentalists cannot readily observe the extent of any preference for ligand attachment on different facets. Hence the assumption of a random pattern is a reasonable starting point.

The ligand length was kept constant at 12 -CH_2 units, while the grafting density was varied from 1.5 ligands/nm^2 to 4.0 ligands/nm^2. This is essentially the entire accessible range up to a close-packed density. Images of the NCs with different ligand grafting densities are shown in Fig 3.7. Plots of these key parameters for the ligand-ligand interaction energy (ε and r_{min}) as a function of grafting density are shown in Figs. 3.8, 3.9. The value of r_{min} increases linearly with increasing grafting density. The "footprint" of the ligands on the NC facets increases in a linear fashion with grafting density. Thus, the number of ligands on a facet interacting with other ligands also increases linearly, preventing the NCs from approaching each other closely. The ligands adopt a more supine conformation on the facets at low density, whereas they stand more upright off the facets at high grafting density. The interdigitation of the ligands becomes more difficult with increasing grafting density since the steric hindrance from the ligands increases the repulsive interactions. This leads to an increase in r_{min} with grafting density.

The minimum interaction energy, on the other hand, displays a more interesting behavior: It is linear for grafting densities from 2.5 to 4.0 ligands/nm^2. Below 2.5 ligands/nm^2, the minimum interaction energy, ε, decreases. The linear behavior arises, as for the effect of ligand length seen in Fig. 3.6, because the addition of more ligands onto the facet means that more -CH_2 groups can interact, increasing the minimum interaction energy. For low grafting densities, ligand-ligand interactions on the NC facet become small, and ligand-core and core-core interactions become more important. Importantly, however, the dominant mechanism of ligand-ligand interactions at sufficiently low ligand densities (of up to around 2.5 ligands/nm^2) is no longer through interdigitation of the ligands. The lack of ligands allows some of them to adopt a more supine conformation with respect to the facet and hence the ligands on opposing NC facets interact with almost the entire backbone of the ligand chain. The ligands are sparse enough to allow a lot of compression of the ligand corona so that the minimum interaction energy (ε) deviates from the linear profile seen for larger grafting densities. This has implications for the stability of superlattices, since the stabilization is improved when the ligands interdigitate rather than when they are simply compressed. Thus, it is better if the grafting density of the ligands is reasonably large. On the other hand, very large grafting densities do not allow interdigitation at all which, once again, is detrimental to superlattice stability. These results suggest that some intermediate value for the density would lead to optimal interdigitation and packing.

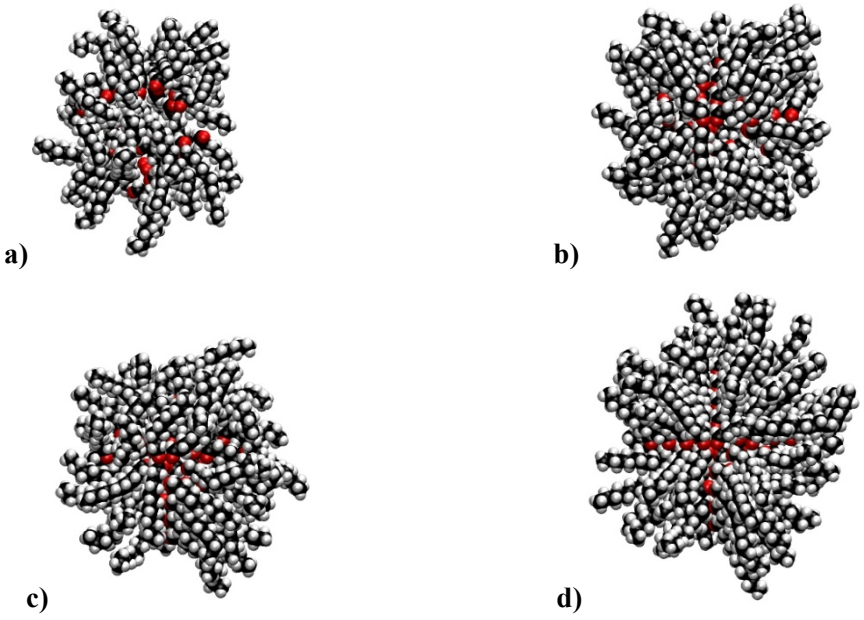

Figure 3.7: Snapshots of 3 nm NC with different ligand coverage densities. a) 2.5 ligands/nm^2, b) 3 ligands/nm^2, c) 3.5 ligands/nm^2 and d) 4 ligands/nm^2.

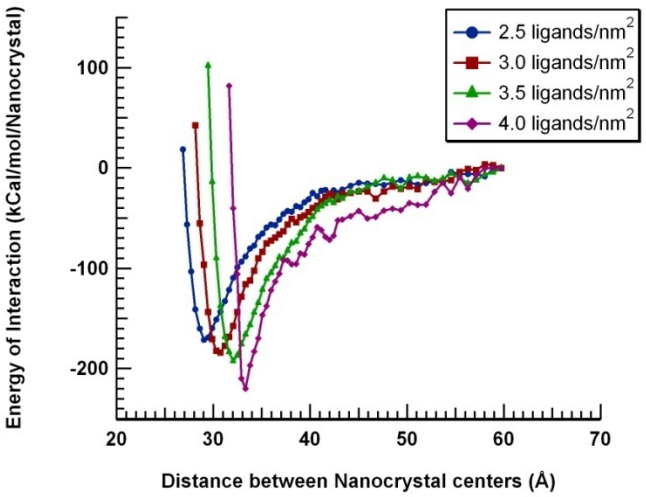

Figure 3.8: Graph of Interaction Energy Curve vs ligand capping density for a 3.1 nm Nanocrystal.

a)

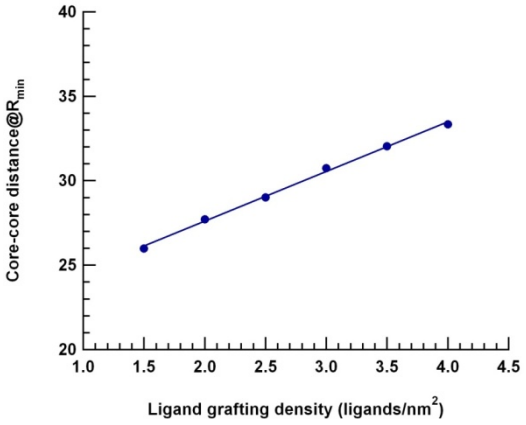

b)

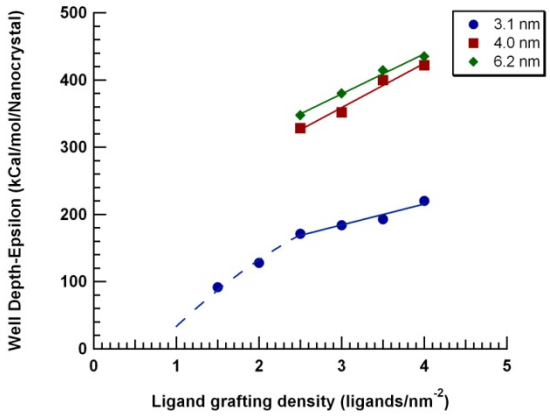

Figure 3.9. Effect of ligand grafting density on a) separation distance (for a 3.1 nm NC) and b) interaction energy at the potential minimum.

3.5.3 Potential of Mean force for a two-nanocrystal system

We used the PMF technique described in section 4 to evaluate the interaction between two isolated NCs as a function of the distance between them. The PMF was evaluated using the Steered Molecular Dynamics (SMD) feature of LAMMPS software package [54]. The final PMF was the average of 10 different simulation trajectories over the same pulling distance. The averaging ensures that unwanted oscillations and noise in the data are damped out. The nature of the PMFs of three different diameters of NCs was evaluated, as shown in Fig. 3.10. In order to calculate the PMF it is important for the NCs in these simulations not to be rotationally confined. Accordingly, the NCs were allowed to translate as well as rotate about their center of mass.

The PMFs show some very interesting features. For all three NC diameters, the PMF exhibits a minimum at a characteristic distance (r_{min}) and then the curve rises sharply as the NCs are brought closer than this optimum distance. But it may be observed that the curves for the NCs behave differently around the minimum: For the smallest NCs (3 nm diameter), the curve is rather broad around the minimum and shallower than the other curves. In fact, the curves get deeper and narrower with increasing NC size. In other words, the interactions become "harder." The change in the shape of the potential well is due to the different mechanism of interaction in the case of the small NCs as compared to the larger NCs. The two dominant mechanisms are inter-(chain) *backbone* interactions versus inter-(chain) *tip* interdigitation. As described in the previous section, the small NC has very little surface area of {111} facets and there are very few ligands on the facets. As a consequence, the ligands lie almost flat on the facets to maximize their interaction with the facets. When the two NCs are brought closer together, the ligands on the

respective NCs are able to interact with the full length/backbone of the ligand. As the interaction continues over the distance separating the facets of the two NCs, the ligands have the freedom to adopt different conformations to minimize the steric hindrance and maximize the interaction with ligands on the other NC. There is interplay between the interaction of the ligands and adoption of more favorable conformation of the ligands on the facets of the two NCs, creating the shallow broad potential energy minimum, which we believe is characteristic of largely supine ligands. This situation is depicted in Fig. 3.10. The repulsive part of the curve is not felt until the NC cores are quite close and at a point where the cores begin to interact as well. Thus, in the 3 nm-diameter NC case, both the ligands and the cores interact, though the cores are not close enough to contribute significantly to the total interaction. This is also the reason why the minimum in the PMF occurs at a much smaller distance of separation compared to the PMF curves of the larger NCs. For larger **(6 nm)** NCs, the ligand-ligand interaction mechanism is somewhat different. The facets on these NCs are larger and can accommodate more ligands. This means that ligands on a facet interact with themselves quite strongly and do not need to maximize their interaction with the underlying core. Thus, the ligands tend to "stand up" and away from the surface of the facets of the core. They are also somewhat restricted in their freedom to adopt all of the possible conformations because of steric hindrance from other ligands on the facets. The interaction between the ligands on adjacent NCs arises mainly from interactions of the top few CH_2 groups (the tips of the chains); the ligands are unable to "feel" the entire backbone of the ligand chain. The interplay described for 3 nm particles, *i.e.*, the interaction of ligands versus the adoption of more favorable conformations by the ligands, is more constrained for larger 6nm NCs since the ligands

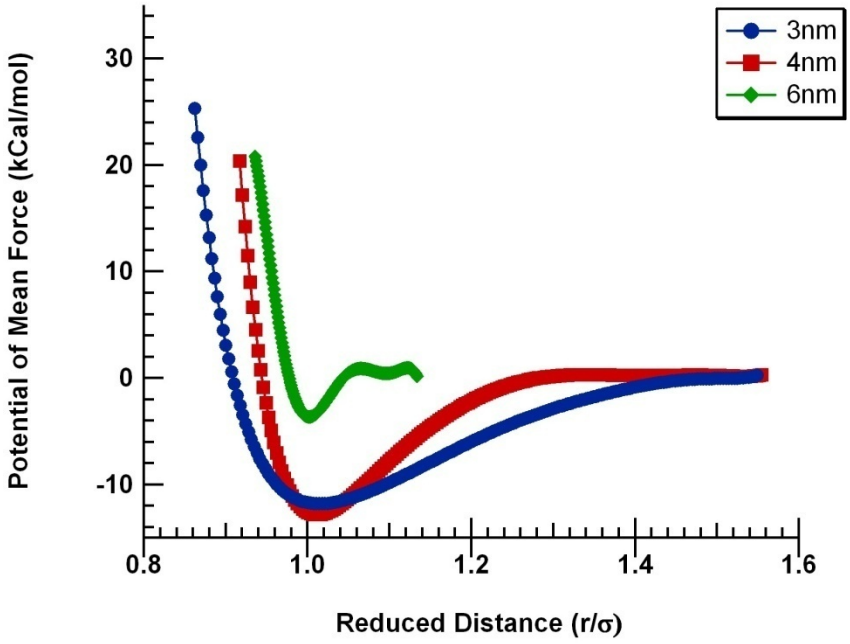

Figure 3.10: Potential of Mean Force of ligand-capped nanocrystals for different NC diameters. The C12 ligands are about 13 Å long; coverage is about 3.3 ligands/nm^2.

have very little conformational "space" to continually adapt to a more favorable conformation as the two NCs are brought closer together. The PMF thus becomes sharper; the repulsive part of the curve begins almost immediately after the minimum is reached and is a lot steeper. Ligands on adjacent NCs interdigitate to maximize their interactions and minimize entropic repulsion, a mechanism not seen in the case of the 3 nm NCs. This can be seen in Fig. 3.10 for the 6 nm-diameter particles. The 4 nm NC showed characteristics intermediate between those of smaller (3nm) and larger (6nm) NCs. The strength of the interaction also depends on the number of ligands on the facets and, since the larger NCs have a larger facet area, they consequently also have a larger number of ligands, which leads to a stronger interaction at the potential minimum. The minimum in the potential occurs at a larger value of r_{min} since the ligands start interacting strongly from a larger distance.

In larger arrays and superlattices of NCs, we shall show below that the ligands can interlock, providing mechanical stability to the superlattice. We believe that this is the reason for the greater ease of formation of stable NC superlattices with larger NCs than with, say, small 3 nm NCs.

3.6. Coarse-graining of ligands on the nanocrystal surface

The explicit all-atom model, used in all the preceding studies in this paper, provides detailed information about the nanocrystal interactions. Unfortunately, the number of interatomic interactions involved is very large, whether considering intermolecular or intramolecular terms. Thus, very quickly, it becomes infeasible to simulate larger systems of NCs.

One technique to overcome this limitation is the method of coarse-graining the representation of the ligands to a less atomically detailed description. A popular method of coarse-graining invokes the United Atom (UA) model, described in the Introduction to this paper. We examine two different UA models adopted from literature. The equations describing Jorgensen's UA model potential [19] are given below. The parameters of this model are given in Table 3.1.

$$E_{bond} = K(r - r_0)^2 \tag{11}$$

$$E_{angle} = K'(\theta - \theta_0)^2 \tag{12}$$

$$E_{torsion} = K_1(1 + \cos(\varphi)) + K_2(1 - \cos(2\varphi)) + K_3(1 + \cos(3\varphi)) \tag{13}$$

$$E_{vdwl} = 4\varepsilon\left[\left(\frac{\sigma}{r}\right)^{12} - \left(\frac{\sigma}{r}\right)^{6}\right] \tag{14}$$

Here, r is the bond distance between two bonded atoms, θ is the angle between three atoms and φ is the dihedral angle between four atoms. The subscript 0 refers to the equilibrium values of bond length and angle between the bonded atoms. K, K′, K_1, K_2 and K_3 are constants. Equation 14 is the intermolecular interaction represented by a Lennard-Jones (12-6) potential; σ, ε and r represent the diameter, well depth and distance between the two interacting atoms. Standard Lorentz-Berthelot mixing rules are used to define the cross-interaction between dissimilar interacting pairs of atoms [55]. The cut-off distance used for the van der Waals interactions is 10 Å. If the Jorgensen *et al.* UA model is used to describe our system of NCs, the final configuration of the ligands on an isolated nanocrystal after equilibration at T=300 K is shown in Fig. 3.11.

Bond	r_0 (Å)	K [kcal/(mol/Å^2)]	
CH_2-CH_2	1.54	260	
CH_2-CH_3	1.54	260	
Angle	θ_0 (˚)	K´ [kcal/(mol/deg^2)]	
CH_2-CH_2-CH_2	109.5	63	
CH_2-CH_2-CH_3	109.5	63	
Dihedral	K_1 (kcal/mol)	K_2 (kcal/mol)	K_3 (kcal/mol)
CH_2-CH_2-C_2-CH_2	1.412	-0.272	3.15
CH_2-CH_2-C_2-CH_3	1.412	-0.272	3.14
Non-bonded Interactions	σ (Å)	ε (kcal/mol)	
CH_2	3.90	0.12	
CH_3	3.90	0.175	

Table 3.1: Force Field Parameters for the Jorgensen United Atom Model [19].

For comparison, the same isolated nanocrystal, modeled using the explicit MM3 model is also shown. It can be seen clearly that ligands modeled with the Jorgensen UA model exhibiting "bundling" that is absent in the all-atom MM3 description. Ligands on each of the faces of the NC interact with each other very strongly and evince a preferential aggregation. Furthermore, the ligands showed very little dynamic motion at 300 K, and preferred to stay at the equilibrium position at 300 K, as shown in the figure. Bundling has also been observed by Landman [1] and Glotzer [56] using the Jorgensen model. In fact, Landman observed the bundling phenomenon even for isolated NCs (at 1K and from 250-300 K). Our experimental partners in the Hanrath group at Cornell have looked specifically for evidence of bundling through detailed analyses [57] and their conclusion, like the all-atom simulations presented here, is that there is insufficient experimental evidence to support the existence of bundling in these systems at room temperature.

Our results suggest that the parameters of the Jorgensen UA model may not estimate the melting temperature of the ligands very well for the system under consideration here. The bundling phenomenon may occur for very long polymeric chains in a very poor solvent. Such ligand morphologies have been observed by Lane *et al.* [16]. But, for the system at hand, the Jorgensen model was unable to duplicate the ligand conformations of the explicit MM3 model. Since the so-called "melting temperature" of the ligands may be exaggerated by the Jorgensen model, we heated the isolated nanocrystal by running NVT simulations at higher temperatures to equilibrate the system, followed by NVE runs at the same higher temperatures. We saw the first hints of "un-bundling" of the ligands at a temperature of around 600 K, well above the 300 K studies that are relevant for the study presented here (and at which experiments are conducted).

Our task then was thus to sort among several existing UA models that have been posited to pick one that would give similar ligand conformations as seen using the MM3 model which we believe to be representative of experiments. We started with Li *et al.*'s suggestion [25] that an increase in the σ parameter of the van der Waals interaction would solve the problem. Unfortunately, the bundling phenomenon persisted after equilibration as we varied σ over what we assumed to be a reasonable range (from 3.5 to 4.2 Å). Refitting the van der Waals parameters to match the interaction energy of the equivalent interactions in the explicit MM3 model for simulations of an isolated NC in vacuum at 300 K did not remove the bundling effect. This led us to believe that the problem lay in the *intra*molecular parameters, namely in the dihedral interactions. Further evidence implicating the overly strong dihedral interactions in the Jorgensen model is provided by observing that the OPLS-AA (an explicit all-atom Jorgensen model) shows the same sort of bundling as for the UA model. Thus, coarse-graining is not responsible for bundling, but the intramolecular interactions themselves. We therefore, used the UA model as defined by Paul *et al.* [26]. The equations describing their optimized UA potential are given below. Parameters for this model are given in Table 3.2.

$$E_{bond} = \frac{1}{2}k(r - r_0)^2 \tag{15}$$

$$E_{angle} = \frac{1}{2}k'(\cos(\theta) - \cos(\theta_0))^2 \tag{16}$$

$$E_{torsion} = \frac{1}{2}k_1(1 - \cos(\varphi)) + \frac{1}{2}k_2(1 - \cos(2\varphi)) + \frac{1}{2}k_3(1 - \cos(3\varphi)) \tag{17}$$

$$E_{vdwl} = 4\varepsilon\left[\left(\frac{\sigma}{r}\right)^{12} - \left(\frac{\sigma}{r}\right)^{6}\right] \tag{18}$$

Here, r is the bond distance between two bonded atoms, θ is the angle between three atoms and φ is the dihedral angle between four atoms. The subscript 0 refers to the

equilibrium values of bond length and angle between the bonded atoms. k, k′, k_1, k_2 and k_3 are constants. The last equation is the intermolecular interaction represented by a (12-6) Lennard-Jones potential; σ, ε and r represent atomic diameter, well depth and distance between the two interacting atoms. Standard Lorentz-Berthelot mixing rules are used to define the cross interaction between dissimilar interacting pairs of atoms [55]. The cut-off distance used for the van der Waals interactions is 10 Å.

The Paul *et al.* model, tested using the same conditions described above for an isolated NC at 300 K, did not show any ligand bundling. Paul-modeled ligands adopted more random configurations and showed appropriate dynamic motion upon equilibration at 300 K similar to the MM3 simulations. Images of the ligand conformations for the MM3 model, the Jorgensen model and the Paul *et al.* model are shown in Figure 3.11.

3.7. Conclusions

We have presented an explicit all-atom representation of nanocrystals, "capped" with alkyl chain ligands, of experimentally relevant sizes in vacuum. The studies included an isolated single NC, pairs of isolated NCs, and (presaging studies of superlattice arrays) unit cells of NC superlattices. The behavior of these ligand- capped NCs, determined by the explicit all-atom model, can serve as a reference standard for future coarse-graining of ligands using united atom models. We have shown that several different parameters that control the conformations adopted by the ligands can lead to the same mechanism of interaction between the NCs. For instance, the shape of the attractive "bowl" of the PMF depends on the size (and coupled shape) of the NCs: Ligands on very small (3 nm) NCs do not interdigitate; they tend to wrap around the core and then compress.

Bond	r_0 (Å)	k [kcal/(mol/Å^2)]	
CH_2-CH_2	1.53	634	
CH_2-CH_3	1.53	634	
Angle	θ_0 (rad)	k´ [kcal/(mol/deg^2)]	
CH_2-CH_2-CH_2	1.92	120	
CH_2-CH_2-CH_3	1.92	120	
Dihedral	k_1 (kcal/mol)	k_2 (kcal/mol)	k_3 (kcal/mol)
CH_2-CH_2-C_2-CH_2	1.6	-0.867	3.24
CH_2-CH_2-C_2-CH_3	1.6	-0.867	3.24
Non-bonded Interactions	σ (Å)	ε (kcal/mol)	
CH_2	4.009	0.09344	
CH_3	4.009	0.22644	

Table 3.2: Force Field parameters for the Paul *et al.* United Atom Model [26].

Ligands on larger NCs (6 nm) only interdigitate and then lock the NCs into place with very little compression. Ligands on intermediate-sized (4 nm) NCs exhibit some interdigitation and some ligand wrapping. A similar range of possible outcomes for the conformations adopted by dendrimers was observed in a paper by Li and Goddard [58]. They classified the conformation of ligands on the cores of their systems according to different hairstyles, ranging from smooth hairstyles (which they dubbed as "Valentino"), to asymmetric or "punk" hairstyles, to "Einstein" hair where the ligands stick out from the core. These classifications convey essentially the same picture as our wrapped/wrapped-interdigitated/interdigitated mechanisms for the 3, 4 and 6 nm diameter systems, respectively. These mechanistically driven results can also be obtained by varying the ligand density or the length of the ligands. Thus, by changing one or more parameters affecting the ligand conformations on the NC cores, we shed some light onto a path by which one could intelligently achieve the desired self-assembly of these NC systems. It also helps explain the inherent complexity of the behavior of real nanocrystal systems.

Coarse-graining is an excellent method of reducing computational complexity in order to save computational time. It provides the ability to model larger NC superlattices over longer time scales. All-atom modeling is essentially limited to systems not much bigger than the ones studied here.

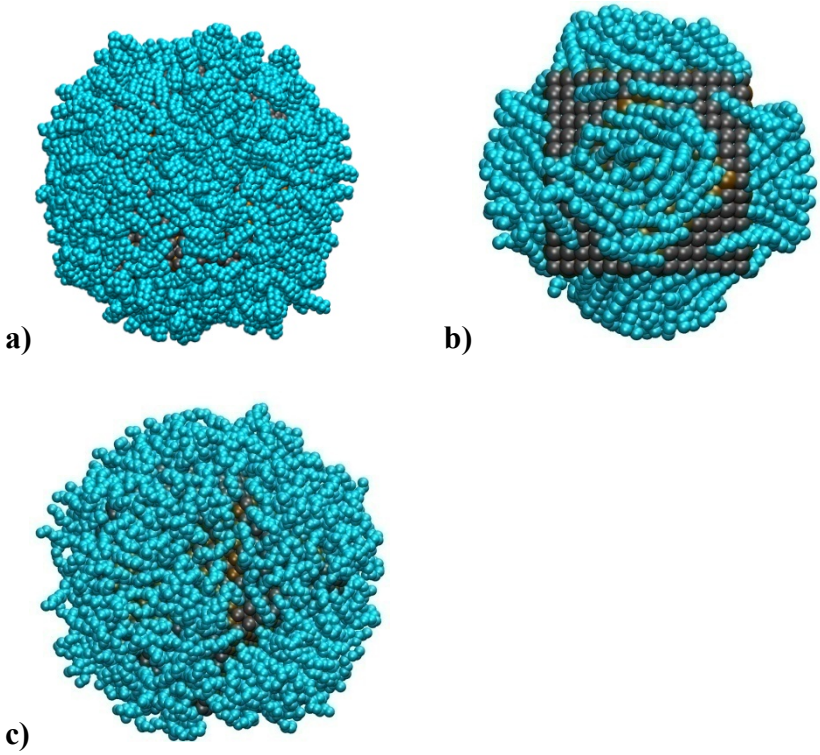

Figure 3.11: Comparison of snapshots from MD simulations using (left to right, top panel) the results of the (a) explicit all-atom MM3 model [36], with (b) United Atom (UA) models due to Jorgensen et al. [19] and (c) Paul et al. [26]. The C12 ligands are 13 Å long; ligand coverage is 3.3 ligands/nm^2.

We found that the specific *choice* of the united atom potential model is crucial for the prediction of properties of the NC system. We experimented with two different UA models selected from literature. The Jorgensen UA model did not adequately capture the dynamics of these NC systems as described by the explicit MM3 model. We also found that the model introduced bundled ligand conformations which were not predicted by the MM3 model. We believe that this may be due to different intermolecular van der Waals force parameters, but mostly because of the difference in stiffness introduced by dihedral interactions in the ligands. We found that the Paul *et al.* UA model mimics the trajectories of the explicit MM3 model sufficiently well. Since reproducing the flexibility of ligands and the conformations of the ligands described by the explicit model is crucial to the study of NC systems, this model may be more suitable to model large NC systems such as the one we have described. At the very least, one must be circumspect, while transitioning from explicit models to coarse grained models, in choosing one coarse grained model over another.

The obvious next steps are to move from small unit cell all-atom representations to superlattices and to explore the effect of having a solvent present. These simulations will be described in a subsequent paper.

REFERENCES

[1] E.V. Shevchenko, D.V. Talapin, N. A. Kotov, S. O'Brien, C. B. Murray, Nature (2006), 439, 55-59.

[2] A. E. Saunders and B. A. Korgel, ChemPhysChem (2005), 6, 61–65

[3] M. Grzelczak, J. Vermant, E. M. Furst and L. M. Liz-Marzán, ACS Nano (2010), 4, 3591-3605

[4] J. Y. Ku, D. M. Aruguete, A. P. Alivisatos and P.L. Geissler, J. Am. Chem. Soc. (2011) 133, 838-848.

[5] Y. Lin, A. Böker, J. He, K. Sill, H. Xiang, C. Abetz, X. Li, J. Wang, T. Emrick, S. Long, Q. Wang, A. Balazs and T. P. Russell, Nature (2005) 434, 55-59

[6] S.Shrestha, Progress in Photovoltaics: Research and Applications (2011), 19, 123-126.

[7] Z. Quan, L. Valentin-Bromberg, W. S. Loc and J. Fang, Chemistry-An Asian Journal (2011) 6, 1126-1136

[8] H. W. Hillhouse and M.C. Beard, Current Opinion in Colloid and Interface Science, 14, 245-259 (2009).

[9] J. H. Bang and P.V. Kamat, ACS Nano (2009), 3, 1467-1476

[10] W. D. Luedtke and U. Landman, J. Chem. Phys. (1996) 100, 13323-13329

[11] P. Schapotschnikow, R. Pool and T. J. H. Vlugt, Nano Lett. (2008) 8, 2930-2934.

[12] P. Schapotschnikow, M.A. van Huis, H.W. Zandbergen, D. Vanmaekelbergh and T. J. H. Vlugt, Nano Lett. (2010) 10, 3966-3971.

[13] P. Schapotschnikow and T. J. H. Vlugt, J. Phys. Chem. C (2010), 114, 2531-2537

[14] S.O. Nielsen, C.F. Lopez, G. Srinivas and M. L. Klein, J. Phys.: Condens. Matter (2004) 16, R481-512.

[15] A. Badia, L. Cuccia, L. Demers, F. Morin and R.B. Lennox, J. Am. Chem. Soc. (1997) 119, 2682-2692

[16] J. M. D. Lane and G. S. Grest, Phys. Rev. Lett., 104, 235501 (2010)

[17] A. Yang and C. Weng, J. Phys. Chem. C, 114, 8697-8709 (2010)

[18] A. Yang, C. Weng and T. Chen, J. Chem. Phys., 135, 034101 (2011)

[19] W. L. Jorgensen, J. D. Madura and C. J. Swenson, J. Am. Chem. Soc., 106, 6638-6646 (1984)

[20] S. Toxvaerd, J. Chem. Phys. (1990) 93, 4290-4295.

[21] J. I. Siepmann, S. Karaborni and B. Smit, Nature, 365, 330-332 (1993)

[22] M. G. Martin, J. I. Siepmann, J. Phys. Chem. B, 102 (14), pp 2569-2577 (1998)

[23] S. K. Nath, F. A. Escobedo and J. J. de Pablo, J. Chem.Phys., 108, 9905 (1998)

[24] S. K. Nath, B. J. Banaszak and J. J. de Pablo, J. Chem. Phys., 114, 3612-3616 (2001)

[25] C. Li, P. Choi and P. R. Sundararajan, Polymer (2010) 51, 2803-2808

[26] W. Paul, Do Y. Yoon and G.D. Smith, J. Chem. Phys. (1995) 103, 1702-1709

[27] H.L. Scott, Curr. Opin. Struct. Biol. (2002) 12, 495-502

[28] S.L. Mayo, B.D. Olafson and W. A. Goddard, J. Phys. Chem. (1990) 94, 8897-8909

[29] W.L. Jorgensen, D.S. Maxwell and J. Tirado-Rives, J. Am. Chem. Soc., 118 (45), (1996) 11225-11236

[30] N. P. Adhikari, X. H. Peng, A. Alizadeh, S. Ganti, S. K. Nayak and S. K. Kumar, Phys. Rev. Lett. (2004) 93, 188301-188305

[31] C. Schliehe, B. H. Juarez, M. Pelletier, S. Jander, D. Greshnykh, M. Nagel, A. Meyer, S. Foerster, A. Kornowski, C. Klinke and H. Weller, Science, 329, 550–553 (2010)

[32] M. A. Sliem, A. Chemseddine, U. Bloeck and R. A. Fischer, Cryst. Eng. Comm., 13, 483-488, (2011)

[33] Moreels, I.; Frintzinger, B.; Martins, J.C.; Hens Z. Surface chemistry of colloidal PbSe nanocrystals. J. Am. Chem. Soc. (2008) 130, 15081-15086

[34] G.Schaftenaar and J. Noordik, J. Comput.-Aided Mol. Design 14, 123 (2000).

[35] J. W. Ponder, Tinker - software tools for molecular design, http://dasher.wustl.edu/tinker/ (2010).

[36] N. Allinger, Y. Yuh, and J.-H. Lii, J. Am. Chem. Soc. 111, 8551 (1989).

[37] A. D. MacKerell, Jr., D. Bashford, M. Bellott, R. L. Dunbrack, Jr., J. D. Evanseck, M. J. Field, S. Fischer, J. Gao, H. Guo, S. Ha, D. Joseph-McCarthy, L.

Kuchnir, K. Kuczera, F. T. K. Lau, C. Mattos, S. Michnick, T. Ngo, D. T. Nguyen, B. Prodhom, W. E. Reiher, III, B. Roux, M. Schlenkrich, J. C. Smith, R. Stote, J. Straub, M. Watanabe, J. Wiorkiewicz-Kuczera, D. Yin, and M. Karplus, J. Phys. Chem. B, 102 (18), 3586-3616 (1998)

[38] K. H. Chen, J. H. Lii, G. A. Walker, Y. Xie, H. F. S. III, and N. L. Allinger, J. Phys. Chem. A, 110, 7202 (2006).

[39] K. H. Chen, G. A. Walker, and N. L. Allinger, Journal of Molecular Structure (Theochem) 490, 87 (1999).

[40] J. E. Goose and P. Clancy, J. Phys. Chem. C 111, 43 (2007).

[41] J. E. Goose, E. L. First, and P. Clancy, Phys. Rev. B 81, 205310 (2010).

[42] R. Cantrell and P. Clancy, Surface Science 602(22), 3499 (2008).

[43] A. P. Kaushik and P. Clancy, Surface Science 605(13-14), 1185-1196 (2011)

[44] J. Nocedal, Mathematics of Computation 35, 773 (1980).

[45] J. J. Choi, C. R. Bealing, K. Bian, K. J. Hughes, W. Zhang, D. M. Smilgies, R. G. Hennig, J. R. Engstrom and T. Hanrath, J. Am. Chem. Soc., 2011, 133 (9), pp 3131–3138.

[46] G. J. Martyna, D. J. Tobias and M. L. Klein, J. Chem. Phys., 101, 4177 (1994)

[47] M. Parrinello and A. Rahman, J. Appl. Phys., 52, 7182 (1981)

[48] W. Shinoda, M. Shiga and M. Mikami, Phys. Rev. B, 69, 134103 (2004)

[49] M. E. Tuckerman, J. Alejandre, R. Lopez-Rendon, A. L. Jochim and G. J. Martyna, J. Phys. A: Math. Gen., 39, 5629 (2006)

[50] G. Ciccotti, M. Ferrario, J. T. Hynesa and R. Kapral, Chem. Phys., 129, 241 (1989)

[51] E. Guardia, R. Rey and J. A. Padro, Chem. Phys., 155, 187-195 (1991)

[52] C. Jarzynski, Phys. Rev. Lett., 78, 2690-2693 (1997)

[53] C. Jarzynski, Phys. Rev. E, 56, 5018-5035 (1997)

[54] S. J. Plimpton, J. Comp. Phys., 117, 1-19 (1995) URL http://lammps.sandia.gov

[55] M. P. Allen and D. J. Tildesley, Computer Simulation of Liquids, Clarendon Press, Oxford (1987)

[56] P. Kr. Ghorai and S. C. Glotzer, J. Phys. Chem. C, 111, 15857-15862 (2007)

[57] Hanrath, T. Private communication (2011).

[58] Y. Li, S-T. Lin, W. A. Goddard III, J. Am. Chem. Soc., 126, 1872-1885 (2004)

CHAPTER 4

Solvent-Driven Symmetry of Self-Assembled Nanocrystal Superlattices

4.1 Introduction

Colloidal nanocrystals (NCs) characterized by controlled size and shape represent a class of materials with unique properties that are different from their bulk counterparts [1-6]. Nanocrystal assemblies have been explored for a variety of applications, including solar cells [1-5, 7-12], field effect transistors [13-15], light- emitting diodes [16, 17], photo-detectors [18] and chemical sensors [19]. Colloidal nanocrystals can be solution-processed and drop-cast onto suitable substrates which provides an inexpensive method of producing devices in comparison to using high temperature or vacuum processing [20, 21]. Nanocrystals formed from lead salts such as PbSe, PbTe, PbS, *etc.*, have received considerable attention in recent years [1-5], mainly due to their large Bohr exciton radius and narrow, yet size-tunable, band gaps [22]. Their ability to provide significant electronic coupling at close proximity [23] and to self-assemble into a variety of large two-dimensional (2D) and three-dimensional (3D) superlattices [20, 21, 24] make them ideally suited for use in photovoltaic devices and other optoelectronic applications [11, 12, 14, 15].

Although the property of self-assembly of nanocrystals to form stable arrays is an attractive way to make devices, precise control over the self-assembly process is still a challenging issue [24]. The nanocrystals are capped by organic ligands, which not only serve to passivate the surface of the nanocrystal cores, but also provide stability to the superlattice. Highly organized ligand-clad nanocrystal superlattices can be obtained from

colloidal solutions using solvent evaporation [25, 28], spin casting [26], or stabilization using a non-solvent [27]. Thus, understanding the precise nature of nanocrystal-nanocrystal interaction in the presence of a solvent will be critical in controlling nanocrystal self- assembly. The efficiency of nanocrystal-based devices, *e.g.,* in photovoltaic cells, depends on a number of materials' parameters including the nanocrystal size, shape, the inter-nanocrystal distance, *etc*., as well as the significant effect of processing conditions [28]. The final symmetry of the superlattice may also have a profound effect on the stability and the charge transfer capacity of the superlattice. Experimentally, the self-organization of nanocrystals in solution invariably begins once they are drop-cast onto a substrate. As the solvent evaporates from dispersion on the substrate, the nanocrystal volume fraction increases, eventually reaching the point where the nanocrystalline array is formed [24, 25, 28-30]. The nanocrystals are able to sample a large number of spatial configurations during the solvent evaporation process before they achieve their lowest energy structures.

The final superlattice symmetry may not necessarily correspond to the one with the lowest energy, but may be kinetically controlled. For example, Bian *et al.* showed that the preference of different superlattice symmetries depends on the rate of evaporation of the solvent [28]. Slow solvent evaporation [28-30] invariably leads to a choice of symmetry corresponding to the lowest energy state. Even after the lattice has been dried, there is evidence of residual solvent in the superlattice [29], which may be expected to influence the selected symmetry.

Korgel *et al.* 's experiments [30] showed that the preference of superlattice symmetry depends on the ratio of the ligand length to particle radius for *spherical* silver NCs.

Fitting a simple Lennard-Jones model to their experimental data determined an effective interaction potential that they used to determine the preference of superlattice symmetry. Since spherical particles were used, effects due to facets on the nanocrystal cores did not need to be taken into account. The explicit nature of the interactions of the solvent and the capping ligands is not captured in their simple model, nor was there any determination of the mechanisms that are responsible for the eventual preference of the superlattice symmetry. These aspects of the problem will be captured in this paper.

Despite the wealth of experimental studies of chalcogenide systems of quantum dots, the corresponding body of work on computational studies using molecular simulation techniques is more limited. This is not surprising given the computational resources needed to model a sizeable superlattice composed of experimentally relevantly sized nanocrystals. For instance, a 1 ns Molecular Dynamics simulation of a system of 54 nanocrystals (4 nm in diameter) immersed in an explicitly modeled solvent of, say, toluene, involves the simulation of around 250,000-300,000 atoms. In this review of the relevant computational work, note that we delineate between covalently bound ligands [31-36] and prior studies of surfaces coated with ligands that are *not* covalently bound to the nanoparticle surface and hence have an extra degree of freedom to form self-assembled patterns on nanoscale surfaces [39].

One of the first atomistically explicit simulation studies of nanocrystals was made by Landman *et al.* [31] who studied gold nanocrystals coated with densely packed alkane thiol ligands. They predicted that the formation of nanocrystal superlattices of various preferred symmetries depended on the temperature of the system, and the length and grafting density of the capping ligands, *etc.* However, the nanocrystals modeled were

very small (less than 3 nm in diameter) and did not include consideration of a solvent, either explicitly or implicitly. More recent studies by Schapotschnikow *et al.* elucidated the importance of two-body and three-body interactions of alkanethiol ligand-capped gold nanocrystals [32, 33]. They showed that ligand length plays an important role in the propensity of more than two nanocrystals to form highly stable 3D superlattices, monolayers or even nanowires.

Since then, there have been several papers analyzing the interactions of nanocrystals with both implicitly and explicitly modeled solvents. Rabani *et al.* [34] used coarse-grained Lennard-Jones spheres as nanocrystals in the presence of implicit solvents to study how the nature of interaction between the nanocrystals depends on the quality of the solvent. They showed that the interaction can be "tuned" from attractive to repulsive with increasing solvent density. Y. Qin *et al.* [35] studied the solvation forces between two nanocrystals modeled in an implicit Lennard-Jones liquid. They showed that the nature of the interaction depends on the interplay between solvent-ordering and surface structure to change the interaction from net attractive to repulsive. They also showed that nanocrystal reorientation can occur due to local solvation forces leading to directed alignment of nanocrystals in solution, which plays an important role in nanocrystal self-assembly. Though the general *trend* of interaction strengths can be obtained from the use of implicit solvents, the precise interaction of solvent molecules with the ligand corona cannot be gained from this method. Lane *et al.* [36] measured the hydrodynamic drag on silica nanocrystals in the presence of explicitly modeled water or decane as the solvent. They observed that the long-range interaction forces were dominated by hydrodynamic drag and short-range interactions by close packing of ligand chains. The overall interaction

was purely repulsive. This is very different from the simulations done in vacuum where both attractive and repulsive regimes are observed, once again highlighting the need to model the solvent explicitly. Yang *et al.* [37, 38] observed the behavior of water molecules close to the surface of gold nanocrystals capped with both polar and non-polar alkane-thiol ligands. They saw that the residence time of the solvent as well as the strength of the hydrogen-bonding depended on the type of functional group present on the ligand. The ligands, therefore, dictate the type of solvation shell formed by the solvent molecules around the ligand corona. This changes the interaction strength between the nanocrystals in solution. Although these simulation studies were performed to study the explicit interaction of solvent with nanocrystals [34-38], they dealt with only one, or at most a few, nanocrystals. The question of leveraging knowledge of these detailed microscopic interaction studies to examine the formation and stability of large macroscopic superlattices and our ability to control the self-assembly process remains to be answered. To the best of our knowledge, no large-scale simulations have been performed of 3D nanocrystal superlattices with explicitly modeled solvents.

In this paper, we present a detailed study of the interaction of nanocrystals in 3D superlattices in the presence of explicitly modeled solvent to determine the stability and preference of superlattice symmetry as a function of the ratio of ligand length to nanocrystal diameter. We have chosen to model two different commonly used solvents – hexane and toluene. The nanocrystals are modeled as 4 nm cube-octahedra composed of PbSe, capped with ligands varying in length from 9- to 18- carbons long. This varies the ratio of the ligand length to NC radius, which relates back to Korgel's earlier studies [30]. The key point addressed in this study is to determine the different mechanisms involved

in the final choice of superlattice symmetry. We show the importance of using an explicitly modeled solvent since many of the results cannot be observed for studies carried out in vacuum or in implicitly modeled solvent. We also find that the choice of the solvent is an important factor affecting the symmetry.

4.2 Configuration of the system

Our interest in this study lies in representing the properties of lead chalcogenide nanocrystalline arrays of a fixed diameter, passivated by long-chain organic ligands of different lengths. The equilibrium structure for PbSe NCs consists of two interpenetrating FCC lattices made of Pb and Se in the rock salt (NaCl) structure. The lattice constant of a PbSe nanocrystal is 6.12 Å. We confirmed Luedtke and Landman's result that ligands dominate nanocrystal-nanocrystal interactions [31], and as a means to decouple ligand-ligand interactions from nanocrystal interactions, we mainly focus this study on ligand-ligand interactions, although the van der Waals' interactions for the cores are also considered.

In the experimental set-up, nanocrystals are grown in solution containing organic ligands as precursors. The ligands passivate the nanocrystal surface as the nanocrystal grows in solution. The size and shape of the nanocrystal is governed by the temperature of the solution and by the concentration of the precursors. Nanocrystals with diameters ranging from 4-7 nm have more or less sharply defined {100} and {111} facets. There is some evidence that there may also be {110} surfaces around the corners and edges [40]. Very large nanocrystals (10 nm or larger) are almost cubic [41]**.** In this study, we have assumed that nanocrystals with diameters of around 4 nm have a cube-octahedral shape with both {100} and {111} facets, as is experimentally predicted; see Fig. 4.1a. The

{100} facets are made of alternating Pb and Se atoms, whereas the {111} facets are Pb-terminated. This shape was chosen because there is experimental evidence that the oleic acid ligands typically used to passivate the nanocrystal surface have a greater preference for Pb atoms, thereby promoting the formation of Pb-terminated {111} facets [42]. The PbSe core is represented by surface atoms alone, that is, the core is a hollow shell and is treated as a rigid body.

The organic ligands chosen for this study consisted of aliphatic chains composed of varying numbers of carbon atoms. The ligands were made up of "beads" of CH_2 groups, represented using a united atom model, as described in the next section. Ligands with a chain composed of 9 CH_2 groups will be referred to as a "C9" ligand, one with 18 CH_2 groups as a "C18" ligand and so on. Four different "capping" ligands were used – C9, C12, C18 and C24. The parameters for all the interactions between the ligands are described in the next section. The ligand molecules were subjected to an energy minimization of the initial guess structure using a standard minimization algorithm - the conjugate gradient minimization algorithm within the LAMMPS software package [43]. The ligands used in experiments are generally acids, often oleic acid, or thiols. The head groups of the ligands are covalently bonded to the Pb atoms of the nanocrystals. We have represented the attachment of the head group by a single C-Pb bond. The ligands were grafted onto the surface of the NC at a predetermined density [44]. We have performed simulations where ligands were grafted with the entire carboxylic acid head group fixed, finding no significant differences in the final morphology of the ligands compared to the case if a simpler C-Pb bond was used. Hence, all the simulations reported in this study used the C-Pb bond to attach the ligand to the Pb atoms on the surface; see Fig. 4.1b.

The grafting density of the ligands plays an important role in the interaction of the nanocrystals. The ligands were grafted onto every *other* Pb atom on the surface, *i.e.,* there is a free Pb atom between every two Pb atoms that are linked to a ligand. This choice of ligand grafting density and location was made from the approximate footprint of ligands determined in accordance with *ab initio* studies of preferential ligand attachment sites [44]. This leads to a greater density of ligands on the {111} surfaces than the {100} surfaces because of the presence of Se atoms in-between Pb atoms on the {100} surfaces. The solvents chosen in this study, hexane and toluene, are two common solvents used in experimental studies of NC superlattices. Their comparison offers a contrast between the aliphatic hexane that is similar to the ligands, and aromatic toluene whose structure can be expected to be dissimilar to the ligands. Both solvents were also represented by the "united atom" model described in the next section and shown in Fig. 4.1c and 4.1d.

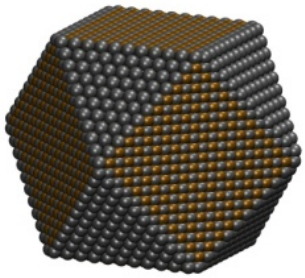

a)

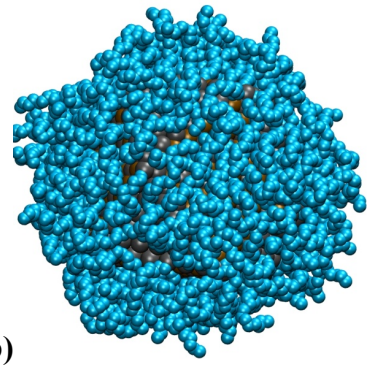

b)

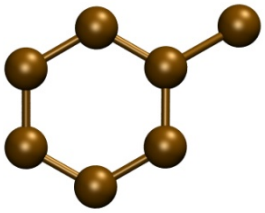

c)

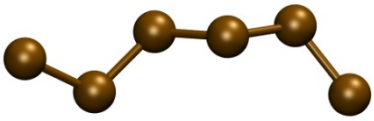

d)

Figure 4.1: Representation of the components of the system: a) Bare 4 nm diameter NC core, b) NC core covered by C12 capping ligands with a coverage of 3.0 ligands/nm^2, c) and d) United Atom representations of the solvent molecules, toluene (c) and hexane (d).

4.3. Intermolecular Potential Model

The choice of intermolecular potential model is a critical part of any molecular simulation. The inter- and intra- molecular potential models and associated parameters determine the trajectory of the system and hence the morphology and conformations of the molecules in the simulation. All-atom explicit models are accurate, but computationally expensive. In practice, simulations using all-atom models are limited to a few thousand atoms. In order to simulate large superlattices of nanocrystals containing hundreds of thousands to atoms, it is necessary to coarse-grain the system. One method of appropriately coarse-graining the system is to treat groups of CH_2 units in the ligands or the solvent as a 'united atom' (UA). As we have described in an earlier paper, the manner in which the coarse-graining is performed can have a profound effect on the structural conformations adopted by the system [45]. Based on our previous studies, we choose to use the model due to Paul *et al.* [46], which gives accurate trajectories and conformations compared to an all-atom explicit model.

Equations describing the Paul *et al.*-optimized UA potential [46] are given in the supplemental information. Parameters for this model are given in Table 4.1. Toluene molecules were modeled using the TraPPE UA model parameters as defined by Siepmann *et al.* [47]. The conjugated surface of the phenyl ring is more or less flat and rigid. In order to achieve this, the bond and angle parameters of the beads forming the phenyl ring were fixed to be very large. The parameters of the interactions are given in Table 4.2. The van der Waals' parameters for self-interaction of Pb and Se atoms are given in Table 4.3 taken from Vlugt *et al.* without modification [48].

Paul *et al.* UA model:

$$E_{bond} = \frac{1}{2}k(r - r_0)^2 \quad (1)$$

$$E_{angle} = \frac{1}{2}k'(\cos(\theta) - \cos(\theta_0))^2 \quad (2)$$

$$E_{torsion} = \frac{1}{2}k_1(1 - \cos(\varphi)) + \frac{1}{2}k_2(1 - \cos(2\varphi)) + \frac{1}{2}k_3(1 - \cos(3\varphi)) \quad (3)$$

$$E_{vdwl} = 4\varepsilon\left[\left(\frac{\sigma}{r}\right)^{12} - \left(\frac{\sigma}{r}\right)^{6}\right] \quad (4)$$

Here, r is the bond distance between two bonded atoms, θ is the angle between three atoms and φ is the dihedral angle between the planes containing four atoms. The subscript 0 refers to the equilibrium values of bond length and angle between the bonded atoms. k, k′, k_1, k_2 and k_3 are constants. The last equation is the intermolecular interaction represented by a (12-6) Lennard-Jones potential; σ, ε and r represent atomic diameter, well depth and distance between the two interacting atoms. Standard Lorentz-Berthelot mixing rules are used to define the cross interaction between dissimilar interacting pairs of atoms [4]. The cut-off distance used for the van der Waals interactions is 10 Å.

Bond	r_0 (Å)	k [kcal/(mol/Å^2)]	
CH_2-CH_2	1.53	634	
CH_2-CH_3	1.53	634	
Angle	θ_0 (rad)	k′ [kcal/(mol/deg^2)]	
CH_2-CH_2-CH_2	1.92	120	
CH_2-CH_2-CH_3	1.92	120	
Dihedral	k_1 (kcal/mol)	k_2 (kcal/mol)	k_3 (kcal/mol)
CH_2-CH_2-C_2-CH_2	1.6	-0.867	3.24
CH_2-CH_2-C_2-CH_3	1.6	-0.867	3.24
Non-bonded Interactions	σ (Å)	ε (kcal/mol)	
CH_2	4.009	0.09344	
CH_3	4.009	0.22644	

Table 4.1: Force Field parameters for the Paul *et al.* United Atom Model [46].

TraPPE UA model:

$$E_{bond} = \frac{1}{2}k(r - r_0)^2 \quad (5)$$

$$E_{angle} = \frac{1}{2}k'(\theta - \theta_0)^2 \quad (6)$$

$$E_{torsion} = k_1(1 - \cos(2\varphi + \pi)) \quad (7)$$

$$E_{vdwl} = 4\varepsilon\left[\left(\frac{\sigma}{r}\right)^{12} - \left(\frac{\sigma}{r}\right)^{6}\right] \quad (8)$$

Here, r is the bond distance between two bonded atoms, θ is the angle between three atoms and φ is the dihedral angle between the planes containing four atoms. The subscript 0 refers to the equilibrium values of bond length and angle between the bonded atoms. k, k′ and k_1 are constants. The last equation is the intermolecular interaction represented by a (12-6) Lennard-Jones potential; σ, ε and r represent atomic diameter, well depth and distance between the two interacting atoms. Standard Lorentz-Berthelot mixing rules are used to define the cross interaction between dissimilar interacting pairs of atoms. The cut-off distance used for the van der Waals interactions is 10 Å.

Bond	r_0 (Å)	k [kcal/(mol/Å^2)]
CH_x-CH_y	1.54	rigid
CH_x(aro)-CH_y(aro)	1.40	rigid
Angle	θ_0 (deg)	k´ [kcal/(mol/deg^2)]
CH_x(aro)-CH_y(aro)-CH_z	120	rigid
CH_x(aro)-CH_y(aro)-CH_z(aro)	120	rigid
Dihedral	k_1 (kcal/mol)	
CH_x-CH_2-C(aro)-CH_x(aro)	0.26	
Non-bonded Interactions	σ (Å)	ε (kcal/mol)
CH(aro)	3.695	0.10032
R-C(aro)	3.88	0.04171

Table 4.2: Force Field parameters for toluene from the TraPPE-UA force field by Siepmann *et al.* [47].

Non-bonded Interactions	σ (Å)	ε (kcal/mol)
Pb	3.29	0.0596
Se	4.36	0.0899

Table 4.3: Non-bonded interaction parameters for Pb and Se from Vlugt *et al.* [48].

The van der Waals' interaction parameters for the core-core, core-ligand and core solvent interactions were taken from the Lennard-Jones potential as described by Vlugt *et al.* [48]. The equation for the interaction is the same as equation (8) given in Table 4.2. The appropriate parameters of Pb and Se were used and standard Lorentz-Berthelot mixing rules were used to define the cross interaction between dissimilar interacting pairs of entities.

4.4. Simulation Methodology

All simulations in this study were performed using the LAMMPS software package [43]. The simulations were carried out in parallel on 8-16 cores of Intel Xeon processors. The first system we studied consisted of two nanocrystals in vacuum to establish a baseline for comparison to the interaction between nanocrystals in the presence of solvent. The system was thermalized at 300 K using a Nosé-Hoover thermostat [49-52] in the canonical (NVT) ensemble for a period of 2 ns using a time step of 2 fs in order to suppress significant fluctuations in temperature and energy and equilibrate the conformations adopted by the ligands. The simulation box used periodic boundary conditions in all three Cartesian directions, with the box size large enough to avoid interaction of the nanocrystals with its images across the periodic boundaries. The center of mass of the cores of the nanocrystals were held fixed during this time to prevent nanocrystal drift, but the nanocrystals were able to rotate freely about their centers of mass.

The next simulations were performed in the presence of solvent – hexane and toluene- to observe the influence of solvent on the interaction between the nanocrystals. A 3D superlattice of nanocrystals consisting of 2x2x2 unit cells was created with the

nanocrystals placed at lattice positions corresponding to either a BCC or FCC lattice symmetry. These systems contained in the range of 250,000-500,000 atoms. The simulation box was large enough to accommodate the nanocrystals and the solvent. The box was then placed under isobaric-isothermal (NPT) ensemble conditions at a temperature of 300 K and a pressure of 1 atm using a Nosé-Hoover thermostat and barostat. The amount of solvent in the simulation box was enough to prevent the nanocrystals from interacting with each other or their periodic images. These equilibration runs were conducted for a period of 2 ns until any large fluctuations in energy of the system were absent. These equilibration runs provided the starting point for the next set of simulations. In order to study the interaction between two NCs in solvent, we calculated the Potential of Mean Force (PMF). The mean force, F_{mean}, for two NCs separated by a distance r is defined as: [53, 54]

$$F_{mean}(r) = \frac{1}{2}\langle(\overrightarrow{F_2} - \overrightarrow{F_1}).\vec{r}\rangle \quad (1)$$

where < > denotes an ensemble average of configurations taken when the system is in equilibrium at a temperature T and $\overrightarrow{F_1}$ and $\overrightarrow{F_2}$ are the total forces acting on NC_1 and NC_2, respectively, and *r* is the vector connecting the centers of mass of the two NCs. The PMF can be obtained from the mean force as:

$$\varphi_{MF}(r) = \int_r^\infty F_{mean}(s)ds \quad (2)$$

A convenient way of evaluating the PMF is to attach a fictitious spring with a known spring constant between the nanocrystals under consideration and then move them relative to one another at a constant velocity. The force of interaction between the NCs is recorded at different points along the path of motion and the force is integrated over the distance between the NCs.

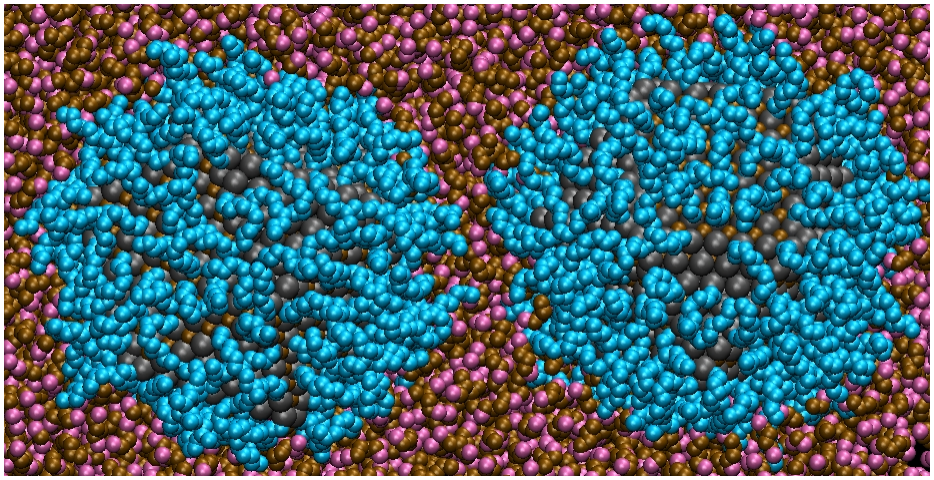

Figure 4.2: Snapshot showing two NCs interacting in the presence of hexane. The pink molecules are hexane solvent molecules. Light blue molecules represent the capping ligands on the grey/ochre NC cores (grey-Pb and ochre-Se). The NCs are being drawn together using steered molecular dynamics.

The integrated force gives the PMF between the NCs. This technique, Steered Molecular Dynamics (SMD), exploits Jarzynski's equality that relates equilibrium free energy difference to irreversible work in a non-equilibrium system [55, 56]. The two nanocrystals are initially separated to a distance at which there is no interaction between them. The cores have the ability to translate as well as rotate about their center of mass as a rigid body. The space not occupied by the nanocrystals was either empty (for the vacuum study) or filled with solvent. The motion of nanocrystal cores was followed using a constant-energy, NVE, microcanonical ensemble with rigid body dynamics. The ligands and solvent were maintained under "equilibrium" conditions at 300 K; their motion was followed using a constant-temperature, NVT, canonical ensemble. In this way, the entire system (nanocrystal core plus ligands), was maintained at thermal equilibrium over the entire course of displacement. A snapshot of the simulation can be seen in Fig. 4.2. The force of interaction between the two nanocrystals was recorded as a function of time (data sampled every 2 ps) and the PMF was evaluated as the sum of the forces over the entire displacement of the nanocrystals. The PMF was computed by averaging multiple trajectories over the same pulling path/reaction coordinate. For the simulations performed in vacuum, NVT and NVE ensembles gave virtually identical results. The results of this study are presented in Section 5. Steered Molecular Dynamics is a useful technique to evaluate the PMF between 2 interacting NCs but in order to evaluate the free energy change for an NC superlattice between an initial state when the NCs are non-interacting to a final state at equilibrium, we need to employ a different technique.

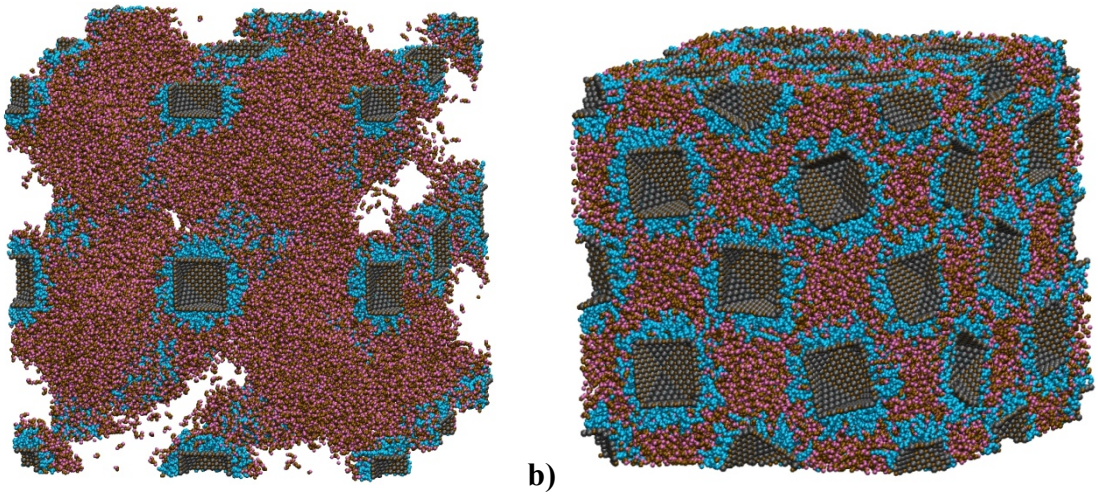

a) **b)**

Figure 4.3: a) Initial configuration of the simulation box with NC restricted to lattice positions and void space filled by solvent (hexane) molecules, b) Final equilibrated configuration of the simulation box in the NPT ensemble. Color key as in Figure 4.2.

For this study, we evaluated the free energy changes using the technique of thermodynamic perturbation based on the equations given by Zwanzig [57]. This technique evaluates the free energy change between two states that are separated by a very small change in energy, typically much lesser than k_BT. In this method, a series of simulations are set up with the NCs at lattice sites of an FCC or BCC lattice. The initial state ensures that the NCs are not interacting with each other. A series of simulations i=1 to N are set up with the lattice constant of the superlattice diminishing such that the NCs are closer to each other in each successive simulation. The free energy change between any two states i and i+1 is given by:

$$\Delta G_i = -k_B T ln\langle \exp(-\beta \Delta U_i)\rangle_i \quad (3)$$

where ΔG_i is the free energy change going from state i to i+1, k_B is the Boltzmann constant, T is the temperature of the system, β is $1/k_BT$ and $\Delta U_i = U_{i+1} - U_i$ is the change in potential energy going from state i to i+1. The angle brackets denote an ensemble average taken for configuration i of the system of nanocrystals. The technique works accurately if the change in energy between the two states is less than k_BT. So, the total free energy change between the initial and final states can be evaluated as the summation of all transitions between the sub-states.

$$\Delta G_{fcc/bcc} = G_{initial} - G_{final} = \sum_{i=1}^{i=N-1} \Delta G_i \quad (4)$$

The simulations were set up with the same initial state for both BCC and FCC lattices with no interaction between the NCs. The total free energy change for each superlattice symmetry is evaluated using equation 4. Thus, the free energy change for a transition from BCC symmetry to FCC symmetry can be evaluated as

$$\Delta G_{fcc-bcc} = G_{fcc} - G_{bcc} \quad (5)$$

In order to achieve the final state of the BCC or FCC lattice from the initial state, the simulation box was set up as described before with the system at equilibrium and with enough solvent in the void spaces of the lattices, see Fig. 4.3, to ensure that the NCs do not interact with each other. A very small number of solvent molecules (~6) were removed from the system corresponding to the steps of the free energy evaluation described above and the system was re-equilibrated. The re-equilibrated system was run for 20 ps until no significant fluctuations in the system energy were observed. This procedure was repeated, with removal of solvent molecules at each step, until the final state was achieved. The system energy was recorded at each step of solvent removal. The entire process was run over 10-12 ns of simulation time. The same simulation was performed for both BCC and FCC superlattices of nanocrystals for each ligand length considered.

The choice of the final state is an important factor in determining when the simulation procedure is to be stopped. For simulations without solvent, the choice is simple – the simulation is stopped when the system nanocrystals can no longer be compressed in the lattice. The end of the simulation is indicated by the achievement of equilibrium by the interacting nanocrystals in the superlattice. In the presence of solvent, however, the amount of residual solvent in the superlattice determines the final state of the system. Korgel *et al.* [29], suggest that there is some void space in the "dry" superlattice that cannot be taken into account by considering just the ligands and NC cores. This void space must, they conjectured, be filled by some residual solvent in the lattice. We obtained the experimentally calculated lattice constants of the "dry" superlattices for both hexane- and toluene- processed NC superlattices [28].

To obtain a comparative computational value, we first estimated the mean diameter of the nanocrystals after the initial equilibration runs of the system were completed. The mean diameter was averaged for a further 1 ns till the diameter of the nanocrystals remained more or less constant with time. We then estimated the amount of void space that should exist in the final superlattice of the simulations based on the nearest neighbor distances obtained from experimentally calculated lattice constants. From this, the amount of residual solvent was determined and used to determine the final state of the simulation. The simulation was terminated when this state was achieved. As shown in Fig. 4.4., the amount of void space in the presence of hexane was found to be more than that in the presence of toluene. The results of the study are presented in the next section.

4.5. Results and Discussion

The interaction of the solvent molecules with the ligand corona is a very important factor to be considered in the solvent-mediated interaction of nanocrystals. Hexane and toluene molecules are structurally distinct and might therefore, be expected to interact differently with the ligand corona. In order to find out how much solvent actually penetrated the ligand corona, we plotted the number of solvent molecules as a function of the radial distance from the center of the NC core. The results are shown in Fig. 4.5. The first observation to note is that the solvent molecules, both hexane and toluene, penetrate almost all the way to the surface of the nanocrystal core. The amount of penetration will depend on the grafting density of the ligand corona on the nanocrystal core. For very high grafting densities (> 4.5 ligands/nm^2) one would not expect much penetration, but for the grafting densities used in this study (around 3.0 ligands/nm^2), the solvent molecules reach the surface of the core. This implies that the solvent molecules are able to fill the space

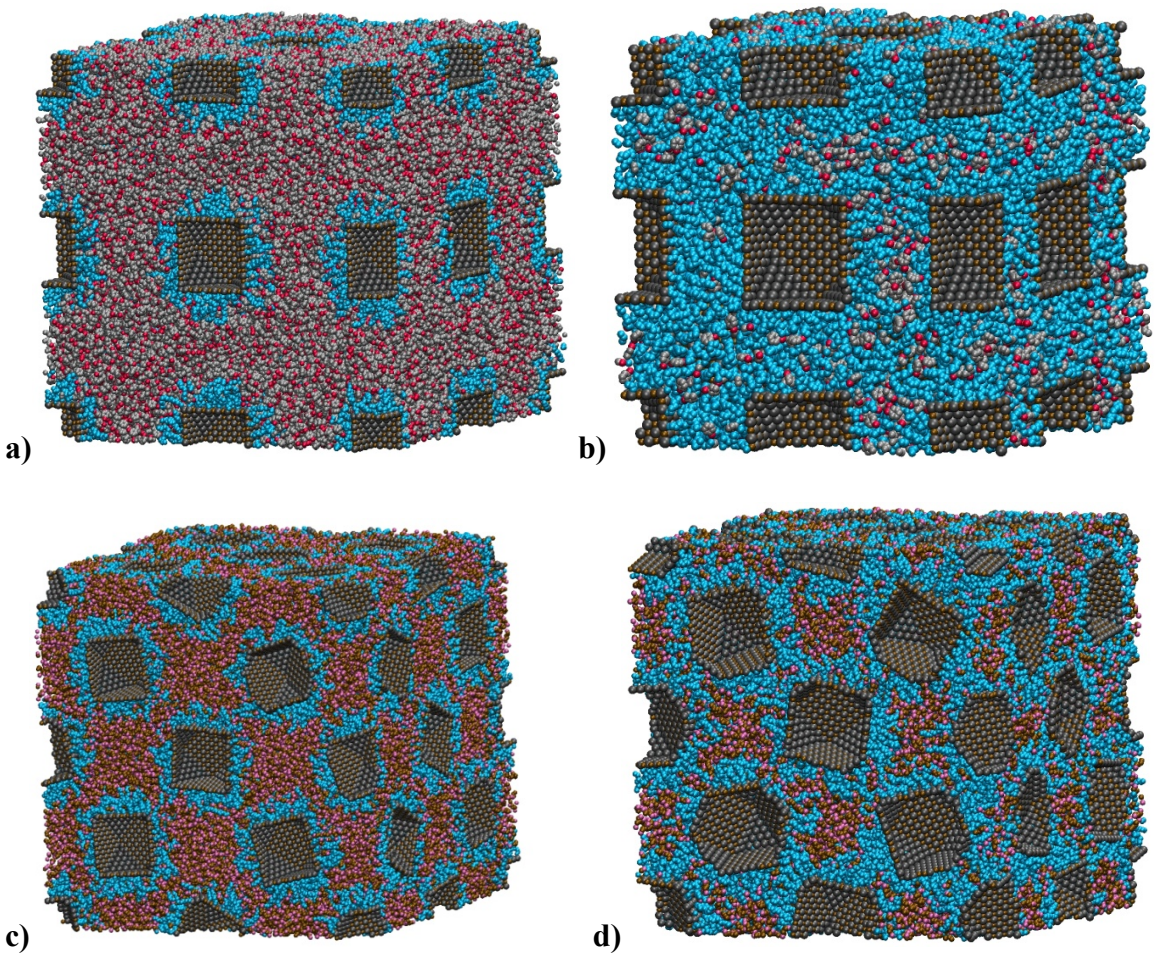

Figure 4.4: a) Initial and final equilibrated lattices with toluene (a and b, respectively) and with hexane (c and d, respectively). Color key as in Fig. 4.2. In a and c, the NC are separated sufficiently to be non- interacting. In b and d, some residual solvent in the lattice can be seen. It can also be noticed that the amount of residual hexane is greater than toluene.

between the ligand molecules, thereby separating or "swelling" the ligand corona with the net effect of making the nanocrystal (core and corona) more spherical in shape. Thus, at large distances, these nanocrystals should behave like interacting spheres.

Another interesting feature in Fig. 4.5 is that there are more toluene molecules than hexane for a given radial distance from the center. This can be explained from the shape of the solvent molecule: Hexane has a zigzag conformation as seen in Fig. 4.1d, similar to the ligand itself. This could introduce steric hindrance when the hexane molecule attempts to penetrate the ligand corona. The toluene molecule, on the other hand, is flat and more or less rigid as seen in Fig. 4.1c. This enables it to cleave the ligand corona more easily than hexane. The π-π interaction between the toluene rings is stronger than the ligand toluene interaction and, consequently, the toluene molecules have a propensity to stack next to each other to maximize this interaction. Thus, more toluene molecules can be accommodated within the ligand corona as compared to hexane.

We computed the PMF between two NCs in vacuum and in both hexane and toluene. Each PMF curve computed has been averaged over 10 different simulations over the same pulling path. As shown in Fig. 4.6, simulations performed in vacuum show an attractive regime as the nanocrystals approach, until the PMF reaches a minimum at a distance denoted as r_{min}. The PMF rises sharply as the nanocrystals are forced closer than this minimum distance. At some point, the ligands on opposing nanocrystals interpenetrate and cannot be pushed much closer. The severe steric hindrance is responsible for the steep repulsive rise in the PMF below r_{min}. The minimum in the PMF represents the ideal distance that the nanocrystals would prefer to reside in the absence of solvent.

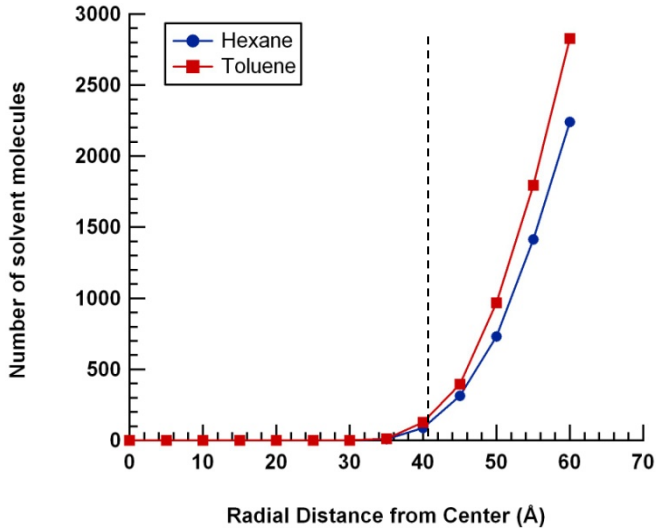

Figure 4.5: Number of solvent molecules as a function of radial distance from the center of the NC core. The surface of the NC core is indicated by the vertical dashed line. Solvent molecules penetrate the ligand corona all the way to the NC surface.

In the presence of solvent, however, the curve is purely repulsive. Similar interactions have been observed by Lane *et al.* in studies of nanocrystals in water [34]. At large distances, the nanocrystals are effectively non-interacting. This is the viscous drag regime characterized by a distance-independent force and a slow and more or less linear increase in the PMF. As the nanocrystals approach, the ligand coronas on the nanocrystals begin interacting. This interaction is attractive in nature, but also causes some solvent molecules to be forced from the space in-between the nanocrystals. This hydrodynamic force is repulsive and stronger than the attractive interactions between the ligand coronas. Thus, the force in this regime is distance-dependent and the PMF begins to rise faster in this regime. Finally, as the nanocrystals are brought very close to each other, the PMF rises sharply due to purely repulsive forces caused by the unfavorable interaction of the ligand coronas on adjacent nanocrystals. The type of behavior in the presence of the solvent exemplifies the well-known "good solvent" effect.

Results for the overall free energy of the 3-D superlattices are shown in Fig. 4.7 where the change in free energy between an FCC to a BCC superlattice symmetry is plotted as a function of the ratio of the length of the capping ligand to the radius of the nanocrystal core. The points on the curves correspond to C9, C12, C18 and C24 ligands. If a point lies above free energy change of zero, a BCC superlattice symmetry is preferred; if it lies below zero, FCC symmetry is preferred. Based on this knowledge of the interaction of the solvent with the ligand corona on the nanocrystal, we can now attempt to explain the mechanisms responsible for the curves obtained in Fig. 4.7. For the simulations we performed in vacuum, the free energy curve lies in the BCC-preferred region for all the ligand lengths we considered.

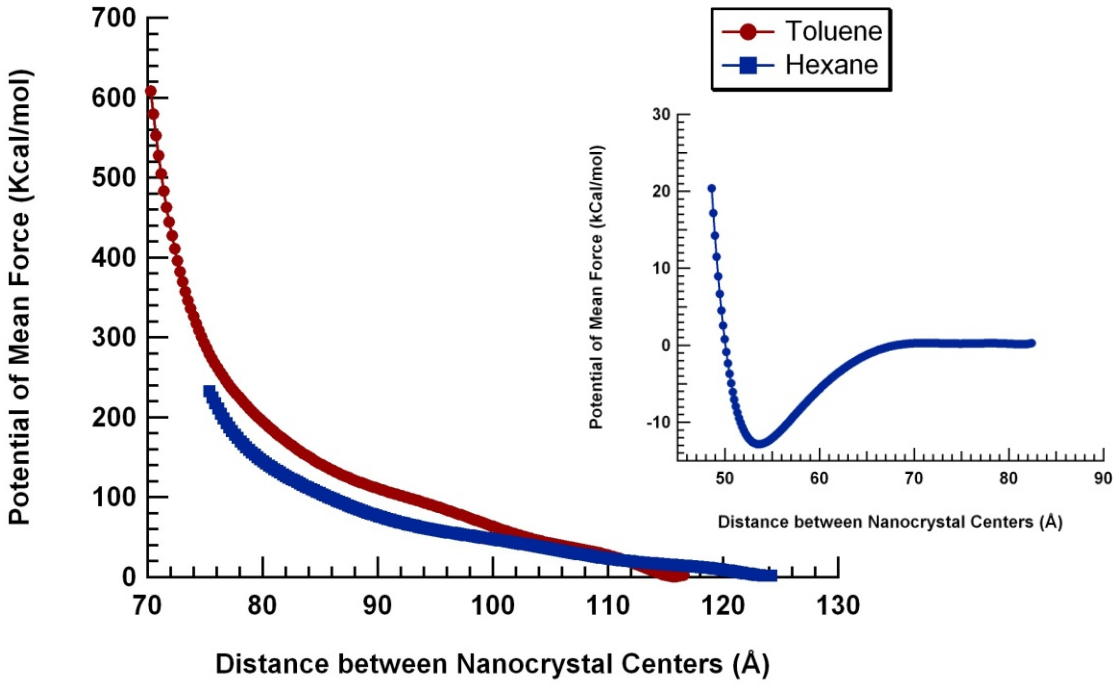

Figure 4.6: PMFs between two 4 nm NCs capped by C18 ligands with a coverage of 3.0 ligands/nm^2 in the presence of hexane (blue) and toluene (red) solvents. The inset shows the PMF in vacuum for comparison.

The consistent preference for BCC symmetry is caused by two different mechanisms. For short ligands, the effect of the shape of the core dominates. The interacting nanocrystals can "feel," or experience, the shape of the core since the passivating ligand corona is small. Thus, the issue essentially, becomes one of hard-core packing. For the cube-octahedral shapes considered here, BCC is the preferred packing symmetry. In contrast, for longer ligands, the shape of the core is masked by the more extensive ligand corona. The interaction is dominated by ligand-ligand interactions and ligand close-packing in the superlattice. The ligands thus prefer a more open BCC lattice due to greater entropic gain for ligand packing. The ligands are able to sample more of the configurational space in a BCC structure as compared to a close packed FCC structure. This case presents the lower limit of solvent quality, *i.e.,* a very "poor solvent."

In the presence of solvent, however, the amount of residual solvent, in addition to the length of the ligand, determines where the free energy difference curve lies. The residual solvent molecules penetrate the ligand layer and swell the ligand corona, making the nanocrystal more spherical. Thus, even for shorter ligands, the shape of the core is masked because of the presence of solvent molecules in the ligand corona. The nanocrystals behave as interacting spheres, and therefore have an energetic preference for the lattice symmetry with a higher coordination, *i.e*., the FCC lattice. The higher coordination of the FCC lattice offers greater enthalpic gain. For longer ligand lengths, even though the higher coordination of the FCC is favored energetically, the more open BCC symmetry prevails since the effect of ligand close-packing in the lattice dominates and the entropic gain offsets the enthalpic gain. Thus, the matter is essentially one of interplay between enthalpic and entropic gain. Here, the ratio L/r is a key factor

determining the choice of superlattice symmetry. For higher L/r, greater entropic gain drives the symmetry towards BCC. The amount of residual solvent determines the L/r value at which the crossover occurs from an FCC to a BCC symmetry. Since the amount of residual toluene in the superlattice is less than the amount of residual hexane, the free energy curve for hexane is shifted below that for toluene. However, in the limit of very long ligands (high L/r values), BCC should eventually be the preferred symmetry. In the limit of zero residual solvent (or poor solvent quality) the curves should coincide with the one carried out in the absence of solvent.

4.6. Anisotropic ligand coverage

The ligand density used in the previous sections is uniform on both the [100] and the [111] facets. But in [44], it has been noted that NCs that have been allowed to age in air may have anisotropic ligand coverages. For instance, Bealing *et al.* note that the binding energy of carboxylate ligands to the [111] surfaces is larger than [100] surfaces [58]. It is probable that oxidation occurs at the [100] surfaces which leads to shedding of the ligands grafted on those surfaces [58-59]. In such systems then, the [111] facets would have much greater ligand coverage than the [100] facets. It has been seen that such NCs tend to form BCC superlattices when dried [59]. The NCs in the superlattice also exhibit orientational alignment with all the [111] facets of nearest neighbor NCs facing each other. It is known that under solvation, the preferred symmetry is FCC even for the NCs with anisotropic ligand coverage and the NCs are usually orientationally disordered. So upon drying of the film, the superlattice symmetry changes from FCC to BCC and the NCs become orientationally ordered.

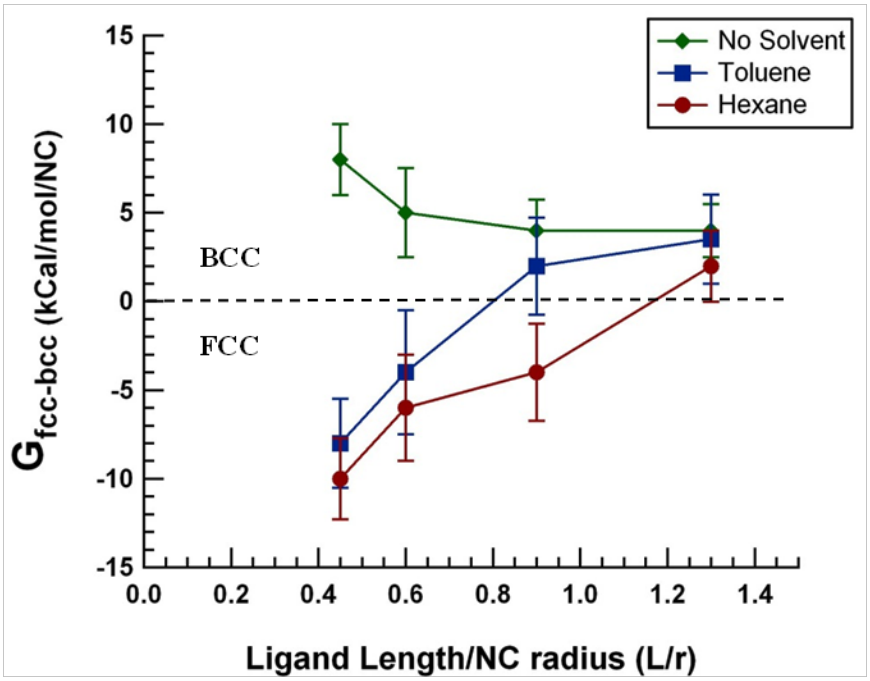

Figure 4.7: Free energy change for the transition from an FCC to a BCC superlattice symmetry as a function of the ratio of ligand length to core radius, L/r. The zero dashed line demarcates the transition region at which FCC and BCC are equally preferable. The error bars denote the standard deviation in the energy difference between the FCC and BCC symmetries.

Fig 4.8a illustrates the GISAXS (Grazing Incidence Small Angle X-Ray Scattering) of the solvated superlattice which confirms that the NC film is disordered. Fig 4.8b shows the WAXS (Wide Angle X-Ray Scattering) image of the dried NC superlattice. The bright spots indicate the orientational alignment of the NCs. As seen in the previous section (4.5), for a NC with uniform ligand coverage, the superlattice symmetry is usually FCC when processed with hexane as solvent. The difference in the symmetry preference is thus, an interesting problem. We studied such a NC system and proposed an explanation as to the nature of the transformation.

In our model system, we have chosen to simulate the NC with ligands only on the [111] facets. The [100] facets are bare and have no ligands grafted on them. This represents the extreme limit of anisotropic coverage of ligands. The model NC with uniform and anisotropic ligand coverages are shown in Fig 4.9 a,b. The FCC and BCC model superlattices of the NCs are shown in Fig 4.9 c,d.

A series of NCs are arranged in either a BCC or an FCC symmetry superlattice far enough away from each other to ensure that there was no interaction between them. All interactions were modeled as described in section 4.3. The simulation box was then shrunk as described in section 4.4 in short steps each time equilibrating the lattice to ensure that the temperature of the system remained more or less constant. The procedure is shown in Fig 4.10. We considered three different ligands, C9, C12 and C18. The first set of simulations consisted of comparing a fully capped NC superlattice and a superlattice composed of NCs with anisotropic ligand coverage which will henceforth be called an “aged” NC system. The simulations were repeated with each of the three types of ligand considered in both BCC and FCC symmetries. Initially when the NCs are far

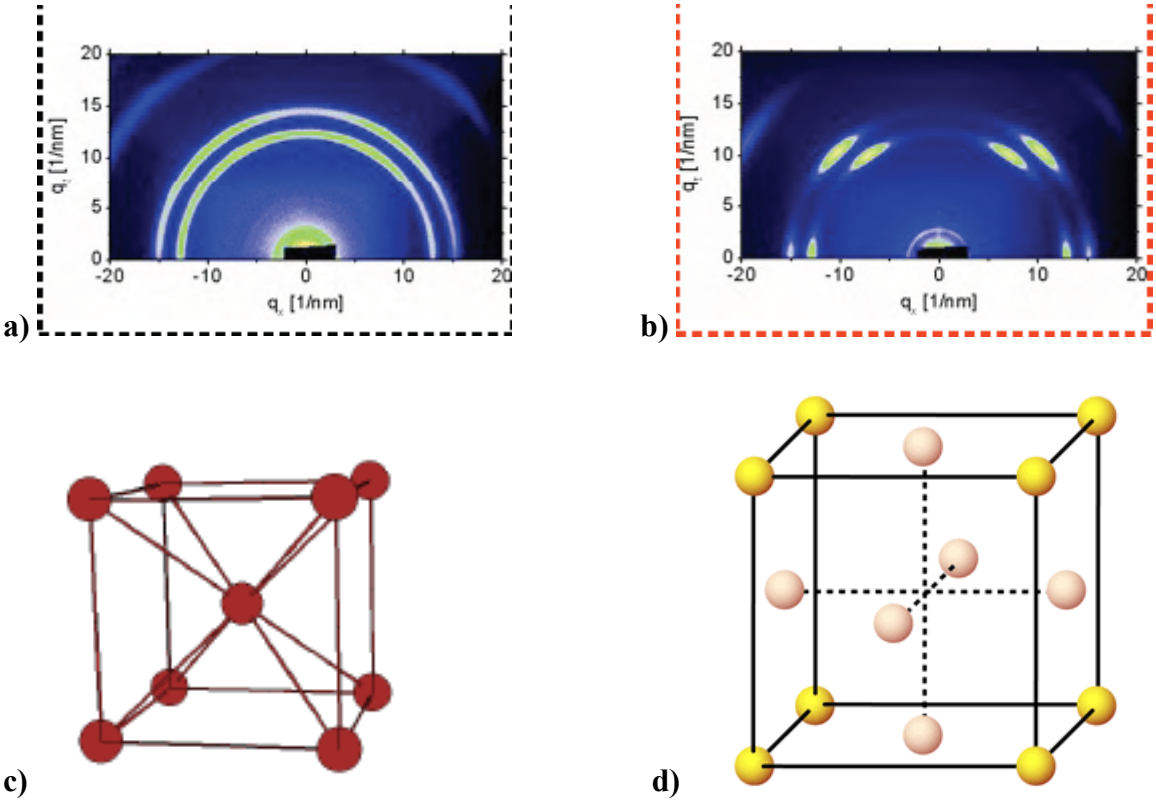

Figure 4.8: Wide Angle X-Ray scattering images of the NC films [44], a) Image of a solvated NC superlattice. The uniform rings indicate orientational disorder, b) Image of the dried superlattice, the bright spots at specific points indicates orientational ordering, c) Schematic of a BCC lattice and d) Schematic of an FCC lattice.

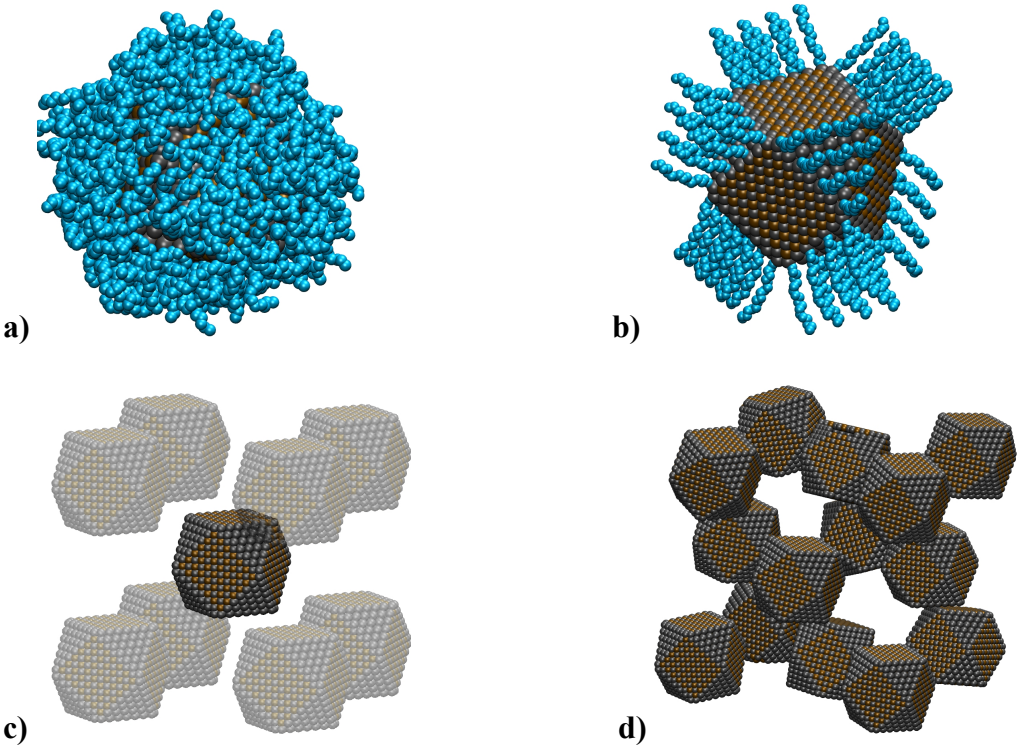

Figure 4.9: a) NC with uniform ligand coverage, b) NC with anisotropic ligand coverage – ligands only on the [111] facets, c) Schematic of the ordered BCC lattice and d) Schematic of a disordered FCC lattice.

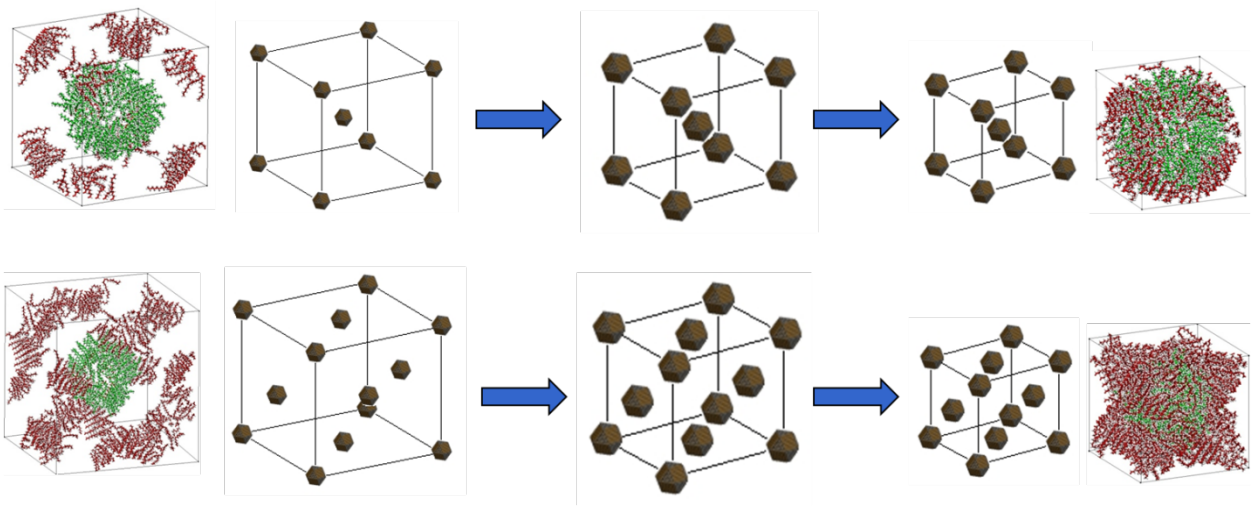

Figure 4.10: Quasi-static compression of unit cells of a BCC lattice (top) and an FCC lattice (bottom). Initially, the brown ligands on the image cores are not in contact with the green ligands of the centrally located NC (LHS images). As the compression proceeds, the ligands eventually interdigitate, as shown in the MD snapshot images on the RHS.

apart from each other, there is no interaction between them. At this point, the NCs have rotational freedom and can move freely because of thermal energy. But as the lattice shrinks, the interactions between the ligands cause the NCs to stop rotating. Fig. 4.11a,b show the fully capped and aged NCs in the BCC superlattice when the interactions between the ligands have become strong enough to stop random thermal motion. Once the NCs are this close to each other, they get trapped in the particular orientation they were in when the ligands intertwined and only perform small oscillations about the mean orientation. As seen in Fig 4.11a,b, fully capped NCs show a disordered orientation with respect to each other, whereas the aged NCs display orientational alignment.

The angle of orientation with respect to the [100] direction of the fully capped and the aged NC system is shown in Fig 4.11c,d. As seen, the disordered fully capped NC system exhibits a spread of angles but the aged system shows a tight distribution around 90 degrees showing orientational alignment. A mean diameter was calculated for the NC core plus the ligand corona as shown in Fig 4.12 a,b and this diameter was calculated for the NCs with each type of ligand considered. The volume fraction of the NCs in the superlattice was calculated using this diameter as the volume of the NCs divided by the total volume of the simulation box. A plot of the position when orientational alignment occurs versus the volume fraction for each ligand considered is shown in Fig 4.12 c. As shown in the figure, the point occurs at the same volume fraction (~ 0.55) irrespective of the ligand considered showing that the orientational alignment is purely ligand driven.

The next set of simulations performed repeated the previous example except using the FCC superlattice symmetry with the aged NCs. As before, the NCs show orientational alignment at the same volume fraction corresponding to the FCC lattice symmetry. This

is shown in Fig 4.14 a. The energy of interaction of the aged NCs with their respective nearest neighbors in the BCC and FCC superlattices is compared and is shown in Fig 4.13. As seen in the figure, the interaction energy in the BCC lattice is stronger. This is because the [111] facets of the NC core are oriented at $\cos^{-1}(1/3)$ or 54 degrees with respect to the [100] direction (shown in Fig 4.14b) which corresponds to the same angle adopted by the nearest neighbors in the BCC lattice with respect to each other. This leads to maximum interaction between the ligands on the [111] facets in this case. In a FCC lattice, however, the nearest neighbors are situated at an angle of 45 degrees with respect to each other. Thus, there is a mismatch in the alignment of the [111] facets in this case which leads to weaker interactions between the ligands on the [111] facets. Therefore, even though the NCs in the well-solvated system (when NCs are far apart) start out with an initial configuration exhibiting FCC symmetry, they transform into BCC lattice symmetry when the NCs come within interaction distance in order to maximize the interaction along the [111] facets. This transformation is depicted in Fig 4.14 b.

The transformation from FCC to BCC depends on the ratio of the surface areas of the [100] and [111] facets and how densely the ligands are grafted onto them and how much the [100] facets are depleted of the ligands. If the [100] facets are completely depleted as considered here, the transformation takes the system from FCC to BCC. If the [100] facets are fully capped, the system remains in FCC as described in section 4.5. If the [100] facets are partially depleted, there will be competition for interaction between the ligands on the [100] and the [111] facets and the result would be a lattice symmetry somewhere in between an FCC and BCC – a distorted FCC lattice with the distortion leading towards a BCC symmetry. The extent of distortion of the lattice depends on the

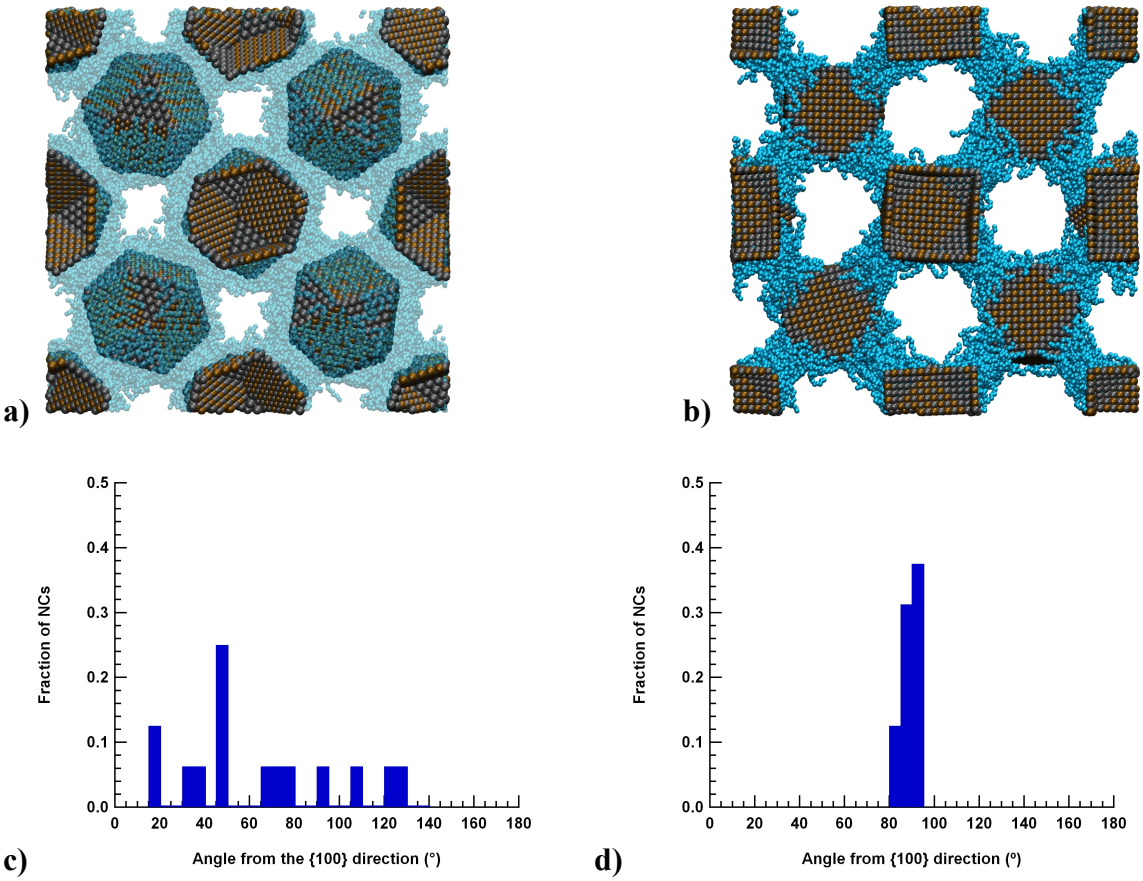

Figure 4.11: a) Fully ligand-capped NC system in a BCC lattice showing disordered alignment, b)Aged NC system in a BCC lattice showing orientational alignment, c) Angular distribution of fully ligand-capped NCs with respect to [100] and d) Angular distribution of aged NCs with respect to [100].

a)

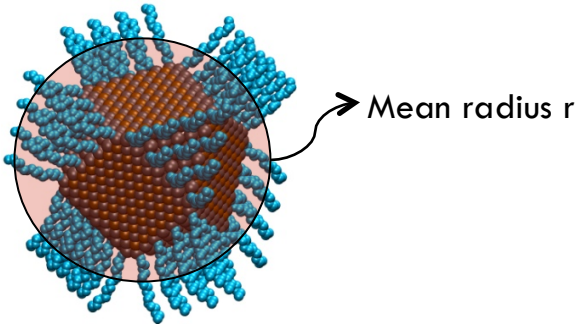

b)

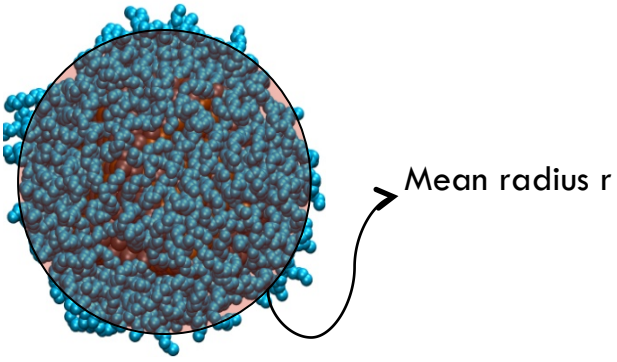

c)

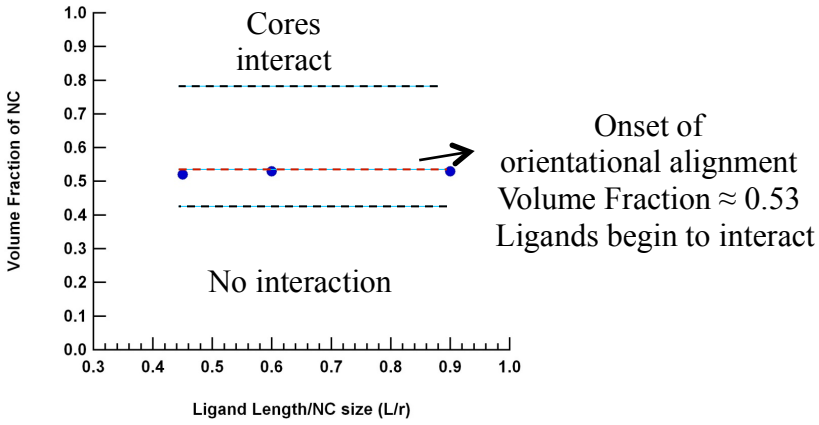

Figure 4.12: a) Mean diameter of an aged NC, b) Mean diameter of a fully capped NC and c) Plot of volume fraction versus ligand length/NC size. The different regions of interactions are as follows: Below a volume fraction of 0.4, there is no interaction. From 0.4 – 0.8 ligand interaction becomes increasingly stronger. Beyond 0.8, the NC cores begin to interact. At a volume fraction of 0.55, the NCs become orientationally aligned regardless of L/r.

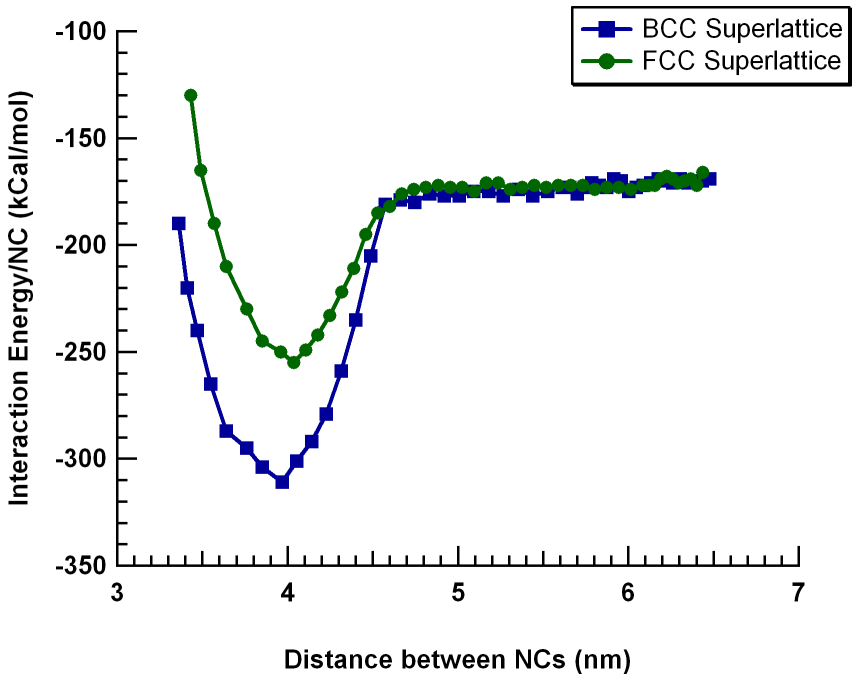

Figure 4.13: Energy of interaction per NC in a BCC and an FCC superlattice symmetry plotted versus the distance of separation between the nearest neighbors in each lattice.

a)

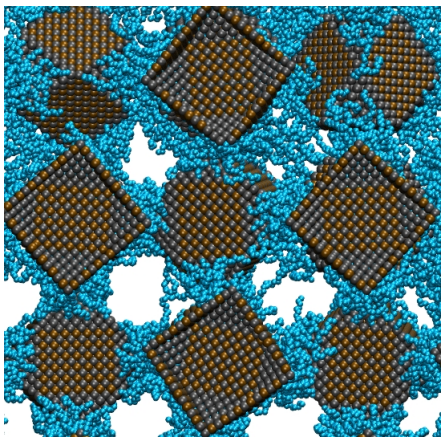

b)

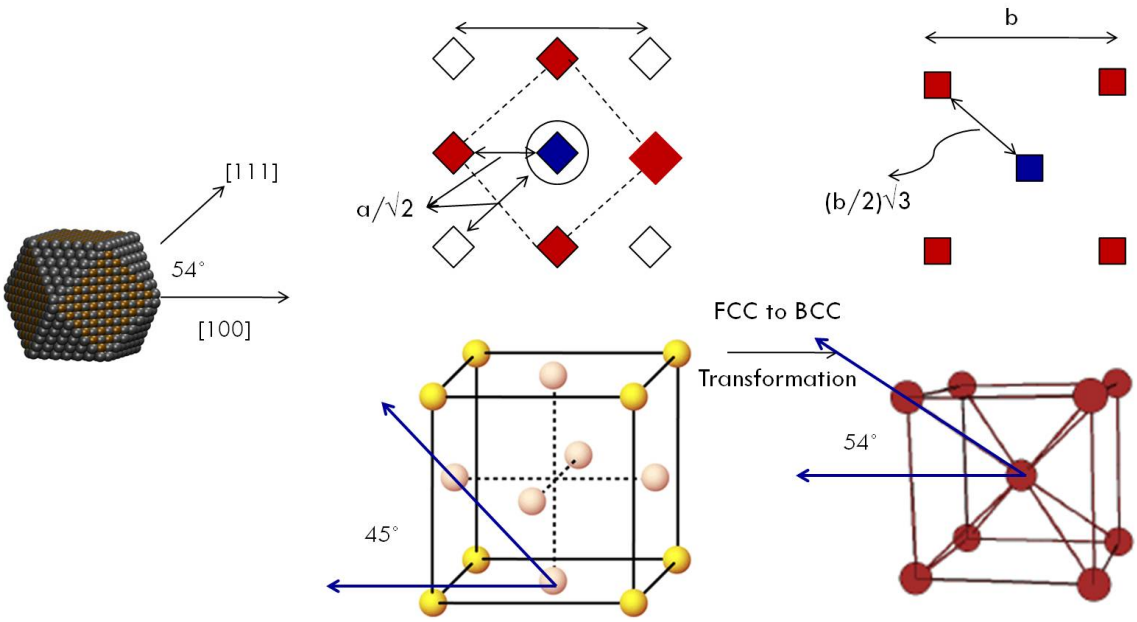

Figure 4.14: a) Aged NCs in FCC lattice symmetry showing orientational alignment and b) Transformation of the system from FCC lattice symmetry to BCC lattice symmetry. The cube-octahedral NC cores have [111] facets oriented at 54 degrees to the horizontal which corresponds to the angle between nearest neighbors in a BCC lattice. The lattice transforms from an FCC symmetry to a BCC symmetry to achieve greater ligand interaction.

extent of competition for interaction between the ligands on the [100] and the [111] facets which would in turn depend on the grafting density and extent of ligand depletion etc.

4.7. Conclusions

In this chapter, we have presented a study of nanocrystal superlattice interactions in the presence of two explicitly modeled solvents, hexane and toluene, used commonly in experiments. The solvent molecules were found to penetrate the entire ligand corona of the nanocrystals thereby swelling the corona and effectively making the nanocrystals appear more spherical in nature (and, as such, showing agreement with Korgel *et al.*'s [30] results for spherical gold/LJ nanocrystals). Solvent penetration of the ligand corona is irrespective of the structure of the solvent molecule, at least for the ligand grafting density (3.0 ligands/nm^2) considered here. This causes the nanocrystal to swell and appear more spherical, masking the faceted shape of the nanocrystal core. The *amount* of solvent within the ligand corona, however, depends on the structure of the solvent molecule as well the strength of interaction of the solvent molecules between themselves as well as with the ligands. This is similar in nature to the effect seen by Yang *et al.* [35-36] in their studies of polar solvents around functionalized ligands on nanocrystals. We found that more toluene molecules penetrate the ligand corona than hexane. The PMF for the interaction between the NCs in the presence of both solvents is purely repulsive which can be attributed to the "good solvent" effect. This is caused by hydrodynamic forces exerted by the good solvent on the nanocrystals as they approach each other.

The free energies of 3-D superlattices in the presence of these solvents were instrumental in determining the stability and preference of superlattice symmetry as the length of the capping ligand molecules (characterized by the ratio L/r) is varied, as well as the amount

of residual solvent in the "dry" superlattice. We have shown how the knowledge of the microscopic scale of solvent-ligand interactions can be used to understand the macroscopic-scale superlattice structure of nanocrystal films. In experiments, the amount of residual solvent in the superlattice would depend on the chemical nature of the solvent used and the vapor pressure of the solvent in the presence of the nanocrystals. It could also depend on the environmental conditions under which the evaporation of the solvent was carried out, *i.e.,* the extent to which the nanocrystal film can be dried.

We have also explored the effect of anisotropic ligand density on the NC surface on the preference of superlattice symmetry. We showed that the for a cubeoctahedral shape of the NC core which has ligands preferentially on the [111] facets, the preferred superlattice symmetry is the BCC symmetry. The NCs which have an FCC symmetry when well solvated transform into a BCC symmetry due to ligand interaction alone when they approach each other as the film is dried. This transformation occurs because of greater ligand interaction in the BCC symmetry since the orientation angle of the [111] facets on the NC core with respect to the horizontal (54 degrees) corresponds to the angle between nearest neighbors in the BCC superlattice but not in an FCC superlattice (45 degrees). Thus, by choosing the type of solvent used, the drying conditions as well as the type of ligand used and the preferential grafting density of the ligands, these results can be utilized to selectively drive the self-assembly process to achieve the desired superlattice symmetry for nanocrystal films.

REFERENCES

[1] P. Bhattacharya; S. Ghosh; A. D. Stiff-Roberts, Annu. Rev. Mat. Res., 34, 1 (2004)

[2] C. Murray; C. Kagan; M. Bawendi, Annu. Rev. Mat. Sci., 30, 545 (2000)

[3] M. Law, J. Goldberger, P. Yang, Annu. Rev. Mat. Res., 34, 83-122 (2004)

[4] M. S. Skolnick, D. J. Mowbray, Annu. Rev. Mat. Res., 34, 181-218 (2004)

[5] D. V. Talapin; J.-S. Lee; M. V. Kovalenko; E. V. Shevchenko, Chem. Rev., 110, 389 (2010)

[6] A. P. Alivisatos, J. Phys. Chem., 100, 13226-13239 (1996)

[7] Y. Wu, C. Wadia, W. Ma, B. Sadtler, A. P. Alivisatos, Nano Lett., 8, 2551–2555 (2008)

[8] M. G. Panthani, V. Akhavan, B. Goodfellow, J. P. Schmidtke, L. Dunn, A. Dodabalapur, P. F. Barbara, B. A. Korgel, J. Am. Chem. Soc., 130, 16770–16777 (2008)

[9] J. J. Choi, Y-F. Lim, M. E. B. Santiago-Berrios, M. Oh, B-R. Hyun, L. Sun, A. C. Bartnik, A. Goedhart, G. G. Malliaras, H. D. Abruna, F. W. Wise, T. Hanrath, Nano Lett., 9, 3749–3755 (2009)

[10] W. Ma, J. M. Luther, H. Zheng, Y. Wu, A. P. Alivisatos, Nano Lett., 9, 1699–1703 (2009)

[11] J. M. Luther, M. Law, M. C. Beard, Q. Song, M. O. Reese, R. J. Ellingson, A. Nozik, J. Nano Lett., 8, 3488–3492 (2008)

[12] K. S. Leschkies, T. J. Beatty, M. S. Kang, D. J. Norris, E. S. Aydil, ACS Nano, 3, 3638–3648 (2009)

[13] J. J. Urban, D. V. Talapin, E. V. Shevchenko, C. R. Kagan, C. B. Murray, Nat. Mater., 6, 115–121 (2007)

[14] B. Sun, H. Sirringhaus, Nano Lett., 5, 2408–2413 (2005)

[15] D. V. Talapin, C. B. Murray, Science, 310, 86–89 (2005)

[16] S. Coe, W-K. Woo, M. Bawendi, V. Bulovic, Nature, 420, 800–803 (2002)

[17] A. H. Mueller, M. A. Petruska, M. Achermann, D. J. Werder, E. A. Akhadov, D. D. Koleske, M A. Hoffbauer, V. I. Klimov, Nano Lett., 5, 1039–1044 (2005)

[18] S. A. McDonald, G. Konstantatos, S. Zhang, P. W. Cyr, E. J. D. Klem, L. Levina, E. H. Sargent, Nat. Mater., 4, 138–142 (2005)

[19] A. N. Shipway, E. Katz, I. Willner, Chem. Phys. Chem., 1, 18–52 (2000)

[20] V. A. Akhavan, B. W. Goodfellow, M. G. Panthani, D. K. Reid, D. J. Hellebusch, T. Adachi, B. A. Korgel, Energy Environ. Sci., 3, 1600–1606 (2010)

[21] V. A. Akhavan, B. W. Goodfellow, M. G. Panthani, B. A. Korgel, Modern Energy Rev., 2, 25–27 (2010)

[22] C. B. Murray, S. Sun, W. Gaschler, H. Doyle, T. A. Betley, C. R. Kagan, IBM J. Res. Dev., 45, 47–56 (2001)

[23] P. Liljeroth, K. Overgaag, A. Urbieta, B. Grandidier, S. G. Hickey, D. Vanmaekelbergh, Phys. Rev. Lett., 97, 096803 (2006)

[24] B. Lee, P. Podsiadlo, S. Rupich, D. V. Talapin, T. Rajh, E. V. Shevchenko, J. Am. Chem. Soc., 131, 16386-16388 (2009)

[25] C. B. Murray, C.R. Kagan, M. G. Bawendi, Annu. Rev. Mater. Sci., 30, 545-610 (2000)

[26] C. B. Murray, C.R. Kagan, M. G. Bawendi, Science., 270, 1335-1338 (1995)

[27] E. V. Shevchenko, D. V. Talapin, A. Kornowski, F. Wiekhorst, J. Kotzler, M. Haase, A. Rogach, H. Weller, Adv. Mater. 14, 287-290 (2002)

[28] K. Bian, J. J. Choi, A. Kaushik, P. Clancy, D-M. Smilgies and T. Hanrath, ACS Nano, 5(4), 2815-2823 (2011)

[29] B. W. Goodfellow, R. N. Patel, M. G. Panthani, D-M. Smilgies and B. A. Korgel, J. Phys. Chem. C, 115, 6397-6404 (2011).

[30] B. A. Korgel, D. Fitzmaurice, Phys. Rev. B., 59, 14191-14201 (1999)

[31] W. D. Luedtke and U. Landman, J. Chem. Phys. 100, 13323-13329 (1996)

[32] P. Schapotschnikow, R. Pool and T. J. H. Vlugt, Nano Lett. 8, 2930-2934 (2008)

[33] P. Schapotschnikow and T. J. H. Vlugt, J. Phys. Chem. C, 114, 2531-2537 (2010)

[34] J. M. D. Lane and G. S. Grest, Phys. Rev. Lett., 104, 235501 (2010)

[35] A. Yang and C. Weng, J. Phys. Chem. C, 114, 8697-8709 (2010)

[36] A. Yang, C. Weng and T. Chen, J. Chem. Phys., 135, 034101 (2011)

[37] E. Rabani, S. A. Egorov, J. Phys. Chem. B, 106, 6771-6778 (2002)

[38] Y. Qin and K. A. Fichthorn, Phys. Rev. E., 73, 020401(R) (2006)

[39] P. K. Ghorai and S. C. Glotzer, J. Phys. Chem. C, 111, 15857-15862 (2007)

[40] M. A. Sliem, A. Chemseddine, U. Bloeck and R. A. Fischer, CrystEngComm, 13, 483-488, (2011)

[41] Moreels, I.; Frintzinger, B.; Martins, J.C.; Hens Z. Surface chemistry of colloidal PbSe nanocrystals. J. Am. Chem. Soc. 130, 15081-15086 (2008)

[42] G.Schaftenaar and J. Noordik, J. Comput.Aided Mol. Design 14, 123 (2000).

[43] S. J. Plimpton, J. Comp. Phys., 117, 1-19 URL http://lammps.sandia.gov (1995)

[44] J. J. Choi, C. R. Bealing, K. Bian, K. J. Hughes, W. Zhang, D. M. Smilgies, R. G. Hennig, J. R. Engstrom and T. Hanrath, J. Am. Chem. Soc., 133 (9), pp 3131–3138 (2011)

[45] A. P. Kaushik and P. Clancy, J. Chem. Phys., 136, 114702 (2012)

[46] W. Paul, Do Y. Yoon and G.D. Smith, J. Chem. Phys. 103, 1702-1709 (1995)

[47] C. D. Wick, M. G. Martin, J. I. Siepmann, J. Phys. Chem. B, 104, pp 8008-8016 (2000)

[48] P. Schapotschnikow, M.A. van Huis, H.W. Zandbergen, D. Vanmaekelbergh and T. J. H. Vlugt, Nano Lett. 10, 3966-3971 (2010)

[49] G. J. Martyna, D. J. Tobias and M. L. Klein, J. Chem. Phys., 101, 4177 (1994)

[50] M. Parrinello and A. Rahman, J. Appl. Phys., 52, 7182 (1981)

[51] W. Shinoda, M. Shiga and M. Mikami, Phys. Rev. B, 69, 134103 (2004)

[52] M. E. Tuckerman, J. Alejandre, R. Lopez-Rendon, A. L. Jochim and G. J. Martyna, J. Phys. A: Math. Gen., 39, 5629 (2006)

[53] G. Ciccotti, M. Ferrario, J. T. Hynesa and R. Kapral, Chem. Phys., 129, 241 (1989)

[54] E. Guardia, R. Rey and J. A. Padro, Chem. Phys., 155, 187-195 (1991)

[55] C. Jarzynski, Phys. Rev. Lett., 78, 2690-2693 (1997)

[56] C. Jarzynski, Phys. Rev. E, 56, 5018-5035 (1997)

[57] R. W. Zwanzig, J. Chem. Phys., 22, 1420-1426 (1954)

[58] C. R. Bealing, W. J. Baumgardner, J. J Choi, T. Hanrath, R. G Hennig, ACS Nano, 6 (3), 2118–2127 (2012).

[59] J. J. Choi, C. R. Bealing, K. Bian, K. J. Hughes, W. Zhang, D-M. Smilgies, R. G. Hennig, J. R. Engstrom, T. Hanrath, J. Am. Chem. Soc., 133, 3131–3138 (2011).

CHAPTER 5

Effect of Shape on Electronic Structure and Charge Transport in Faceted PbSe Nanocrystals

5.1 Introduction

Quantum dots (or nanocrystals) are well known to exhibit the defining characteristic that the properties of the same material can be controlled by their size, and that these unique properties are different from their bulk counterparts in a manner inconsistent with mere scaling [1-6]. Interest in nanocrystal (NC) assemblies has been manifested in a variety of applications, including solar cells [1-5, 7-12], field effect transistors [13-15], light-emitting diodes [16-17], photo-detectors [18] and chemical sensors [19]. In this paper, we focus on colloidal NCs can be easily solution-processed and drop-cast onto suitable substrates to provide an inexpensive method of producing electronic devices in contrast to using high temperature or vacuum processing fabrication approaches [20-21]. NCs formed from lead salts such as PbSe, PbTe, PbS etc., have received considerable attention in recent years [1-5], mainly due to their large Bohr exciton radius and narrow, yet size-tunable, band gaps [22]. Their ability to provide significant electronic coupling at close proximity [23] and to self-assemble into a variety of large two-dimensional and three-dimensional superlattices [20-21, 24] make them ideally suited for use in photovoltaic devices and other optoelectronic applications [11-12, 14-15].

The exploitation of these unique nanocrystal properties in effective electronic devices is currently constrained by our lack of understanding charge transport in NC systems. This transport is determined by a complex and interacting set of variables: the size distribution

of the NCs, surface chemistry and stoichiometry, morphological order, and inter-NC distances. The effect of the (usually insulating, long-chain alkyl) ligands that are invariably employed to prevent NC sintering is also important in determining charge transport characteristics of NCs, both in terms of their physical intervention to deleteriously increase the inter-NC separation and in terms of providing a medium through which charge transport has to travel and hence creating a tunneling barrier. This has led to the use of shorter chains and conducting ligands to improve charge transport. One dramatic example of this is the orders of magnitude larger charge transport in PbSe NC thin films using hydrazine [25]. Similar improvements were seen using 1,2 ethanedithiol [26] and by $Sn_2S_6^{4-}$ [27]. Other approaches involved embedding PbSe NCs in a matrix of CdSe NCs affixed to a substrate to form molecular aggregates [28]. Most recently, Kagan has shown that compact ammonium thiocyanate ligands on lead chalcogenide NCs can promote impressive electron mobilities (on the order of $10cm^2/Vs$) while retaining quantum confinement. [29,30].

The effect of NC *shape* is often invoked in this discussion, but the nature of its role in charge transport processes has achieved little attention. This is not surprising since it is difficult to tease apart the contribution of shape alone from among the many variables that contribute to experimental observations. This provides considerable motivation for a computational study, but this is constrained by the cost of the *ab initio* calculations that are required for a study of charge transport.

Many studies have been performed to study charge transfer in NCs by approximating the structure of the NCs is some manner or other. These studies have assumed the NCs are some form of a truncated bulk crystal or whose surface pseudo atoms have been

passivated. Luo et al. [31] for example studied the manner of decay of excited photons in truncated bulk semiconductor crystals which were used to approximate NCs. They introduced a figure of merit for carrier multiplication in a variety of NCs and found some materials like CdSe, PbSe etc to have greater carrier multiplication than others. Franceschetti and Wang et al. [32] have studied the carrier localization due to confinement versus electron correlation in semiconductor nano dumbbells. They showed that the shape and size of the dumbbell wire could affect the localization. An et al. [33,34] have studied the excitonic splitting and radiative lifetime in *spherical* PbSe NCs using Configuration Interaction methods. Califano et al. [35] have studied the hole relaxation in CdSe NCs and show how the size and aspect ratio of nanostructures such as nanorods etc. can affect hole relaxation. All these studies use screened atomic pseudopotentials to model the electronic structure which are not as accurate as *ab initio* methods like DFT. They also use ligand pseudopotentials at the surface to provide passivation. While this approach is efficient enough to overcome the computational cost of using larger ligand-passivated NCs, they completely ignore the specific ligand chemistry and the contribution of ligands to the total electronic structure of the NC. Studies performed by Talapin et al. [25] have shown that the ligand chemistry is extremely important in determining the electronic structure and charge transfer in NC systems.

There have been many studies using *ab initio* methods such as DFT of Si, CdSe, CdTe, PbSe etc. NCs. Kiran et al. used DFT to find $(PbS)_{32}$ to be the smallest cubic cluster for which its inner $(PbS)_4$ core enjoys bulk-like coordination [36]. This helps provide a rubric for understanding the pattern of aggregation when $(PbS)_{32}$ clusters are deposited on

a suitable surface. Gai et al. have studied the structural and electronic properties of non-stoichiometric PbSe NCs [37]. They hypothesized that dangling bonds may be responsible for introducing in-gap states. Contrary to this study, O. Voznyy has claimed that it is not dangling bonds but ligands that are responsible for surface traps and in-gap states [38]. There have also been DFT and Time-Dependent DFT (TD-DFT) studies of the role of different ligand chemistries and the role of different solvents on the electronic structure of CdSe NCs [39]. More recently, there have also been studies of multi exciton generation and hot carrier relaxation in Si and PbSe NCs using *ab initio* methods [40,41].

The "cost" of using *ab initio* computational approaches to study charge transport in NCs is sufficiently high that, in practice, it essentially limits the study of such systems to those containing less than a few hundred atoms. This difficulty is exemplified in a recent a study of charge transport between two spherical CdSe NCs linked by a compact $Sn_2S_6^{4-}$ connector [42]. While the charge transport has to be calculated using *ab initio* calculations, it is infeasible to study realistically sized NCs without making several assumptions. Chu *et al.* [42], studied charge transport in 2.5-5nm diameter spherical NC dimer systems which involved a patchwork of electronic structure calculations for a representative motif of the spherical NC, linked to a set of other theoretical models to represent charge hopping. This study made predictions of the effect of NC size and temperature on mobility which await experimental confirmation. This study though, did not take into account the effect of shape of the NCs on the charge transport.

Past *ab initio* studies of NCs thus roughly fall into two categories: either they involve assumptions about the ligand coverage and the electronic structure (pseudopotentials are used) [31-35] when charge hopping is considered or else charge transport calculations are

not performed if the actual ligand bonding is simulated and full *ab initio* methods are used (the studies tend to limit to calculations of Density of States (DOS) and description of structure of the NCs) [36-42]. In this paper, we present a detailed study of the electronic structure of small PbSe NCs taking the vantage that we have calculated both the full electronic structure and charge transport in bare as well as ligand clad NCs (no pseudo passivation) using DFT alone. While we have chosen PbSe as the primary system, the analysis we believe, is not limited to this system alone. We have performed simulations of PbS NCs as well and found that the electronic structure of PbS NCs is very similar to that of PbSe. While the largest NC we have studied is only ~2 nm in diameter, far below the size typically studied in experiments (3-10 nm in diameter), this study will provide insights that, we predict, will be relevant for larger diameter NCs. We believe that the NCs used here are representative of the NCs used in experiment even though they are smaller because the effect of shape of the NC is more important than the size since the shape determines the distribution of the charge densities in the NC and hence affects the charge transport. The qualitative trends obtained in this study can be used to guide the charge transport calculations for larger NCs composed of PbSe or PbS and the design of self-assembled superlattices of these NC films.

Here, we present a detailed study of the electronic structure of PbSe NCs. We have considered a $Pb_{40}Se_{40}$ NC containing a total of 80 atoms as our primary system. Such a NC is 1.53 nm in diameter which is easily accessible to a DFT study. The shape of the NC considered is considered to be an octahedron. We have also performed simulations of a 1.53 nm cube-octahedral NC (which has the same [111] facet area as the octahedral NC but larger [100] facet area) to perform comparisons with the primary system when

applicable to study the effect of shape of the NCs on the charge transport properties. We begin with a study of the surface reconstructions on the NC and the binding of ligands to the surface of the reconstructed NC. This leads to a study of the electronic coupling between two NCs and the determination of electron and hole transfer rates between them. We calculate the charge coupling and transfer rates for bare NCs of different shapes to study the effect of shape and also for ligand clad NCs to study the effect of ligands on the charge transport. We also calculate the electron and hole mobility in an FCC and a BCC lattice to compare charge transport in different superlattice symmetries. The details of these studies are presented below.

5.2. Theory

To describe charge transport in a NC superlattice, we consider a charge-hopping model in which charge can transfer only between adjacent NCs, i.e. between nearest neighbor NCs. A similar approach has been used successfully to describe charge transfer in organic semiconductors in many previous studies [43-54]. Viewing each hopping event as a nonadiabatic electron transfer reaction, we use standard Marcus theory to express the rate of charge motion between neighboring NCs, $k_{ij,}$ in terms of the reorganization energy $\lambda_{ij,}$ and the coupling matrix element $V_{ij,}$ as

$$k_{ij} = |V_{ij}|^2 \sqrt{\frac{\pi}{\hbar^2 k_B T \lambda_{ij}}} exp\left(-\frac{(\lambda_{ij}+\Delta E)^2}{4\lambda_{ij} k_B T}\right) \quad (1)$$

where k_B is the Boltzmann constant, T is the temperature and ΔE is the energy difference between the initial and final state, which, for self-exchange reactions, is zero. Given the hopping rate between two neighbors, the diffusion coefficient can be evaluated from the hopping rates as

$$D = \frac{1}{2n}\sum_i r_i^2 k_i P_i \quad (2)$$

where, n=3 is the dimensionality, k_i is the charge hopping rate to the i^{th} neighbor, r_i is the the distance to the i^{th} neighbor and P is the relative probability of the charge hop to the i^{th} neighbor given by

$$P_i = k_i / \sum_i k_i \quad (3)$$

where the summation is taken over all possible hops. The drift mobility of hopping, μ, is then evaluated from the Einstein relation

$$\mu = \frac{e}{k_B T} D \quad (4)$$

where e is the electronic charge and D is the diffusion coefficient as above. The mobility can be evaluated along any particular direction as required in the NC superlattice and would depend on the type of the superlattice considered (FCC, BCC etc.).

5.2.1. Electronic Coupling Element

The electronic coupling between the NCs arises from the overlap of the frontier orbitals (HOMO-HOMO and LUMO-LUMO) of the two individual NCs forming the dimer. In order to evaluate the extent of the overlap between the orbitals, we need to project the Hamiltonian of the dimer system on to the space defined by the molecular orbitals of the isolated NCs as

$$V_{ab} = \langle \psi_a | \mathcal{H} | \psi_b \rangle \quad (5)$$

where $\mathcal{H}$ is the electronic Hamiltonian for the dimer and ψ_a and ψ_b are the wavefunctions of the frontier orbitals of the isolated NCs respectively. This requires that the Hamiltonian of the dimer be reconstructed from the molecular orbitals of the dimer. For hole transport (for example), assuming that the dimer HOMO and HOMO-1 result from

the interaction of only monomer HOMOs, the orbital energies of the dimer are described by the following secular equation

$$\boldsymbol{H\Psi} = E\boldsymbol{S\Psi} \tag{6}$$

where **H** is the Hamiltonian for the system and **S** is the overlap matrix for the system. Since the molecular orbitals of the dimer are constructed by linear combinations of the atomic orbitals of the constituent atoms, they do not form an orthonormal basis. Thus, in order to reconstruct the Hamiltonian from the molecular orbitals of the dimer, the orbitals need to be transformed into an orthonormal basis using the symmetric transformation by Löwdin [55]. In the transformed basis, we obtain the new Hamiltonian $\mathcal{H}$. The molecular orbitals of the isolated NCs φ_a and φ_b are also orthonormalized by the same transformation to produce ψ_a and ψ_b. The coupling matrix element is then calculated using eq.(5) as

$$V_{ab} = \begin{cases} V_{elec} = \langle \psi^a_{Lumo} | \mathcal{H} | \psi^b_{Lumo} \rangle \\ V_{hole} = \langle \psi^a_{Homo} | \mathcal{H} | \psi^a_{Homo} \rangle \end{cases} \tag{7}$$

5.2.2. Reorganization Energy

The reorganization energy in (1) is evaluated using the classical Marcus theory formulation [56]. The total reorganization energy is assumed to be the sum of contributions from the inner sphere reorganization energy λ_i and the outer sphere reorganization energy λ_o. The inner sphere contribution is evaluated using the standard 4 point scheme

$$\lambda_i = \left[E_{charged}(R_{neutral}) + E_{neutral}(R_{charged})\right] - \left[E_{charged}\left(R_{charged}\right) + E_{neutral}(R_{neutral})\right] \tag{8}$$

where $R_{charged}$ and $R_{neutral}$ denote the geometry at the minimum of the potential energy surface of the charged and neutral NC, respectively and $E_{charged}$ and $E_{neutral}$ are the

potential energies of neutral and charged NCs respectively. The outer-sphere contribution was estimated using the Marcus formula

$$\lambda_o = \Delta e^2 \left(\frac{1}{\varepsilon_{opt}} - \frac{1}{\varepsilon_s}\right)\left(\frac{1}{r} - \frac{1}{R}\right) \quad (9)$$

where ε_s and ε_{opt} are the static and optical dielectric constants, respectively, r is the cavity radius for the NC and R is the center-to-center distance between the two NCs and $\Delta e=1$ (e is the electronic charge). We used the experimental values of the dielectric constants for octane - ε_s = 1.9406 and $\varepsilon_{opt} = n^2$ = 1.9463, since it is a commonly used solvent in colloidal NC systems [57,58] (n is the refractive index). It must be noted that the outer sphere reorganization energy is about two orders of magnitude smaller than the inner sphere contribution and may in fact, be neglected for this system.

5.3. Simulation Details

All the simulations in this study were carried out using the GAUSSIAN 09 suite of programs [59] and we have used DFT level of theory to calculate the electronic structure. We have used the HSEh1PBE hybrid functional since it has been shown to provide reasonable values for the energy gap of molecules [60]. As a check on the reasonable values obtained using this functional, we tested other functionals and levels of theory to determine the band energies of the NCs considered here. For example, we used Hartree Fock theory and the commonly used B3LYP functional within our DFT calculations. We found that the HSEh1PBE gave least error in the band gap and energy levels of the NCs considered in comparison to experimental values [61]. The LANL2DZ basis set with effective core potentials (ECPs) was used for both Pb and Se atoms that make up the core of the NCs. In expertiments, the surface of the NC is usually passivated with ligands; accordingly, we have chosen alkyl thiolate ligands (a commonly used ligand in ligand

exchange experiments with oleic acid) in this study. For computational efficiency, we have used representative, albeit much shorter ligands in these calculations, namely methyl thiolate (CH_3S^-) and HS^- to represent the ligands. For the ligand atoms, we have used the LANL2DZ basis set for all optimization runs, but for the single point energy calculations, we have used the 6-31+G(d,p) basis set. The electronic coupling calculations were performed with split basis sets (LANL2DZ for the Pb and Se atoms and 6-31+G(d,p) for the ligands) in conjunction with the wB97X functional since it has been used to perform coupling calculations in the past and has been found to provide accurate values for the coupling [49].

PbSe NCs have a rock salt lattice structure with a lattice constant of 0.612nm. The structure of the 1.53nm NC was chosen to be an octahedron since it is known from experiments that very tiny NCs are more or less octahedral in shape [57-58]. In this structure, the NC exhibits two different facets – [100] facets and [111] facets. We have also modeled a 1.53nm NC with a cube-octahedral shape since we wanted to study the effect of shape on the electronic coupling between NCs. Initially, the NC is created with a stoichiometric quantity of Pb and Se atoms as shown in Fig 5.1a. This leads to the NC displaying alternating [111] facets made of Pb and Se and to the creation of dipoles, which has not been observed experimentally for this system [62]. As hypothesized in [62, 63], the NC undergoes surface reconstruction to reduce the extent of dipoles by creating an excess of Pb in the system. This leads to predominantly Pb terminated facets on the NC surface, which is consistent with the facet that there is usually an excess of Pb precursor in the experimental systems in which the NCs are grown. In light of this fact, we have used the technique of reconstructing the facets as described in [62]. Roughly half

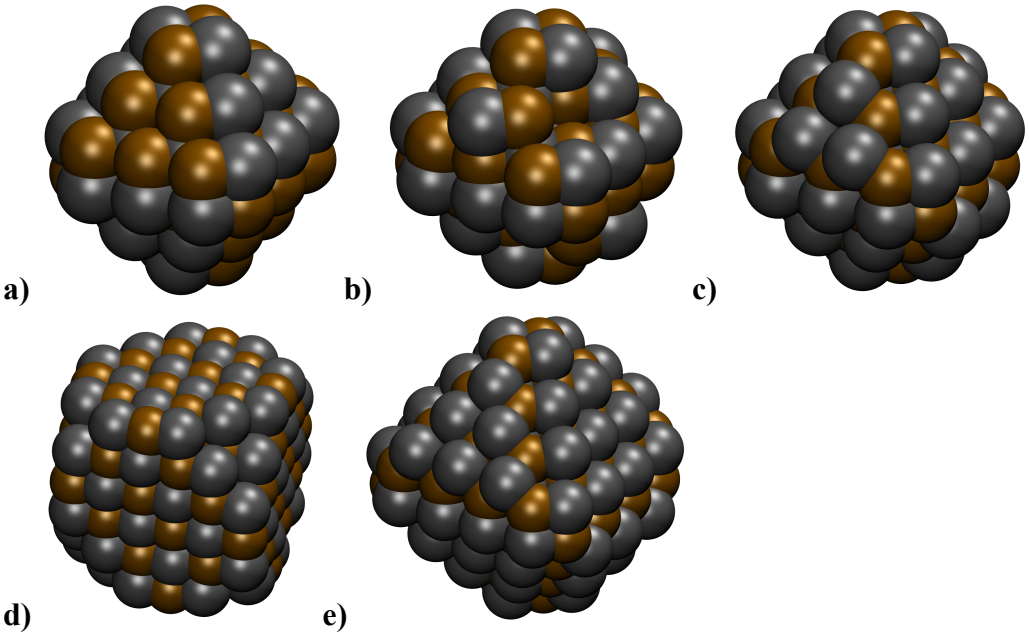

Figure 5.1: Optimized structures of bare NCs: a) 1.53nm stoichiometric NC, b) 1.53nm NC with surface reconstruction, c) 1.53nm NC with excess Pb atoms, d) 1.53nm cube-octahedral NC and e) 2.1nm NC.

the Pb atoms on the Pb terminated facets are removed and transplanted on to the Se terminated facets.

We performed structural optimizations of both the original structure and the reconstructed structure of the NC and found that the energy of the reconstructed NC decreased by about 0.5 eV as compared to the original structure. The reconstructed NC is shown in Fig 5.1b. Since there is an excess of Pb in the system, the empty locations left behind on the facets are occupied by the excess Pb atoms thereby forming purely Pb terminated [111] facets. This results in the overall dipole moment of the NC becoming negligible. The reconstructed NC with excess Pb atoms is shown in Fig 5.1c.

Once the structure of the NC core had been optimized, we studied the grafting of alkyl thiolate ligands onto the surface of the NC. The thiolate ligands can be grafted onto the [100] or [111] facets of the NC and the binding energy is different on both facets. Dispersed PbSe NCs exhibit only small net charges [64]. If the ligands were bound to the surface as deprotonated RS^- anions, the NC would have an excess negative charge depending on the number of ligands grafted on the surface of the NC. This would lead to an anomalously large internal energy of the NC, sufficient to break apart the NC. In order to ensure that the NC remains charge neutral, the excess anions have to compensated by surplus cations in the system. This surplus of cations is most likely provided by the excess Pb on the surface of the [111] facets of the NC [65-67].

One excess Pb^{2+} cation is capable of neutralizing two RS^- anions thus, maintaining charge neutrality. With this in mind, we tested the binding of the thiolate ligand to the Pb atoms on the surface of the NC. A number of trial optimizations were performed with slightly different initial positions of the ligands with respect to the surface Pb atom. Once the

optimizations had converged, a frequency calculation was performed to ensure the optimized structure obtained was indeed a minimum and not a saddle point. If the structure was a minimum, a Natural Bond Orbital analysis was performed to ensure the ligand was indeed bound to the Pb atom on the surface and not merely adsorbed on the surface. We found that the thiolate anion binds to two adjacent atoms on the surface forming a bridge between them. This is shown in Fig 5.2c,d. Of all the optimized structures we tested, this was the only structure in which the ligand was truly bound to the Pb atoms on the surface. Thus, one thiolate ligand binds to two Pb atoms or every two ligands bind to every three adjacent Pb atoms on the surface. This structure maintains the overall charge neutrality of the NC. The [111] facets of the 1.53nm NC consist of three Pb atoms on each of them, which would support two CH_3S^- ligands on each facet. We grafted two ligands on each of the eight [111] facets and optimized the structure of the NC. This is shown in Fig 5.2c,d with ligands on one of the [111] facets. The binding of ligands on the [100] surface is slightly different from that on the [111] facets. The [100] facets have alternating arrangements of Pb and Se atoms such that three Pb atoms are not found in close proximity to each other to support the binding of two ligands. Thus, we used the mechanism proposed in [62] to reconstruct the [100] facets to support the ligands. An extra Pb atom with two CH_3S^- ligands attached to it sits atop a Se atom on the [100] facet. The newly transplanted Pb atom shares its two ligands with the two Pb atoms adjacent to the Se atom on top of which it sits. This is shown in Fig 5.2a,b. Since the 1.53nm NC is very small, it's [100] facets are large enough to support just two ligands per facet. We re-optimized the structure of the NC with two ligands grafted on to each of the [100] facets. The optimized structure is shown in Fig 5.2a,b with ligands shown on

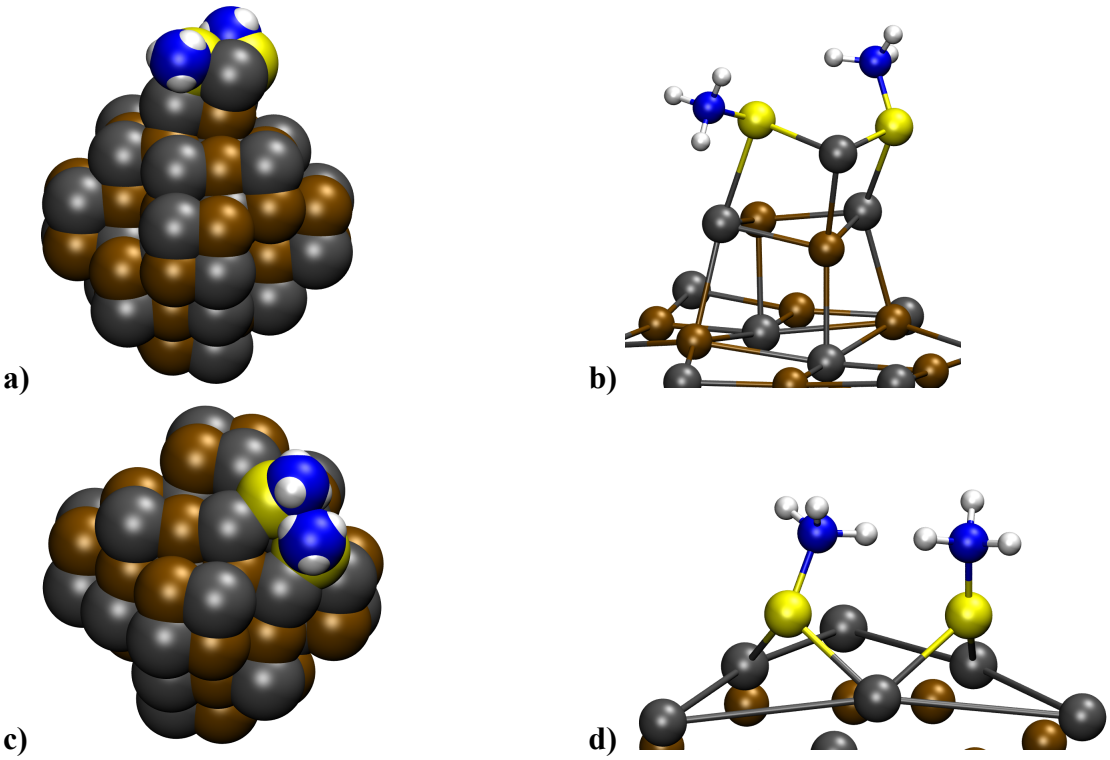

Figure 5.2: Optimized structures of bare NCs with SCH_3^- ligands on one facet: a) Ligands on a [100] facet, b) Enlarged view of ligand binding on the [100] facet, c) Ligands on a [111] facet, d) Enlarged view of ligand binding on the [111] facet.

only one facet for clarity. This passivates the surface of the NC thereby, reducing the surface energy. We have used this structure to calculate the Density of States (DOS) spectrum in the next section, but for the electronic coupling calculations, we replaced the CH_3S^- ligands with HS^- ligands for computational efficiency.

All geometry optimizations were performed using the HSEh1PBE hybrid functional with the LANL2DZ basis set. It must be noted however, that we have neglected the dispersion interactions between the adjacent ligands in our calculations. The dispersion interactions would affect ligand placement for longer and densely grafted ligands. A discussion of this is given in [62].

The binding energy of the thiolate ligands on the surface can be calculated as

$$E_{binding} = \left(E_{ligand} + E_{NC}\right) - E_{ligand/NC} \tag{10}$$

where, $E_{binding}$ is the binding energy of the ligand to the NC, E_{ligand} and E_{NC} are the energies of the isolated ligand and NC respectively and $E_{ligand/NC}$ is the energy of the NC with the ligand. We calculated the binding energy of the thiolate ligands on the [100] facets to be 1.25 eV and on the [111] facets to be 1.34 eV. Thus, the ligands tend to bind more strongly to the [111] facets as compared to the [100] facets of the NC.

Once the optimized structures of the bare NC and the ligated NC were obtained, we performed single point energy calculations using the HSEh1PBE functional in conjunction with the LANL2DZ basis set for the bare NC and the split LANL2DZ/6-31+G(d,p) basis sets for the ligand-clad NC. We also performed electronic coupling simulations of the NC dimers by placing the NCs at different distances from each other along the [100] and [111] directions. The wB97X functional was used for these calculations since it has been used in previous studies to calculate coupling and has been

found to perform well [49]. The NCs were rotated appropriately so that their [100] and [111] facets were aligned for these calculations. A similar procedure was used for the 1.53nm cube-octahedron NC as well although these NCs were not ligand-clad and only the bare reconstructed structures were used. The results of these simulations are presented in the next section.

5.4. Results and Discussion

The structure of the bare, relaxed 1.53 nm NC is shown in Fig 5.3. The structure is different from that of bulk PbSe, which has a lattice constant of 0.612 nm. The NC has a tendency to curve inwards at the outer surface trying to maximize internal interaction. Thus, the lattice constant near the core of the NC is approximately the same as that of bulk PbSe but the lattice constant at the surface is about 0.605 nm, which is less than the lattice constant of bulk PbSe. This phenomenon has also been observed by Franceschetti et al. [68-69]. The reason for this deviation is that the surface of the NC does not have any passivation. When capped by ligands however, the outer surface curvature is reduced as the surface atoms relax and the lattice constant near the surface atoms becomes more or less equal to that of bulk PbSe.

All simulations have been carried out at the DFT level of theory. DFT is known to yield inaccurate values for the band gap and energy states [78] and the results for these properties should be viewed more for qualitative comparison rather than quantitative measurements. The results are explained in the next few sections.

5.4.1 Density of States

We measured the density of states of the bare as well the ligand-clad NCs using the HSEh1PBE functional in conjunction with the split basis sets of LANL2DZ/6-31+G(d,p)

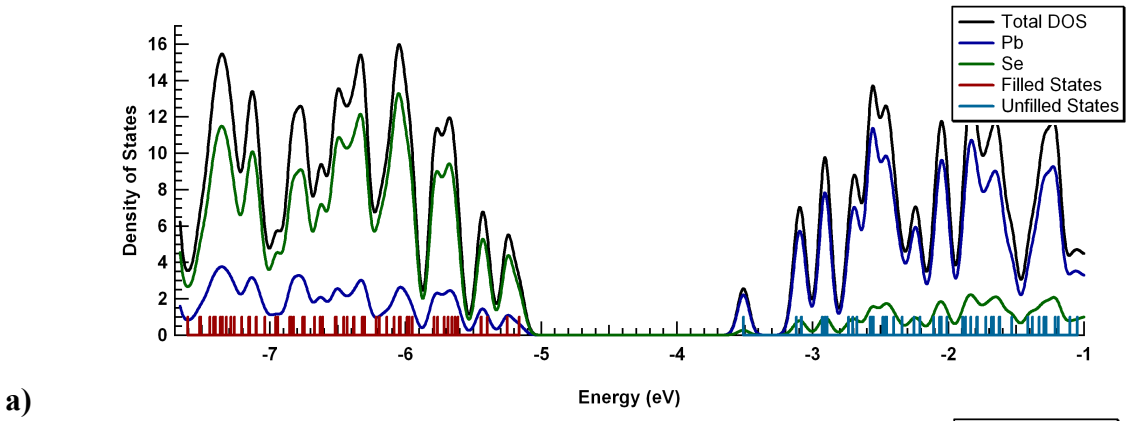

a)

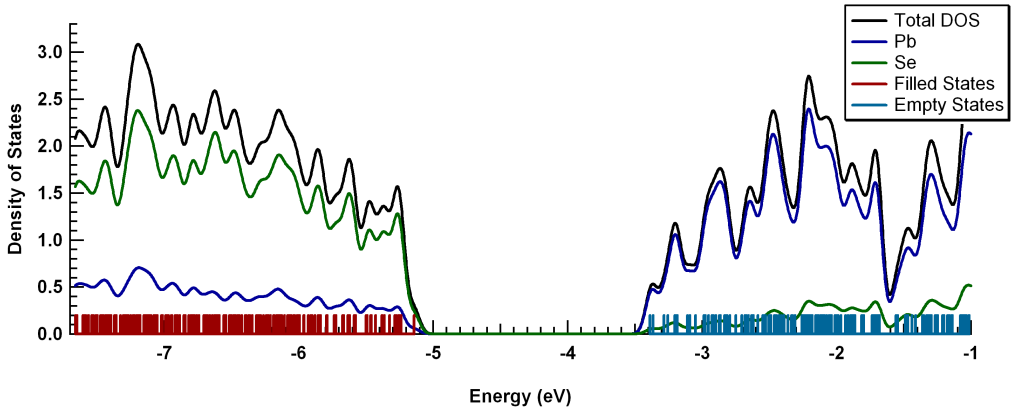

b)

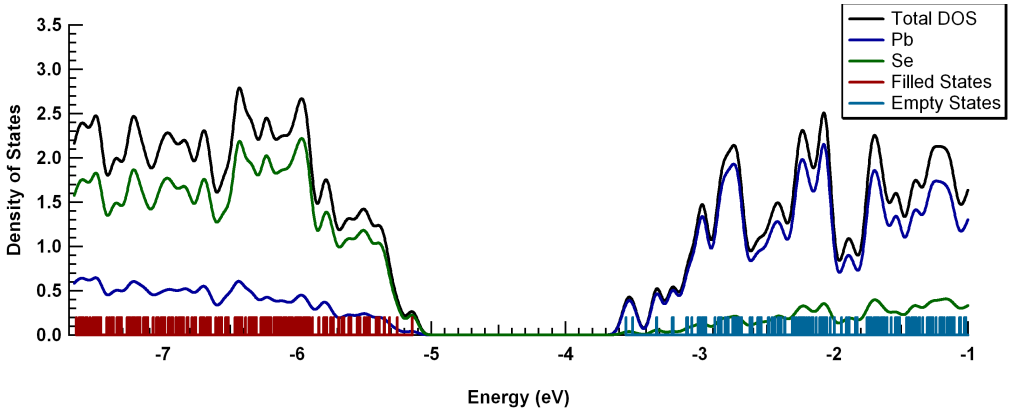

c)

Figure 5.3: Projected Density of States of a NC. A 100 meV Gaussian broadening of peaks has been used: a) Bare 1.5nm octahedral NC (the individual orbital energies are also shown), b) Bare 1.5nm cube-octahedral NC and c) Bare 2.1nm octahedral NC.

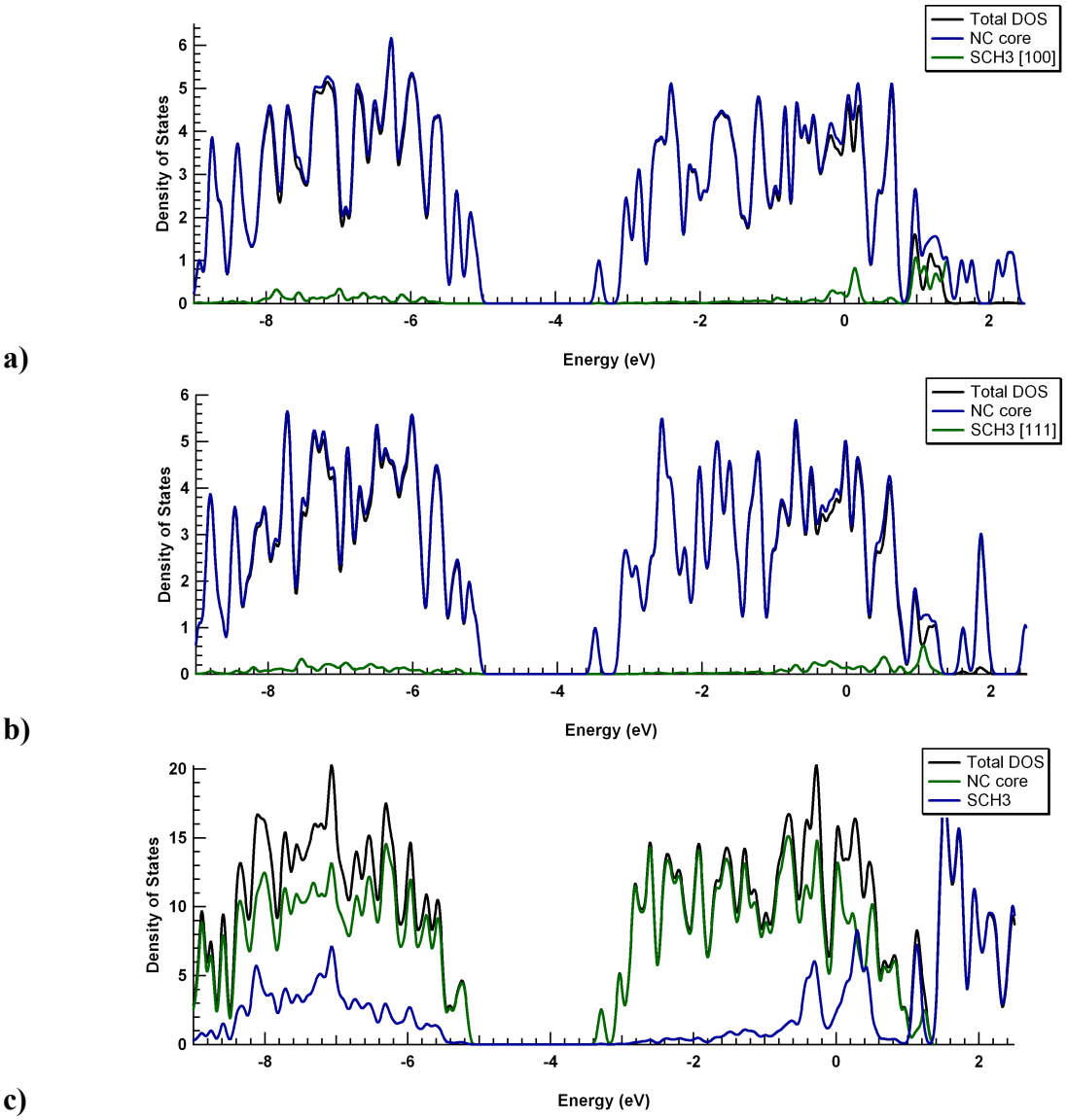

Figure 5.4: Projected Density of States of a NC. A 100 meV Gaussian broadening of peaks has been used: a) NC with SCH_3^- ligands covering the [100] facets, b) NC with SCH_3^- ligands covering the [111] facets and c) NC with $SCH3^-$ ligands covering all facets.

for the core and ligands respectively. The Projected Density of States (PDOS) for the bare 1.5nm octahedral NC is plotted in Fig 5.3a. The valence orbital (HOMO) of the NC is formed predominantly from Se *p* states, whereas the LUMO consists of Pb *p* states. The corresponding localization of the holes on Se and electrons on Pb atoms is visible in the orbital plots of the HOMO and LUMO shown, respectively in Fig 5.5a,b. Isosurfaces for the wavefunctions have been plotted at an isovalue of 0.0075. The blue isosurface corresponds to the positive part of the wavefunction and the red isosurface corresponds to the negative part of the wavefunction. In the absence of ligands for the bare NC, the HOMO and LUMO are delocalized over the whole NC, both forming *p*-like envelopes on Se and Pb respectively as shown in Fig 5.3a which is in agreement to the findings of [37]. This is however, in contrast to the findings of [38] for CdSe NCs where the valence states are comprised of Se *p* states while the conduction states are comprised of Cd *s* states. In the studies performed in [58], the valence and conduction states of the CdSe NCs do not appear to be symmetric. Also, the valence states appear to be far more dense than the conduction states whereas in our system, both the valence and conduction states are similar and not very dense. The PDOS appears to be symmetric on both sides of the band-gap. This is in contrast to the findings of An et al. [34] where they find the PbSe NCs have sparse electron states and dense hole states. This has implications for exciton dissociation and recombination rates since it is more difficult for excitons to decay if both the conduction and valence states are equally sparse giving rise to longer exciton life times (if the valence states were denser than the conduction states, the electron could transfer energy to the hole and the hole could relax easily in the dense valence states). The NC has no surface traps despite the fact that the surface atoms are not covered by

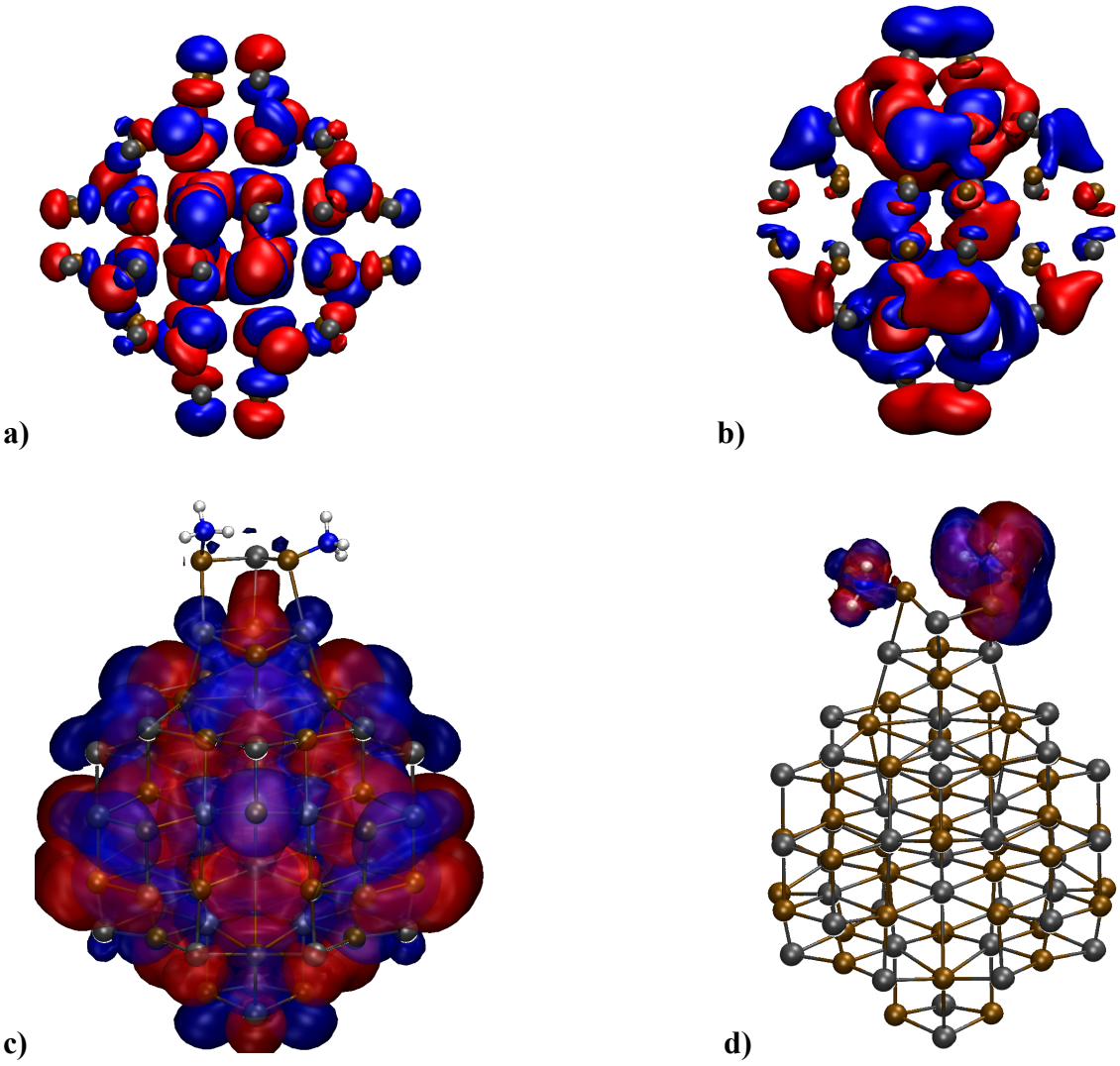

Figure 5.5: Orbital Diagrams of the NC: a) HOMO of the bare NC, b) LUMO of the bare NC, c) HOMO of the ligand-clad NC, d) Orbital with strong contribution from the ligands (Orbital Energy ~ 2eV).

ligands. Since the electroneutrality condition is satisfied, the resulting dangling bonds are either completely filled (Se) or completely empty (Pb) and do not appear in the band gap. The absence of the trap states in the gap is a well-known fact for reconstructed flat surfaces [70-71]. Similar observations were also made previously for the bare [72-73] and ligated CdSe NCs [74] and PbSe NCs [37], where surface traps were observed only on surface atoms with more than one dangling bond. Fig 5.3b shows the PDOS of the 1.5nm cube-octahedral NC, which looks quite similar to the 1.5nm octahedral NC.

Fig 5.4a shows the PDOS (Projected Density of States) for the ligated NC with CH_3S^- ligands on the [100] surface and on the [111] surface (Fig 5.4b). As seen in the figures, the ligand-related levels in the NC remain deep in the valence and conduction orbitals and their significant broadening compared to a free ligand molecule indicates strong mixing with PbSe. It can be seen that the ligand contribution to the frontier orbitals (HOMO and LUMO) is negligible and most of the contribution comes from the core atoms of Pb and Se. This can be seen in the isosurface (isovalue=0.003) orbital plots of the HOMO of the ligand-clad NC in Fig 5.5c. The holes are localized over the Se atoms and the electrons over the Pb atoms. The wavefunctions are distributed primarily deep in the core of the NC and are not delocalized over the ligand atoms so there would not be any optical transitions into the ligands from the HOMO to the LUMO (which comes primarily due to the overlap of these wavefunctions). The ligand contributions can be seen high in the conduction orbitals (~2 eV) as indicated in Fig 5.4a,b,c. In these states, the wave functions are localized over the ligand atoms and the contribution from the NC core is negligible. This can be clearly seen in Fig 5.5d where the isosurface (isovalue=0.003) is shown for the orbital with primary contribution from the ligands. The

overlap of these state wavefunctions with the HOMO is negligible and there will not be any optical transitions into these states. The optical transitions are primarily due to the core atoms of the NC and the ligand atoms do not contribute to the strong visible excitations.

5.4.2 Electronic Coupling

All calculations in this section were carried out using the wB97X functional with the split basis sets of LANL2DZ/6-31+G(d,p). Two sets of coupling calculations were performed: (1) with the [100] facets of the NCs aligned and (2) with the [111] facets of the NCs aligned as shown in Fig 5.6. The NCs were placed at a distance of 0.35nm and then moved away from each other in steps of 0.1nm. A single point calculation was performed at each step. This allowed us to determine the electron and hole coupling as a function of distance. This procedure was carried out for the 1.53nm bare NC, the 1.53nm ligated NC and the 1.53nm cubeoctahedral bare NC. The coupling along the [100] direction for the 1.53nm bare NC is shown as a function of distance in Fig 5.7a,b,c. The coupling falls exponentially with distance allowing us to fit the data to an exponential curve of the form $f(x) = a\exp(-bx)$. This is also shown in Fig 5.7. This fitting procedure was carried out for all the simulations since all of them showed a similar exponential decay with distance. It is therefore, more convenient to plot the data on a semilog plot. Note that the distances are very small – all lie within a range of 0.50-0.7nm. In experimental systems, the NCs in the superlattices do not get closer than a 1nm even for very short ligands (typically a long alkyl chain ligand of about 12-18 C atoms would separate the NCs by about 1.5-2.5 nm). Thus, all further plots will be shown on a semi-log scale and the fitted curves will be plotted instead of the actual data itself.

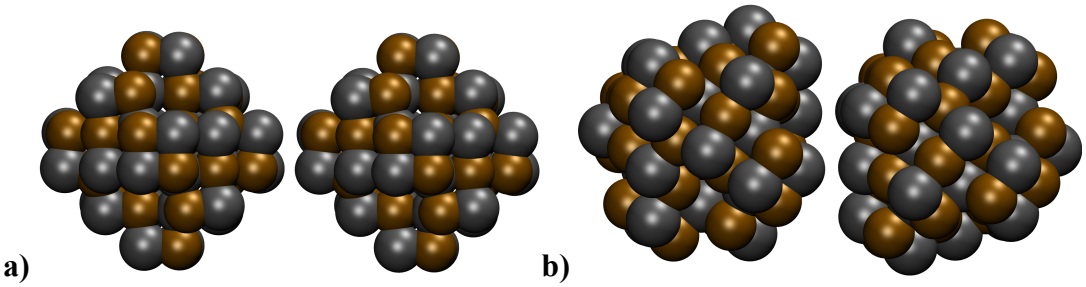

Figure 5.6: Charge coupling calculations for two NCs: a) NCs with [100] facets aligned and b) NCs with [111] facets aligned.

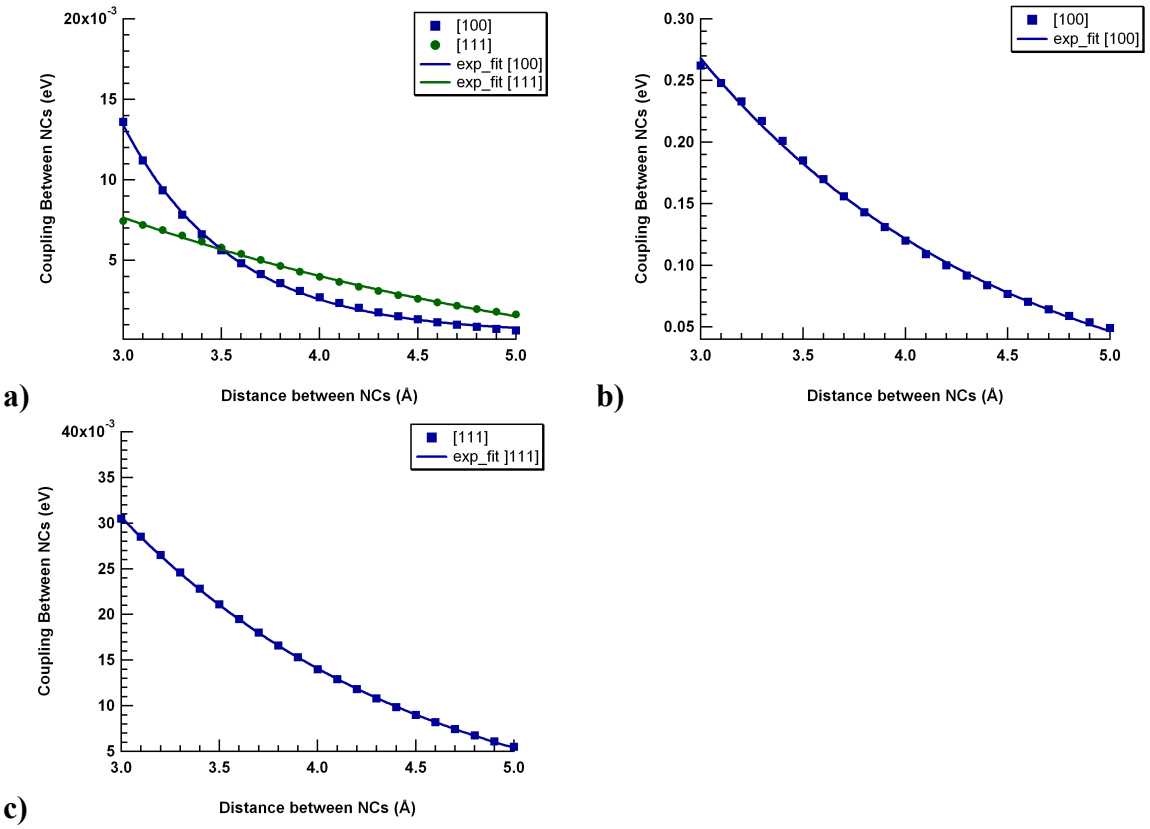

Figure 5.7: Coupling between the bare NCs: a) Hole coupling along the [100] and [111] directions, b) Electron coupling along [100] and c) Electron coupling along [111].

5.4.2.1 1.5nm Bare NC

Plots of the electron coupling and the hole coupling along the [100] direction and the [111] directions are shown in Fig 5.8. The Se atoms contribute towards the hole coupling since the HOMO is centered on the Se atoms and the Pb atoms contribute to the hole coupling since the LUMO is centered on the Pb atoms. The octahedral shape of the NC makes the HOMO wavefunction "bulge" along the [111] directions (since there are more Se atoms along the [111] direction) and is flattened along the [100] directions. This makes the LUMO wavefunction spread in a complementary way to the HOMO. Thus, the LUMO wavefunction is spread more strongly along the [100] directions and more weakly along the [111] directions. This can actually be seen in Fig 5.5a,b. The electron coupling comes from the overlap of the LUMO wavefunctions and the hole coupling from the overlap of the HOMO wavefunctions. Thus, as seen in Fig 5.8, the electron coupling is stronger along the [100] directions and weaker along the [111] directions while the inverse is true for the hole coupling. In addition, the electron coupling is stronger than the hole coupling because the NC is bare and the surface is not passivated. This tends to make the charge wrap tightly within the NC core and thus, the HOMO wavefunction does not "spill out" of the NC core as much as the LUMO. This makes the hole coupling weaker than the electron coupling.

An interesting point to note here is that the [100] facet has an alternating arrangement of Pb and Se atoms due to the rock salt lattice structure of the NC. This means that if one NC was displaced along the [100] direction from the other NC, the Pb atom on the first NC would be aligned with the Se atom on the second and the Se atom on the first NC with the Pb atom on the second as shown in Fig 5.9a. The total wavefunction of the NC

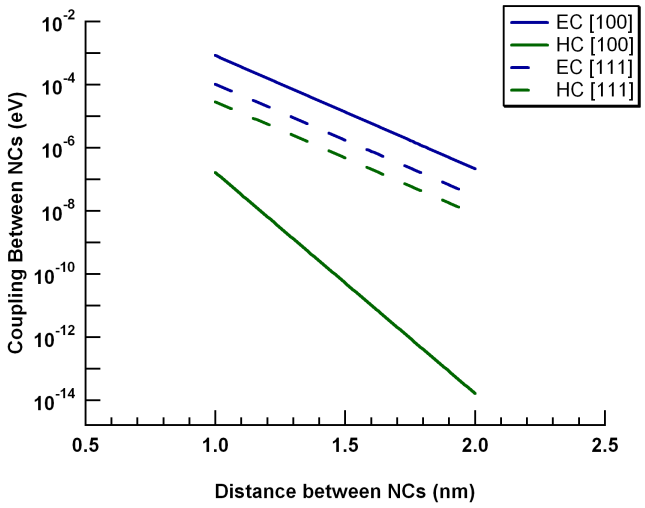

Figure 5.8: Coupling between bare NCs. EC – Electron coupling, HC – Hole coupling. The plot is on a semi-log scale. Coupling along [100] and [111] directions are shown as solid and dashed lines.

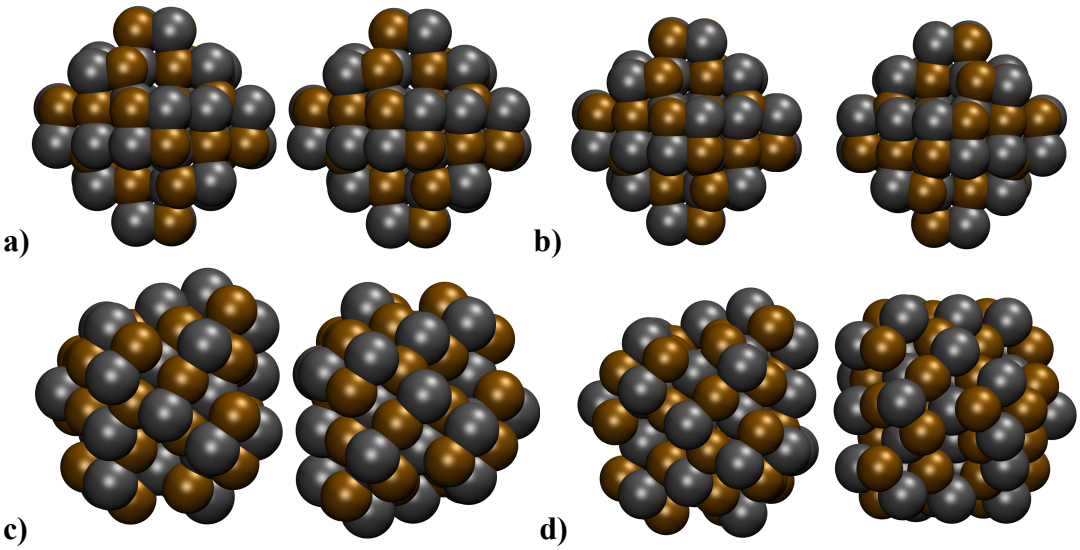

Figure 5.9: Two NCs aligned for coupling: a) Pb and Se atoms on adjacent NCs aligned along the [100] direction corresponding to 0 degrees, b) Pb-Pb and Se-Se atoms aligned along the [100] direction corresponding to 90 degrees, c) NCs with triangular [111] facets orientationally displaced by 30 degrees and d) NCs with triangular [111] facets orientationally aligned.

along the [100] direction is the convolution of the wavefunctions due to the Pb and the Se atoms on the surface. The wavefunctions due to the Pb and Se atoms have opposite parity. Thus, aligning the Pb and Se atoms reduces the coupling of the wavefunctions due to interaction between positive and negative parts. If, on the other hand, the second NC were rotated by 90˚ with respect to the first, the Pb atoms on both NCs would be aligned and so would the Se atoms as shown in Fig 5.9b. This would lead to enhanced coupling. We conducted a series of simulations in which we rotated the second NC with respect to the first in steps of 10˚. The NCs were held at a constant separation of 0.5nm. The results in Fig 5.10a,b. show the variation of the electron and hole coupling as a function of the rotation angle ø. The electron/hole coupling depends on the whether the LUMO/HOMO wavefunction is positive or negative along the [100] direction. The hole coupling decreases with the increase in ø, passes through zero and becomes negative. The zero crossing point occurs somewhere between 50˚ and 60˚.

At this point, the positive and negative components exactly annihilate each other leading to a completely decoupled dimer. A similar curve can be seen in the electron coupling as well (Fig 10b) where the electron coupling becomes stronger (more negative) when the NCs are rotated by 90 degrees with respect to each other. It would be natural at this point to think that the exact angular orientation of the NCs would be determined by the energetic interactions between the NCs and the minimum in energy would determine the orientation. But in order for the energetics of the NC cores to play a role, the NCs would need to be very close to each other and be devoid of ligands. This would not happen in a colloidal system where the NC cores are invariably covered by long chain alkyl ligands.

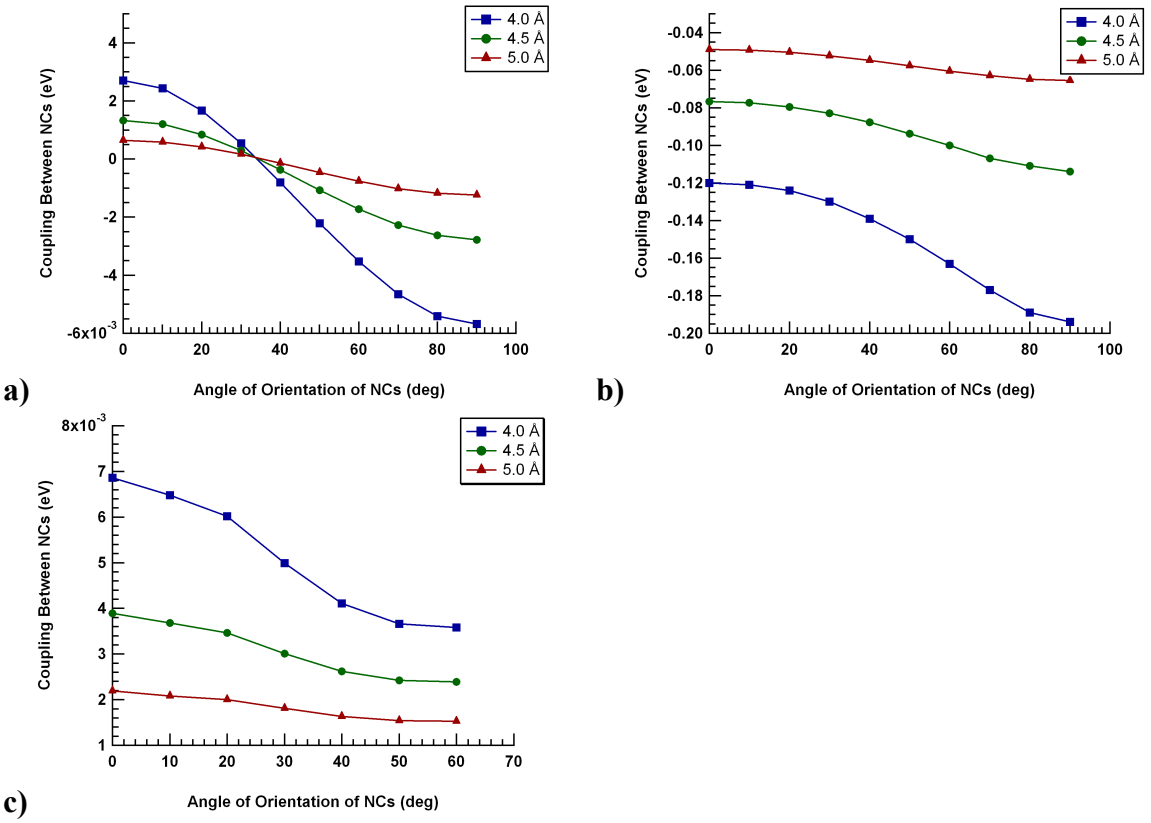

Figure 5.10: Electron and Hole coupling of bare NCs at different distances: a) Hole coupling along [100] as a function of angle of orientation – 0 degrees corresponds to alternating Pb and Se atoms and 90 degrees corresponds to an orientation with Pb-Pb and Se-Se atoms adjacent to each other, b) Electron coupling along [100] as a function of angle of orientation and c) Hole coupling along the [111] direction as a function of the orientation angle – 0 degrees corresponds to a staggered alignment and 60 degrees corresponds to an eclipsed alignment.

The orientation of the NC cores would be determined by the ligand interactions and one would generally encounter an ensemble average of orientations in a superlattice (it is possible to observe aligned cores in a BCC superlattice which has been processed using toluene as a solvent, for further details see [57,75]). Thus, it is important to understand that the charge mobility obtained in the superlattice represents an ensemble average arising from different orientations of the cores.

A similar set of simulations was performed for alignment along the [111] directions as shown in Fig 9c,d. For the [111] facets which are triangular, a rotation by 120 degrees returns the NC to its original orientation. Plots of the hole coupling are shown in Fig 10c where the initial orientation is such that the triangular facets of the adjacent NCs are staggered. It can be seen that the hole coupling is strongest when the triangular facets are staggered which corresponds to 0 degrees on the plot and weakest when the facets are completely eclipsed which corresponds to 60 degrees on the plot. It has been seen that the [111] facets of NCs can be orientationally aligned in a BCC lattice [57]. The hole coupling in such a lattice would be better than say, an FCC lattice where the NCs are orientationally disordered [57].

5.4.2.2 2.1nm Octahedral Bare NC – Effect of Size

The NC considered above is an octahedron. The ratio of the areas of the [100] facet to the [111] facet is about 0.3. In order to investigate our hypothesis of the spatial orientation of the HOMO/LUMO based on the area of the [100] and [111] facets and to investigate the effect of ratio of area of facets, we simulated a 2.1nm octahedral NC. This NC has the same [100] facet area as the 1.5nm NC but has larger [111] facets.

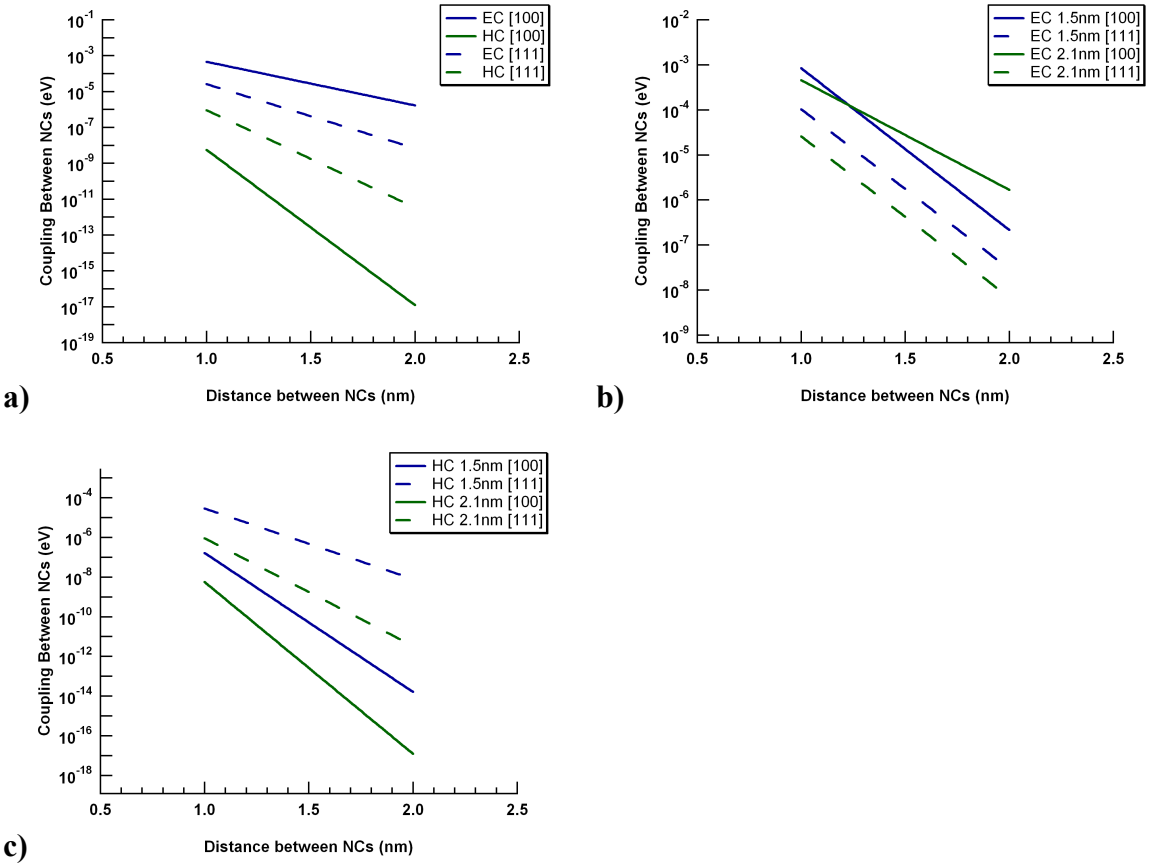

Figure 5.11: Coupling between bare 2.1nm octahedral NCs: a) Electron and hole coupling of 2.1nm octahedral NCs along [100] and [111], b) Electron coupling comparison of 1.5nm octahedral and 2.1nm octahedral NCs and c) Hole coupling comparison of 1.5nm octahedral and 2.1nm octahedral NCs.

If our earlier hypothesis is accurate, the HOMO coupling of this NC should also be much greater along the [111] direction than the [100] direction, similar to the 1.5nm NC.

Fig 5.11a shows the HOMO and LUMO couplings of two 2.1nm NCs. It can be seen from the figure that the HOMO coupling along the [111] direction is indeed greater than along the [100] direction. This is due to the HOMO being oriented more along the [111] facets than along the [100] facets since this NC also has larger [111] facets as compared to the [100] facets similar to the 1.5nm NC. This shows that keeping the [100] facet area the same and increasing the [111] facet area does not change the spatial orientation of the HOMO wavefunction. The LUMO spreads along the [100] directions and hence the electron coupling along the [100] facets is greater than the [111] facets.

Fig 5.11b,c show the comparison of the electron and hole coupling between the 2.1nm NC and the 1.5nm NC. Both the electron and hole coupling of the 2.1nm NC are weaker than the 1.5nm NC since smaller NCs produce stronger couplings than larger NCs. But as can be seen in Fig 5.11c, the hole coupling of the 2.1nm NC along the [111] direction has become stronger than the hole coupling of the 1.5nm NC along the [100] direction even though the 2.1nm NC is clearly larger (has twice the number of atoms of the 1.5nm NC) than the 1.5nm NC. This is clearly the effect of increasing the [111] facet area in the 2.1nm NC. The HOMO is more orientationally aligned along the [111] facets than the 1.5nm NC since the [111] facet area is larger in the 2.1nm NC. Consequently, the LUMO is more oriented along the [100] facets and hence the electron coupling of the 2.1nm NC along the [100] direction is stronger than the electron coupling of the 1.5nm NC as seen in Fig 5.11c. This is a clear indication of the fact that the facet area of the NC has an

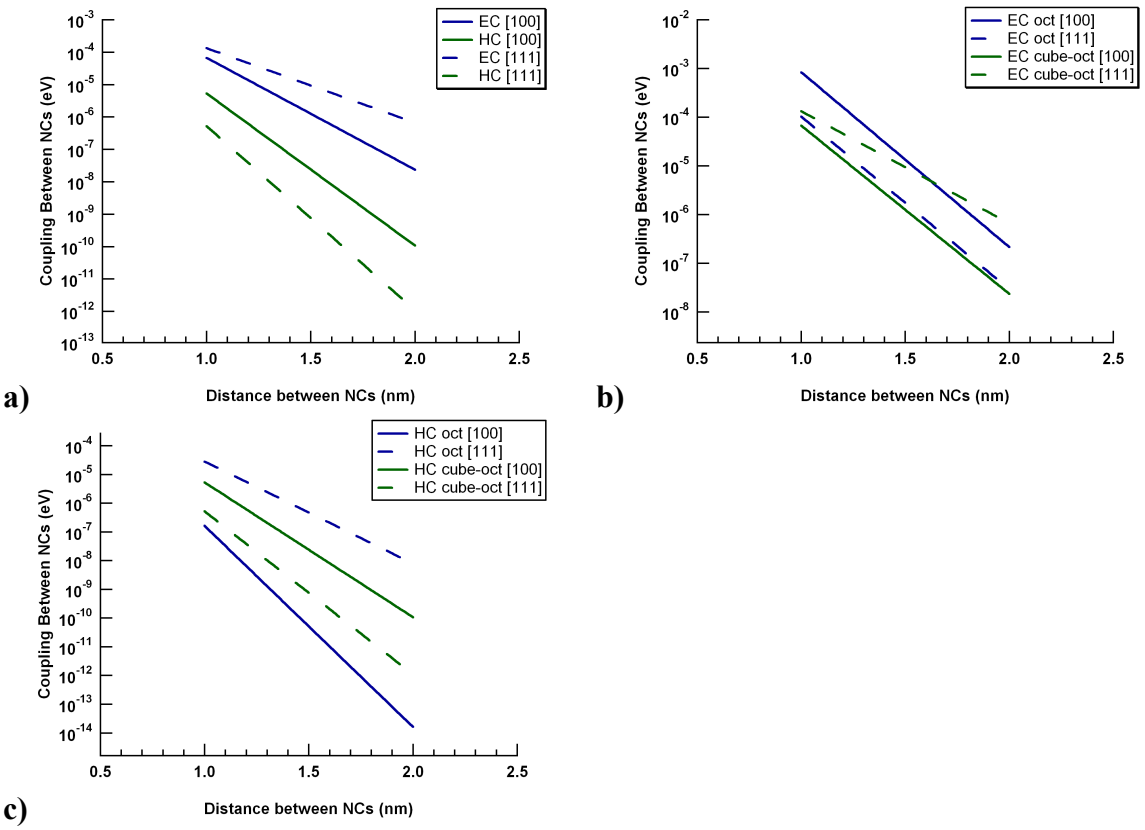

Figure 5.12: Coupling between bare cube-octahedral NCs: a) Electron and hole coupling of cube-octahedral NCs along [100] and [111], b) Electron coupling comparison of octahedral and cube-octahedral NCs and c) Hole coupling comparison of octahedral and cube-octahedral NCs.

effect on the spatial orientation of the HOMO and LUMO wavefunctions and consequently, on the electron and hole couplings.

5.4.2.3 1.5nm Cube-Octahedral Bare NC – Effect of Shape

The shape of the NC considered above is an octahedron. In an octahedron, the area of the [111] facets is larger than that of the [100] facets and there are more Pb atoms on the [111] facets (consequently, more Se atom just underneath the [111] surface) as compared to the [100] facets. The ratio of the areas of the [100] facet to the [111] facet is about 0.3. In order to examine the effects of increasing the area of the [100] facets, we calculated the electronic coupling of a 1.5nm cube-octahedral NC. The cube-octahedral NC is the same size as the octahedral NC and has the same [111] facet area as the octahedral NC but it has a larger [100] facet area. The ratio of areas of the [100] facet to the [111] facet is about 3.3 for the cube-octahedron. Fig 5.12a shows the plots of the electron coupling and hole coupling of the cube-octahedral NC along the [100] and [111] directions. It can be seen that the electron coupling along the [111] direction has become stronger than the electron coupling along the [100] direction while the hole coupling along the [100] direction has become larger than along the [111] direction. The increase in [100] facet area has increased the number of Se atoms. This makes the HOMO wavefunction "bulge" more in the [100] direction and pushes the LUMO wavefunction away from the [100] facets and towards the [111] facets. Importantly, this is not simply an effect of size or the number of atoms in the NC but an effect arising from the shape of the NC and the related ratio of areas of the [100] facets to the [111] facets, which gives a certain directionality to the spatial orientation of the HOMO and LUMO wavefunctions. The electron coupling is thus, weaker along the [100] direction than the [111] and *vice versa* for the hole coupling.

Fig 5.12b,c show the comparison of electron coupling and hole coupling between the octahedral NC and the cube-octahedral NC. The electron coupling along the [100] direction has decreased and has increased along the [111] direction as compared to the octahedral shape. The inverse is true for the hole coupling. Thus, increasing the [100] facet area of the NC changes the spatial orientations of the HOMO and LUMO wavefunctions. In experimental systems, very small NCs (~2-3nm diameter) tend to have a more octahedral shape while larger NCs (~6-7nm diameter) have a cube-octahedral or a truncated cube like shape with larger [100] facets and smaller [111] facets. In fact, as the NC diameter increases, the area of the [111] facets shrink and large NCs (~12-15nm diameter) are almost cubic in shape with almost no significant [111] facets at all.

5.4.2.4 1.5nm Ligand-clad NC – Effect of Ligands

Colloidal NCs studied in a solution processed experimental system are not bare. The surface of the NCs is passivated by ligands. To study the effect of the ligands, we used the method described in section 3 to "cap" the NCs with HS^- ligands to provide surface passivation as shown in Fig 5.13. We used the tiny ligand HS^- rather than a longer alkyl chain for computational efficiency. There is, in any case, a growing tendency to consider shorter ligands in experimental studies, since it is hoped they will promote more closely spaced NC superlattices. We then calculated the coupling between two NCs as described in the previous section. Fig 5.14 shows the electron and hole couplings of the ligand-clad NCs. One of the first observations to make is that the hole coupling has become much stronger along both [100] and [111] facets. This is perhaps because the ligands passivating the surface aid hole transport. Since the NC is no longer bare, the HOMO wavefunction spreads outside the NC much more than the bare NC aided of course, by

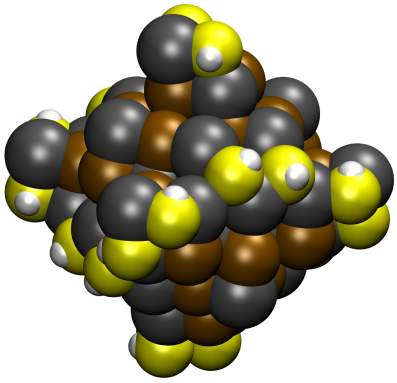

Figure 5.13: A 1.5nm NC core passivated by HS^- ligands.

the presence of the ligands. The slope of the hole coupling along [111] shows that it decreases much more gradually with distance than the other curves. On the [100] facets, the ligands sit atop the Se atoms where they block the electron transfer and aid hole transfer. Consequently, as shown in Fig 5.14a, the hole transfer curves have increased in magnitude and become comparable to those for electron transfer.

Fig 5.14b shows a comparison of the electron coupling between the bare and ligand-clad NC. Electron coupling along the [100] direction has decreased because of the shielding effect of the ligands. Electron transfer along the [111] direction is large in magnitude at small distances (less than 1nm) because the ligands on the [100] facets on adjacent NCs are very close to each other and thus there is some electronic coupling between the ligands themselves. This is manifested as electron coupling between the NCs. But the electron coupling has a sharp slope and falls off very quickly as the distance increases because of shielding by the ligands. Thus, the ligands alter the wavefunctions of the NC so that hole transfer is greatly enhanced. It can also be seen that the electron transfer curves have a sharper slope showing that the electron coupling decays faster with distance on the ligand-clad NC as compared to the bare NC along the respective directions.

We computed the reorganization energy as described in section 5.2.2 and then computed the electron and hole transfer rates as described in the section 5.2. The resulting curves are shown in Fig 5.15. The curves are of course, proportional to the square of the electron and hole coupling values as described in section 5.2. The magnitude of the electron/hole transfer rate has been reported in ns^{-1}. Thus, the time scale for hole transport over a

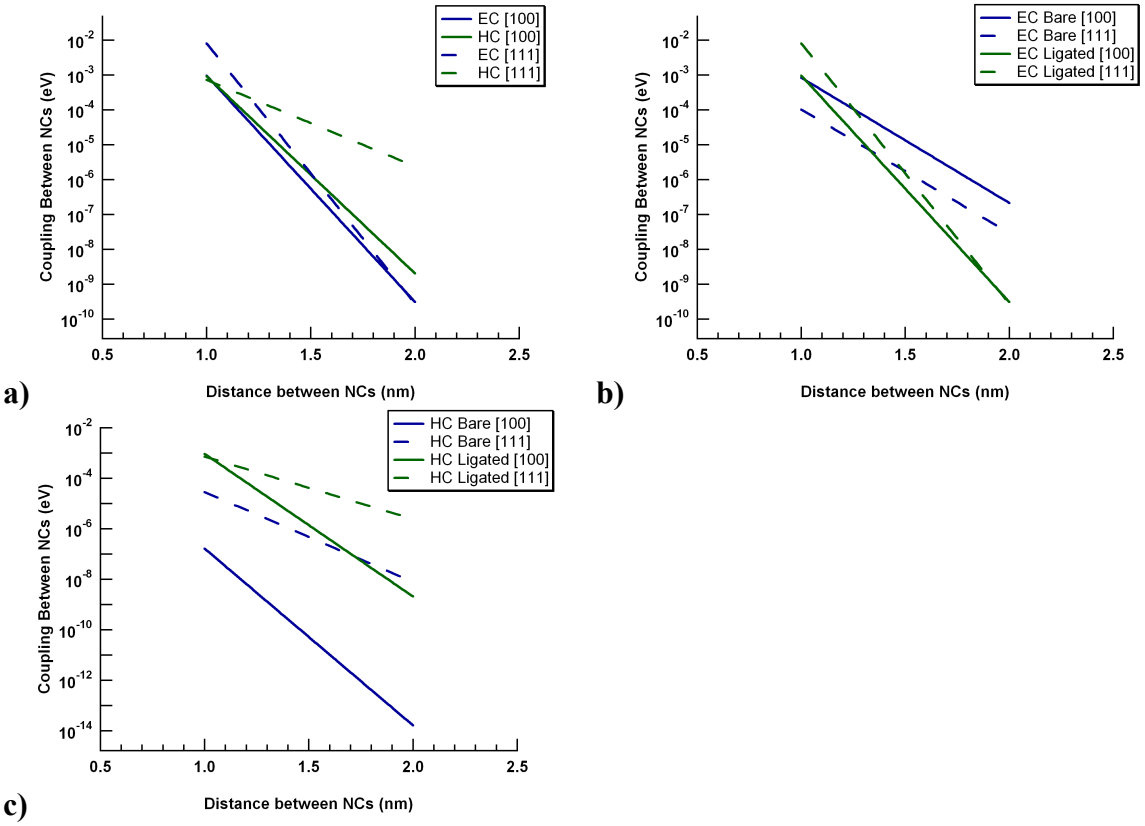

Figure 5.14: Coupling between ligand-clad NCs: a) Electron and hole coupling of ligated NCs along [100] and [111] directions, b) Comparison of electron coupling between bare and ligand-clad NCs and c) Comparison of hole coupling between bare and ligand-clad NCs.

distance of 1-2nm ranges from 10 to 100 hundred nanoseconds. This rate is considerably smaller than experimentally determined rates for NC systems [76]. To compare with [76], at a distance separation of 1.5nm, the experimentally computed transfer rate for a 2.7nm diameter PbS NC is about 0.5-1.0ns whereas the hole transfer rate in our system is about 100ns. But the experimental fit relates to NCs linked through a bidentate linker molecule (benzene-dithiol) and the authors report that for PbS NCs capped with oleic acid, the transfer rate is an order of magnitude smaller which would make it about 10ns. They report a rate of decay of the charge transfer curve to be about 2.6 (slope of the line). Our decay rates for the curves shown in Fig 5.15 range from 0.75 to 3.5. Thus, the range of our decay rates covers the experimentally fitted one which implies that our curves are qualitatively accurate with respect to the experimental ones but differ by a constant factor. There may be several reasons for the order of magnitude difference. The capping ligands in experimental systems are much longer than the ones used here which may enhance hole transport. The presence of solvents can also change the transfer rates as well and while colloidal NCs are typically solution processed, our simulations have been carried out in vacuum and do not take the effect of solvents into account [77]. The coupling and the rate are also dependent on the functional and basis sets used in our calculation. It is known that the charge transfer rate falls off exponentially with distance. In our calculations, we are using the LANL2DZ basis set which has gaussian functions primarily. This means that we are approximating an exponential decay as a function of gaussian functions which decay much more rapidly than an exponential function. To get better accuracy, one must use a larger basis set with more diffuse functions which can approximate exponential decay better.

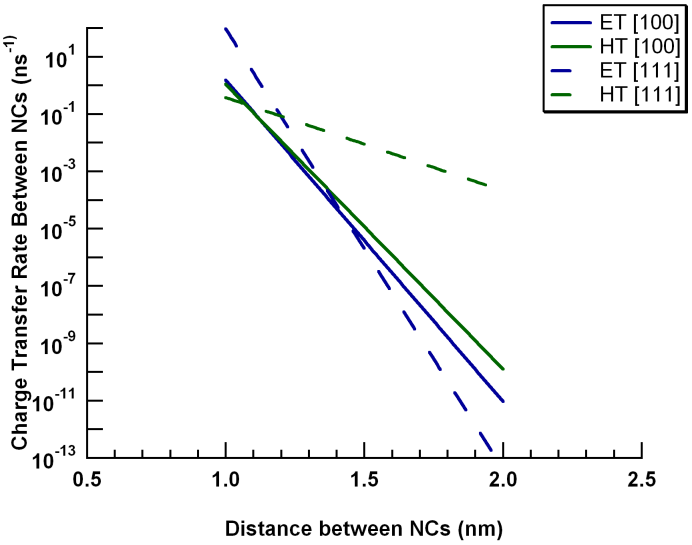

Figure 5.15: Charge transfer rates between ligand-clad NCs. Electron and hole transfer rates are shown along the [100] and [111] directions.

But even with all these differences, our calculations are only about an order of magnitude off from the experimentally determined value. Thus, the qualitative trends are more important to consider here than the absolute magnitude of the transfer rates.

5.4.3 Charge Carrier Mobility

We computed the electron and hole mobility for the 1.5nm octahedral ligand-clad NC as described in section 2 for BCC and FCC superlattices along the [100] (2^{nd} NN) direction and along the nearest neighbor (NN) directions – [111] in BCC and [110] in FCC. The mobility was computed using the charge transfer rates obtained from section 5.4.2.4 above. The plots of the mobility are shown in Fig 5.16. The x-axis is the distance d between the two NCs along the nearest neighbor (NN) direction. The distance along the [100] direction will be $2d/\sqrt{3}$ for BCC and $\sqrt{2}d$ for FCC. It can be seen from Fig 5.16a,b that both the electron and hole mobilities along the NN direction are much greater than along the 2NN direction. In a BCC lattice, the NCs are orientationally ordered [57] and the [100] and [111] facets are aligned. Thus, the hole mobility is greater than the electron mobility along the [111] direction and the electron mobility decays much faster (has a sharper slope) than the hole mobility. In the FCC lattice however, the NCs are orientationally disordered and this allows for alignment between the [100]-[100], [100]-[111] and [111]-[111] facets. The mobility along any direction would be the weighted average of all the above rates of charge transfer noted above. This results in the electron and hole mobility being comparable along the [100] and the [111] directions. Fig 5.16c,d show a comparison of the electron and hole mobilities between a BCC and an FCC lattice. As shown in Fig 5.16a, as the NN distance between the NCs increases, both the electron and hole mobility along the [100] direction is higher in an FCC lattice as

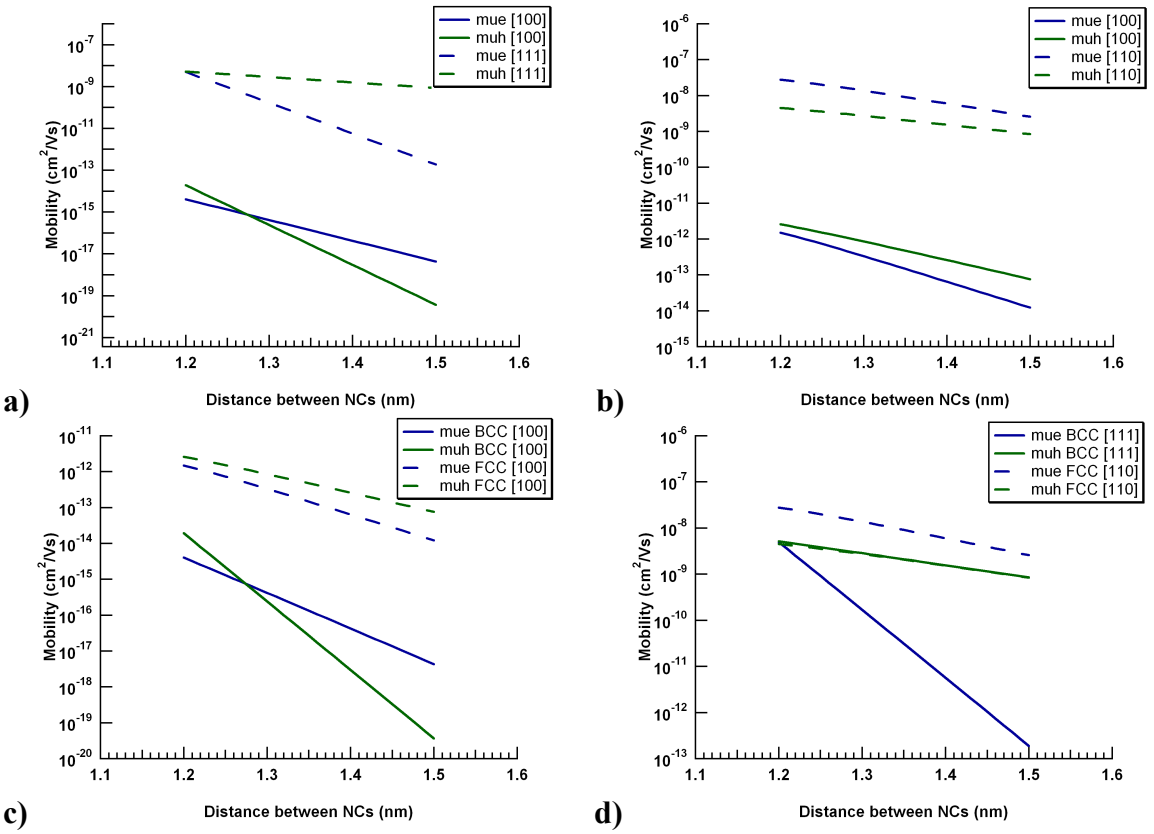

Figure 5.16: Mobility in BCC and FCC superlattices as a function of Nearest Neighbor (NN) distance: a) Mobility in BCC lattice, b) Mobility in FCC lattice, c) Mobility comparison along the [100] direction in BCC and FCC lattices and d) Mobility comparison along the Nearest Neighbor (NN) direction in BCC (111) and FCC (110) lattices.

compared to a BCC lattice since the mobility in the FCC lattice is an average of charge transfer between the [100]-[100], [100]-[111] and [111]-[111] facets while in BCC it is only between the [100]-[100] facets. Along the NN direction, the electron mobility in the BCC lattice is very low and falls off very steeply with distance since the electron transfer rate between the [111] facets is very small. But the hole mobility in the BCC lattice and the electron and hole mobility in the FCC lattice are comparable. Thus, the highest mobility depends on the type of lattice as well as the direction along which the mobility is measured which in turn, is governed by the shape of the NCs and the ratio of areas of the [100] and [111] facets. In general, if choice is between a BCC and an FCC lattice symmetry and if the NCs had large [111] facets, either a BCC or an FCC lattice symmetry would be desirable whereas if the NCs had large [100] facets, an FCC lattice symmetry would be much more desirable over a BCC lattice symmetry.

5.5. Conclusions

We have presented a detailed calculation of electronic structure of PbSe NC systems using DFT. We have calculated the structure of the bare NCs and also shown how reconstruction of the surface can lower the energy of the NC. We have not considered here the existence of [110] facets which have been alluded to in [63]. Even if they do exist, it is likely that they are very small in comparison to the [100] and [111] facets and would appear in larger NCs than considered here. We have shown a method of ligand attachment which ensures charge neutrality of the whole NC. The grafting density of the ligands would be an important factor in the determining the electronic structure of the NCs. We have not considered dispersion forces between the ligand molecules in this study, but they would need to be considered if a larger NC were considered with longer

chain ligands. The dispersion forces would dictate how densely the ligands could be grafted on the facets [62]. Also, the reconstruction and ligand attachment considered here are such that all possible atomic sites are filled. In real systems, the facet reconstruction may not be perfect and all possible sites may not be occupied by ligands. The random arrangement of reconstructed atomic sites and ligand arrangement could alter the envelope of the wavefunctions and would be an interesting problem for a systematic study.

The density of states of the bare and ligand-clad NC show that the filled states are centered around the Se atoms and unfilled states around the Pb atoms. The ligand states are well mixed with the core atoms and do not directly contribute greatly towards the frontier orbitals but lie deep in the DOS. Some ligand attachments on CdSe and PbSe NCs have been found to produce trap states in the DOS [37-38]. These states usually arise when the bonding is not complete and there are dangling bonds or oversaturated bonds. Such bonding could occur in the NCs considered in this study although we have not attempted to study them here. If the trap states do exist, they can produce transitions into the LUMO by absorption of unintended frequencies of light. They would also affect the frontier orbitals directly and thus alter the charge transfer characteristics of the NCs.

Assuming a charge hopping model and Marcus theory, we have seen that the charge transfer rate is directly proportional to the square of the coupling strength (or the transfer integral). The electron and hole coupling depend on the overlap of the LUMO and HOMO wavefunctions of adjacent NCs respectively which in turn depends on the spatial distribution and orientation of the respective wavefunctions. Importantly, we have shown here that the spatial orientation of the wavefunction depends on the shape of the NC and

the areas of the [100] and [111] facets. The larger the facet area, the more the HOMO is oriented along that direction which makes the LUMO spread in the complementary direction. We have also shown that orientational alignment of the NC itself can lead to stronger or weaker coupling and charge transfer. The orientation of the HOMO and LUMO determines how much overlap occurs along a particular direction and thus, determines the strength of the coupling. We have compared two different shapes of NCs in this regard – the octahedral and the cube-octahedral. The octahedral shape showed strong electron coupling along the [100] direction and strong hole coupling along the [111] direction whereas the cube-octahedral shape showed strong electron coupling along the [111] direction and strong hole coupling along the [100] direction.

Our studies of the effect of ligands on the electronic coupling shows that the type of ligands considered here enhance hole coupling and shield the electron coupling. There have been studies where the NCs have been treated appropriately in order to enhance electron coupling as well (for example, with PbSe NCs treated with hydrazine showed reversible transitions from n-type to p-type) [25]. Thus, appropriate ligand chemistry can be utilized to produce both electron and hole transfer in these NC systems and can provide a gateway to produce ambipolar devices. Some NC systems are known to have anisotropic ligand coverage [62] typically because some of the facets have lost the ligands. Such defective grafting could lead to enhanced charge transfer along certain preferred directions. NCs that have been exposed to air for a long time have been hypothesized to lose ligands on the [100] facets preferentially [62] and self-assemble into orientationally aligned BCC superlattices. This would mean that hole transport along the [111] directions would be large. If the details of ligand attachments were known in

advance such as described above, then one could potentially seek to make self-assembled superlattices with an appropriate symmetry to produce the greatest charge transfer possible.

We have also calculated the charge mobility in BCC and FCC superlattices. The mobility is a function of all possible orientations of the adjacent NCs where charge hopping would occur. The charge transfer rates calculated here are far smaller in magnitude than experimental systems for several reasons, the small size of the NC considered, the level of theory used, the type of ligands chosen etc. The typical transfer rates for large NCs (~6-7nm diameter) in experimental systems is about 10-100 ns^{-1} for a distance of about 2-3nm which happens to be the NN distance in the superlattices formed through self-assembly. This is still very slow for efficient charge transfer to produce viable photovoltaic cells. We have also shown that the transfer rates fall exponentially so small defects in the lattice can quickly kill charge transfer between NCs. Effective charge transfer can occur if the NCs are much closer (~1nm). This is consistent with the improvement in transport observed experimentally using compact linker molecules such as Ethane di-thiol (EDT), pyrazine, hydrazine, benzene di-thiol (BDT) etc. [25-30,76]. Such systems would bring the NCs much closer together (below 1nm) and thus can produce higher coupling. But the use of linker molecules does not come without drawbacks. Since these molecules link the NCs together through chemical bonds, the NCs lose some of their quantum confinement. It also results in disordered superattices [26,76]. Nevertheless, they form an interesting study and we hope that the study presented here will encourage others to model such systems of NCs linked though small molecules using computational tools like DFT.

REFERENCES

[1] P. Bhattacharya; S. Ghosh; A. D. Stiff-Roberts, Annu. Rev. Mat. Res., 34, 1 (2004)

[2] C. Murray; C. Kagan; M. Bawendi, Annu. Rev. Mat. Sci., 30, 545 (2000)

[3] M. Law, J. Goldberger, P. Yang, Annu. Rev. Mat. Res., 34, 83-122 (2004)

[4] M. S. Skolnick, D. J. Mowbray, Annu. Rev. Mat. Res., 34, 181-218 (2004)

[5] D. V. Talapin; J.-S. Lee; M. V. Kovalenko; E. V. Shevchenko, Chem. Rev., 110, 389 (2010)

[6] A. P. Alivisatos, J. Phys. Chem., 100, 13226-13239 (1996)

[7] Y. Wu, C. Wadia, W. Ma, B. Sadtler, A. P. Alivisatos, Nano Lett., 8, 2551–2555 (2008)

[8] M. G. Panthani, V. Akhavan, B. Goodfellow, J. P. Schmidtke, L. Dunn, A. Dodabalapur, P. F. Barbara, B. A. Korgel, J. Am. Chem. Soc., 130, 16770–16777 (2008)

[9] J. J. Choi, Y-F. Lim, M. E. B. Santiago-Berrios, M. Oh, B-R. Hyun, L. Sun, A. C. Bartnik, A. Goedhart, G. G. Malliaras, H. D. Abruna, F. W. Wise, T. Hanrath, Nano Lett., 9, 3749–3755 (2009)

[10] W. Ma, J. M. Luther, H. Zheng, Y. Wu, A. P. Alivisatos, Nano Lett., 9, 1699–1703 (2009)

[11] J. M. Luther, M. Law, M. C. Beard, Q. Song, M. O. Reese, R. J. Ellingson, A. Nozik, J. Nano Lett., 8, 3488–3492 (2008)

[12] K. S. Leschkies, T. J. Beatty, M. S. Kang, D. J. Norris, E. S. Aydil, ACS Nano, 3, 3638–3648 (2009)

[13] J. J. Urban, D. V. Talapin, E. V. Shevchenko, C. R. Kagan, C. B. Murray, Nat. Mater., 6, 115–121 (2007)

[14] B. Sun, H. Sirringhaus, Nano Lett., 5, 2408–2413 (2005)

[15] D. V. Talapin, C. B. Murray, Science, 310, 86–89 (2005)

[16] S. Coe, W-K. Woo, M. Bawendi, V. Bulovic, Nature, 420, 800–803 (2002)

[17] A. H. Mueller, M. A. Petruska, M. Achermann, D. J. Werder, E. A. Akhadov, D. D. Koleske, M A. Hoffbauer, V. I. Klimov, Nano Lett., 5, 1039–1044 (2005)

[18] S. A. McDonald, G. Konstantatos, S. Zhang, P. W. Cyr, E. J. D. Klem, L. Levina, E. H. Sargent, Nat. Mater., 4, 138–142 (2005)

[19] A. N. Shipway, E. Katz, I. Willner, Chem. Phys. Chem., 1, 18–52 (2000)

[20] V. A. Akhavan, B. W. Goodfellow, M. G. Panthani, D. K. Reid, D. J. Hellebusch, T. Adachi, B. A. Korgel, Energy Environ. Sci., 3, 1600–1606 (2010)

[21] V. A. Akhavan, B. W. Goodfellow, M. G. Panthani, B. A. Korgel, Modern Energy Rev., 2, 25–27 (2010)

[22] C. B. Murray, S. Sun, W. Gaschler, H. Doyle, T. A. Betley, C. R. Kagan, IBM J. Res. Dev., 45, 47–56 (2001)

[23] P. Liljeroth, K. Overgaag, A. Urbieta, B. Grandidier, S. G. Hickey, D. Vanmaekelbergh, Phys. Rev. Lett., 97, 096803 (2006)

[24] B. Lee, P. Podsiadlo, S. Rupich, D. V. Talapin, T. Rajh, E. V. Shevchenko, J. Am. Chem. Soc., 131, 16386-16388 (2009)

[25] D. V. Talapin, C. B. Murray, Science, 310, 86-89 (2005).

[26] J. M. Luther, M. Law, Q. Song, C. L. Perkins, M. C. Beard, A. J. Nozik, ACS Nano, 2(2), 271-280 (2008).

[27] M. V. Kovalenko, M. Scheele, D. V. Talapin, Science, 324, 1417 (2009).

[28] K. Overgaag, P. Liljeroth, B. Grandidier, D. Vanmaekelbergh, ACS Nano, 2, 3, 600-606 (2008).

[29] C. Kagan, APS March Meeting 2012.

[30] J-H. Choi, A. T. Fafarman, S. J. Oh, D-K. Ko, D. K. Kim, B. T. Diroll, S. Muramoto, J. G. Gillen, C. B. Murray, C. Kagan, Nano Letters, 12, 2631−2638 (2012).

[31] J-W. Luo, A. Franceschetti, and A. Zunger, Nano Letters, 8, 10, 3174-3181 (2008).

[32] A. Franceschetti, L. W. Wang, G. Bester, A. Zunger, Nano Letters, 6, 5, 1069-1074 (2006).

[33] J. M. An, A. Franceschetti, A. Zunger, Nano Letters, 7, 7, 2129-2135 (2007).

[34] J. M. An, A. Franceschetti, S. V. Dudiy, A. Zunger, Nano Letters, 6, 12, 2728-2735 (2006).

[35] M. Califano, G. Bester, A. Zunger, Nano Letters, 3, 9, 1197-1202 (2003).

[36] B. Kiran , A. K. Kandalam , R. Rallabandi , P. Koirala , X. Li, X. Tang, Y. Wang, H. Fairbrother, G. Gantefoer, K. Bowen, J. Chem. Phys., 136, 024317 (2012).

[37] Y. Gai, H. Peng, J. Li, J. Phys. Chem. C, 113, 21506–21511 (2009).

[38] O. Voznyy, |J. Phys. Chem. C, 115, 15927–15932 (2011).

[39] S. A. Fischer, A. M. Crotty, S. V. Kilina, S. A. Ivanovc, S. Tretiak, Nanoscale, **4**, 904 (2012).

[40] H. Bao, B. F. Habenicht, O. V. Prezhdo, X. Ruan, Phys. Rev. B 79, 235306 (2009).

[41] H. M. Jaeger, S. Fischer, O. V. Prezhdo, J. Chem. Phys. 136, 064701 (2012).

[42] I-H. Chu, M. Radulaski, N. Vukmirovic, H-P. Cheng, L-W. Wang, J. Phys. Chem. C, 115, 21409–21415 (2011).

[43] H. Oberhofer, J. Blumberger, Phys. Chem. Chem. Phys., 14, 13846-13852 (2012).

[44] H. Oberhofer, J. Blumberger, J. Chem. Phys. 133, 244105 (2010).

[45] W-Q. Deng, W. A. Goddard III, J. Phys. Chem. B, 108, 8614-8621 (2004).

[46] E. F. Valeev, V. Coropceanu, D. A. da Silva Filho, S. Salman, J-L. Bredas, J. Am. Chem. Soc., 128, 9882-9886 (2006).

[47] K. Senthilkumar, F. C. Grozema, C. F. Guerra, F. M. Bickelhaupt, F. D. Lewis, Y. A. Berlin, M. A. Ratner, L. D. A. Siebbeles, J. Am. Chem. Soc., 127, 14894-14903 (2005).

[48] K. Senthilkumar , F. C. Grozema , F. M. Bickelhaupt , L. D. A. Siebbeles, J. Chem. Phys. 119, 9809 (2003).

[49] G. Sini, J. S. Sears, J-L. Bredas, J. Chem. Theory Comput., 7, 602–609 (2011).

[50] E-G. Kim, V. Coropceanu, N. E. Gruhn, R. S. Sanchez–Carrera, R. Snoeberger, A. J. Matzger, J-L. Bredas, J. Am. Chem. Soc., 129, 13072-13081 (2007).

[51] P. Winget, J-L. Bredas, J. Phys. Chem. C, 115, 10823–10835 (2011).

[52] J. Arago, J. C. Sancho-García, E. Ortí, D. Beljonne, J. Chem. Theory Comput., 7, 2068–2077 (2011).

[53] C. Butchosa, S. Simon, A. A. Voityuk, Org. Biomol. Chem., **8**, 1870–1875 (2010).

[54] R. C. I. MacKenzie , J. M. Frost , J. Nelson, J. Chem. Phys., 132, 064904 (2010).

[55] P. Löwdin, J. Chem. Phys., 18, 365 (1950).

[56] R. A. Marcus, J. Chem. Phys., 24, 966 (1956).

[57] K. Bian, J. J. Choi, A. Kaushik, P. Clancy, D-M. Smilgies, T. Hanrath, ACS Nano, 5, 4, 2815–2823 (2011).

[58] J. J. Choi, Y-F. Lim, M. B. Santiago-Berrios, M. Oh, B-R. Hyun, L. Sun, A. C. Bartnik, A. Goedhart, G. G. Malliaras, H. D. Abruna, F. W. Wise, T. Hanrath, Nano Letters, 9, 11, 3749-3755 (2009).

[59] Gaussian 09, Revision A.1, M. J. Frisch, G. W. Trucks, H. B. Schlegel, G. E. Scuseria, M. A. Robb, J. R. Cheeseman, G. Scalmani, V. Barone, B. Mennucci, G. A. Petersson, H. Nakatsuji, M. Caricato, X. Li, H. P. Hratchian, A. F. Izmaylov, J. Bloino, G. Zheng, J. L. Sonnenberg, M. Hada, M. Ehara, K. Toyota, R. Fukuda, J. Hasegawa, M. Ishida, T. Nakajima, Y. Honda, O. Kitao, H. Nakai, T. Vreven, J. A. Montgomery, Jr., J. E. Peralta, F. Ogliaro, M. Bearpark, J. J. Heyd, E. Brothers, K. N. Kudin, V. N. Staroverov, R. Kobayashi, J. Normand, K. Raghavachari, A. Rendell, J. C. Burant, S. S. Iyengar, J. Tomasi, M. Cossi, N. Rega, J. M. Millam, M. Klene, J. E. Knox, J. B. Cross, V. Bakken, C. Adamo, J. Jaramillo, R. Gomperts, R. E. Stratmann, O. Yazyev, A. J. Austin, R. Cammi, C. Pomelli, J. W. Ochterski, R. L. Martin, K. Morokuma, V. G. Zakrzewski, G. A. Voth, P. Salvador, J. J. Dannenberg, S. Dapprich, A. D. Daniels, Ö. Farkas, J. B. Foresman, J. V. Ortiz, J. Cioslowski, and D. J. Fox, Gaussian, Inc., Wallingford CT, 2009.

[60] J. Heyd, J. E. Peralta, G. E. Scuseria, R. L. Martin, J. Chem. Phys., 123, 174101 (2005).

[61] J. Jasieniak, M. Califano, S. E. Watkins, ACS Nano, 5 (7), 5888–5902 (2011)

[62] C. R. Bealing, W. J. Baumgardner, J. J Choi, T. Hanrath, R. G Hennig, ACS Nano, 6 (3), 2118–2127 (2012).

[63] C. Fang, M. A. van Huis, D. Vanmaekelbergh, H. W. Zandbergen, ACS Nano, 4, 211–218 (2010).

[64] E. V. Shevchenko, D. V. Talapin, N. A. Kotov, S. O'Brien, C. B. Murray, Nature, 439, 55–59 (2006).

[65] I. Moreels, K. Lambert, D. D. Muynck, F. Vanhaecke, D. Poelman, J. C. Martins, G. Allan, Z. Hens, Chem. Mater., 19, 6101–6106 (2007).

[66] V. Petkov, I. Moreels, Z. Hens, Y. Ren, Phys. Rev. B, 81, 241304 (2010).

[67] Q. Dai, Y. Wang, X. Li, Y. Zhang, D. J. Pellegrino, M. Zhao, B. Zou, J. Seo, W. W. Yu, ACS Nano, 3, 1518–1524 (2009).

[68] A. Franceschetti, Phys. Rev. B, 78, 075418 (2008).

[69] A. Franceschetti, Phys. Rev. B, 76, 161301 (2007).

[70] M. D. Pashley, Phys. Rev. B, 40, 10481–10487 (1989).

[71] G. P. Srivastava, Rep. Prog. Phys., 60, 561–613 (1997).

[72] A. Puzder, A. J. Williamson, F. Gygi, G. Galli, Phys. Rev. Lett., 92, 217401 (2004).

[73] M. Yu, G. W. Fernando, R. Li, F. Papadimitrakopoulos, N. Shi, R. Ramprasad, Appl. Phys. Lett., 88, 231910 (2006).

[74] S. V. Kilina, S. Ivanov, S. Tretiak, J. Am. Chem. Soc., 131, 7717–7726 (2009).

[75] A. P. Kaushik, P. Clancy, J. Comp. Chem. (accepted).

[76] J. J. Choi, J. Luria, B-R. Hyun, A. C. Bartnik, L. Sun, Y-F. Lim, J. A. Marohn, F. W. Wise, T. Hanrath, Nano Letters, 10, 1805–1811 (2010).

[77] B-R. Hyun, A. C. Bartnik, J-K. Lee, H. Imoto, L. Sun, J. J. Choi, Y. Chujo, T. Hanrath, C. K. Ober, F. W. Wise, Nano Letters, 10, 318-323 (2010).

[78] M. S. Hybertsen, S. G. Louie, Phys. Rev. B, 34, 5390 (1986).

CHAPTER 6

Future Work

6.1 Introduction

Typical charge transfer rates between large NCs (~6-7 nm diameter) in experimental systems are about 10-100 ns^{-1} for a distance of about 2-3 nm corresponding to the NN distance in the superlattices formed through self-assembly. This is still very slow for the efficient charge transfer rates necessary to produce viable photovoltaic cells. Effective charge transfer can occur if the nearest neighbor distance between the self-assembled NCs is much lesser (~1 nm). This idea is consistent with the improvement in transport observed experimentally using "compact" linker molecules that form covalent bonds between NC pairs, such as Ethane di-thiol (EDT), pyrazine, hydrazine, benzene di-thiol (BDT) etc. [1-7]. Such systems are capable of bringing the NCs much closer together (below 1 nm) and thus can produce higher coupling. Fig 6.1 shows the various possible types of linkers between two NCs [8]. There have been advances recently in producing such NC dimers, although the films that are produced do not possess long-range order and hence, do not form ordered superlattices. Films of NCs capped with relatively long oleic acid ligands produce superlattices with well-defined symmetries whereas films of NCs dimers produced through ligand exchange with oleic acid become glassy and lose their ordered symmetries [2,7]. Nevertheless, they form an interesting system to study computationally, using DFT for example.

There have been a few studies of charge transport through NCs connected by linker molecules or nano wires. Studies by the Zunger group for instance, have shown that the shape and size of a nanowire linking NCs can determine the extent of localization of

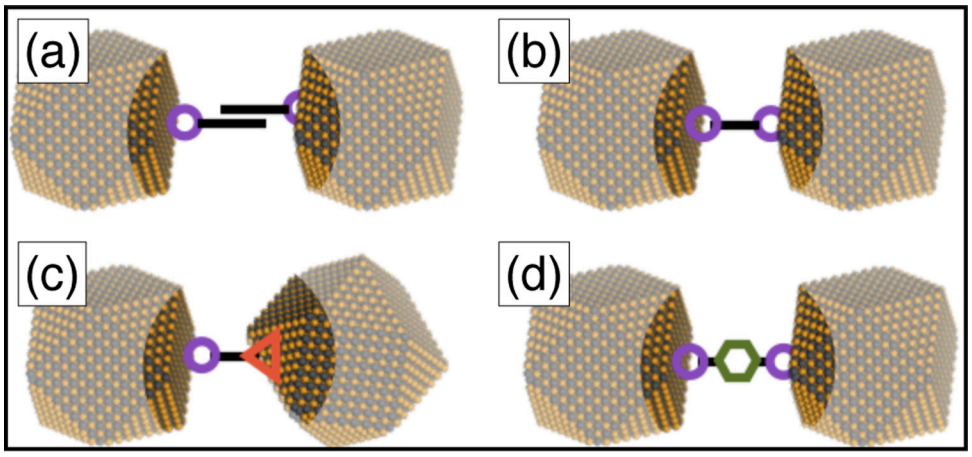

Figure 6.1: Illustration of various molecular inter-dot coupling configurations. (a) basic ligand (e.g., ethanethiol), (b) symmetric bidentate linker (e.g., 1,2-ethanedithiol), (c) asymmetric linker (e.g., mercaptopropionic acid), and (d) aromatic linker (e.g., 1,4-benzenedithiol). Figure reproduced from [8].

charge densities and other critical properties such as exciton binding energies and wavefunction entanglement [9].More recently, a study of two CdSe NCs linked by Sn_2S_6 linker molecule was performed by Chu *et al*. [10]. They found that the most probable mechanism for charge transfer in such a system is through phonon-assisted hopping. In chapter 5, we discussed the mechanism of charge transfer through a hopping model consistent with Marcus theory [11]. Since the NCs were not connected but merely within close proximity of each other, the assumption of simple charge hopping is sufficient. But if two NCs are linked through a linker molecule, there could be more than one mechanism by which charge transfer takes place between the NCs. Fig 6.2 illustrates the mechanisms by which charge transfer could take place between two NCs linked through a bidentate linker molecule. Fig 6.2d shows the mechanism of phonon-assisted hopping of charge. Here, localized charge couples with a localized phonon mode forming an electron (hole)-phonon pair. The electron-phonon pair is then transported across the linker molecule into the adjacent NC thus, accomplishing charge transfer.

6.2 Nanocrystals Connected by Linker Molecules

We have performed simulations of compactly linked NC dimers. We constructed PbSe NC dimers of 1.5 nm diameter linked by an EDT (ethane di-thiol) molecule, as shown in Fig 6.3a. The LUMO and LUMO+1 wavefunctions are shown in Fig 6.3c,d. The LUMO wavefunction is slightly more localized on NC2 and the LUMO+1 wavefunction is slightly more localized on NC1 (the HOMO and HOMO-1 wavefunctions behave in a similar manner). But the wavefunctions do, in fact, spread over both the NCs; they are simply stronger on one or other of the NCs. If, however, a different linker molecule is

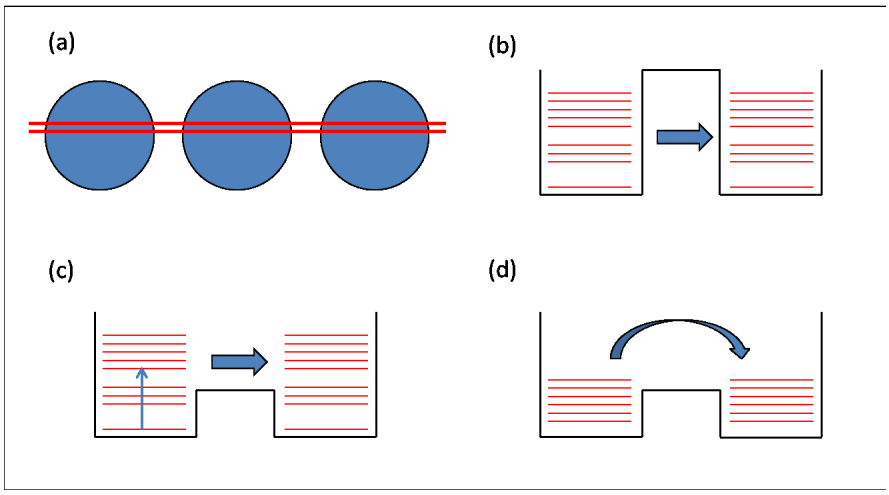

Figure 6.2: Different possible mechanisms for the electron transport in a NC dimer: (a) bulk crystal-like Bloch state electron transport; (b) direct tunneling mechanism without the help of a phonon; (c) over-the-barrier activation mechanism; and (d) phonon-assisted hopping. Figure reproduced from [10].

chosen, say BDT (benzene di-thiol), as shown in Fig 6.4c, the LUMO is almost completely localized on NC2 and the LUMO+1 on NC1 (Fig 6.4d). Thus, the linker chemistry is clearly influencing the envelope of the wavefunctions. In such a case, it may be necessary to consider the role of electron-phonon coupling assisting the charge transfer between the NCs.

6.3 Constrained Density Functional Theory (CDFT)

To calculate the charge coupling between the NCs, it is no longer possible to transform the Hamiltonian onto a separate basis of the individual NCs since the NCs are now linked to each other. One of the techniques that can be used in this situation is called Contrained DFT [12]. Constrained DFT gives an accurate description of long-range charge transfer states. By optimizing the geometries of constrained systems, it is possible to explore the relaxation effects of diabatic states and thus directly calculate the inner-sphere reorganization energy. This reorganization energy fully considers the donor-acceptor interactions as compared to the indirect four-point approach as described in chapter 5. The basic idea of constrained DFT is to find an effective external potential - the constraining potential $V_c w_c(r)$ to add to the Hamiltonian so that the resulting ground-state density satisfies some specific density constraint, i.e., $\int w_c(r)\rho_c(r)dr = N_c$, where $w_c(r)$ is the operator that defines the property of interest. Here $\rho_c(r)$ is the charge density and N_c is the total charge. The constraint can be a local charge q, for instance, a charge-separated state D+A−. In the case described here, one NC would become the donor D and the other NC would become the acceptor A. The constraint may be applied as $\Delta q = -1$ for the donor NC and $\Delta q = +1$ for the acceptor NC.

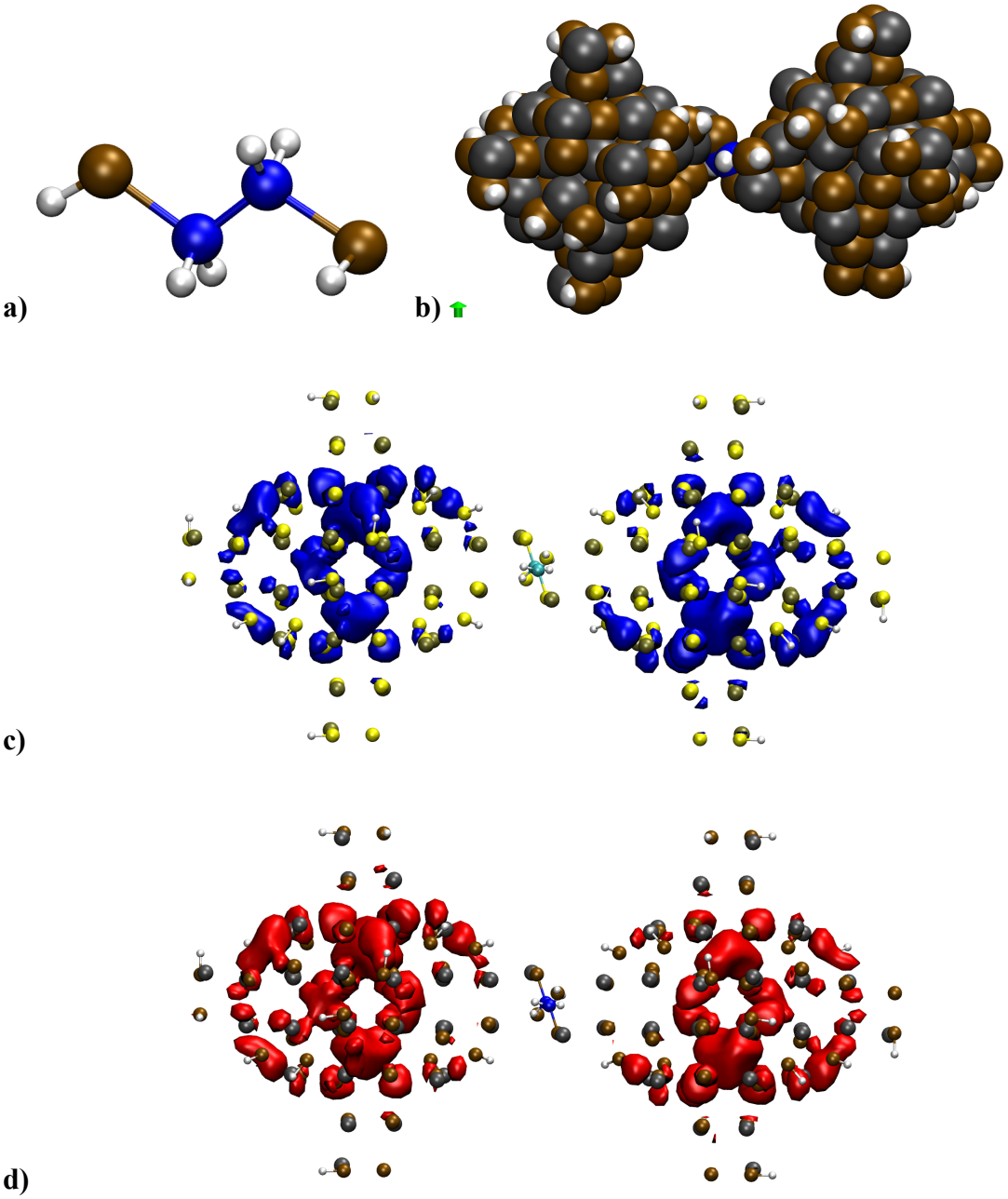

Figure 6.3: a) Ethane di-thiol (EDT) molecule, b) Two NCs linked by EDT, c) LUMO of the NC dimer and d) LUMO+1 of the NC dimer.

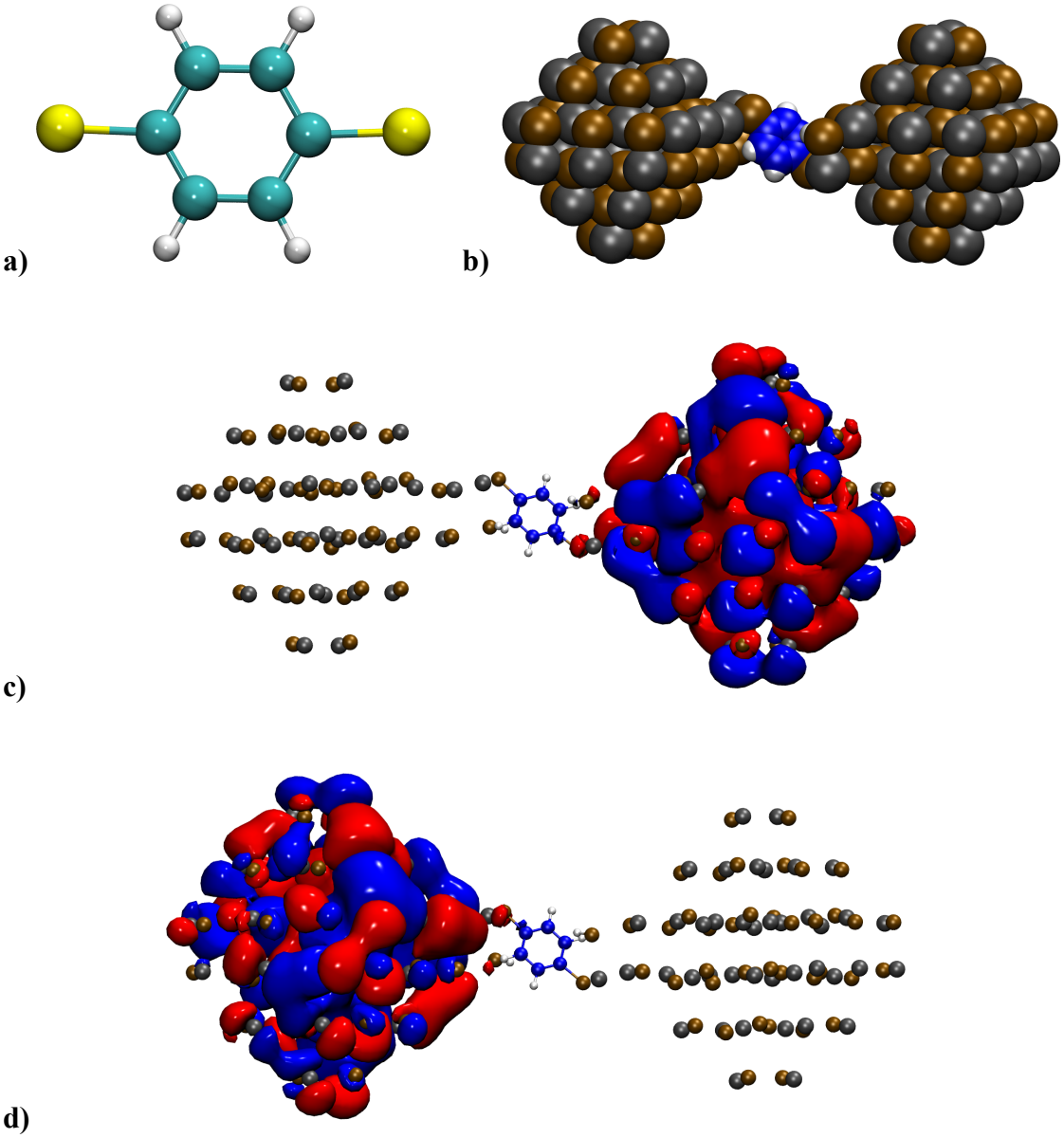

Figure 6.4: a) Benzene di-thiol (BDT) molecule, b) Two NCs linked by BDT, c) LUMO of the NC dimer and d) LUMO+1 of the NC dimer.

The Hamiltonian formed from the donor-acceptor complex does not have an orthogonal basis since the basis formed from the diabatic states of the donor and acceptor need not be orthogonal to each other. By orthogonalizing the projector matrix formed from $w_c(r)$ and solving the generalized eigen value problem for the projector matrix, the eigen basis for the projector matrix can be obtained. The Hamiltonian of the donor-acceptor complex can then be projected on this basis and the coupling energy can be obtained from the off-diagonal components of the resultant matrix.

6.4 Electron-Phonon Coupling

To understand the role of phonons in the electron transport, the key task is to calculate the electron-phonon coupling. The electron-phonon coupling $C_{i,j}$ can be calculated as:

$$C_{i,j} = \left\langle \psi_i \left| \frac{\partial H}{\partial \mu} \right| \psi_j \right\rangle \tag{1}$$

where μ is the phonon mode, H is the single particle Hamiltonian and $|\psi_i\rangle$ is the i^{th} eigenstate of H [10]. The displacement of atomic position under phonon mode μ causes a change of potential energy in H, which induces the electron-phonon coupling. But, as shown in Fig 6.4, for the LUMO and LUMO+1 coupling, the electron wavefunction has a very small amplitude near the linker molecule and a small phonon density of state. Thus, one can ignore the phonon modes of the linker molecule. The dominant process is the multi-phonon process described by Marcus theory, where the electron-phonon coupling causes reorganization energy and the electron-electron coupling comes from state anticrossing. In that case, the diagonal electron-phonon coupling constants, $C_{i,i}$, and the spring constants of the phonon modes are used to calculate the reorganization energy (the atomic relaxation energy due to the occupation of the electronic state "i"). For this

purpose, we can restrict the electron-phonon coupling within each NC. So, the left (right) electron state will only couple to the phonon modes within the left (right) NC. We can thus calculate the electron-phonon coupling inside an isolated NC.

Under the Marcus theory, what is most important is the reorganization energy. This is the atomic relaxation energy after the electron transfer from one state to another state. As discussed above, this energy can be calculated from the diagonal electron-phonon coupling constant: $C_{i,i}$. More specifically, if $C_{i,i}(R) = \left\langle \psi_i \left| \frac{\partial H}{\partial R} \right| \psi_i \right\rangle$ is calculated for each atomic coordinate R , then $C_{i,i}(R)$ can be considered as the additional force on each atom R when the electron is removed from (or added on) electron state ψ_i . We can employ the Marcus theory formula to calculate the charge transfer rate τ^{-1} from one quantum dot to a neighboring quantum dot:

$$\tau^{-1} = |V_c|^2 \sqrt{\frac{\pi}{\hbar^2 k_B T \lambda}} exp\left(-\frac{(\lambda+\Delta E)^2}{4\lambda k_B T}\right) \quad (2)$$

where V_c is the coupling constant and λ is the reorganization energy given by $\lambda = \sum_j \lambda_j$ where $\lambda_j = 2\frac{|C_{i,i}(R)|^2}{2\hbar\omega_j}$. Here, λ_j is the contribution to the total reorganization energy from the phonon mode of frequency ω_j. The above Marcus theory treats the phonon degree of freedom classically within the harmonic approximation and does not allow quantum tunneling of the atomic movement. One can however treat the atomic movement quantum mechanically under harmonic approximations. The corresponding charge transfer rate formula is [13-15]

a)

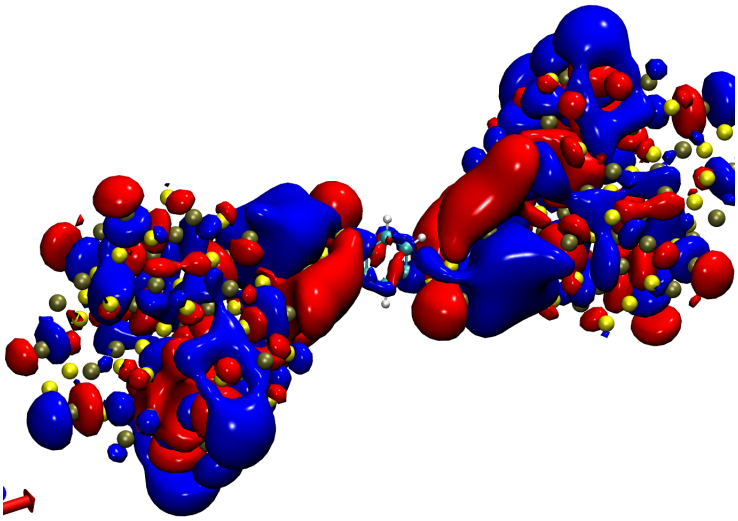

b)

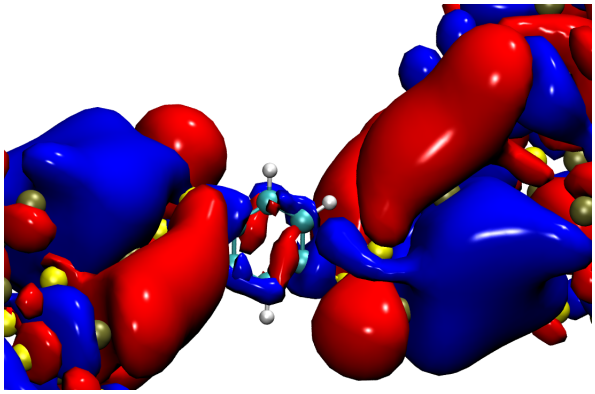

Figure 6.5: a) LUMO+2 level of the NC dimer linked by a BDT linker molecule and b) Zoomed image of the same dimer – delocalization of the wavefunction through the linker molecule can bee seen.

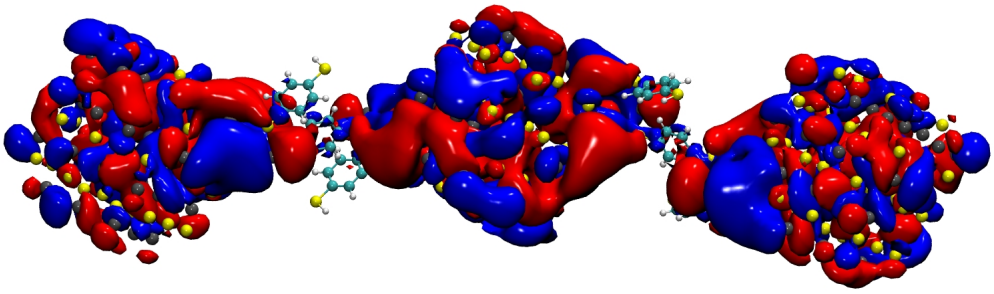

a)

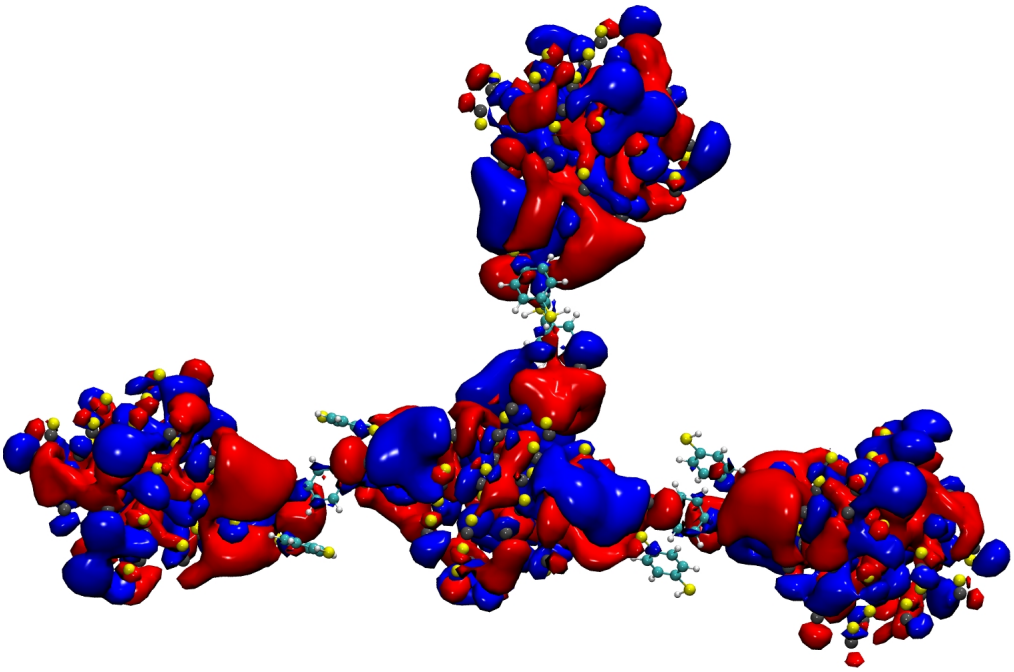

b)

Figure 6.6: a) LUMO+2 level of the 3 NCs linked by BDT linker molecules and b) LUMO+2 level of the 4 NCs linked by BDT linker molecules.

$$\tau^{-1} = \frac{1}{\hbar^2}|V_c|^2 \int_{-\infty}^{\infty} dt exp\left\{ i\,(\varepsilon_a - \varepsilon_b)t/\hbar \right.$$

$$\left. - \sum_j S_j\left[(2n_j - 1) - n_j e^{-i\omega_j t} + (n_j + 1)e^{i\omega_j t}\right] \right\} \qquad (3)$$

Here, $n_j = 1/[\exp(\hbar\omega_j/k_BT)-1]$ is the phonon occupation number for phonon mode j at frequency ω_j, $S_j = \lambda_j/\hbar\omega_j$ is the Huang-Rhys factor for the phonon mode ω_j and λ_j is the reorganization energy for mode ω_j. To calculate λ_j, one first transforms the atomic force $C_{i,i}(R)$ (due to electron-phonon coupling) to the force on phonon mode ω_j, and then calculates the relaxation on each phonon mode as a harmonic oscillator.

To calculate the single phonon transitions caused by a phonon-induced coupling between the "i" and "j" electron states from two neighboring NCs through the linker molecule it is necessary to include the phonon modes from the linker molecule. This is seen in Fig 6.5 where the wavefunctions associated with the two degenerate LUMO+2 levels have been shown. The wavefunctions are delocalized between the two NCs through the linker molecule. In fact, this system could be extended to include many more NCs, all connected through the linker molecules. Fig 6.6 shows such systems of NCs with the degenerate LUMO+2 levels of the entire system. As can be seen, the wavefunctions simply extend over the entire network of NCs completely delocalized through the linker molecules. In experimental systems, it is possible that many NCs are connected in this way and perhaps, through more than one linker between any two NCs. In this case, it is possible that the charge transfer is assisted to a much larger extent through electron-phonon coupling between these wavefunctions and the phonon modes of the linker

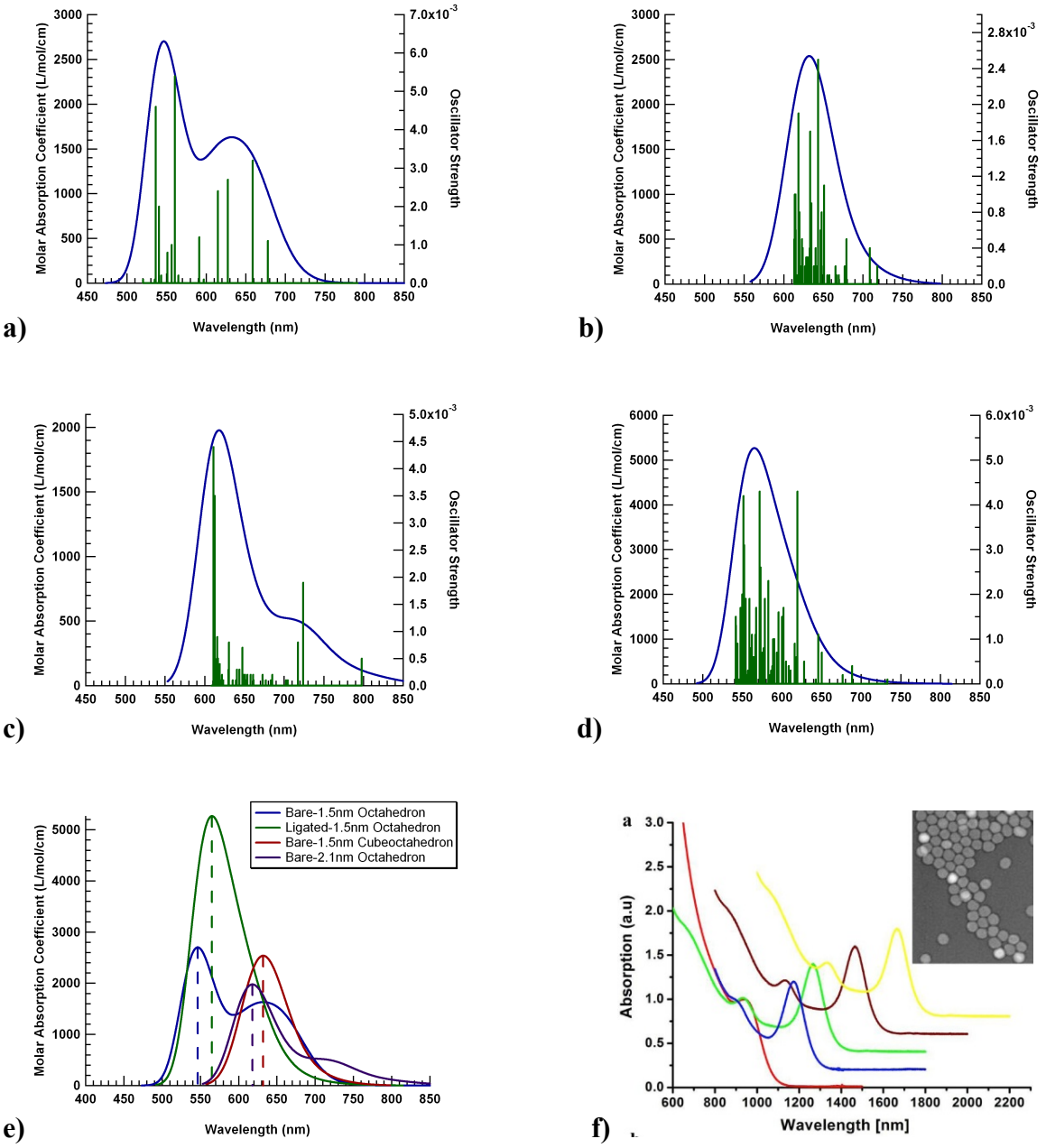

Figure 6.7: Absorption spectrum of NCs – a 5eV Gaussian broadening has been used: a) 1.5nm diameter octahedral bare NC, b) 1.5nm diameter cube-octahedral NC, c) 2.1nm diameter bare octahedral NC, d) 1.5nm diameter ligand-clad octahedral NC, e)

Comparison of absorption spectra of (a),(b),(c),(d) and f) Experimental absorption spectrum of PbSe NCs from a 2.85nm diameter NC to a 5.6nm diameter NC [20].

molecule. In fact, the entire system could be vibrating through coupled phonon modes of all the NCs and linker molecules. The method described above could be applied to eigen states that come primarily from the linker molecule to evaluate charge transport in the NC dimers. Also, the particular ligand chemistry of the linker molecule and type of bonding to the NC surfaces would determine the phonon modes of the linker molecule and hence, the electron-phonon coupling. A systematic study of different types of ligands and the evaluation of the charge transport through phonon assisted processes would be of great value in guiding experiments to probe energy levels beyond the traditional HOMO/LUMO.

6.5 Time Dependent Density Functional Theory (TD-DFT)

All the studies carried out in this thesis have been on the ground state of the NCs. It is possible to model the excited states of the NCs within the DFT formalism through Time Dependent DFT or TD-DFT. TD-DFT can be used to study the evolution of the charge density in the excited states and also get information about which excitations are allowed, the energy required for the excitation and how strong the excitations are comparatively. This can used to plot the photo-excitation and decay spectra of the NCs to compare qualitatively to experimental spectra. Systematic studies could be performed on different ligand chemistries producing different excitation and emission spectra. We performed a TD-DFT calculation on a 1.5 nm bare octahedral NC, a 1.5 nm bare cube-octahedral NC, a 2.1 nm bare octahedral NC and a 1.5nm octahedral ligand-clad NC described in

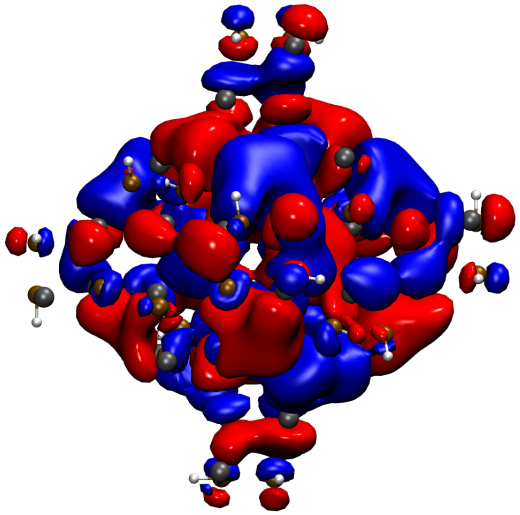

a)

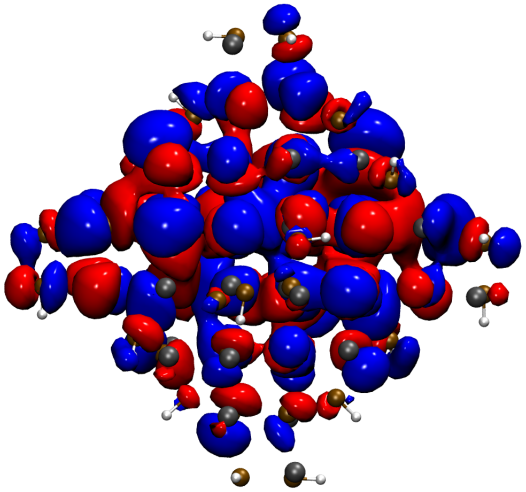

b)

Figure 6.8: a) Wavefunction of the electron in the excited state and b) Wavefunction of the hole in the excited state.

chapter 5. TD-DFT computes single electron vertical excitations corresponding to different energies of transitions. The output from the TD-DFT calculation gives the nature and symmetry of the transition, the particular orbitals between which the transition happens, the energy for the excitation, the wavelength of light that produces the excitation and the oscillator strengths for each excitation. The oscillator strengths in TD-DFT correspond to intensities of absorption in experimental systems. Thus, a higher oscillator strength would correspond to a brighter line in the absorption spectrum. A zero oscillator strength would correspond to a forbidden transition. The absorption spectrum of the NCs is shown in Fig 6.7a,b,c,d. The transition lines are convoluted with Gaussian broadening function of 5eV. As can be seen, the peak in the absorption spectrum shifts towards the red region of the spectrum with increasing size of the NC from 1.5 nm diameter octahedral to 2.1 nm diameter octahedral. This is due to the shrinking band-gap with increasing size of the NCs. As shown in Fig 6.7 d,e, capping the surface of the bare NC with ligands also produces a small red shift in the absorption peak. This shift would be sensitive to the particular ligand chemistry involved. The absorption spectra thus obtained can be used to compare to experimental absorption spectra as shown in Fig 6.7f. Also, once the excited state corresponding to a particular excitation has been computed, the geometry of the NC can be relaxed at the selected excited state and the emission spectrum from this state to the ground state can be found. This would also be sensitive to the ligand chemistry and can be very useful in comparing emission spectra obtained from experimental systems.

TD-DFT computes an excitation as a linear combination of several transitions from the valence states into the conduction states.

a)

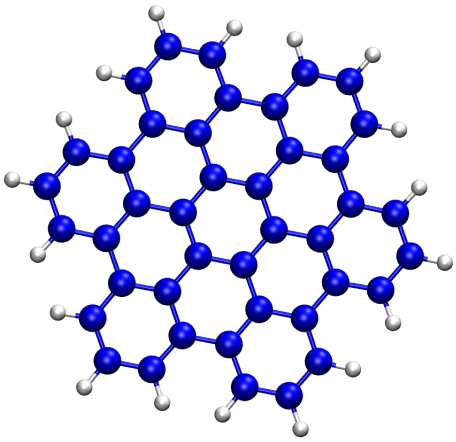

b)

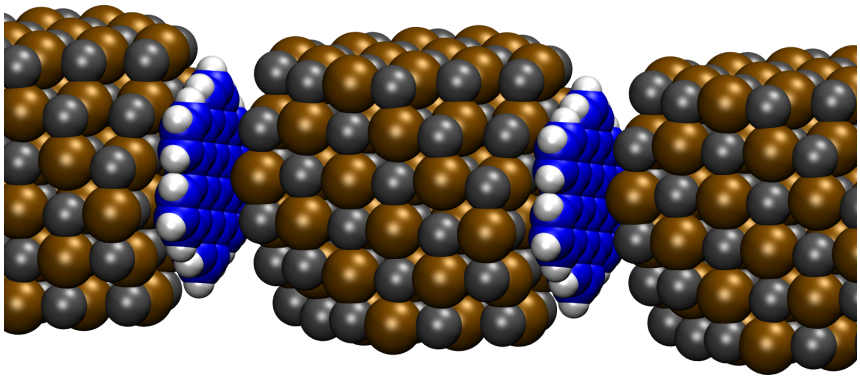

Figure 6.9: a) Hexabenzocoronene (HBC) molecule and b) NCs separated by HBC molecules used as spacers.

Thus, it is difficult to separate the electron and hole wavefunctions in the excited state from the eigen basis of the excited state alone. To overcome this problem, if a Singular Value Decomposition (SVD) of the exited state transition electron density matrix is performed, then the eigen basis can be represented as a separate left and right orthonormal bases and the left and right singular vectors corresponding to the largest singular value could be considered – the left singular vector would correspond to the hole and right singular vector would correspond to the electron. A plot of the electron and hole for a particular excitation corresponding to 618 nm absorption line in Fig 6.7c is shown in Fig 6.8a,b. Once the electron (hole) wavefunction has been obtained, other properties of the system can be determined. Typically, if charge transfer has to occur, the time for charge transfer should be smaller than the decay time of the exciton from the excited state. This would be modified by the distance of separation of the NCs and the type of the linker molecule connecting them. *Ab initio* studies of this nature on NC systems would be of immense value to the scientific community.

6.6 Future Directions

The specific chemistry of the ligands alters the envelope of the wavefunctions of the NC. In chapter 5, we saw that the alkyl ligands used to passivate the NC surface enhanced hole coupling. Treating the NCs with hydrazine, for example, would enhance electron coupling for hydrazine and would alter the surface chemistry of the NC through ligand exchange [1]. There have been several studies about altering ligand chemistry to enhance charge transport since the molecular structure of the linker can be used to tailor the electronic coupling between NCs. But, inherently organic molecules are generally insulating. To address this problem, Talapin *et al.* introduced Metal Chalcogenide

Complexes (MCCs) such as zintl ions, which are inorganic, as short ligands for NCs [16-18]. In contrast to bulky alkyl chain ligands that provide colloidal stability in NCs solutions through steric hindrance. MCCs induce negative charges on NCs surfaces and this results in electrostatic repulsion between the NCs providing colloidal stability. Thus, even with the short length of MCCs, a variety of NCs passivated with MCCs can be dispersed in polar solvents such as water, hydrazine, dimethylsulfoxide, and ethanolamine. Upon deposition on a substrate, MCC-passivated NCs form structures with short inter-NC distances and have strong inter-dot coupling. These structures can be transformed into amorphous or crystalline metal chalcogenides upon thermal annealing [17]. Thus, annealing of MCC-passivated NC superlattices results in structures where NCs are embedded in an inorganic semiconductor metal chalcogenide matrix. Since the inorganic semiconductors provide a lower potential barrier between NCs compared to organic molecules, such structures provide exciting opportunities for achieving strong coupling strength. A critical drawback of conventional thermal annealing is that the NCs are prone to sinter under conditions far below the melting point of the corresponding bulk material. Baumgardner *et al*. recently demonstrated pulsed laser annealing as a promising approach to transform self-assembled PbX NC superlattices into so-called "confined-but-connected" structures without sintering encountered in thermal annealing [19]. Another technique of having "almost confined but connected" structures is being tested by the Hanrath group here at Cornell using covalent organic frameworks (COFs) made of molecules such as hexabenzocoronene (Fig 6.9a) as spacers between the NCs as shown in Fig 6.9b. Since there are potentially thousands of linker materials that can be used, it very quickly becomes infeasible to test all of them in experiments. It is here that *ab initio*

computational studies would be of great help, not only to understand the fundamental physics of each process, but also to test candidate ligand chemistries with greater ease than can be studied experimentally. It can therefore, be used to screen potentially viable candidates for enhanced charge transport, thereby guiding experiments. Given the tremendous research effort currently directed towards a better understanding of the electronic structure of NCs, many such studies are likely to emerge in the near future.

REFERENCES

[1] D. V. Talapin, C. B. Murray, Science, 310, 86-89 (2005).

[2] J. M. Luther, M. Law, Q. Song, C. L. Perkins, M. C. Beard, A. J. Nozik, ACS Nano, 2(2), 271-280 (2008).

[3] M. V. Kovalenko, M. Scheele, D. V. Talapin, Science, 324, 1417 (2009).

[4] K. Overgaag, P. Liljeroth, B. Grandidier, D. Vanmaekelbergh, ACS Nano, 2, 3, 600-606 (2008).

[5] C. Kagan, APS March Meeting 2012.

[6] J-H. Choi, A. T. Fafarman, S. J. Oh, D-K. Ko, D. K. Kim, B. T. Diroll, S. Muramoto, J. G. Gillen, C. B. Murray, C. Kagan, Nano Letters, 12, 2631−2638 (2012).

[7] J. J. Choi, J. Luria, B-R. Hyun, A. C. Bartnik, L. Sun, Y-F. Lim, J. A. Marohn, F. W. Wise, T. Hanrath, Nano Letters, 10, 1805–1811 (2010).

[8] T. Hanrath, J. Vac. Sci. Technol. A, 30, 030802 (2012).

[9] A. Franceschetti, L. W. Wang, G. Bester, A. Zunger, Nano Letters, 6, 5, 1069-1074 (2006).

[10] I-H. Chu, M. Radulaski, N. Vukmirovic, H-P. Cheng, L-W. Wang, J. Phys. Chem. C, 115, 21409–21415 (2011).

[11] R. A. Marcus, J. Chem. Phys., 24, 966 (1956).

[12] Q. Wu, T. V. Voorhis, J. Chem. Phys., 125, 164105 (2006).

[13] H. K. Rhys, A. Proc. R. Soc., 204, 406 (1950).

[14] M. Lax, J. Chem. Phys., 20, 1752 (1952).

[15] G. J. Nan, X. D. Yang, L. J. Wang, Z. G. Shuai, Y. Zhao, Phys. Rev. B, 79, 115203 (2009).

[16] D. V. Talapin, J.-S. Lee, M. V. Kovalenko, E. V. Shevchenko, Chem. Rev. 110, 389 (2010).

[17] M. V. Kovalenko, M. Scheele, D. V. Talapin, Science 324, 1417 (2009).

[18] D. B. Mitzi, L. L. Kosbar, C. E. Murray, M. Copel, A. Afzali, Nature, 428, 299 (2004).

[19] W. J. Baumgardner, J. J. Choi, K. Bian, L. Fitting Kourkoutis, D.-M. Smilgies, M. O. Thompson, T. Hanrath, ACS Nano 5, 7010 (2011).

[20] W. Hu, R. Henderson, Y. Zhang, G. You, L. Wei, Y. Bai, J. Wang, J. Xu, Nanotech., 23, 375202 (2012).

CHAPTER 7

Conclusions

Over the last two decades the field of colloidal NCs has grown immensely, from early studies colloidal NC synthesis and their fundamental structure-property relationships to the creation of isolated NCs with programmable optoelectronic properties and their directed self-assembly into functional superstructures. The field has progressed from its humble origins as a mere theoretical model of artificial solids to being a machine to guide the study and engineering of NCs with properties by design. An improved understanding and control over the NC surface properties has been essential in this regard. A deep understanding of interfacial properties has played a critical role in transforming the field from a mere understanding of growth and stabilization to controlled coupling and self-assembly of these NC solids. But despite the tremendous progress observed in the field, several critical deficiencies remain in the knowledge of the fundamental physics guiding the behavior of these NC assemblies. From a technological perspective, some of the key challenges today concern inter-dot coupling and device integration and the resolution of these challenges are essential for continued progress and development of the field and the fabrication of commercially viable NC based devices. Some of the key challenges faced by NC based technologies today are (i) the detailed physiochemical nature of the NC surface, (ii) the inherent inhomogeneity of the NC ensemble, (iii) the true electronic structure of NC solid, and (iv) the connection between NC model systems in the laboratory and commercially deployable NC technologies. Nevertheless, colloidal synthesis and self-assembly of these semiconductor materials offer significant advantages of precision size and shape engineering over current lithographic techniques available

today. The modular design of electronic materials by assembling these solution-processed functional building blocks can make a significant impact on the development of novel materials and devices.

One of the biggest challenges in the field is the detailed physical and chemical nature of the NC surface. There are several open questions that need to be addressed such as the binding of ligands to the NC surface, the grafting density of ligands, preferential binding to different facets, reconstruction and nature of the facets themselves and most importantly the influence of the specific ligand chemistry and surface faceting on the electronic structure of the NC and the coupling between NCs in a solid. To sustain the rapid pace of progress in NC based energy technologies, detailed *ab initio* models of charge transport within and across NCs films are therefore, required.

In this thesis, in summary, we have addressed the following topics:

7.1 Behavior of isolated Nanocrystals

We presented an explicit all-atom representation of nanocrystals, "capped" with alkyl chain ligands, of experimentally relevant sizes in vacuum. The behavior of these ligand-capped NCs, determined by the explicit all-atom model, can serve as a reference standard for future coarse-graining of ligands using united atom models. We showed that several different parameters that control the conformations adopted by the ligands can lead to the same mechanism of interaction between the NCs. Ligands on very small (3 nm) NCs do not interdigitate, ligands on larger NCs (6 nm) exhibit interdigitatation alone and ligands on intermediate-sized (4 nm) NCs exhibit some interdigitation and some ligand wrapping. These mechanistically driven results can also be obtained by varying the ligand density or

the length of the ligands. We also analyzed united atom representations of NCs and found that the specific *choice* of the united atom potential model is crucial for the prediction of properties of the NC system and care must be taken, while transitioning from explicit models to coarse grained models, in choosing one coarse grained model over another.

7.2 Influence of solvent on Nanocrystal Self-Assembly

We presented a study of nanocrystal superlattice interactions in the presence of two explicitly modeled solvents, hexane and toluene, used commonly in experiments. The solvent molecules penetrate the entire ligand corona of the nanocrystals thereby swelling the corona and effectively making the nanocrystals appear more spherical in nature. The *amount* of solvent within the ligand corona, however, depends on the structure of the solvent molecule as well the strength of interaction of the solvent molecules between themselves as well as with the ligands. The free energies of 3-D superlattices in the presence of these solvents are instrumental in determining the stability and preferred superlattice symmetry as the length of the capping ligand molecules (characterized by the ratio L/r) is varied, as well as the amount of residual solvent in the "dry" superlattice. We have shown how the knowledge of the microscopic scale of solvent-ligand interactions can be used to understand the macroscopic-scale superlattice structure of nanocrystal films and by choosing the type of solvent used and the drying conditions as well as the type of ligand used, these results can be utilized to selectively drive the self-assembly process to achieve the desired superlattice symmetry for nanocrystal films.

7.3 Electronic Structure of Nanocrystals

We have presented a detailed calculation of electronic structure of PbSe NC systems using DFT. We have calculated the structure of the bare NCs and also shown how

reconstruction of the surface can lower the energy of the NC. We have shown a method of ligand attachment which ensures charge neutrality of the whole NC. The density of states is quite symmetric about the band gap. The ligand states are well mixed with the core atoms and do not directly contribute greatly towards the frontier orbitals but lie deep in the DOS. The electron and hole coupling between NCs depend on the overlap of the LUMO and HOMO wavefunctions respectively determined by the spatial distribution and orientation of the respective wavefunctions which depends on the shape of the NC and the areas of the [100] and [111] facets. We have shown that orientational alignment of the NC itself can lead to stronger or weaker coupling and charge transfer. We have also studied the effect of ligands on the electronic coupling. If the details of ligand attachments were known in advance such as described in this thesis, then one could potentially seek to make self-assembled superlattices with an appropriate symmetry to produce the greatest charge transfer possible.

In summary, the field of synthesizing and utilizing colloidal NCs to fabricate novel and precise materials and devices has shown tremendous potential and progress over the last couple of decades. However, a number of key challenges need to be surmounted if the rapid progress is to continue and if NC based devices are to become commercially deployable. We hope that the information in this thesis can be used to improve our understanding of these unique materials and has addressed some of the unknowns expressed above.